High power laser systems with actuated beam delivery

Ian Andrew Baker

Submitted for the degree of Doctor of Engineering

Heriot-Watt University

School of Engineering and Physical Sciences
05/04/2017

ABSTRACT

Lasers with kilowatt average powers and pulse durations in the nanosecond range are used for a variety of applications requiring surface alteration or removal. A novel surface removal application required development of a pulsed laser beam delivery system to track and target the position of a substrate to deliver a shaped homogenised beam to its surface. A solution is investigated using a fibre delivered multi-spatial mode laser source a seam tracking vision system, customised electronics and software algorithms, an inline Risley prism optical actuator and a beam shaping optical delivery system. The system has been modelled from the laser cavity through to final beam delivery and this approach yields a novel, compact size currently not available commercially and a highly homogenised laser beam, free of laser speckle, with edge widths of <160 µm. Beam shaping for spot sizes in the range of 0.3 mm - 3.0 mm, actuation ranges of up to ±10 mm and tracking accuracies of <50 µm are demonstrated when tracking substrate surface features of size >50 µm. The system reduces substrate placement tolerances and delivers the laser power reproducibly to the target region. At the time of writing, three tracking systems are utilised in heavy industry environments producing, to date, a cumulative output of six million substrates. In addition, four systems utilising the optical techniques detailed in this thesis have also been also operating in heavy industrial environments since 2015.

DEDICATION

I dedicate this thesis to my partner Samantha and daughter Chloe without whose support and understanding this would not have been possible. I would also like to acknowledge Dr Nick Hay, Dr Young Kwon and Professor Derryck Reid for their continual guidance and support throughout this project. I extend thanks to the team at Powerlase Photonics Ltd with a special thank you to HyeonSeok So for support with the electronics and algorithm development in this project.

DECLARATION STATEMENT

ACADEMIC REGISTRY
Research Thesis Submission

Name:	Ian Andrew Baker		
School/PGI:	School of Engineering and Physical Sciences		
Version: *(i.e. First, Resubmission, Final)*	Final	Degree Sought (Award **and** Subject area)	Engineering Doctorate (EngD)

Declaration

In accordance with the appropriate regulations I hereby submit my thesis and I declare that:

1) the thesis embodies the results of my own work and has been composed by myself
2) where appropriate, I have made acknowledgement of the work of others and have made reference to work carried out in collaboration with other persons
3) the thesis is the correct version of the thesis for submission and is the same version as any electronic versions submitted*.
4) my thesis for the award referred to, deposited in the Heriot-Watt University Library, should be made available for loan or photocopying and be available via the Institutional Repository, subject to such conditions as the Librarian may require
5) I understand that as a student of the University I am required to abide by the Regulations of the University and to conform to its discipline.

* *Please note that it is the responsibility of the candidate to ensure that the correct version of the thesis is submitted.*

Signature of Candidate:		Date:	

Submission

Submitted By *(name in capitals):*	
Signature of Individual Submitting:	
Date Submitted:	

For Completion in the Student Service Centre (SSC)

Received in the SSC by *(name in capitals):*			
1.1 Method of Submission *(Handed in to SSC; posted through internal/external mail):*			
1.2 E-thesis Submitted (**mandatory for final theses)**			
Signature:		Date:	

TABLE OF CONTENTS

LISTS OF TABLES AND FIGURES

Chapter 1 - Introduction to laser systems with high peak and high average power

1.1 High power lasers and applications

As of 2013 the market for lasers worldwide was estimated to be \$8.5 billion US dollars [1]. Of that market, \$1.7 billion (approximately 20%) is accounted for by lasers above 1kW output power that are used for material processing, such as welding, surface preparation and machining. Within this laser market there are various laser technologies that service the different applications. Solid state lasers serve applications that require high pulse energy and average powers and are typically based upon Nd:YAG, or other crystal gain media and these lasers account for a total market by revenue of \$130 million. Lasers with fibre based gain media, which typically service the continuous wave (CW) and some pulsed applications, account for \$779 million and carbon dioxide (CO_2) lasers, which predominantly service welding applications account for \$500 million. According to [1] there is little expected growth in the overall sector up to 2017 but an increasing trend is foreseen that the fibre laser technologies are replacing much of the CO_2 applications and also pushing into areas where they can displace much of the solid state laser applications. Fibre lasers, until recently, have struggled to displace solid state lasers as laser damage thresholds obtainable in the free space laser systems tend to exceed those which are achievable within fibre media [2] and this largely prevents them from entering this niche market sector, where large peak powers and high average powers are required and provides a barrier to entry. However fibre lasers are starting to challenge the solid state market sector as developments are made.

Market segmentation of the laser types into their application areas can be performed by wavelength, power and whether the lasers are continuous wave (CW) or pulsed. CO_2 lasers have relatively long wavelengths between 9.4 μm and 10.4 μm, when compared to the other laser types in this category. These longer wavelengths absorb well in water and make them ideal for surgical cutting, where the laser also acts to cauterise. The scalability of CO_2 lasers to very high CW powers in excess of 30 kW or more power also make them ideal for welding and cutting applications or surface modification applications where CW power can be applied to large areas, such as paint removal. A weakness of these lasers however is the cost of ownership and maintenance, another more subtle weakness is that the laser radiation cannot be delivered to the target substrates using fibre, due to strong absorption in fused silica at these wavelengths. The delivery is normally via a precision mechanical mirror arrangement covered in beam tube to protect the user.

Fibre lasers are typically based around Yb:YAG with output wavelengths between 1060 nm and 1070 nm, commercial CW fibre lasers are now routinely in excess of 10 kW. The wavelength and fibre delivery of these lasers is ideal for industrial applications and fibre lasers also service a variety of wavelengths by external non-linear crystals, typically 532 nm or 355 nm in a similar manner to the solid state lasers. The amplification of the laser beam in the fibre medium also enables high powers combined with very low M^2 making them highly suitable for precision cutting. Pulsed fibre lasers do exist commercially but they are limited in their output pulse energies due to the high energy densities of the fibre and, in particular, the damage to the ends of the fibres when pulsed strongly, most commercial fibre lasers are less than 50 mJ per pulse. Pulsing of these lasers is commonly attained using a pulsed semiconductor seed laser, amplified by a powerful fibre based amplifier section; this technique can also lead a distorted pulse shape when compared to solid state lasers.

Solid state lasers are commonly based upon Nd:YAG lasers that emit at 1064 nm, and form the main products of Powerlase Photonics. These lasers can be designed to achieve a combination of high peak and average power. They can also be frequency doubled via a second harmonic generation crystal to a wavelength of 532 nm and also tripled to wavelength a UV wavelength of 355 nm. Generation of pulses in these lasers is commonly achieved by Q-switching the cavity via means of modulating the intra-cavity losses, typically using an Acousto-Optic modulator (AOM). The AOM when energised with high frequency acoustics will diffract the beam away from the feedback path and hence stop the laser from lasing. This cause a considerable storage of optical power within the gain Nd:YAG gain medium analogous to electrically charging a capacitor. When the electrical power to the AOM is turned off the laser feedback condition returns and the laser produces a laser pulse which can easily be several MW. By periodically modulating the AOM a stable pulse condition can be reached simultaneously enabling large peak powers, typically MW and average power of many kW. The pulse shape is almost Gaussian in temporal appearance much cleaner than pulse shapes achieved with fibre lasers. The free space design of these lasers enables large mode volumes and hence internal fluence of the laser system can be managed to avoid damage of the internal components. These features of the solid state lasers make them ideal for application where combinations of high peak and average power are required, such as larger area processing like green laser annealing and manufacturing where the higher average powers translate into optimised production line speeds. A key weakness of the solid state lasers however is they are more expensive than the fibre lasers, which, as per the market research, are rapidly encroaching on this market space as the fibre laser technology develops.

This thesis concerns applications based upon free space Nd:YAG solid state lasers within a niche market sector where large peak and average powers are needed simultaneously. The laser emission is typically in the Infrared (IR) region of the electromagnetic spectrum, most typically with an output wavelength of 1064 nm or a frequency doubled or tripled beam via a non-linear crystal at 532 nm and 355 nm respectively. Given the increased competition that the solid state lasers face [3], and the pressure from rival laser technologies [4-6], such as ever higher power pulsed fibre lasers, there is a need to develop the solid state laser technology as a system level offering. This approach is to deliver more functionality to the system and solving installation challenges as part of the customer package, thus delivering a complete turnkey system. Delivering the system into viable production processing as a whole unit and maintaining comprehensive service availability is seen as crucial to maintaining business.

The main topic of this thesis is a response to a customer request that requires not only the laser technology but a new approach that solves mechanical and optical delivery to the customer's substrates within tight spatial constraints of their existing machinery. The technical requirement is to deliver infrared laser radiation to the surface of the substrate with a rectangular homogenised profile with as large a depth of focus as possible. Actuation of the beam is required to eliminate mechanical loading errors of the substrates and lateral motion of the substrates during production. Modifications to the machine are permitted, but only to allow physical attachment of the beam delivery system and no parts can be removed that would otherwise reduce the functionality of the original system. No major physical modifications are permitted and the tight spatial envelope is non-negotiable. The transmission of the radiation to the substrate has also to be as efficient as possible.

The context of this system is a Q switched pulsed laser and beam delivery system that removes several layers of the target material to a defined thickness. The purpose of the process is to remove a thickness of surface layer from the material to clean the metal substrate before it continues to another following process. The Fluence required to initiate the removal the material is in excess of 10 J/cm^2 and the substrate is in motion at a constant velocity beneath the processing heads less than 250 mm/s, the depth of focus must accommodate all substrate thickness variants up to 3 mm step heights. The machine space constraints of the system are the main driver for adopting a novel approach to the beam delivery, as the permitted size for the processing heads is analogous to a tube of square cross section approximately 100 mm × 160 mm × 500 mm wide. As described in later chapters the combination of size, beam shaping and actuation was, at the time of writing, not commercially available and required a new approach. Figure 1 shows the system diagram of the whole complete system.

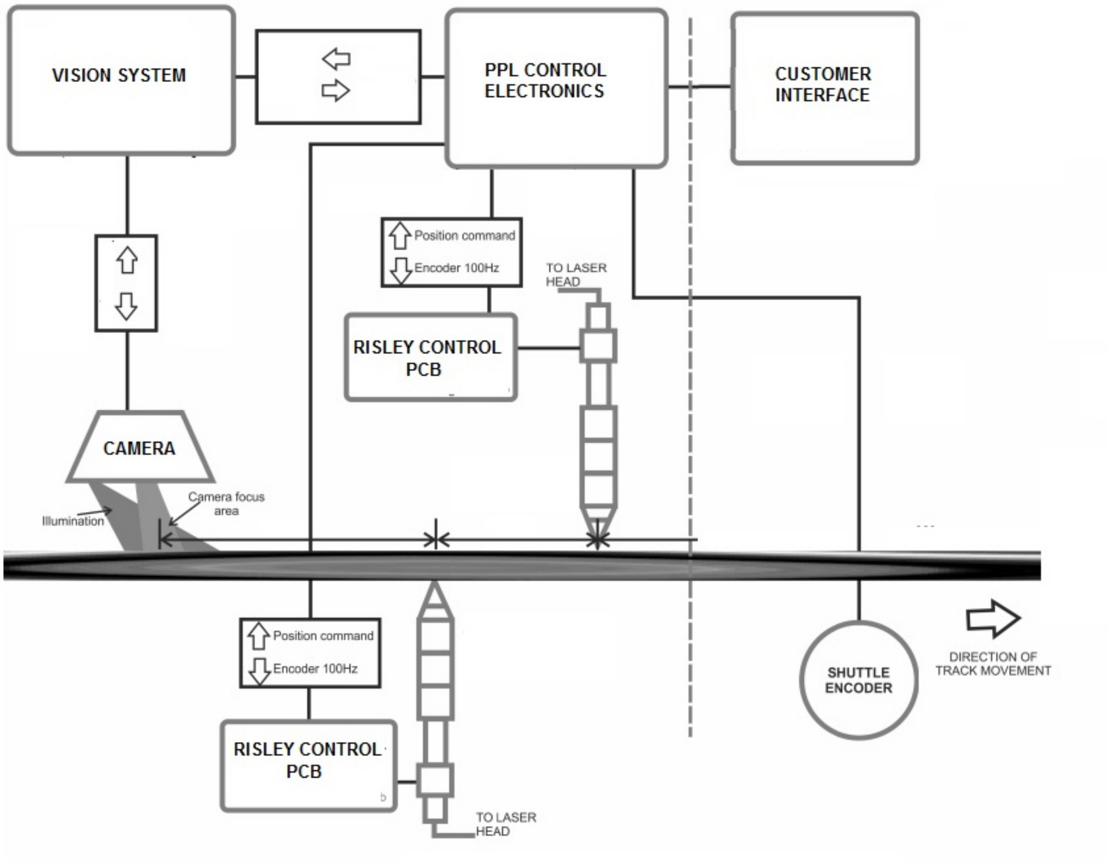

Figure 1 – Final system diagram.

The system is split into its constituent sub-systems and a literature review undertaken to understand the state of the art technologies from both academic and commercial literature. The sub-system functions required are: a high power pulsed laser, laser beam shaping and homogenisation of the laser beam, vision tracking and targeting of a feature on a substrate and synchronised actuation of the beam onto the substrate via beam processing delivery head. The following sections detail the background research on each of the sub systems.

1.1.1 Beam shaping

The laser product offering from Powerlase is a high power IR laser with $16 < M^2 < 30$ with average powers up to 2 kW and peak powers up to 3 MW. The laser cavity is Q-switched between 10 - 20 kHz achieving peak energies of up to 160 mJ, the average power output of the laser and hence the delivered pulse energy is controlled via an internal attenuator which taps light away from the main beam. The oscillator is kept at a constant internal power to operate where the laser has the most stable operation correlating to the optimal thermal lens in the Nd:YAG gain medium. Any beam shaping technology considered needs to take into account the large spatial mode content and the damage thresholds associated with these laser beams. Beam shaping and homogenisation for these lasers are not generally commercially available in the form required. Techniques found in academic literature involved refractive beam shaping using cylinder form lenses or freeform optical surfaces to shape the beam [7-11]. Often these techniques are appropriate for round top hat profiles but required loss if power rectangular profile was created by truncating the beam. Diffractive beam shaping was researched from fundamental literature [12] and also application data [13-15], where computer generated holograms, often referred to as kinoforms, are used. The diffractive techniques typically generate profiles that are not homogenous, due to laser speckle and also tended to have large (> 15%) scattering losses associated with them. However they remain a source of interest due to the flexibility of the shape of the irradiance pattern, also little in the literature applies holographic imaging to lasers with larger M^2 values. A beam homogenisation technique for high power lasers using a fibre as the homogenising medium with varying cores was reviewed [16], this paper details delivery of a highly homogenised beam of high power multimode lasers similar to those provided by Powerlase. These fibres emitted the homogenised beam with a relatively small exit numerical aperture (NA). This small NA is congruent with the need to design the beam delivery optics within a small volume to deliver the laser emission from the fibre exit to the target substrate. This fibre based approach coupled with the refractive beam shaping is believed the most likely to yield the simplest solution with the highest transmission, homogeneity and resistance to laser damage.

1.1.2 Vision and tracking systems

There is a large amount of vision tracking information available for laser delivery for continuous wave welding lasers and also a large selection of research activity based upon vision analysis of the seam position. An approach detailed in [17] locates the seam between the substrates by image processing of the associated weld pool and uses a coding technique to stabilise the tracked weld seam position by using digitally buffered weld position data or rolling algorithms [18-19]. A very important and frequently cited algorithm for achieving this was the Kalman algorithm [20], or Kalman filter, which removes noise from the signal and predicts the future position of a data point from previously recorded data. This approach forms the basis of much of the tracking techniques reviewed. The acquisition of the position of the seam was predominantly performed via an optical technique, either a triangulation sensor approach or via a suitably illuminated and imaged of the area of the seam [21-22]. One approach coupled weld pool optical imagery with magnetic imagery of the seam [23]. Commercially there are many products aimed at this seam tracking market complete with their own proprietary algorithms and acquisition techniques and therefore there is little value for the development of a wholly new system for this development project, hence a selection of commercial systems were reviewed that would perform the task of tracking the target with a simple output.

1.1.3 Actuated beam delivery systems

There are several actuated beam delivery systems that are commercially available for high power CW weld lasers their processing heads. At the time of development they provided no beam shaping functionality as they are based upon diffraction limited imaging of the laser beam in order to maximise the fluence at the weld surface. Actuation is very common for these laser systems and a variety of commercially available actuated processing heads are shown in the following figures, with a short description of each.

Figure 2 shows a processing head from the manufacturer highyag that delivers a laser beam to a focus at the substrate where the actuation by physical rotation of the optical train by a stepper motor in the region indicated. The visual seam tracking signal fed to the actuator can be performed by mounting a camera at either an offset location or co-linear with the delivered laser beam via an imaging camera with a dichroic mirror.

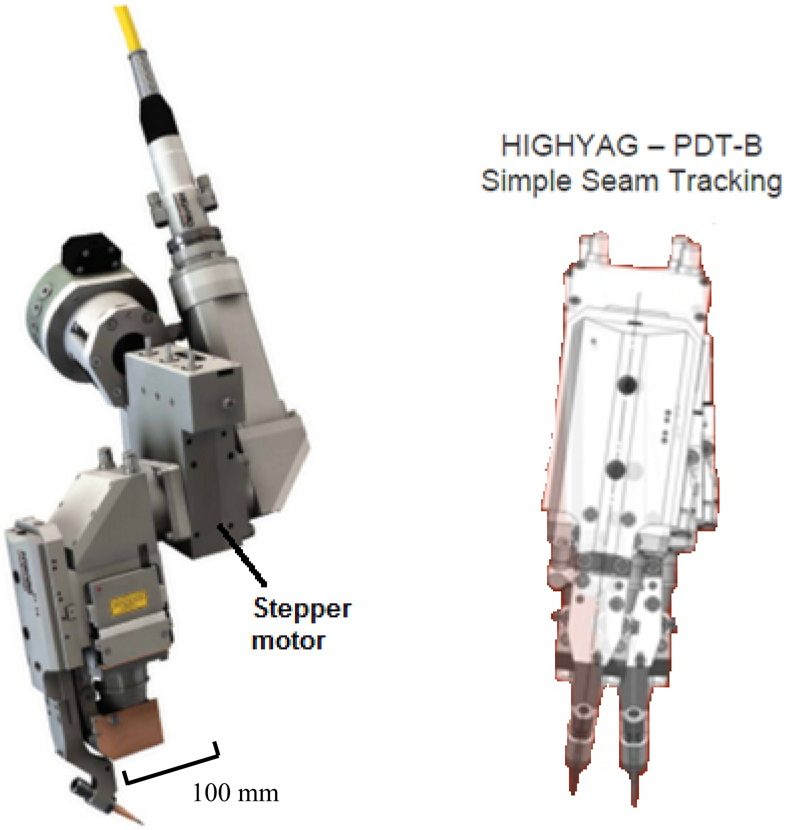

Figure 2 – A seam tracking system offered by highyag which uses a rotating joint to actuate the beam [24].

A key performance parameter required by the customer is that the whole seam tracking systems need to fit within a narrow space envelope 100 mm wide. The physical size of the highyag system is shown in an extract from their website in Figure 3, the 198.5 mm dimension highlighted would not fit within the customer's space constraints and this form of lateral movement would have been a collision risk to the processing head and the shuttle that moved the substrates, the shuttle weighed several tonnes and in the case of the a collision would likely fatally shear the processing head.

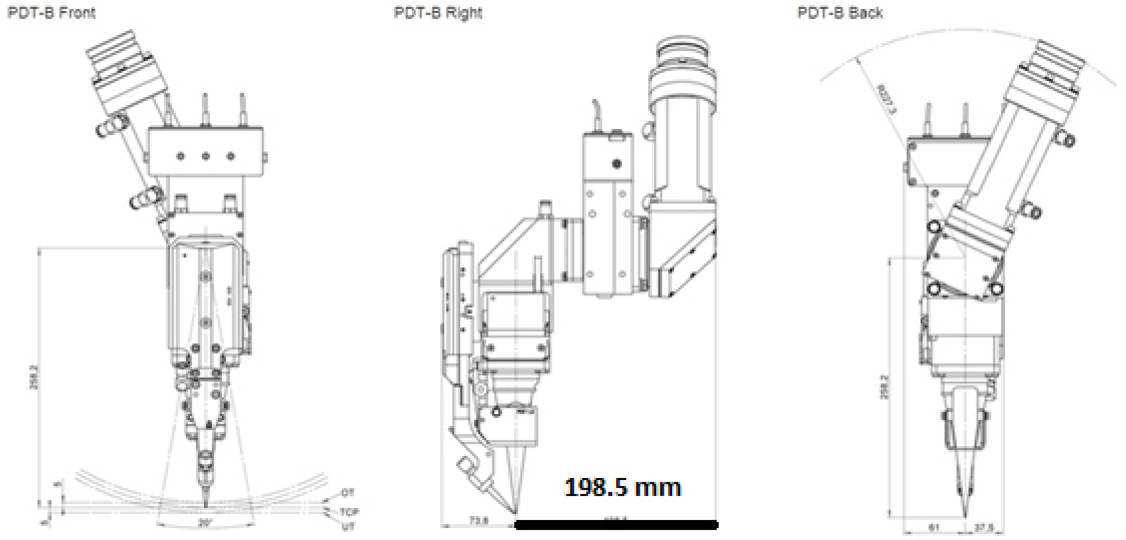

Figure 3 – Highyag processing head and seam tracker system showing dimensions [24].

Another approach to the actuation of the processing heads is shown in Figure 4 in a system provided by Precitec. This system also does not offer beam shaping. Actuation of the beam is provided by a galvanometer embedded in the optical path from the fibre to the substrate. This approach does not require the physical movement of the head, which is an advantage but, this approach also requires a twin 90º mirror arrangement to deflect the beam, which increases the physical size of the unit.

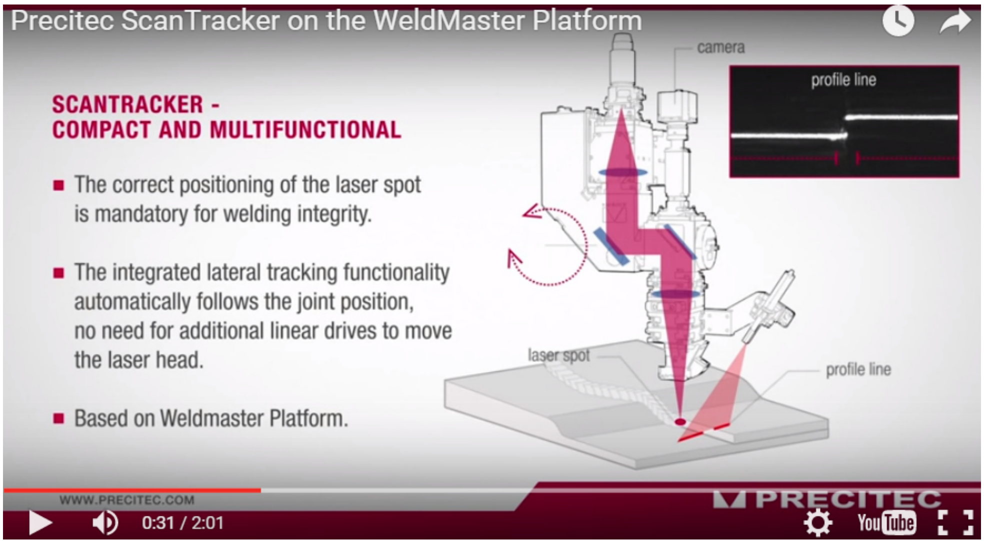

Precitec ScanTracker on the WeldMaster Platform

SCANTRACKER -
COMPACT AND MULTIFUNCTIONAL

- The correct positioning of the laser spot is mandatory for welding integrity.
- The integrated lateral tracking functionality automatically follows the joint position, no need for additional linear drives to move the laser head.
- Based on Weldmaster Platform.

Figure 4 – A commercial screenshot of a seam tracker system offered by Precitec utilising a galvanometer [25].

A major disadvantage of the 90º beam deflection is that the customer requires a relatively large physical standoff distance from the process to the final focussing lens to avoid debris form the process. For a given numerical aperture, the standoff distance that is required always leads to a large separation being required between the turning mirrors, as shown in Figure 5 below. A typical NA for the proposed laser system would be 0.1 and a typical standoff distance of 200 mm yields approximately a 40 mm beam waist at the mirrors, the mirror pair would therefore consume a width of 80 mm minimum before the size of the optical mounts were even considered.

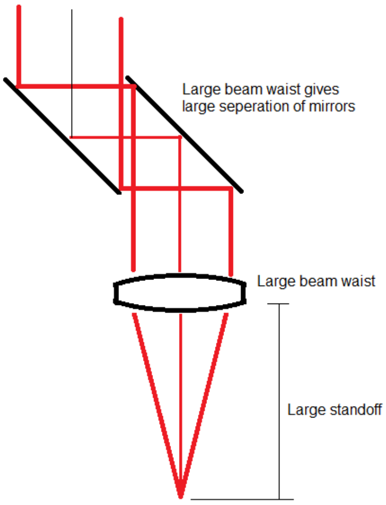

Figure 5 – Graphic showing that a large standoff distance form the process to the first optics results in a larger beam waist at the 90° turning mirrors.

Because of the mirrors size they also have a relatively large inertial mass, which requires a powerful galvanometer to actuate mirror for a given actuation speed, this issue also extended to gimbal based actuation [26]. The galvanometer motors for the required speeds are large enough to cause further difficulty when fitting to available space envelope available for the processing heads. Galvanometer beam deflection systems are readily commercially available and do provide the optical performance required [27] but despite some attempts at compact galvanometer approaches to beam deflection [28], this approach was not considered viable for this application, as it is unlikely they can be made to fit the volume. A brief comparison of power consumption between the Risely prism and a galvanometer shows them to be comparable at start up but the Risley is more efficient during operation. An Optra RP25S Risely prism consumes 200W upon start up and then reduces to less than 24W during production. A comparable Scanlab galvanometer consumes 180W continuously.

Moving the entire processing head via physical actuators is also a common approach and observed often during commercial studies. This is either implemented by directly driving the processing head position using a linear stage or by driving the processing head position on an arc. Issues with this direct driving of the processing head in this manner surround the inertial mass of the processing head. The processing heads typically have masses in excess of 5kg and hence require powerful motors to actuate them with any speed. This approach is found to be used when the substrate moved slowly, but when the lateral movement is rapid it invites control and oscillation issues for fast moving variations. Again given the space constraints (100 mm × 160 mm × 500 mm) this approach was not considered viable.

An approach worthy of note and particularly relevant to this industrial field is the mounting of the processing beam delivery heads directly onto specialist robot arms [21]. These robots are both very quick and very powerful but also occupy a large volume. The seam tracking systems, hardware and software are found to be often written specifically for this scenario. The seam tracker vision system presented in this report is specifically designed for this configuration and maintains its seam tracking by minimising the deviation of the vision feedback of the seam from the physical centre of the camera, this deviation signal is then sent to the robot arm actuators. This approach of minimising the deviation from the seam to the camera centre is not practical for the application targeted by this thesis, as the camera is in a stationary fixed position and not attached to a freely moving robot arm. This causes challenges with the implementation of the system as the main output controls of the laser path finder system as described later in chapter 4 are based upon the camera's free movement.

A review of academic texts yields some more unconventional approaches to beam manipulation, [29] and [30] detail a number of techniques for beam steering for various applications. Approaches based upon Mechanical Optical Electric Machines (MOEMs) [31], these have the potential to give compact beam steering but are unlikely to survive the power requirements of the laser, likewise for grating structures [32] or phased arrays [33-34]. Acousto-optic deflection was also studied [35], the technology is commonly used in pulsed lasers and is robust to the laser damage but the technique involves diffraction of the laser beam to deflect the beam and although larger diffraction angle are possible, a significant proportion, up to 50%, of the light is lost into other diffracted orders [36]. Losses of this magnitude are not acceptable as transmission of > 90% were desired and also the power scattered into the other orders would need to be managed in order not to cause damage the processing head optic.

A technology frequently used to deliver laser beams onto a target with a high degree of accuracy is the Risley prism [37-44]. A Risley prism is a pair of wedge prisms that can be rotationally oriented to alter the pointing direction of a collimated laser beam or other optical path. A basic schematic of the principle is given in Figure 6 below.

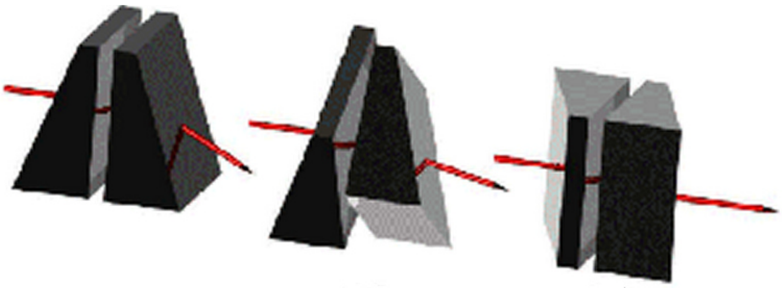

Figure 6 – General principle of a Risley Prism.

This technology is capable of steering a laser beam to a very high degree of precision [41], accuracy and speed [42]. The angular range of motion is tuneable by choosing different wedge angles for the prisms. Control of the Risley prism, in particular the inverse solution of the targeting parameters is a considerable challenge in a two dimensional plane [43-44] as there are frequently multiple prism orientations that correspond to the same angular output or input angles. This is unlikely to cause an issue in the application requested by the customer as only a linear motion in one axis is required. The speed, accuracy and the compact in-line nature of the beam steering using Risley prisms is seen as an advantage of the technology. It also has the potential to be a modular technique that could be appended to different processing head designs.

The commercial and academic searches and review reveal that there is no complete supplier of the laser and beam delivery system that is required by the customer and no complete optical delivery system that can perform the complete task of beam shaping, homogenisation and beam actuation in the spatial envelope permitted. An approach of utilising various commercial technologies and a novel approach to the beam actuation using Risley prisms is presented in this thesis that resolves this challenge. The author was responsible for the full delivery of this project including, specification, budget, customer interface, schedule, multi-disciplinary team management and technical performance. All optical and optical system designs in this thesis are solely designed by the author, system tests, field test and customer installation are also the sole responsibility of the author. Mechanical and electronic designs and implementations were developed with assistance from specialists within Powerlase Ltd and are credited where applicable in the text and acknowledgements.

1.2 Roadmap of the thesis

This thesis describes the full design of the system from the design of the laser that produces the laser radiation, through to the final delivery of the radiation to the substrate in the format required by the end user. The overall roadmap of the thesis is shown in Figure 7 and forms a narrative of the system approach used to design, manage risk, develop and successfully deploy the system into serial manufacture. Beyond this introductory chapter, the description of this process is given as follows; chapter 2 details modelling techniques that are applied to the solid state laser technology to predict and design the key laser beam parameters. Chapter 3 details the development of the fibre coupling homogenisation of the laser beam and beam shaping optics and the final beam shaped delivery. Chapter 4 details the development of a vison tracking and actuated beam delivery system including optics, electronics, software algorithms, mechanics and system design used to track and process substrates. Chapter 5 concludes with summary findings and conclusions based upon the deployment of this technology and suggestions to further work that can be performed to continue to develop this technology.

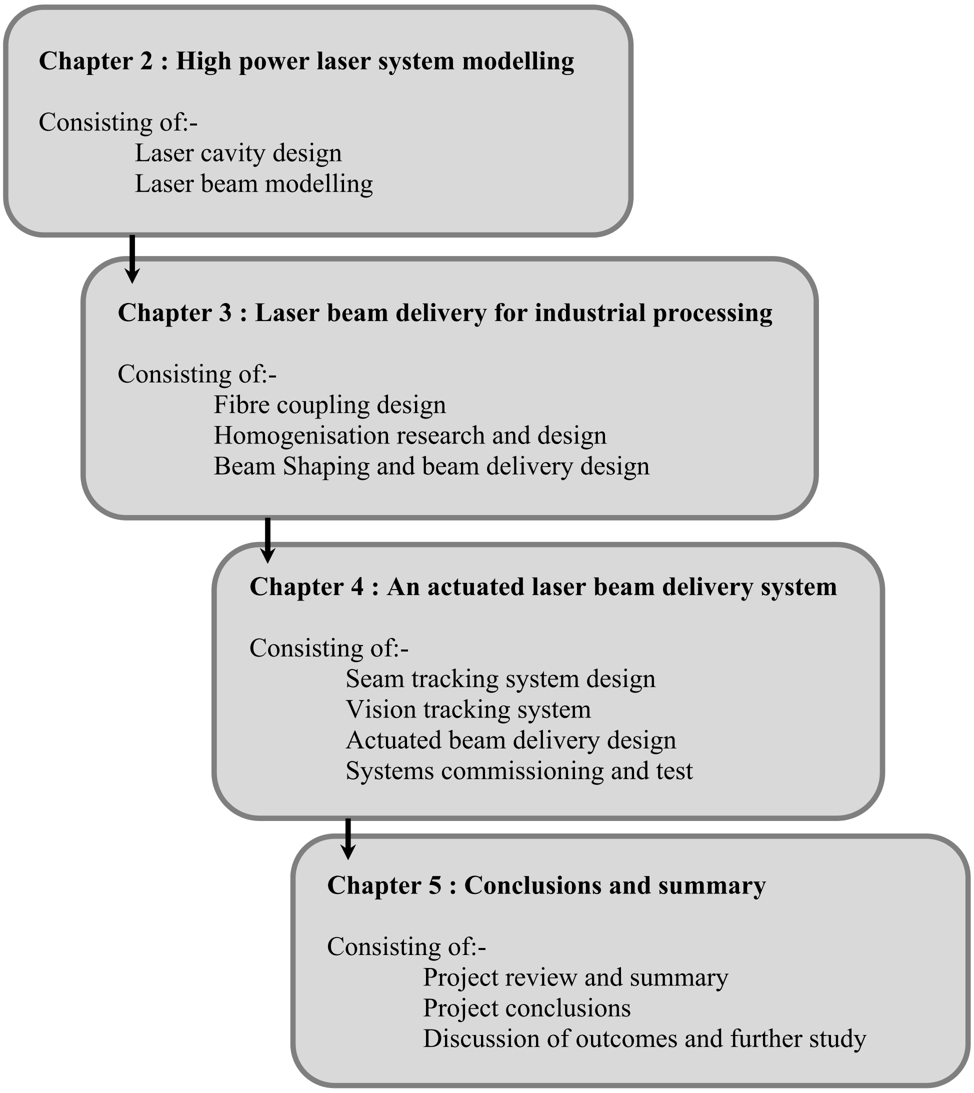

Figure 7 – Thesis roadmap.

Chapter 2 - High power laser system modelling

2.1 Introduction and motivation for the research

The laser technology to generate the laser beam for this project is a multi-spatial mode, high power diode side-pumped solid state laser (DPSS). This laser is based upon the well-known neodymium yttrium garnet (Nd:YAG) laser crystal gain material. The laser architecture is a five-fold side pumped cylindrical rod laser, consistent with the Rigel i-series lasers as produced by Powerlase Photonics Limited. This laser architecture generates laser beams with a wavelength of 1064 nm and with an $M^2 > 15$, solid state lasers of this design generate significant thermal lensing within the Nd:YAG gain medium as a result of the non-radiative decay of a proportion of the pump light. This significantly changes the optical characteristics of the laser as the pump power increases, the changing optical behaviour with increasing pump power laser creates a challenge to design and optimise both the laser cavity and the amplifier sections of these lasers systems. The ability to model and understand the behaviour of these laser cavities, positions of internal mirrors and apertures is of crucial importance to the development of this laser beam delivery system and an iterative modelling approach is required to facilitate the design of the laser systems.

Modelling techniques based upon ray tracing are generally not successful for modelling this type of laser system due diffraction effects that are still observable even in strongly multimode laser beams. A good practical example of this is the case of a multimode collimated beam, using a ray tracing method a collimated beam would continue propagation forever with no change in beam radius, whereas in reality the beam is observed to diverge as it propagates in accordance with the natural diffractive properties of the beam [45]. A reasonable approach to overcome this issue is to model the laser beam using an optical field propagation algorithm, such as Finite Element Analysis (FEA), Finite Difference (FD), or the beam propagation method (BPM), all of which are commonly used to model low M^2 laser beams or confined waveguide modes [46-48]. To model the multimode laser cavities the field modelling techniques need to repeatedly cycle a field through the cavity and requires significant diffractive losses to resolve the shape of the beam though this iterative procedure. In the specific case of side pumped, free space Nd:YAG lasers however the cavity diffraction losses, per pass, are typically very small and the method is typically overwhelmed by the combination of the number of spatial modes and the small diffraction losses of the cavity and fails to settle within a reasonable timeframe. The large number of spatial modes also causes issues with prediction of the beam irradiance profile. It is impractical to reconstruct the beam shape from the sum of its constituent individual Laguerre-Hermite spatial modes, as the precise power content of each mode cannot be exactly known or changes dynamically.

A technique that is fast, reliable and straightforward that adequately models both the cavity and the free space propagation of these $M^2 > 5$ laser beams is the ABCD method [47][49]. It is neither field modelling nor ray tracing, but is an envelope solution to the paraxial optical field equation [50] the solution gives a contour of the beam, such as a $1/e^2$ slicing level, Full Width Half Maximum (FWHM) or a second moment [51] beam waist value without the need to express details of the mode content or irradiance profile. The model uses the TE_{00} mode profile as a guide beam and then scales the propagation as a beam that is M times the diameter and M times the divergence of this Gaussian beam [51] as confined within the laser cavity, this guide beam is referred to as the embedded Gaussian in [51]. Another key advantage of the ABCD techniques is that it is directly compatible with the mathematics of paraxial ray tracing matrices [52] this is useful where there is interest in the export and comparison of ray models from the ABCD data.

A proprietary model was developed upon mathematical descriptions of the technique in references [50] and [52-54]. Although commercial products were available (Paraxia^{TM} and LASCAD^{TM}), it was decided to develop code in Matlab^{TM}, as this permitted the customisation of the system and modelling code. The commercial code was found to be biased either towards free space or cavity modelling and for this project a combination of both was required. As an additional novelty, the model is also able to predict beams produced in laser cavities with multiple apertures spaced along the cavity. This is not found to be a common feature in commercial software. Along with the practical learning benefit of the coding the ABCD matrix, the model is used regularly to model both laser cavities and free space propagation of the Powerlase laser systems. The model components are also developed and standardised in order to re-use designs of gain sections and control laser configurations.

The ABCD model written is found to be of sufficient accuracy to model the position of the internal active optical components of a laser cavity, with some additional experimental adjustment. The ABCD model is then found to be highly accurate in modelling free space propagation of the multimode laser beams permitting the subsequent accurate design of the free space component positions and power. A brief mathematical overview of the techniques and its application are given in the following sections.

2.2 Brief mathematical overview of technique

The ABCD matrix method is described by a solution to the paraxial wave Eqn. (1) as given after reference [50]

$$i\frac{\partial u}{\partial Z} + \nabla_{XY}{}^{2}u + k^{2}u = 0 \tag{1}$$

An example solution of this equation can be given by reducing Eqn. (1) into just two dimensions, *X* and *Z*, $\partial^2 u/\partial Y^2 = 0$, is given by Eqn. (2)

$$u(X,Z) = e^{\frac{i\pi X^2}{\lambda}\left(\frac{1}{q(Z)}\right)} \tag{2}$$

The solution of the complex beam parameter *q* in Eqn. (2) is given by a complex number, which contains information about the laser beams phase (or radius) and its width, *w* [50] and [52] and the relationship between these parameters is given by Eqn. (3).

$$\frac{1}{q} = \frac{1}{R(Z)} - \frac{i\lambda}{\pi w(Z)^2 n} \tag{3}$$

In Eqn. (3), *R* is the phase front radius, λ is the wavelength of the laser beam, *w* is the beam waist of the 'embedded Gaussian' [51] and *n* is the refractive index that the laser beam is propagating in. The calculation of the *q* factor is possible at any position in Z and hence the beam radius and phase front radius can be determined for any propagation in *Z*. Calculation of the variation in *q* throughout a more complex optical system is performed by solving a matrix equation for q_{out} as per Eqn. (4), where *A,B, C* and *D* are also complex numbers describing the response of the optical system the beam is propagating through and q_{in} is the complex input value of the beam in terms of its radius and beam waist.

$$q_{out} = \frac{Aq_{in} + B}{Bq_{in} + D} \tag{4}$$

A feature of this modelling technique is that the values for *A, B*, *C* and *D* for any large system of optical components can be calculated by stacking matrices from each of the individual component matrices. This useful property means the beam size can be calculated for any position along *Z* in any optical system, by simply stopping at the matrix of interest, or the whole system can be solved in one calculation by multiplying out the whole stack of component matrices into one system matrix. This optical design methodology of stacking unitary matrices to solve a larger optical system is frequently employed in optics from paraxial ray matrices to optical coatings and distributed feedback laser designs [59].

Eqn. (5) shows the stacking of component matrices, a_n, b_n c_n d_n, multiplied using the usual rules for matrices into one system solution *A*, *B*, *C*, *D*.

$$\begin{bmatrix} A & B \\ C & D \end{bmatrix} = \begin{bmatrix} a_n & b_n \\ c_n & d_n \end{bmatrix} \cdots \begin{bmatrix} a_2 & b_2 \\ c_2 & d_2 \end{bmatrix} \begin{bmatrix} a_1 & b_1 \\ c_1 & d_1 \end{bmatrix} \tag{5}$$

A few examples of matrices commonly used in the design of laser beams, cavities and optical trains are given in Table 1 and can be found in literature [50] and [52].

Matrix formula	**Purpose**	**Eqn.**
$A_T = \begin{bmatrix}1 & d\\ 0 & 1\end{bmatrix}$	Propagation in Z to distance *d*	(6)
$A_L = \begin{bmatrix}1 & 0\\ -\left(\frac{1}{f}\right) & 1\end{bmatrix}$	A lens on focal length *f*	(7)
$A_D = \begin{bmatrix}\cos(\gamma Z) & \sin(\gamma Z)\,/n\gamma\\ -n\gamma\sin(\gamma Z) & \cos(\gamma Z)\end{bmatrix}$	Gaussian duct / Gradient index lens	(8)
$\gamma = n_2 + \frac{i\lambda}{2\pi n}$	Definition of γ in Eqn (8).	(9)

Table 1 – **Examples of ABCD matricies.**

Eqn. (6) is the matrix for a spatial translation of length d along the optical axis, Eqn. (7) is the matrix for a lens of paraxial focal length f, and Eqn. (8) is the matrix for a Gaussian duct where; γ is given by Eqn. (9) where n_2 is the quadratic focal strength of duct on the laser beam, λ is the wavelength and n is the bulk refractive index of the duct, typically n=1.803 for Nd:YAG at λ=1064 nm.

In the case of a laser cavity where the laser beam is oscillating between two mirrors then a value for *q* is sought by solving the ABCD matrix values that give a stationary phase radius and beam radius for a round trip of the cavity. Once the full cavity round trip is described by the matrix then the beam waists and phase radii that are supported by the cavity can be solved by the quadratic equation in Eqn. (10) after reference [52].

$$\frac{1}{q} = \frac{D-A}{2B} \mp \frac{1}{B}\sqrt{\left(\frac{A+B}{2}\right)^2 - 1} \tag{10}$$

An important comment on Eqn. (10) is that there are two potential solutions for q and hence two eigenmodes that can be supported by the laser cavity. These are often expressed as being either side of a stability diagram; which is commonly used to depict these laser cavity designs and is shown in Figure 8. The area marked *E1* in Figure 8 is the first stable eigenmode and *E2* the second stable eigenmode.

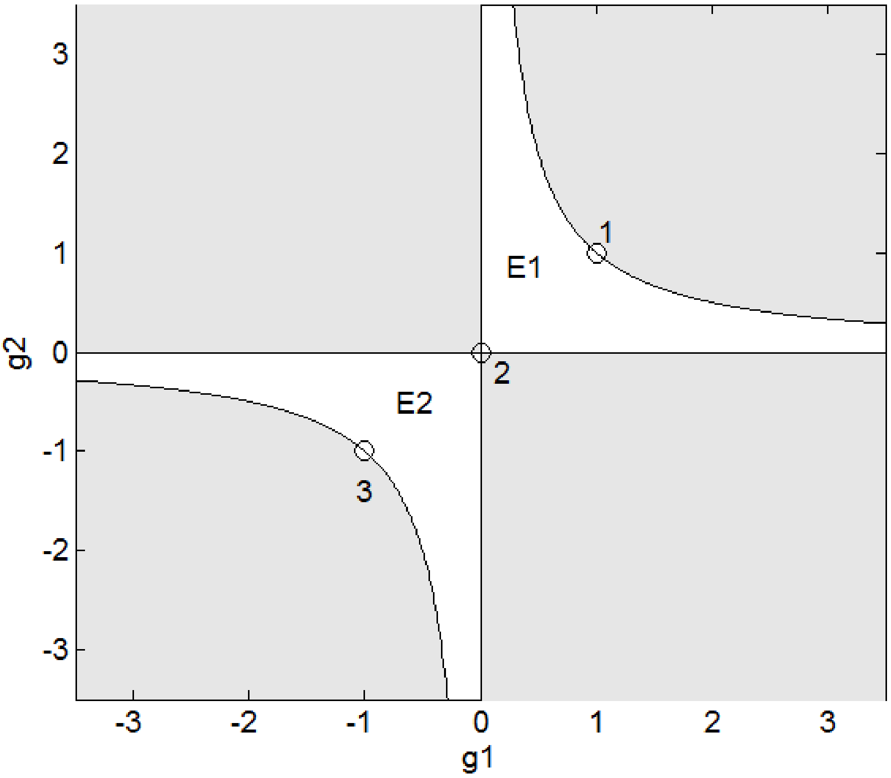

Figure 8 – Stability diagram for a free space laser cavities, shaded regions indicate that there is no solution and no mode is possible. The two regions E1 and E2 are for supported eigenmodes from Eqn 10.

The g parameters in the axes of Figure 8 are given by Eqns. (11) (12). In the case where the internal focal length $f = \infty$, i.e. there is no thermal lens present, then the cavity can be described by the mirror radii R_1 and R_1 alone. The position marked 1 in Figure 8 shows where the cavity mirrors are planar, $R_1=R_2=\infty$, this is known as the plane parallel condition. Position 2 shows the where the mirror radii are the same as the length of the cavity, known as the confocal condition and position 3 shows where the mirror radii are half the length of the cavity, known as the concentric condition.

$$g_1 = 1 - \frac{L_2}{f} - \frac{L_0}{R_1} \tag{11}$$

$$g_2 = 1 - \frac{L_1}{f} - \frac{L_0}{R_2} \tag{12}$$

In the case of a varying thermal lens, where $f < \infty$ the laser cavity is observed to traverse across the stability diagram with increasing pump power and the laser can be tuned to operate on either of the eigenmodes by changing the pump power, hence strength of the internal lens. The typical trajectory for a laser, which is initially close to plane-parallel, on this diagram is shown in Figure 9 from 0% of its operational power to 100% of its operational power.

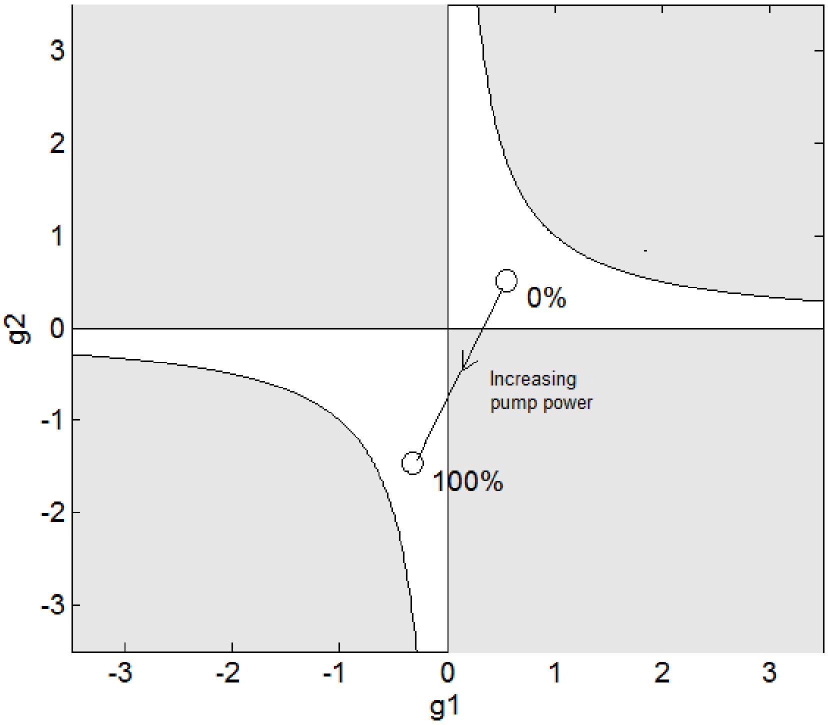

Figure 9 – Stability diagram showing typical trajectory of a laser with an asymmetric cavity and gain region with thermal lens that increases with pump power.

The laser stability parameters, g_1 and g_2, start in a region close to the plane-parallel condition, as the thermal lens strength increases the focal length, *f*, decreases and the laser cavity traverses diagonally. If the laser is symmetric, then $L_1 = L_2$ and the trajectory on the stability diagram will pass through the origin, $g_1 = g_2 = 0$. If the laser cavity is not symmetric, then the stability parameters traverse through a region which does not support a lasing mode. This would lead to the laser ceasing to lase, unless strong polarisation effects such as isogyres are present. If isogyres are present in the laser system then the cavity M^2, irradiance profile, polarisation content and stability are strongly affected.

2.3 Development of an ABCD modelling tool

The ABCD model is developed as a modular construction in Matlab as shown in Figure 10. The individual modules and system matrices are transportable and can be re-used easily by calling from a Matlab work area.

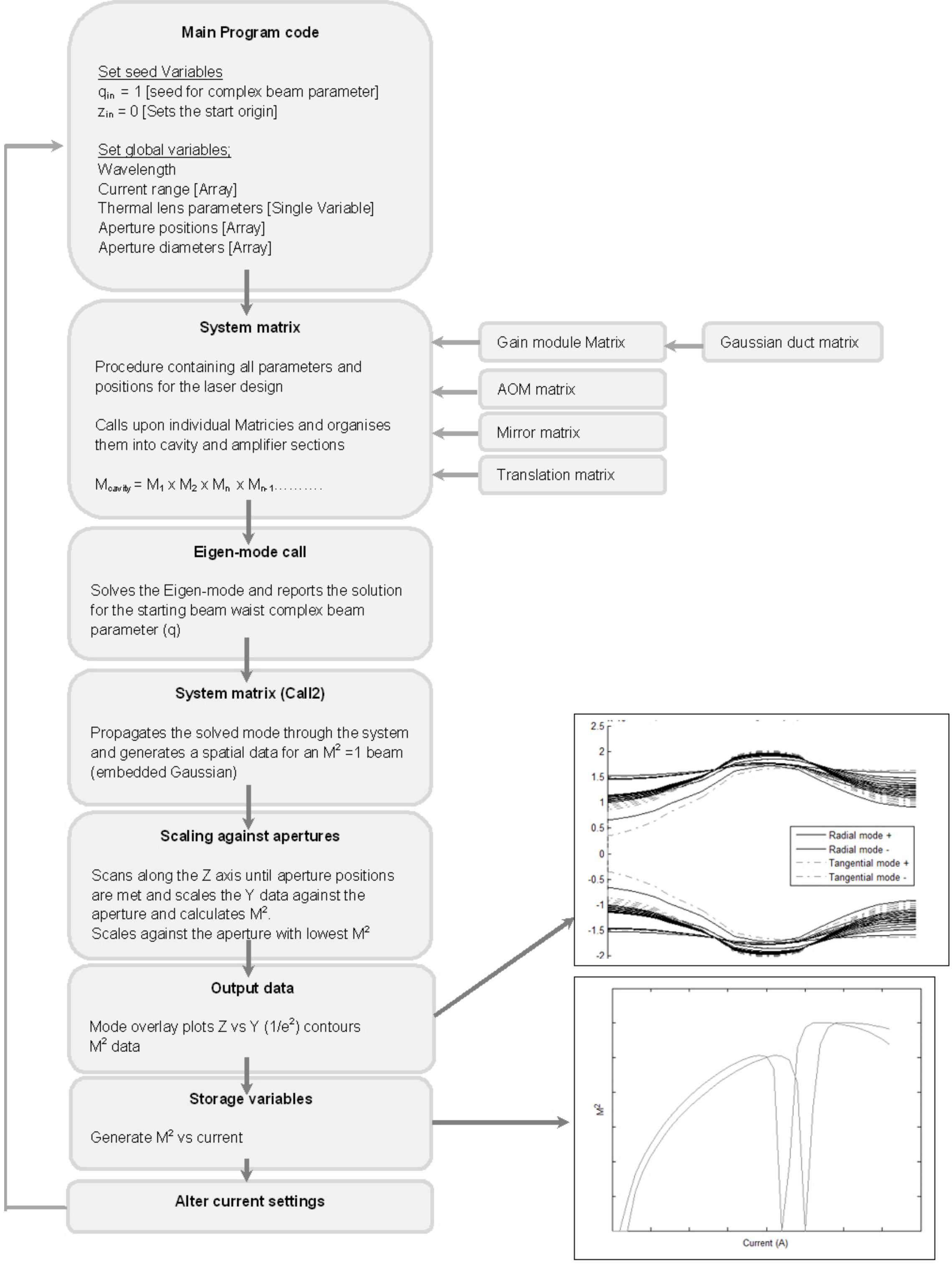

Figure 10 – System diagram showing the steps taken to model the laser cavities.

The main program sets up the initial conditions and arrays then calls the system matrix. The system matrix contains all the individual matrices that make up the laser cavity, free-space, and amplifier sections. The section of the matrix that describes the cavity is then sent to an eigenmode solver, which determines whether an eigenmode exists and solves the value for the complex q value on the first object in the cavity. This value of q then becomes the initial conditions for a second matrix call, which report the size of the embedded Gaussian beam along the length of the optical axis. The embedded Gaussian is then compared to the size of the apertures along the Z axis locations and scaled so the minimum M^2 and $1/e^2$ contours are determined. An overlay of the $1/e^2$ irradiance contours are plotted and the value for M^2 for the current is stored, the value for the current is then incremented and the process is repeated until the maximum current values giving 100% operational power is reached. The M^2 vs current, or pump power, curve is generated by storing the results for each solution for a given current.

The model as depicted in Figure 10 is also used for free space propagation or in the case of the laser cavity followed by an amplifier. This is achieved by omitting the eigenmode call, which then treats subsequent components as free space.

The Nd:YAG rods, as aforementioned, exhibit considerable thermal lensing and their optical response on the beam can be modelled as a Gaussian duct as given in Eqn.(8), where the thermal lensing is expressed in terms of the laser current delivered to the diode pump bars. A transform required to scale the operating current of the laser system to the quadratic refractive index, n_2, is required to relate the strength of the thermal lens to the applied current. This is achieved by equating Eqn. (13) obtained from [50] and Eqn. (14) obtained from [53-54] and manipulating them to get the pump power in terms of the applied diode current.

$$n(r) = n_0 - \frac{1}{2} n_2 r^2 \tag{13}$$

$$\Delta n(r) = \frac{Q}{4K} \frac{dn}{dT} r^2 \tag{14}$$

Q is power density of pump light on the rod, *dn/dT* is the change in refractive index with temperature, *r* is the radial co-ordinate and *K* is the thermal conductivity. By linking the thermal lens parameter n_2 between the two equations, a transform for Q is made to produce Eqn. (15) which links the thermal lens parameter n_2 in the ABCD matrix to the applied current to the pump diodes. It is noted that Eqn. (14) is assumed to be quadratic with radial position *r*, which in general is not the case either where abberations are present due to the pumping regime or where *r* is close to the extremes of the rod diameter, but provides a good approximation of the paraxial thermal lens strength.

$$n_2(I) = \frac{\varepsilon\chi\sigma_d V(I - I_{th})}{2\pi R^2 LK}\frac{dn}{dT} \tag{15}$$

Where *V* is the diode laser bar voltage, *I* is the diode current, I_{th} is the diode threshold current, *K* is the thermal conductivity of the Nd:YAG, *dn/dT* is the change in refractive index with temperature, *R* is the radius of rod, *L* is the length of rod, σ_d is the efficiency of diode lasers ε is the coupling efficiency of diode power to rod and χ is an additional parameter to correct when for the temperature reduction in the rod when the laser is lasing. In pulsed operation the laser is storing more pump power than in CW operation and more of this absorbed pump power decays non-radiatively, thus contributing to a stronger thermal lens in pulsed operation. It is experimentally determined by comparing the kink location in the operational pump power verses cavity output power curves between pulsed and CW operation in an asymmetric cavity as shown in Figure 11. The increase in the thermal lens, χ, for these lasers is typically varies from 1 to 1.2.

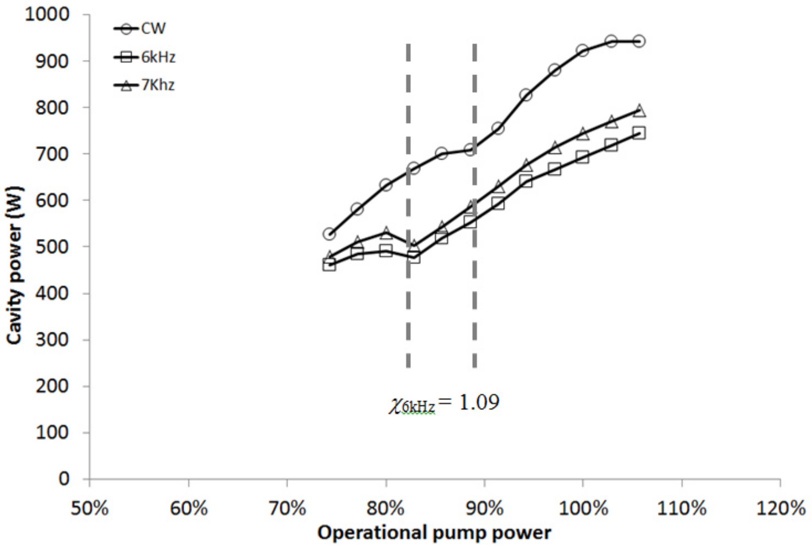

Figure 11 – Cavity power vs operation pump power showing the difference in thermal lensing between CW and pulsed operation for a Rigel i-series laser.

2.4 Validation of model

Validation of the Matlab model is performed against two leading ABCD laser design packages; Paraxia ABCD, Version 2.01.06 release Nov 21, 2005 from Stanford University and Rezonator from UCLA University. Paraxia and Rezonator give equivalent output but Rezonator is constrained to cavity only designs and does not support free-space propagation.

In order to check the validity of the model it is important to pick a test where a standard ray trace approach fails. To achieve this a model is created with an $M^2 = 26$ laser beam of beam waist diameter 7.5 mm propagating 500 mm before being focussed by lenses of various focal lengths. A ray trace assuming a collimated beam of 7.5 mm would, incorrectly, always predict focal positions of a thin lens to be equal the focal length of the lenses. It would also, incorrectly, predict an infinitely small focussed spot. The ABCD models predict both the beam size and the position of the focus accounting for the laser beam divergence due to diffraction. The $1/e^2$ contours of the beam are shown in Figure 12 for the range of this numerical experiment. The results shown are Matlab derived results but are repeated in all sets of test software.

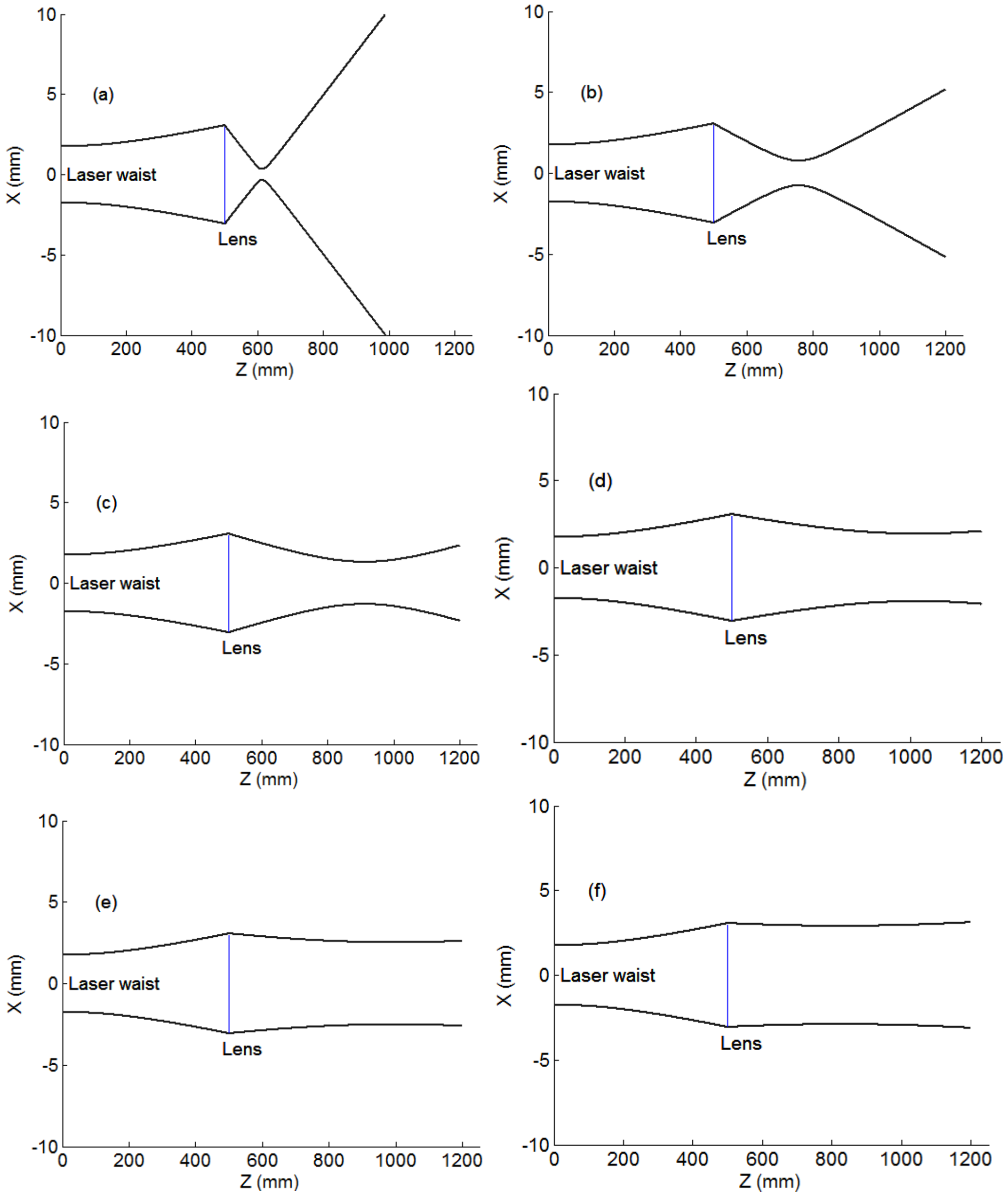

Figure 12 – Plots of $1/e^2$ beam contours for different EFL thin lenses, (a) 100 mm, (b) 200 mm, (c) 300 mm, (d) 400 mm, (e) 500 mm (f) 600 mm. The focussed waist position can be seen to move back towards the lens between (e) and (f).

The plots in Figure 12 show both the diverging diffractive behaviour of the laser beam as it propagates from its initial waist, the finite size of the beam waist and the resulting change in the position of the beam waist in *Z* as a result of the balance between the diffraction of the laser beam and focussing of the lens.

Figure 13 shows the *Z* location of the beam waist for this numerical experiment as a result of the ABCD modelling and it clearly shows the beam waist moving back towards the lens in *Z* for lenses with focal lengths greater than 450 mm, contrary to a ray trace result.

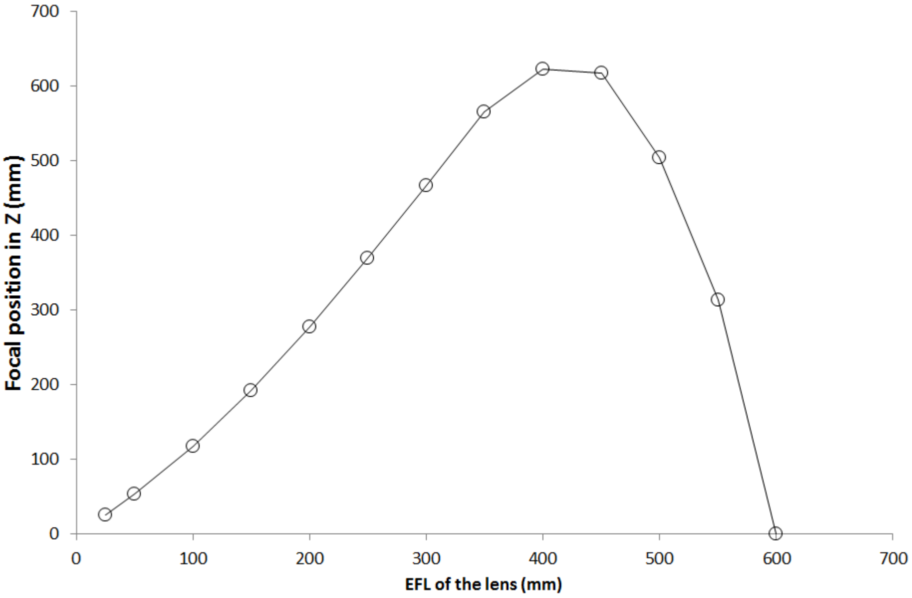

Figure 13 – Location in Z of best beam waist for different EFLs of lens.

Figure 14 shows the comparison of the prediction of the beam waist size at focus between the two modelling packages; predictions from both packages are within 3% of each other and the residuals indicate a strong linear fit.

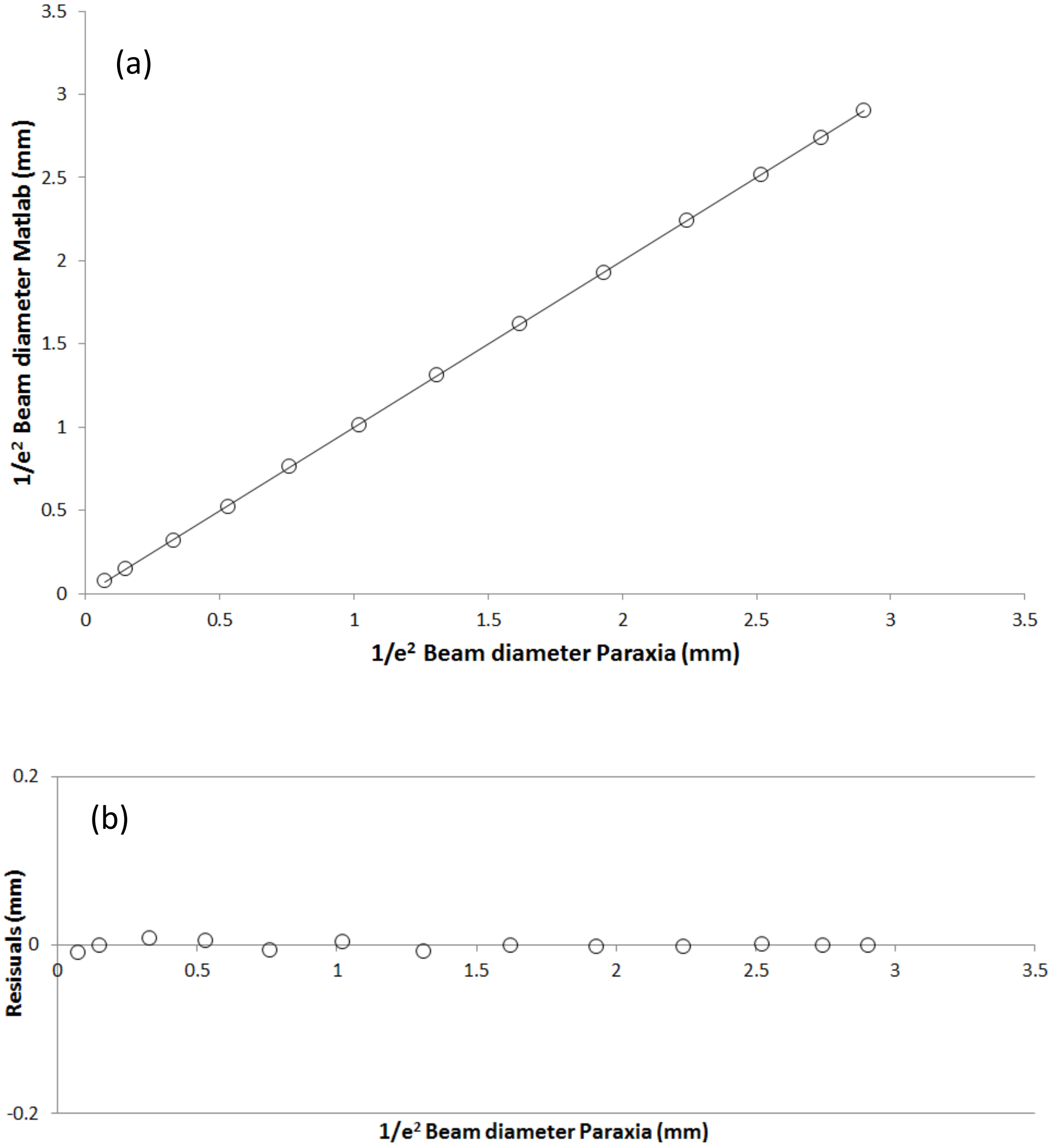

Figure 14 – (a) Direct comparison of spot sizes between Paraxia and Matlab software, a linear fit between the data points is shown R^2 = 1.000, gradient =1.002, intercept=0.006. (b) residuals.

A second test, to validate the performance of the Gaussian duct is crucial to the modelling of the laser gain modules. Using Eqns. (8) (9) (15). A Gaussian duct is created in free space with a length of 150 mm. The n_2 parameter is varied in both Paraxia and Matlab models and the resulting beam waists and positions compared. Figure 15 shows the Matlab output for this system. The 1/e^2 irradiance contours of the beam as it propagates thought the model in Z are shown and the position of the input and exit of the Gaussian duct is marked by the vertical lines and annotation in the figure.

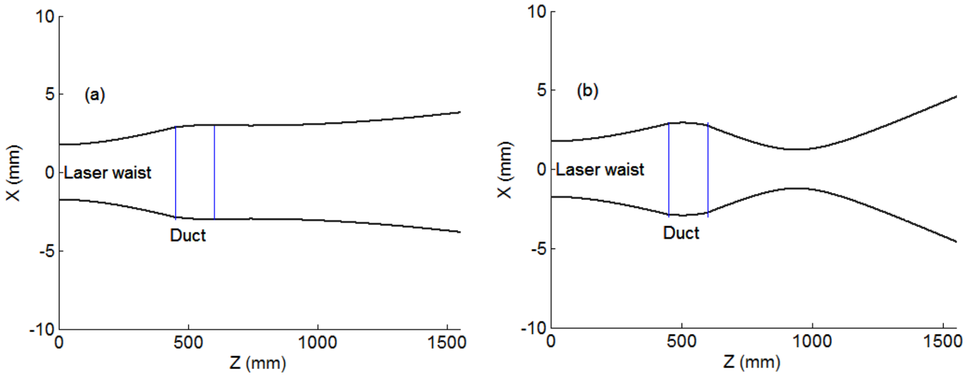

Figure 15 – Gaussian duct models for (a) n_2 = 10.5 (b) n_2 = 25.

Figure 16 shows the predicted beam waist position and beam waist size are again in good agreement between the two models although the residuals indicate a minor non linearity between the two models, it is likely this is due to the fixed sampling length in Paraxia.

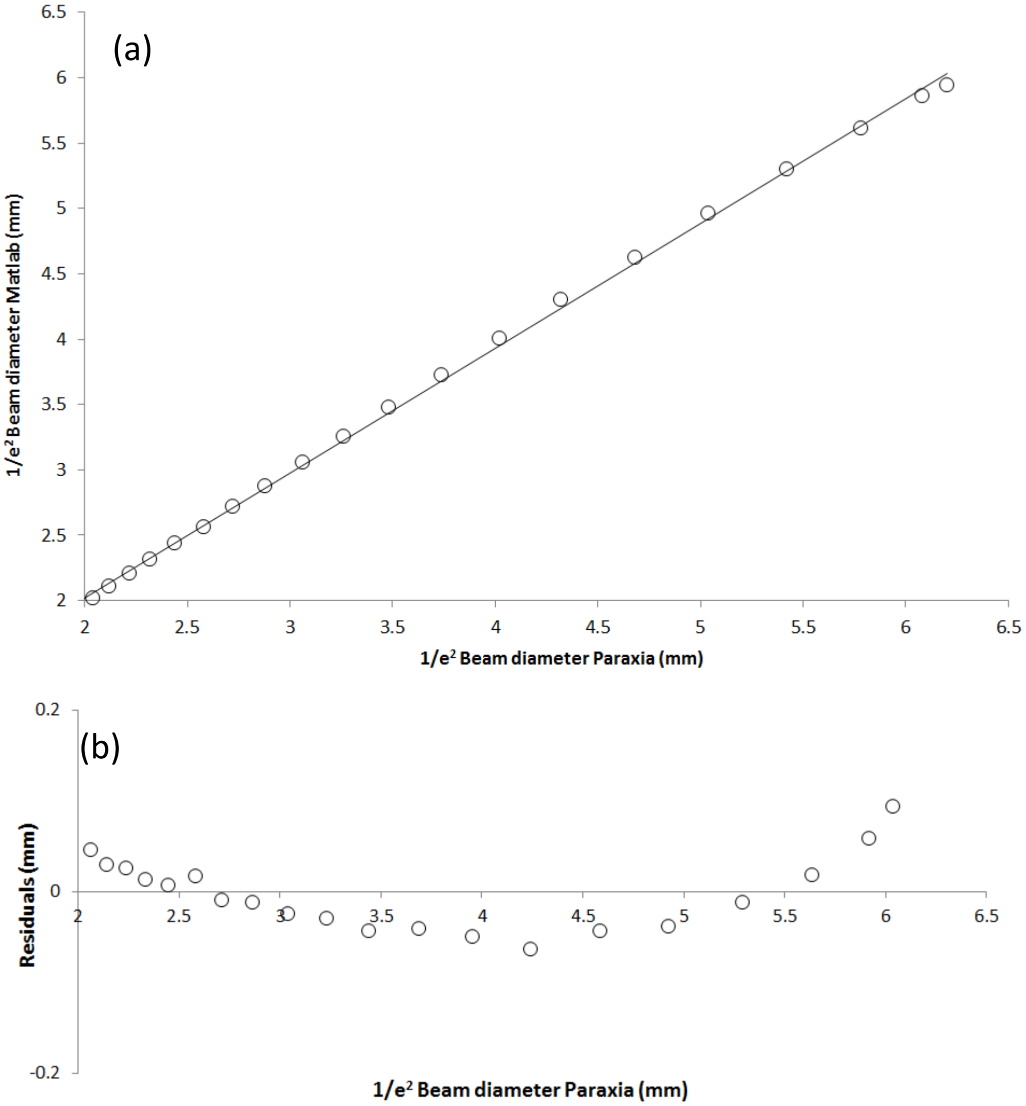

Figure 16 – (a) Comparison of models for Gaussian duct test a linear fit between the data points is shown $R^2 = 0.999$, gradient =0.96, intercept=0.12. (b) Residuals.

A demonstration of the ABCD model accuracy as modelled against a real laser beam is given in Figure 17. A green laser λ=532 nm of known size and position is focussed into a spot by a lens and then compared to the modelled prediction. The predicted modelled data matched very closely to the 1/e^2 contour as measured by a Cinogy CinSquare CS200, measured to standard ISO1146/1/2.

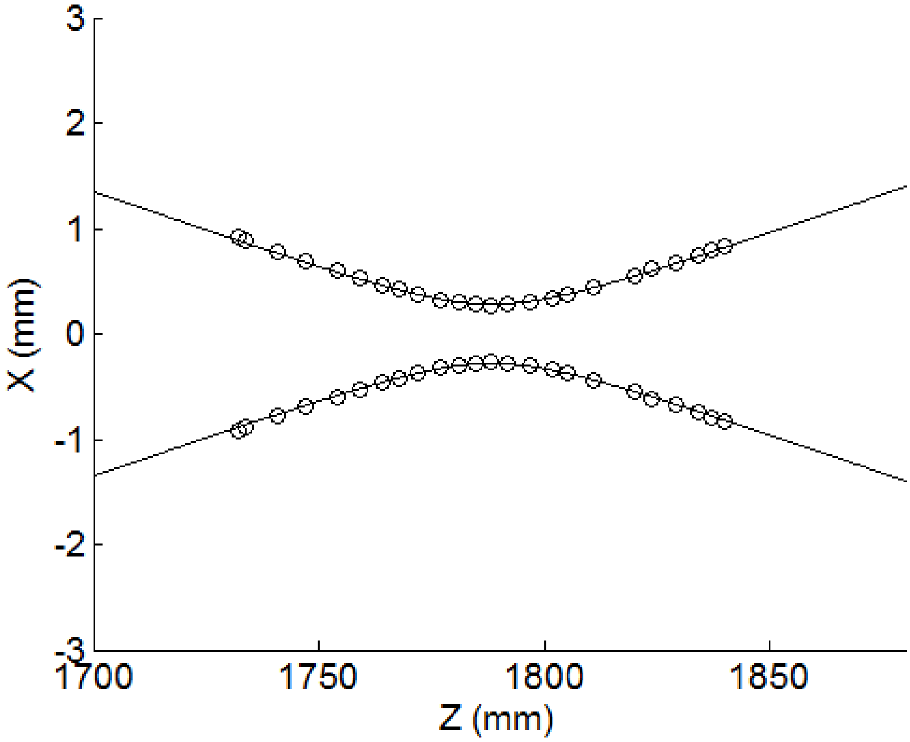

Figure 17 – ABCD modelled data (lines) plotted against the measured (circles) data for a focussed laser beam of M^2 = 26.

2.5 Application of modelling tool and comparison to real data

Now the validation of the free space propagation, mirror positions and Gaussian duct models are completed, the modelling of a complete laser cavity is possible. A typical cavity solution is shown in Figure 18 showing the $1/e^2$ contours of the solved eigenmodes for a range of pump currents and resulting thermal lenses given by Eqn. (15) and accounting for all intra-cavity apertures.

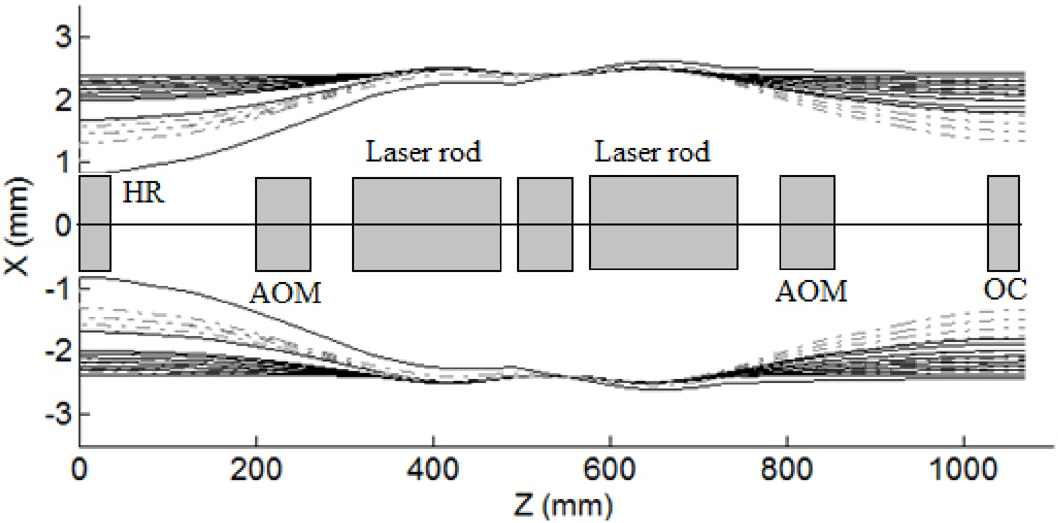

Figure 18 – Showing the $1/e^2$ contours of the beam solution for this cavity, the cavity shown consists of two gain modules as modelled as Gaussian ducts and two terminating mirrors. Key:AOM, acoustic optic modulator; HR, high reflector; OC, output coupler.

An important note with modelling this particular laser cavity is that the thermal stresses induced upon the Nd:YAG crystal during the absorption of the pump light give rise to a strong birefringence within the rod caused by thermal strain against the crystal structure of the Nd:YAG. If a polarising analyser were to be placed in a free-space laser beam sampling this region of de-polarisation, then the patterns shown in Figure 19 would be observed. These are known as isogyre patterns [53] and indicate polarisation that is radially and tangentially polarised with respect to the Nd:YAG rods cylindrical geometry.

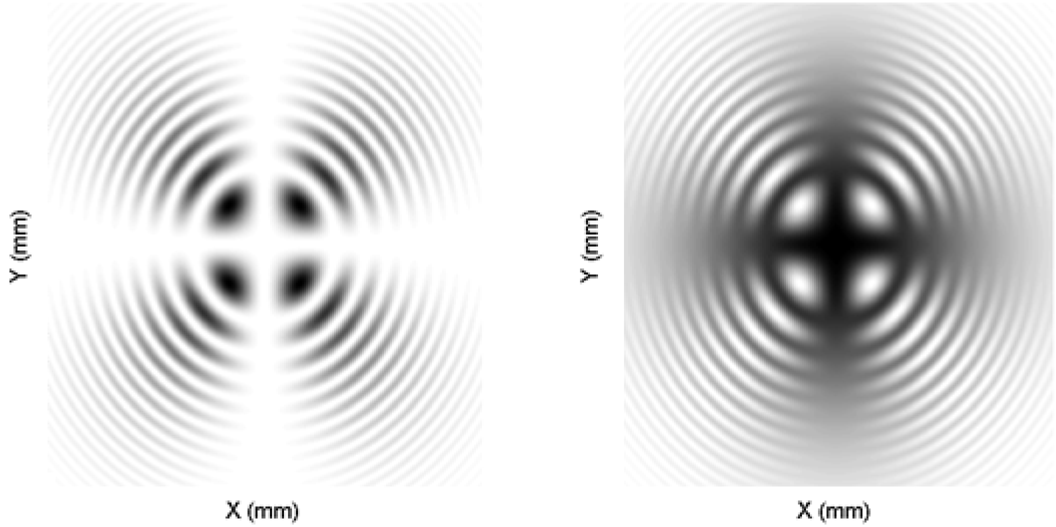

Figure 19 – (a) Isogyre pattern with polarisation analyser oriented in the vertical and (b) with polarisation analyser oriented in the horizontal.

The importance of this behaviour to the ABCD modelling is that the laser beam is de-polarised as it circulates the laser cavity and the radial and tangential polarisations experience a different thermal lens as a result. In general the n_2 value for the radial thermal lens is 10% more than that of the tangential [53]. This is addressed in the ABCD modelling by overlaying the results for the radial and tangential at their extreme thermal lens values. The isogyres also tend to smooth out any cut off regions between the two stable eigenmodes. During the cut off regions the laser continues to lase on any remaining available polarisations that give a cavity solution. In these regions laser beam is observed to be more patterned, reduces in M^2 and the dynamic stability of the laser is poorer.

Figure 20 shows modelling results of anticipated M^2 and beam waist values for radial and tangential extremes of a known symmetric cavity, where measured unpolarised results of the cavity are overlaid for comparison. The operating M^2 of approximately 25 is predicted and the behaviour of the beam waist with increasing current is reasonably predicted within the tangential and radial values. The value of 100% of operational power is the optimum operation point for the laser cavity determined to balance a high average output power and the centre of the dynamic stability range of the laser. This region tends to coincide with the peak in the M^2 vs. operational output curve. At powers significantly above, typically 10% above or below this operational point the laser can become dynamically unstable, this is unsuitable for most processes. The laser is also typically dynamically unstable during the transition between the eignemodes.

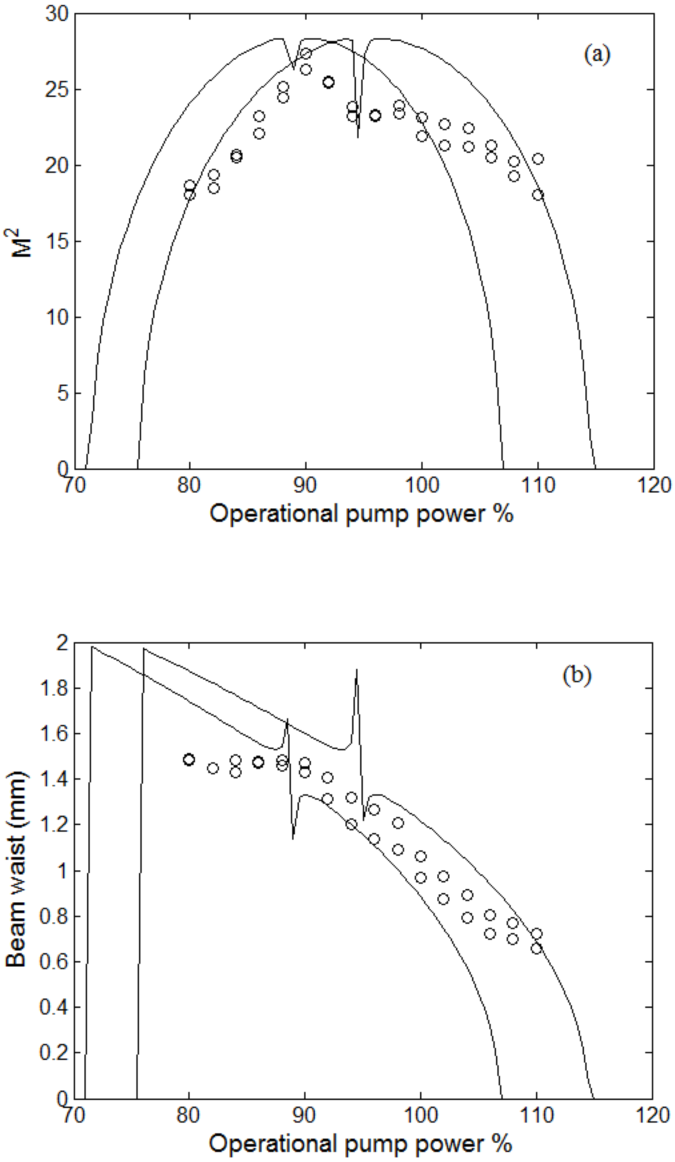

Figure 20 – A comparison of models and measured data for (a) M^2 against operational pump power and (b) beam waist against operational pump power for a typical near symmettric laser cavity.

A further modelling prediction is performed for an asymmetric cavity and the results are shown in Figure 21(a). In this case there was also an intra-cavity aperture placed inside the oscillator section of the laser in order to alter the M^2 profile of the laser which was accounted for in the model. The M^2 curve is shown to follow the curve labelled as the envelope; which is the maximum M^2 the cavity can achieve by combining the radial and tangential polarisations. The cavity response is observed to follow this curve in this case. For completeness Figure 21(b) displays a graph of the laser when operated at CW and at different repetition rates. There is a significant kink in output power of the output power vs pump power in the region where the transition from one eigenmode occurs. The kink position moves to an increased pump power when operated in CW mode, this is due to an increased optical power extraction from the laser medium as the laser is always lasing and not pulsed, the increased power extraction effectively cools the laser rod as less power remains within the rod to generate heat through non-radiative decay, this subsequently reduces the strength of the rod's thermal lens.

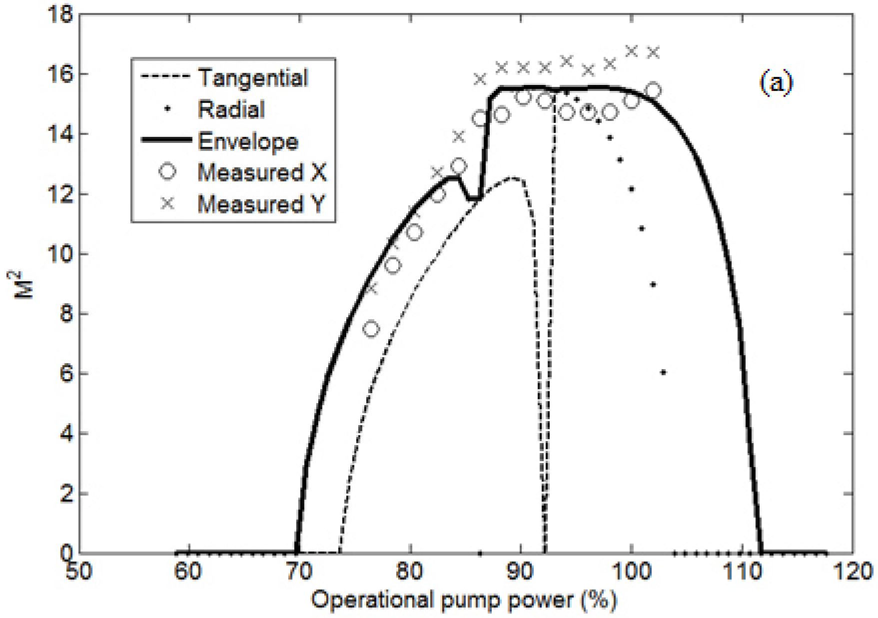

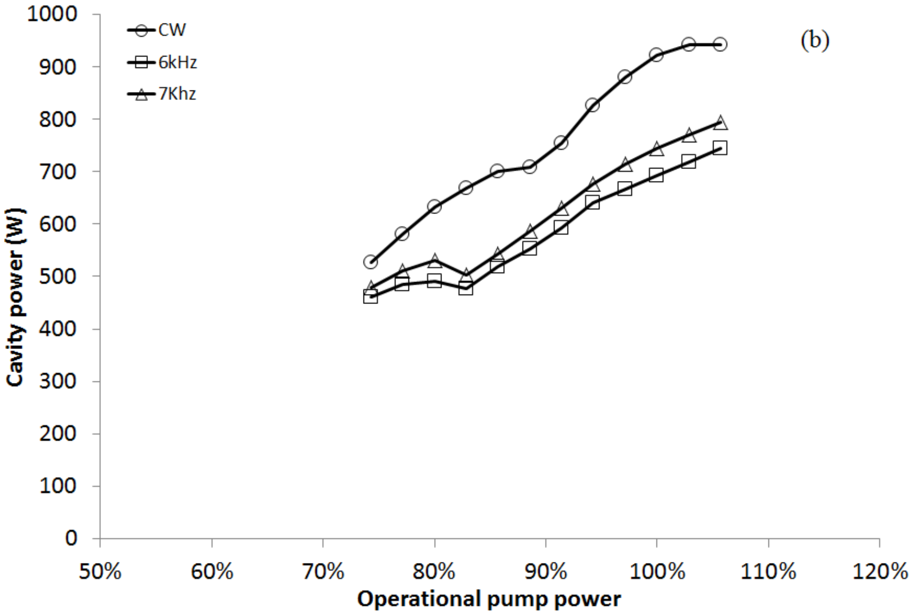

Figure 21 –(a) Predicted maximum M^2 against operating power, measured values are overlaid for X and Y dimensions of the beam (b) laser output power of the measured cavity showing different repetition rates.

Figure 22 details the predicted $1/e^2$ diameters of the irradiance profile and the full angle divergence against their measured values. The model tends to over-predict the beam waist and under-predict the divergence slightly and converges onto the measured values for operational pump powers greater than 80%. A reason for this is that field values for the apertures may be smaller than the actual physical extent of the aperture in the system.

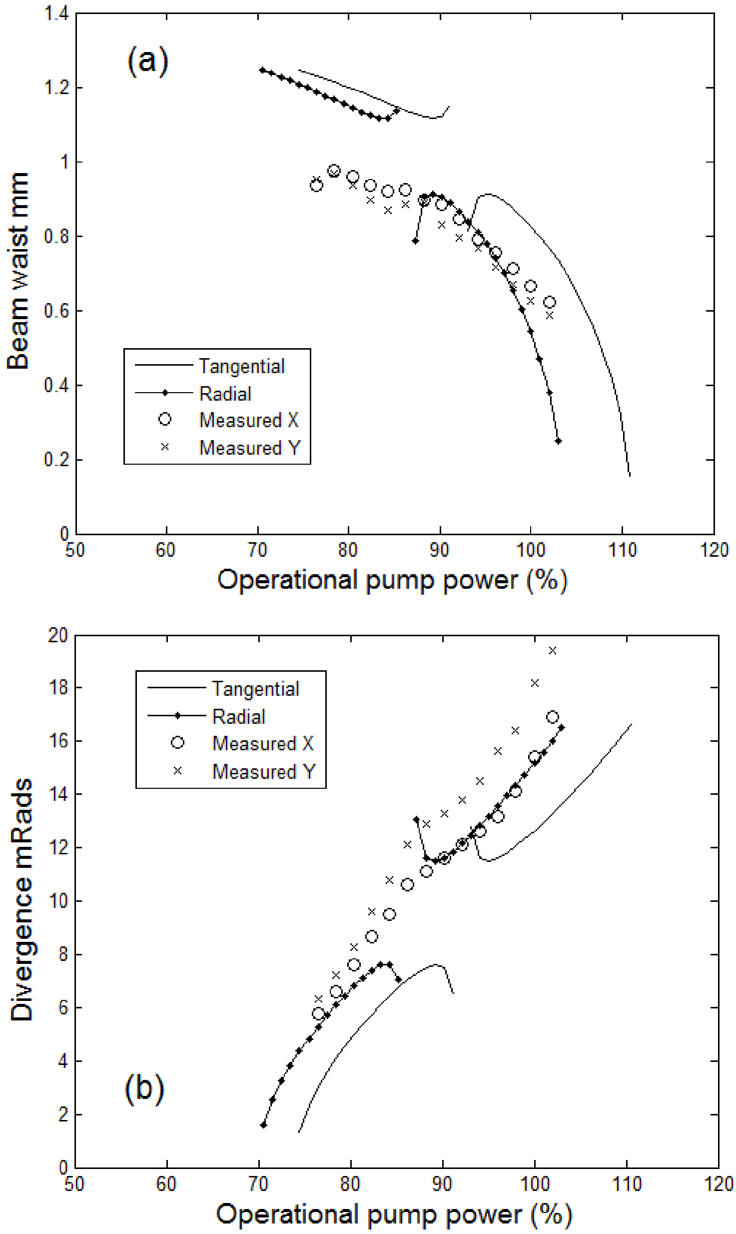

Figure 22 – (a) Predicted beam diameter plotted against the diode pump power (b) full angle divergence plotted against the pump power. Measurements are overlaid for X and Y axes.

Further amplification stages and lenses were also added to the model as free space components as shown in Figure 23.

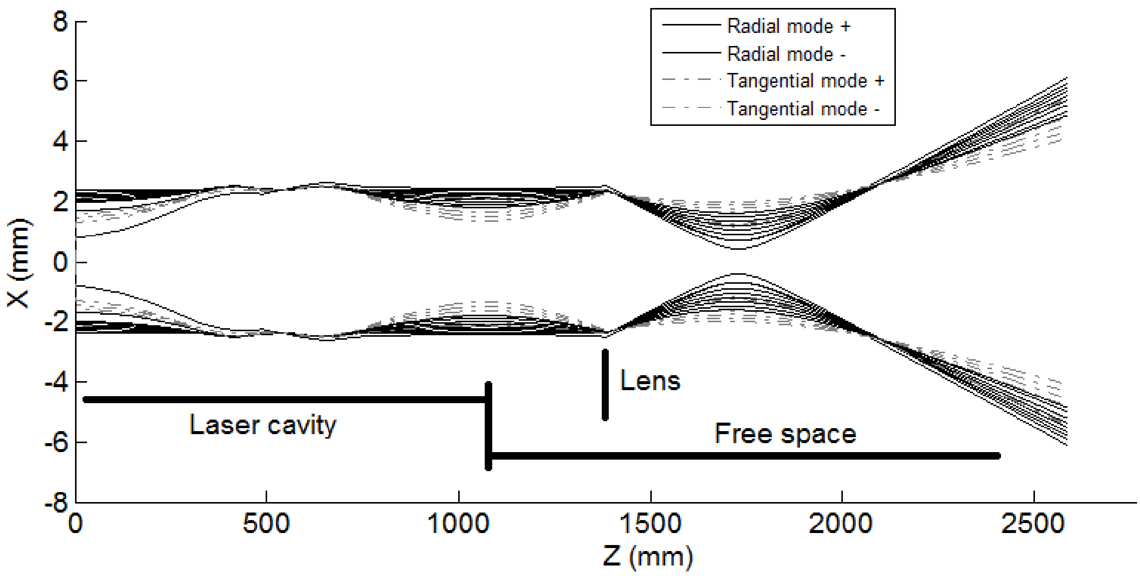

Figure 23 – ABCD model with confined beam generation in the laser oscillator and free space propagation.

The code is also designed to permit any number of limiting apertures along the cavity. This is achieved by scanning along the length of the solved TE_{00} embedded Gaussian and solving against the specified apertures in their location along the Z axis. Once each aperture is analysed then the beam- profile which was constrained to the lowest calculated M^2 value is used to scale the beam diameter within the cavity. This allows analysis of cavities with multiple limiting apertures to be modelled and also to examine or tune the behaviour of this cavity by deliberately placing apertures into strategic positions.

A modelling demonstration of multiple apertures within cavities is given in the following figures. Figure 24 shows $1/e^2$ irradiance contour overlays of an asymmetric cavity and the M^2 values for increasing pump power. The cavity has a strong distinct region between the eigenmodes for stable oscillation; these can be seen both in the overlays of the $1/e^2$ contours in and the M^2 vs current. The laser cavity is formed between two planar mirrors and the only limiting aperture is the gain medium and its location is shown in Figure 24(a).

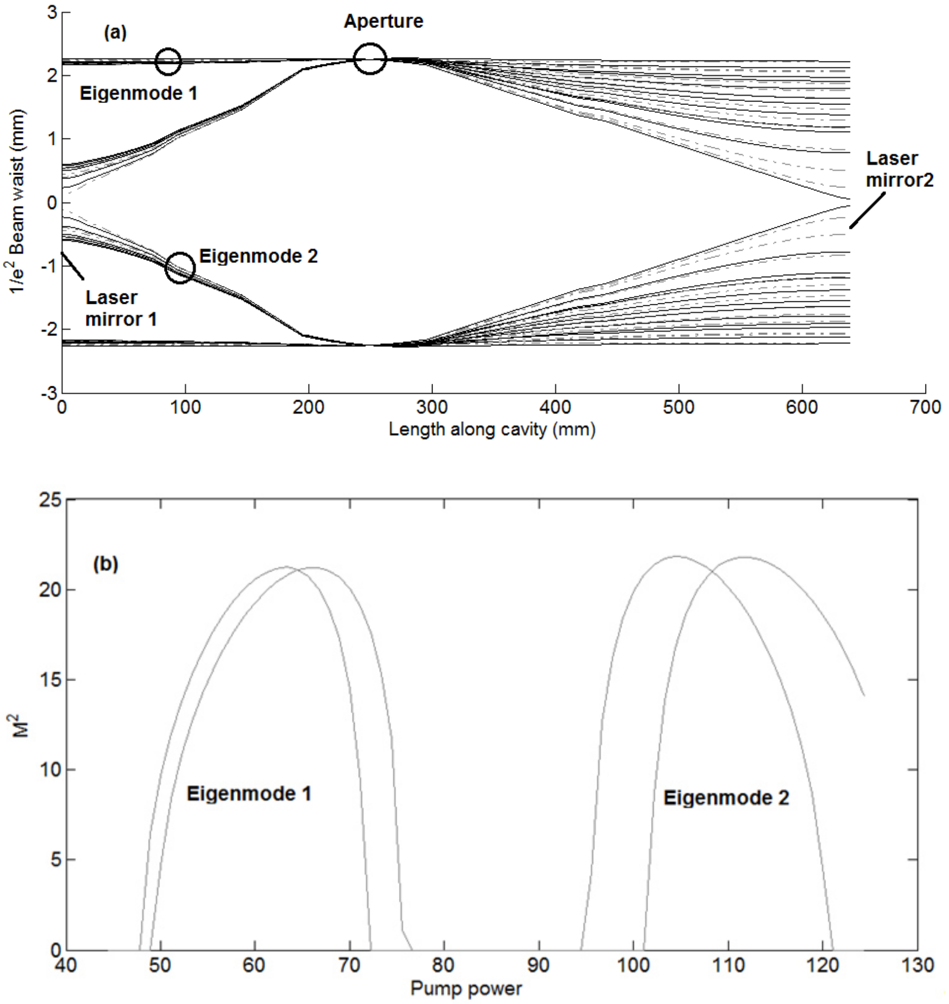

Figure 24 – (a) $1/e^2$ Irradiance contour overlays of an asymmetric laser cavity formed between two mirrors and (b) M^2 values for increasing pump power.

A limiting aperture of 1.5 mm diameter is then placed in the vicinity of the left mirror as depicted in Figure 25(a); a strong suppression in the M^2 value for the first eigenmode is observed in Figure 25(b) at low operation power.

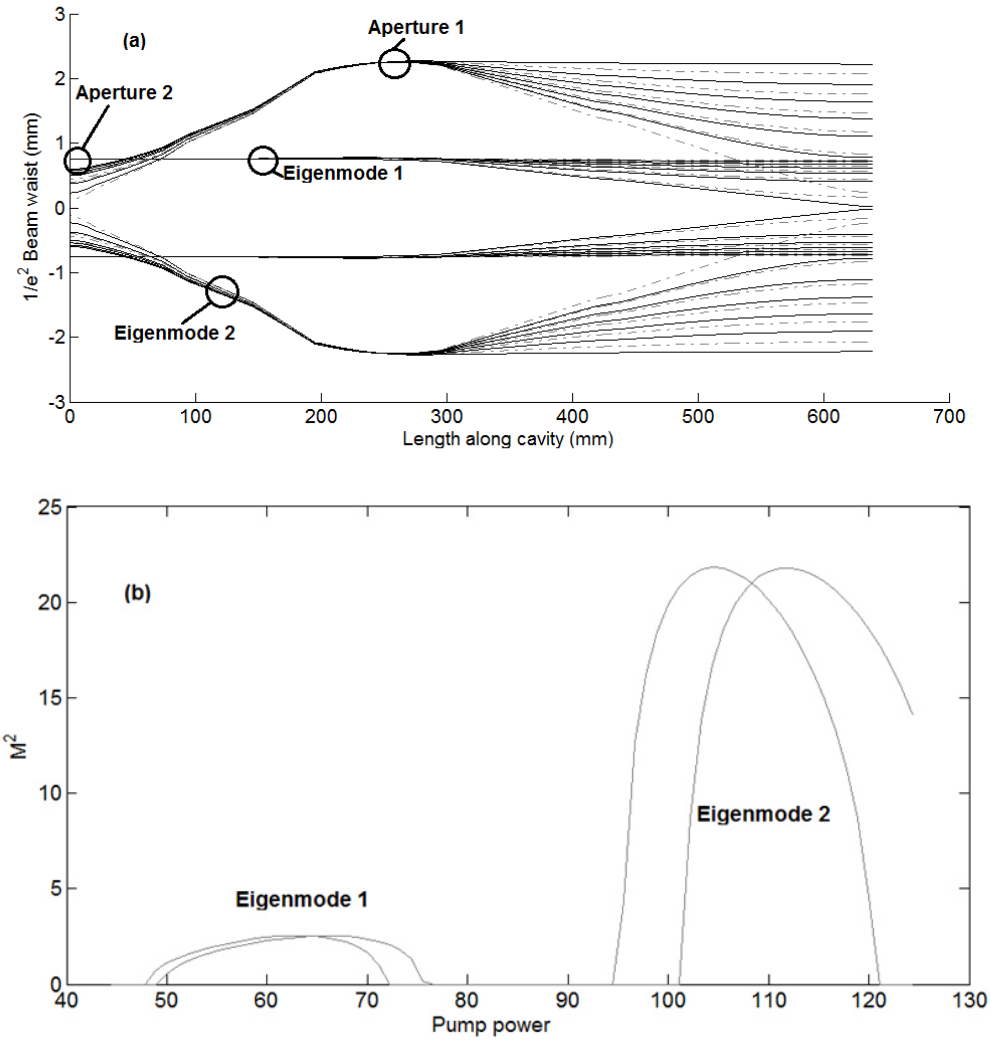

Figure 25 – (a) $1/e^2$ Irradiance contour overlays of an asymmetric laser cavity formed between two mirrors and (b) M^2 values for increasing pump power, with a second intra-cavity aperture added at the left hand mirror as indicated in (a).

If a third limiting aperture is additionally placed in the vicinity of the second cavity mirror, the M^2 profile with increasing pump power also changes. The peak M^2 achieved by the laser is still $M^2 = 20$ but the M^2 value are suppressed at lower operational pump values as shown in Figure 26.

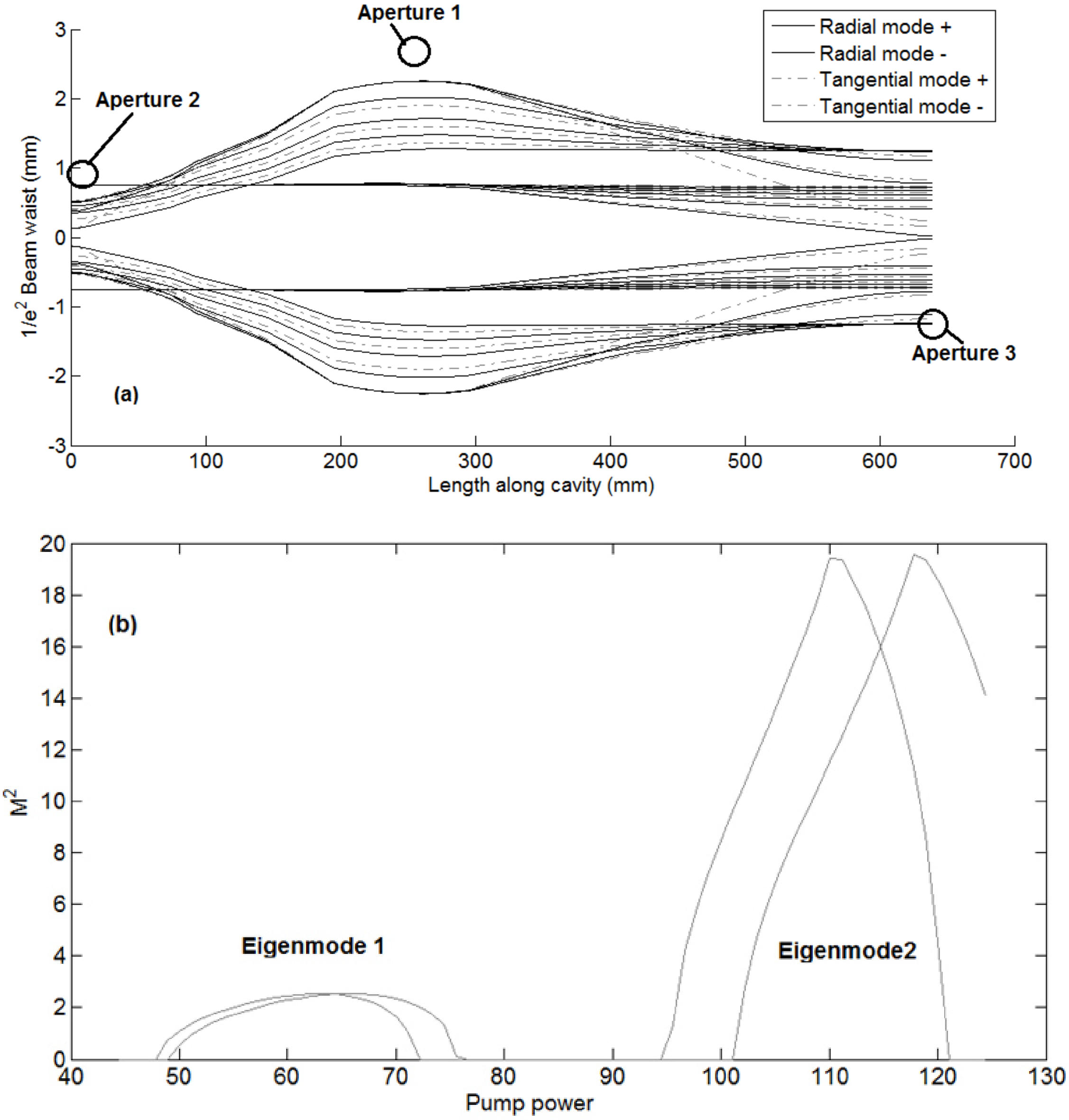

Figure 26 – (a) $1/e^2$ Irradiance contour overlays of an asymmetric laser cavity formed between two mirrors and (b) M^2 values for increasing pump power, with a third intra-cavity aperture added at the right hand mirror as indicated in (a).

2.6 Summary

An ABCD model is presented that accurately models free space propagation and confined laser cavities for high power multimode laser sources that is at least as accurate as leading ABCD software. The key advantage of this proprietary code approach is that the generation of M^2 vs operational pump power models and beam output predictions can be completed much quicker via the automation in the Matlab source code. The code is also configured, as shown in Figure 10, to be re-usable by generating standard models, or system matrices for laser systems or gain modules. It is also possible to conceive of iterative algorithms that optimise the system for a particular behaviour with operational pump power or placement accuracies of components. An element of novelty is added into the code which permits the use of multiple limiting apertures within the same cavity model. This is not observed in any of the commercial packages available, neither is the ability to swiftly model the laser cavities against increasing operational pumping power.

2.7 Conclusion

The model presented in this chapter can predict the behaviour of the propagating multimode laser beam; it is most accurate when modelling from a known measured data point and predicting the future evolution of the beam or modelling through other optical elements such as lenses. The accuracy of the ABCD model is more difficult to quantify against confined laser cavities, mainly due to the described isogyre behaviour of this laser generating a range of thermal lens conditions for different polarisation states, which acts to blur the resolution of the model. The model does however provide a strong insight into the likely stable regions of operation for the laser, detailing the beam waists, the divergence and the sensitivity of the cavity to displacements of components. Accuracy based upon the results for predictions of laser cavities was within ±20%, for free space beam waists and divergence an accuracy of ±5% is established by comparing statistics on measured and modelled results. The model accuracy is not better or worse than commercial packages but is significantly faster at generating model output and therefore is of more use for quickly assessing alterations to cavities, or optical trains. The ability to model multiple apertures within the cavity is believed to be a novel and inventive step, which is useful for modelling strongly asymmetric laser cavity designs.

There remains considerable scope to develop models for these lasers; however the ABCD modelling of the laser cavities and the free space modelling was sufficient to complete the development stages of the laser system as detailed in the following chapters. A more advanced approach to modelling of these free space laser cavities can be found after references [56-58].

Chapter 3 - Laser beam delivery for industrial processing

3.1 Introduction and motivation for the research

This chapter covers the design of a laser system which is required to remove a surface layer of material from both sides of a metal substrate. The requirement is to deliver the laser radiation from a pulsed laser source with kilowatt average power and pulse powers in excess of 1 MW via an optical fibre and to shape the beam to be the optimum irradiance profile in the XY plane for the process. The typical repetition rate for this process is between 10 kHz and 20 kHz, with pulse energies in excess of 80 mJ. Apart from the specific requirements of the customer, the motivation of this project was a deliberate commercial move to increase the commercial capabilities of Powerlase from supplying singular lasers, into delivering complete turnkey solutions for this process. At the time of introduction these systems were not common and no beam shaping processing heads were available on the commercial market.

3.2 Description and system design

The design approach taken to remove the surface layers is to use a pulsed laser source, delivered to the substrate material via fibre delivery and a custom processing head optic. The laser is pulsed by means of an intra-cavity acousto-optic modulator (AOM), which provides a mechanism to modulate the intra-cavity losses in order to Q-switch the laser. The AOMs are selected to provide full hold off at the maximum output power of the cavity, typically greater than 800 W, with higher output powers achieved by optical amplification. The cavity is deliberately de-polarised by means of a quartz polarisation retarder to optimise the power extraction from the gain media. The overall layout of the system and the individual components is shown in Figure 27, the orientation of the system is shown in the X-Z plane. The Z dimension is aligned along the optical axis of the beam delivery, X is in the direction of motion of the substrate and Y is perpendicular to the motion of the substrate and this axis convention is adopted throughout this thesis.

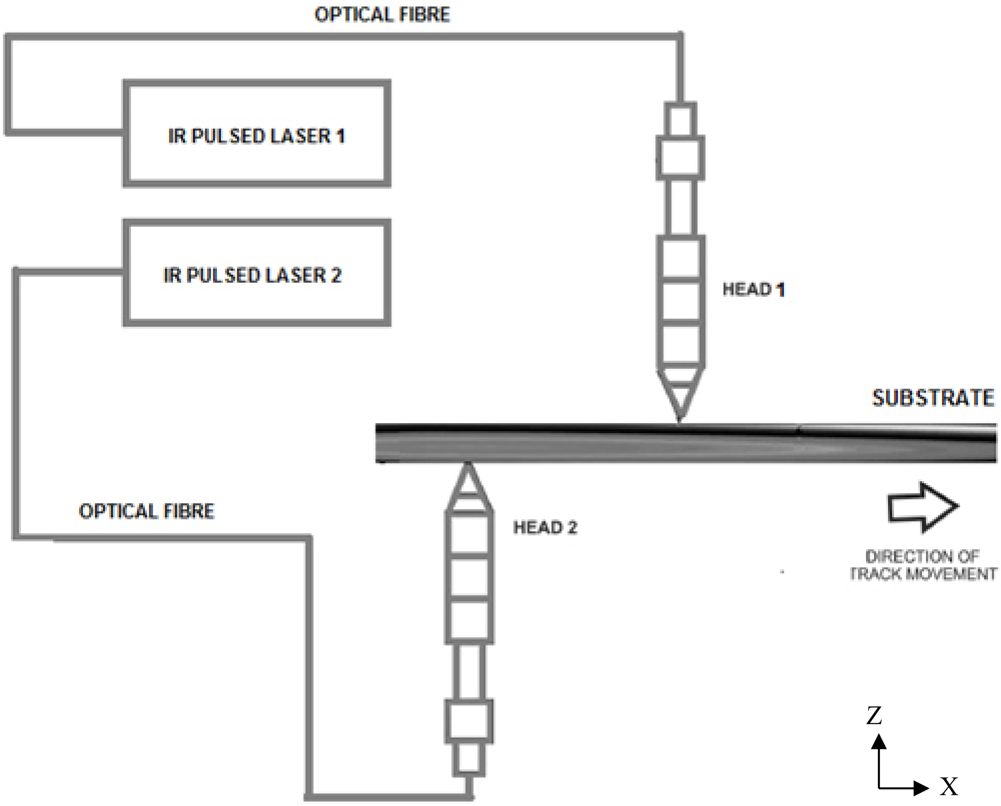

Figure 27 – The laser delivery to the substrate and the motion of the substrate.

The optical system is split into the following component parts, two pulsed infrared (IR) lasers, optical fibres and optical processing heads. Each section of the system affected the design constraints of the following component; hence each component is presented here in the order in which they progress through the system, starting first with the laser source and progressing through the optical train to the processing head delivery of the beam to the substrate. The delivery fibre has a minimum length of 10 m and a maximum delivery length of 30 m, this means any reflected pulses from the substrate arrive back at the laser between 97 ns and 200 ns after the emission of the pulse. The Q-switched pulse duration of this laser is between 60 ns and 80 ns, so the reflected pulse arrives at the laser when the cavity is not active, hence causes no back reflection issue. The repetition rate is also such that the pulses are a minimum of 50 µs apart so that it is not possible for back reflections to interfere with following pulses either, as any reflected pulse will have ceased before the laser opens the Q-switch for the next pulse.

3.2.1 Infrared laser sources

The laser sources utilised operate in the repetition range 10 kHz to 20 kHz, with a pulse duration of 30 ns to 100 ns. These are typical values for the Rigel i-series laser range offered by Powerlase Photonics. The Rigel I series laser range offers different laser layouts that can produce lasers of average powers between 800 W and 1.6 kW, with pulse durations of 30 ns to 120 ns, dependent upon the repetition rate. Pulse energies from 10 mJ to 250 mJ are possible, with M^2 values typically between 16 and 30.

Due to the large mark to space ratio in the temporal delivery of power from this laser in this range, the peak power and energy delivery of the pulse can be easily estimated by the following equations. Eqns. (16) describes the energy per laser pulse, E, where P_A is the average power and R is repetition rate of the laser.

$$E = \frac{P_A}{R} \tag{16}$$

Eqn. (17) describes the peak power per laser pulse, P_p is the average power of the laser at the given repetition rate, and t_d is the FWHM pulse duration.

$$P_p \approx \frac{E}{t_d} \tag{17}$$

The peak power, P_p and the pulse duration t_d are shown diagrammatically in Figure 28 obtained by solving a representative laser rate equation as given in [50], [59] by using numerical methods.

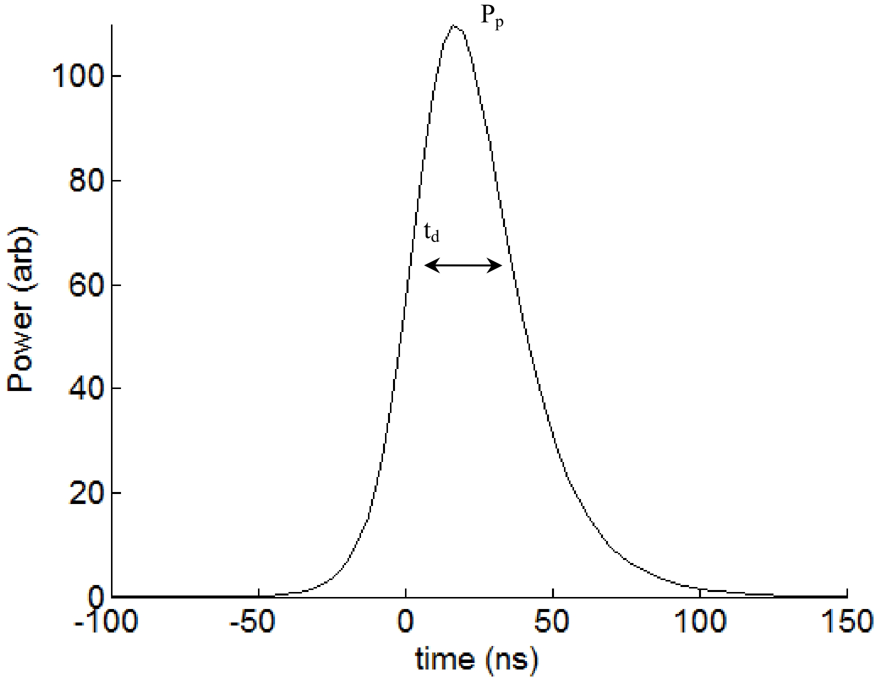

Figure 28 – Modelled laser pulse envelope showing FWHM pulse duration (P_d) and peak power (P_p).

Given the typical scenario of 10 kHz pulses at an average power of 1 kW and 60 ns pulse duration gives a pulse energy of 0.1 J and a peak power of approximately 1.7 MW. These figures are of direct importance to the design of the fibre delivery system as the large peak and average powers lead to constraints on the deliverable power.

In order to establish design rules for the pulsed power some research into the industrial specification for the laser coatings was undertaken. Pulsed laser damage is covered by ISO standard by ISO/DIS 11254-1.2 for single shots, and for multiple shots it is ISO/DIS 11254-2:1995. Laser damage thresholds are quantified to these standards by the manufacturers in terms of the fluence in J/cm^2 at a specified wavelength and pulse duration. A supplier of these parts, CVI (Now Idex), quotes damage thresholds for typical coatings at λ=1064 nm as 10 J/cm^2 to 30 J/cm^2 measured with a 20 ns pulse duration.

As the peak irradiance changes with pulse duration, the damage threshold scales according to Eqn. (18)

$$L_{DT_2} = L_{DT_1}\sqrt{\frac{P_2}{P_1}} \tag{18}$$

Where L_{DT2} is the damage threshold at the new pulse duration, P_2 is the new pulse duration, P_1 is the original pulse duration and L_{DT1} is the damage threshold at the original pulse duration.

For most practical optics used in these high power applications the coating specification is 10 J/cm^2 at 1064 nm with 20 ns pulse duration, the laser was operated at 60 ns giving a fluence damage threshold limit of approximately 17.3 J/cm^2 at 60 ns, using Eqn. (18).

As per Eqns. (16) and (17) the average power decreases with decreasing repetition rate but a much higher peak power is generated. This was potentially damaging to the fibre and Eqns. (16), (17) were used with the beam waist information from the optical models to predict the fluence and the peak irradiance experienced by the fibre and processing heads over the required pulse durations for the process.

3.2.2 Beam delivery fibre and fibre coupling

The first step in the optical delivery of the laser radiation to the substrate is the coupling of the laser beam into a suitable optical fibre. The fibre utilised is a fused silica square core optical fibre with a core width of 600 µm ± 15 µm, an automotive industry standard fibre with a maximum NA of 0.22. This fibre is selected not only because of ease of beam delivery but also because it performs a homogenisation action [16] on the laser beam, this is defined in detail in the later section describing the homogenisation in more detail.

The coupling of the laser beam into the fibre is achieved by focussing the laser beam to a known spot size via a spherical focussing lens (or lens doublet). The selection of the optics for the injection lenses is determined by the following parameters; the desired 1/e^2 beam diameter of the focussed beam, the M^2 of the laser beam, the diameter (1/e^2) of the laser beam as incident upon the focussing lens and the position of the laser beam waist. For initial lens selections the focal length of the focussing lens is estimated by Eqn. (19)

$$F = \frac{\pi D w_0}{2M^2\lambda} \tag{19}$$

F is the focal length of the lens, *D* is the $1/e^2$ diameter of the beam as measured at the lens entrance, w_0 is the $1/e^2$ beam radius of the desired focussed spot, M^2 is the measure of beam quality given by [51] and λ is the laser wavelength.

The Rigel series of lasers have typical specifications of, $18 < M^2 < 25$, λ=1064 nm ± 2 nm and *D* varies between 2 mm and 10 mm dependent upon design layout.

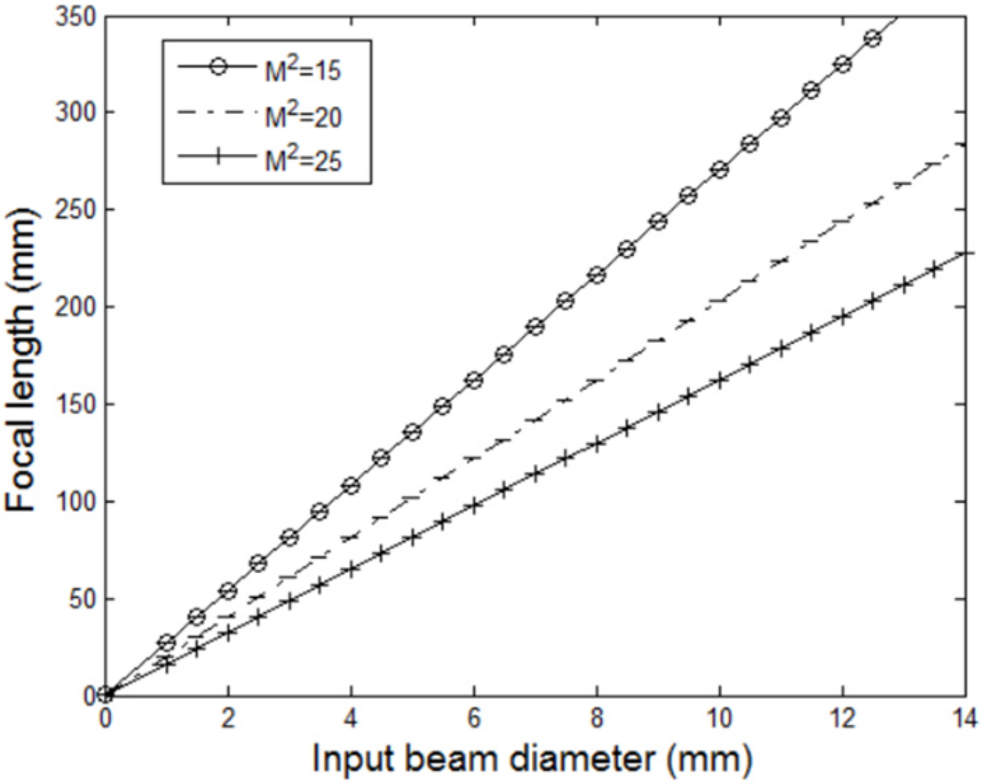

Figure 29 – Range of focal lengths for different collimated laser beams.

Figure 29 shows the range of focal lengths for different collimated laser beam diameters with a range of beam qualities indicated by their M^2. In the case where the desired focussed spot radius is 0.28 mm $1/e^2$, wavelength of the laser is 1064 nm and the M^2 of the laser is 20, then this graph indicates that, for an entrance beam diameter of 6 mm, a focal length of 110 mm is desired.

This simple analytical approach is useful for the selection of the focal length of the lens but is not in general adequate for the opto-mechanical design of the lens assembly. This is because the laser beam is not generally collimated when incident upon the focussing lens, which led to an increase in the back focal length. In order to model the focussed beam position the ABCD model, described in Chapter 2 was used in free space to locate the beam waist position. The ABCD model result shown in Figure 30 indicates the locations of the waist of the incoming laser beam and the waist of the focussed beam. This permitted the accurate design of the mechanical housing of the lens.

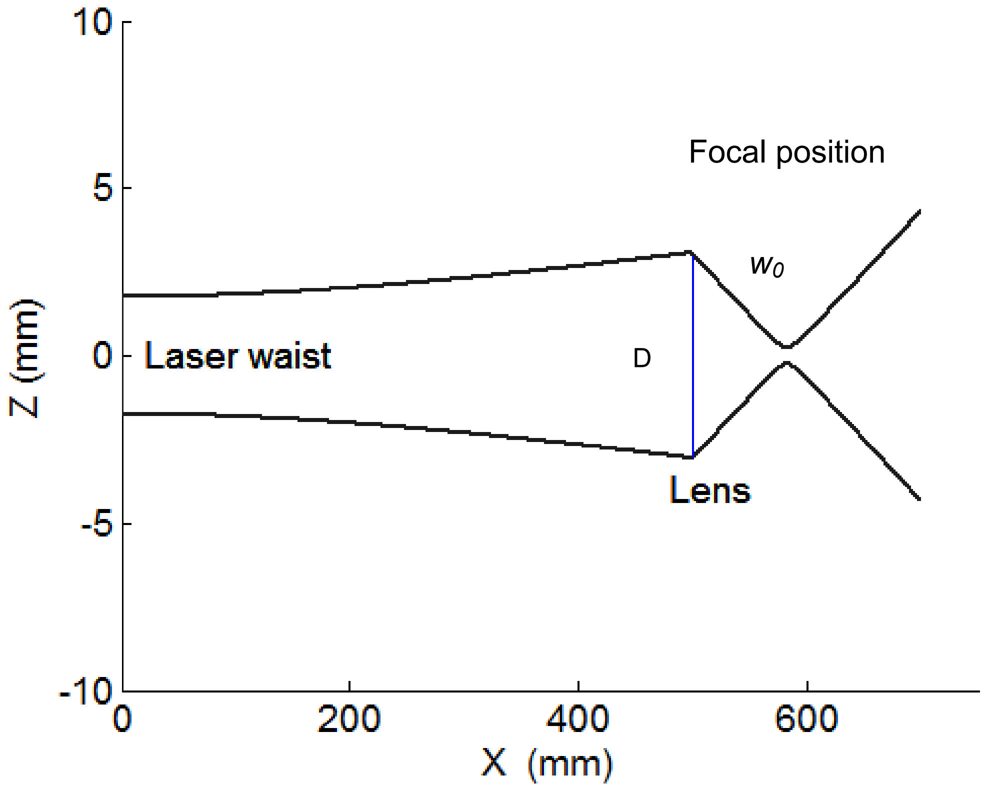

Figure 30 – ABCD model of laser beam focussed by a lens of EFL 75mm.

The ABCD model however does not predict the irradiance profile of the laser beam and the measured irradiance profile shape of the focussed laser beam emitted from a Rigel series laser is shown in Figure 31 and XY-slices shown in Figure 32. For practical laser beam measurements, the laser waist position and M^2 of the laser beam is determined by a beam quality measurement tool, either a Spiricon M^2-200 or a Cinogy CinSquare CS200, measured to standard ISO1146/1/2.

Even though the laser is strongly multimode the resulting irradiance profile of the focussed beam takes the form of a nominally Gaussian line-shape, albeit noisy and a typical measured profile is shown in Figure 31 and Figure 32. The irradiance profile did not show signs of sharp discontinuities that would lead to hotspots that could damage the fibres.

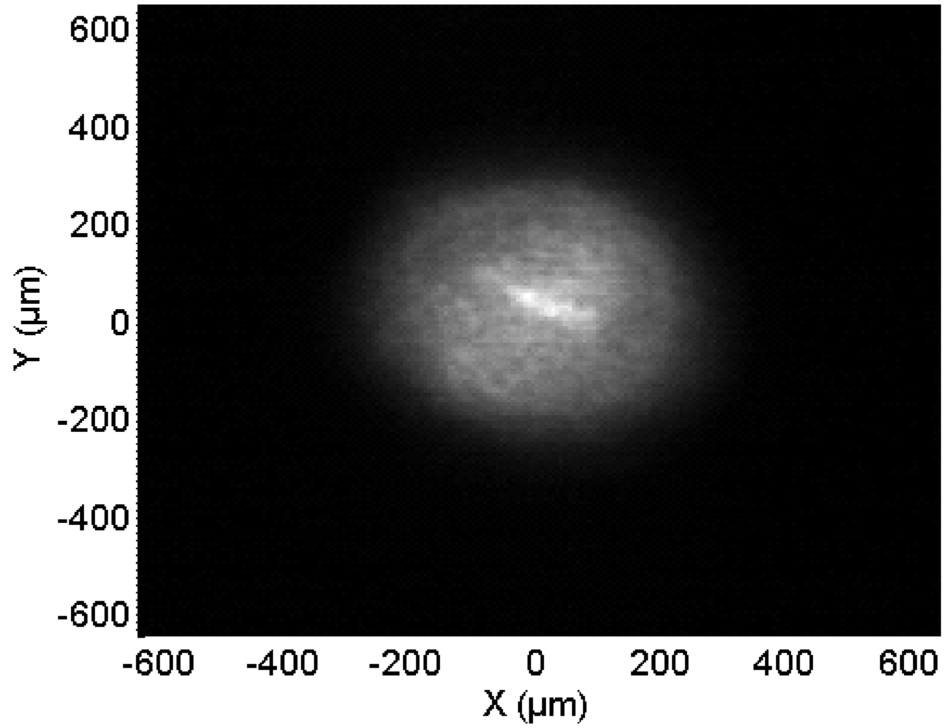

Figure 31 – Rigel i-series laser irradiance profile at focus.

Figure 32 shows the line cuts through the irradiance profile of the focussed laser beam.

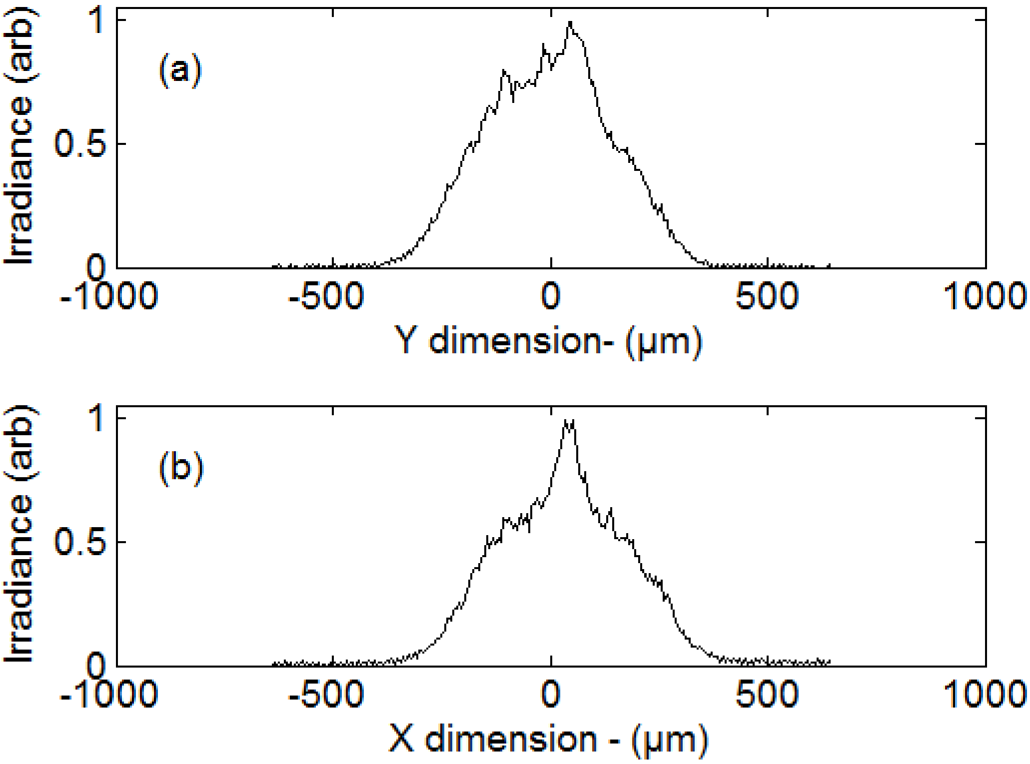

Figure 32 – Rigel series laser irradiance profile at focus. Line cuts through (a) the horizontal and (b) the vertical planes of the beam show 1/e^2 diameters of 561 μm and 542 μm respectively.

Using the approximate Gaussian line-shape of the focussed beam profile the coupling efficiency *C* was estimated by Eqn. (20). Fresnel reflection losses at the entrance to the fibre can be neglected as the fibre end cap has an anti-refection coating R < 0.5%.

$$C \cong \frac{\int\int_{-\infty}^{\infty} I_0 e^{\left[-\left(\frac{\sqrt{2}X}{g_X}\right)^2-\left(\frac{\sqrt{2}Y}{g_Y}\right)^2\right]} \times e^{\left[-\left(\frac{X}{h_X}\right)^{20}-\left(\frac{Y}{h_Y}\right)^{20}\right]} dXdY}{\int\int_{-\infty}^{\infty} I_0 e^{\left[-\left(\frac{\sqrt{2}X}{g_X}\right)^2-\left(\frac{\sqrt{2}Y}{g_Y}\right)^2\right]} dXdY} \qquad (20)$$

I_0 is the peak irradiance, g_X and g_Y are the 1/e^2 radii of the beam irradiance profile and h_X and h_Y are the 1/e half widths of the fibre.

The fibre transmitted the laser radiation and homogenised has a 600 µm square core with a length that varies from 10 m to 20 m long depending upon customer installation requirements. The maximum supported NA of the fibre was 0.2 and the injected NA is calculated form the ABCD models to be approximately 0.024 and well within this NA limit of the fibre. The coupling into the fibre for different input beam waists is modelled using Eqn (20), the fibre shape is approximated to a super-Gaussian line shape with order (n) of twenty, which describes a square profile in two dimensions with similar sized edge-widths to the actual measured irradiance profile of the fibre. The profile of this super-Gaussian is shown in Figure 33.

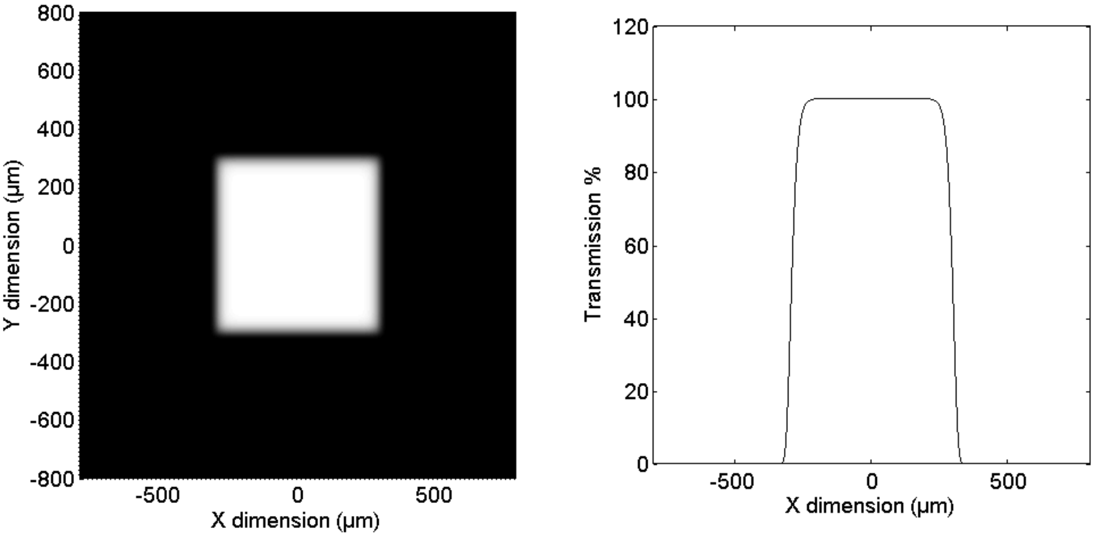

Figure 33 – Super-Gaussian model of square core fibre. Inset (a) shows the 2D profile of the fibre and (b) shows the line cut thought the X axis.

Figure 34 shows the modelled trade-off between coupling and the peak irradiance at the focal point of the focussed laser beam. If the input beam waist is too small there is a high risk of shattering the core due to the high peak irradiance of the laser beam, typically >40 GW/mm^2. Conversely too big a spot is generated at the focus this gave a lower coupling efficiency and also risks shattering the fibre core due to radiated power being dissipated in the fibre cladding rather than being transmitted into the fibre.

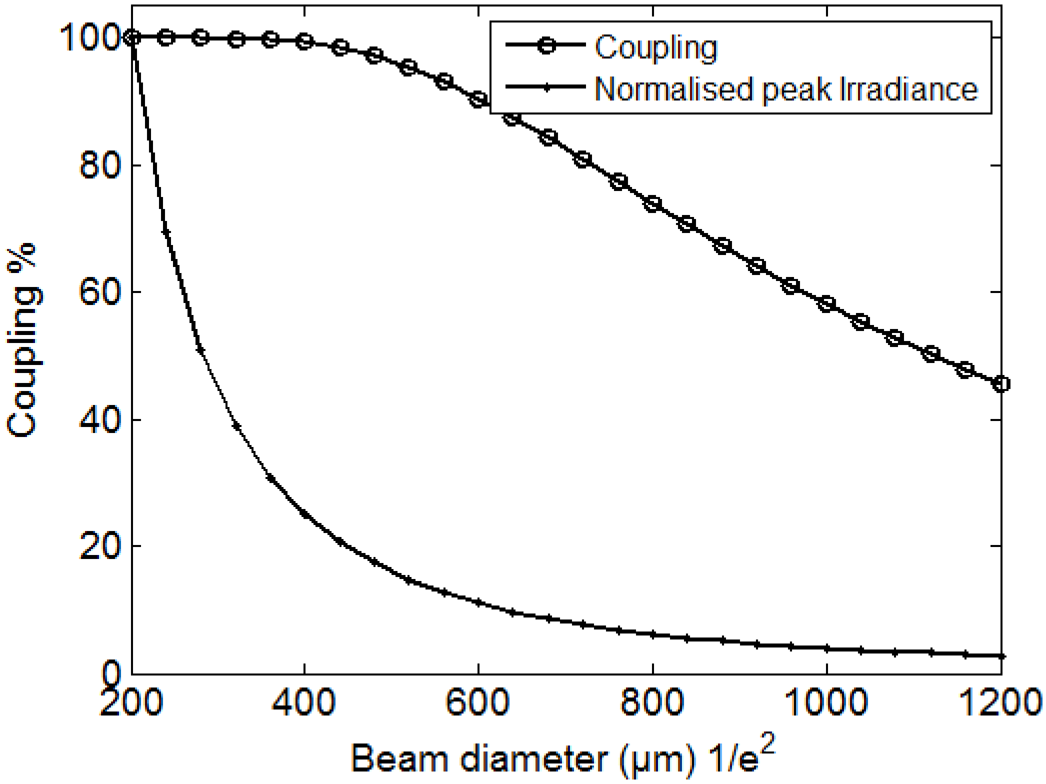

Figure 34 – Irradiance and coupling efficiency variation with beam waist size.

In order to assess the optimum input beam waist, the exact value for the peak irradiance of the focussed laser beam can be established by Eqn. (21), where P is the peak power of the pulse, ω_X is the 1/e^2 radius of the focussed profile in the X axis and ω_Y is the 1/e^2 radius of the focussed profile in the Y axis.

$$I_0 = \left(\frac{2}{\pi}\right)\left(\frac{P}{\omega_X \omega_Y}\right) \tag{21}$$

Similarly the peak fluence, F_0, is given by Eqn. (22), where E is the pulse energy.

$$F_0 = \left(\frac{2}{\pi}\right)\left(\frac{E}{\omega_X \omega_Y}\right) \tag{22}$$

For this application a design beam diameter ($1/e^2$) in the range 500 µm to 550 µm is found to give optimum coupling, which yields the largest practical spot size, while still achieving coupling efficiencies of greater than 98%. Using this beam waist size, the value of peak irradiance for a focussed spot of a laser with 1.6 kW average power is 25 GW/mm^2 and the peak fluence is 125 J/cm^2. These figures are high enough to damage most coatings or optical surfaces. In order to resolve this modern optical fibres used to couple to high power lasers are designed to have an end cap design as shown in Figure 35. In this design the fibre is physically fused to the end cap to make a the region subjected to the high fluence a section of homogenous bulk fused silica, provided the fusing of the end cap to the fibre is of sufficient quality the damage threshold achieved at this join should approach the bulk damage threshold [60-61] of fused silica of 3854 J/cm^2 ± 10 J/cm^2 as measured at 1064 nm with a 14 ns pulse duration. In practice this higher value laser induced damage threshold is seldom achieved due to process of fusing the fibre onto the back of the end cap and the damage threshold can vary from manufacture. For this reason all the fibres used in the high power laser systems were stress tested before shipment by a factor of two by fluence and peak power. The fibres utilised in this project are commercially available from a number of suppliers, with surface typical fluence limits for the incident light on the end cap of < 50J/cm^2. The fused joint between the fibre and end cap is manufactured either by electrical arc or by clean flame, depending upon manufacturer. Two manufacturers were used for the supply of fibres, Optoskand and Highyag, both using a flame process.

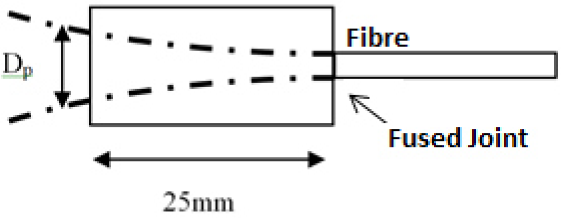

Figure 35 – Diagram of the fibre coupling end cap, the dashed line indicates the $1/e^2$ contour of the irradiance profile.

D_p, as referenced in Figure 35, was calculated using the ABCD model propagating from the fibre core and was determined to be approximately 1.2 mm diameter at the entrance to the end cap. Setting a limit of 17 J/cm^2 @ 60 ns yielded a maximum average power of 1 kW for a 10 kHz pulsed laser, that can be safely coupled using this method.

The size of the spot and the coupling efficiency are predicted by the Eqn. (20). By translating the offset of the focussed beam and the fibre core, a coupling curve can be generated that can be used to compare to the practical result of translating a fibre across the focussed laser beam in X or Y. Using this approach the measured vs modelled fit is shown in Figure 36 for eleven different lasers. A good fit is observed and this is an approximate measurer of the spot size and variance in the coupling achieved for a sample of laser builds.

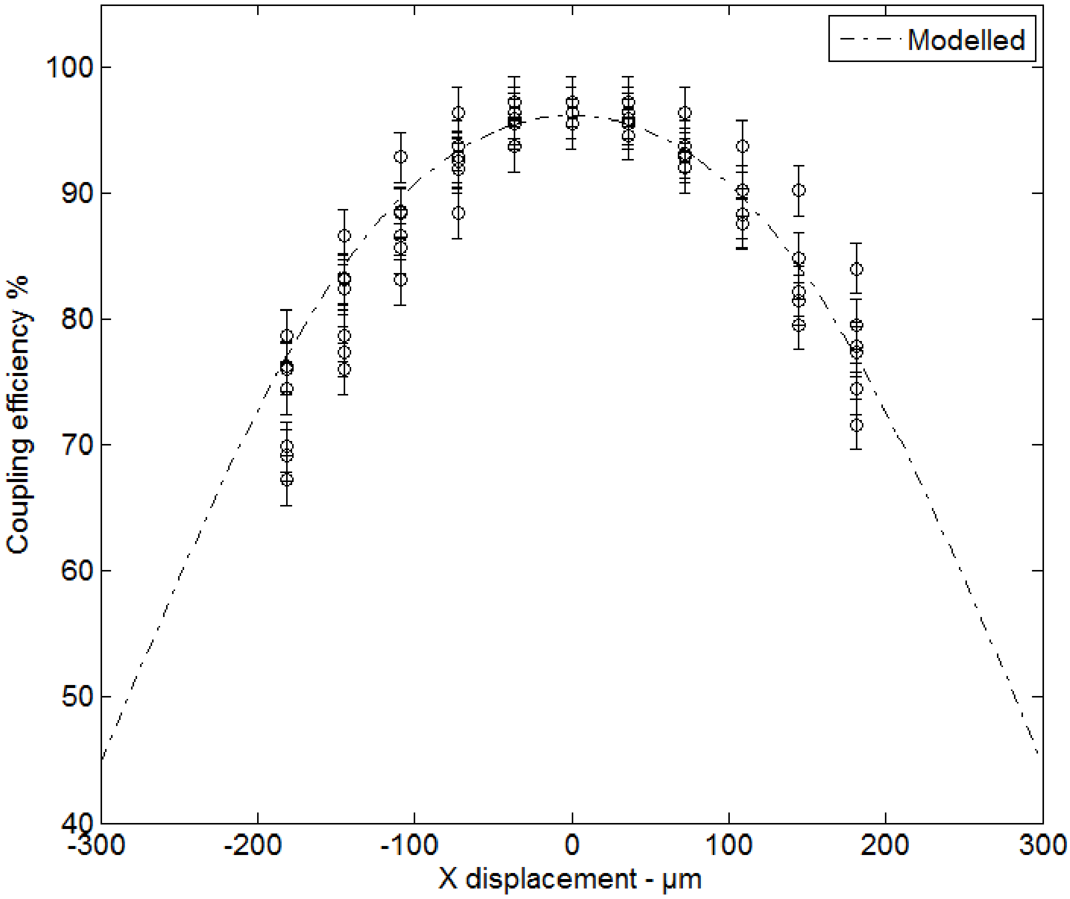

Figure 36 – Fibre coupling curve for different displacements of the beam from the fibre centre, fibre had a 600 μm core diameter and the laser beam was 550 μm 1/e^2 beam diameter.

The source of the uncertainties in Figure 36 are the variations in laser M^2 between the different lasers, the variations in beam waist position (in Z) due to different amplifier thermal lens strengths and, to a smaller degree, variation in the fibre diameters between systems.

3.2.1 Note on first pulse control of the laser

The lasers utilised in this process are typically pulsed between 10 kHz and 15 kHz. The time between pulses for these repetition rates are significantly less than the upper state fluorescent lifetime of the Nd;YAG, typically 230 μs. In the case when the laser is first Q switched from a period of hold off, via the internal AOMs this causes the first pulse emitted to be considerably more powerful than the following laser pulses at a stable repetition frequency, as there is more stored power for the first pulse.

This giant first pulse of the laser is indicated in the schematic in Figure 37, where the laser is held off from lasing by the AOM before pulsing is applied and the first pulse is shown at 400 µs, the following pulses are even but have much lower peak powers. A large initial large pulse generally causes damage to sensitive components if not removed, especially to the fibre coupling joint as described in this chapter and the laser internal optics.

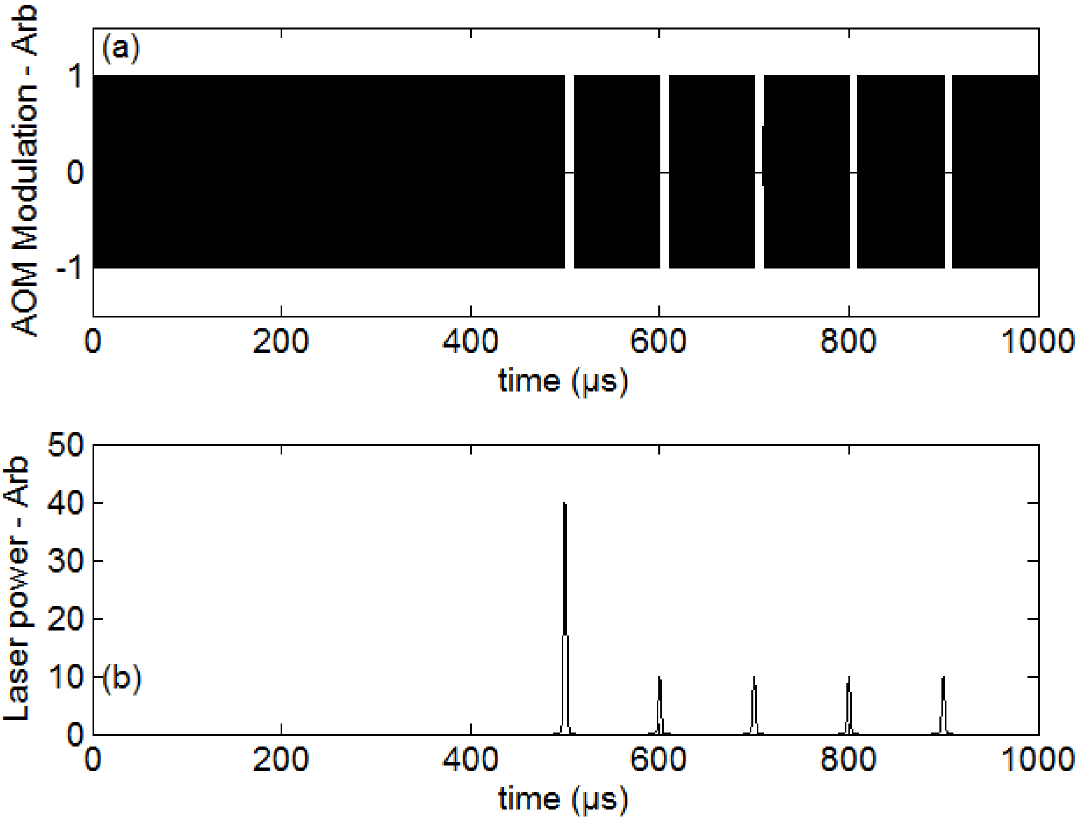

Figure 37 –(a) laser AOM drive and (b) lasers pulses.

The scheme employed to remove the giant first laser pulse is shown in Figure 38. In this scheme the acousto-optic modulation (AOM) is reduced linearly over a period of 250 µs prior to the repeated Q switching of the laser cavity. During the linear release of the AOM a pulse of large temporal width, but small peak power is released. This removes the energy from the first Q switched pulse and the height of the subsequent first pulse can be tuned by the timing following the first hold-off cycle of the AOM. By tuning the slope and the timing of the linear AOM region the first pulse height can be reduced to the same peak height as the following peaks when continuously pulsed. This protects the laser and optical components from first pulse damage.

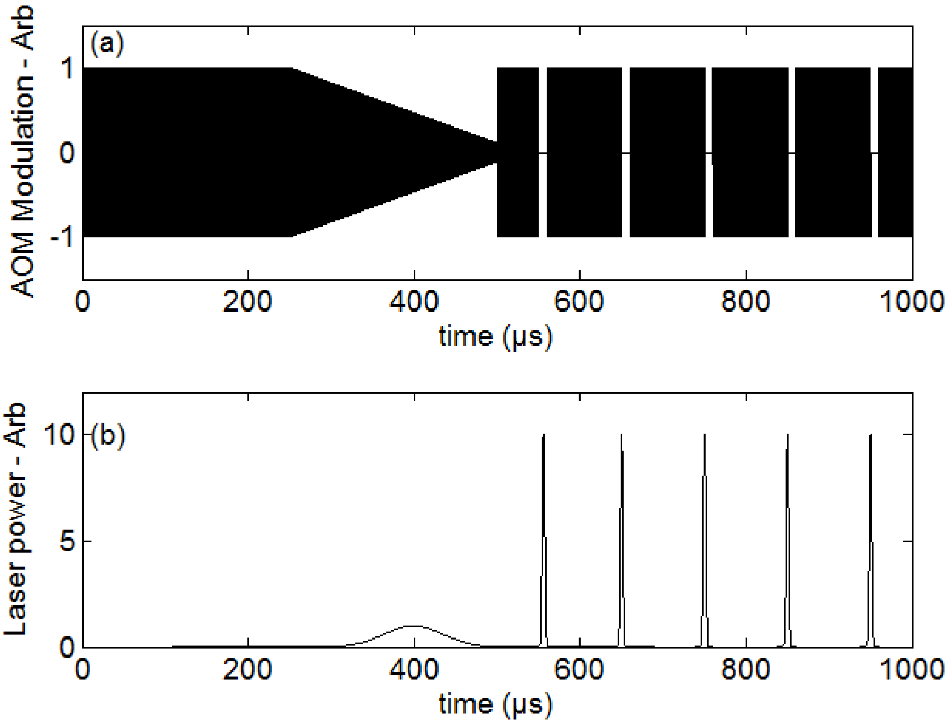

Figure 38- Laser AOM signal and even first pulses as a result of electrical first pulse control

This first pulse control is a standard part of the laser alignment procedure for the Rigel i-series.

3.2.2 Summary of fibre coupling

A summary of this section is that a focussed spot from the Rigel i-series laser of approximately 550 um $1/e^2$ gives the optimum balance between coupling efficiency and physical damage to the fibre.

Figure 39 shows the coupling efficiencies achieved over fourteen lasers, manufacturing variance in M^2, hence spot size accounts for most of the deviation from the modelled line. In all cases the fibre coupled up to 1 kW average power at 10 kHz with 60 ns pulse duration, with no damage to the fibre or the optics. The same coupling arrangement was also explored at 1.6 kW 10 kHz with 60 ns pulse with no damage to the fibre, even though it exceeded the damage limits specified in this chapter.

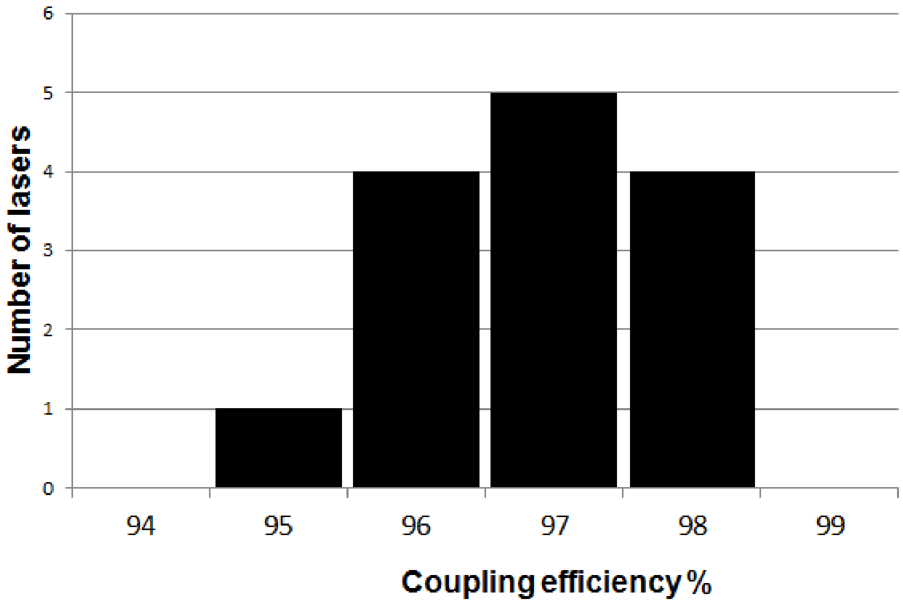

Figure 39 – Histogram of coupling efficiencies achieved with Rigel i-series lasers.

3.2.3 Conclusion of fibre coupling

The conclusion of this section on fibre coupling is that for a 550 μm $1/e^2$ diameter spot the mean coupling efficiency is 97% and there is a safe average power of 1 kW for a 60 ns, 10 kHz laser, which scales accordingly with repetition rate.

3.3 Fibre homogenisation

The fibre serves another more subtle purpose than the physical transport of the laser power to the processing head. As the laser radiation propagates through the fibre, the laser light is homogenised and de-polarised by the fibre into the same core shape and dimensions as the fibre. In addition the laser output of $M^2 = 20$ has a large spatial mode content. This acts to destroy the spatial coherence of the laser beam and, as a consequence, the serendipitous removal of speckle. The net result of this process was that the output of the fibre has a very homogenous square profile, as shown in Figure 40 and in the XY-slices in Figure 41. The profile was homogenous even if the profile was observed for a single pulse of the laser. The image in Figure 40 was obtained with a Thorlabs DCC1545M CCD camera and an optical relay with a magnification of approximately 1.5 ×. The X and Y dimensions were calibrated by mounting the camera on a micro-meter driven linear stage, the gamma correction was intentionally set to one, so the irradiance profile is not distorted. The images of the fibre and the holograms were acquired without damage to the camera at high powers by means of a series of reflective attenuators with mounted internally or externally and the excess power was dumped into water cooled beam terminations. Calibration of the image size was performed by mounting the fibre on a linear stage with a micrometer actuator and comparing the displacement of the image in pixels with the physical motion of the fibre.

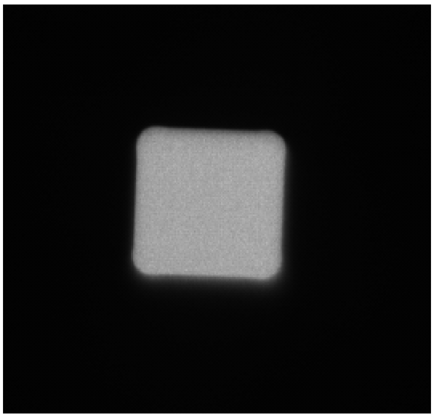

Figure 40 – Irradiance profile of the 600 µm square core fibre.

Measurements techniques and details of the quality measures for the irradiance profile such as, spot width, edge width and homogeneity is given in later chapters.

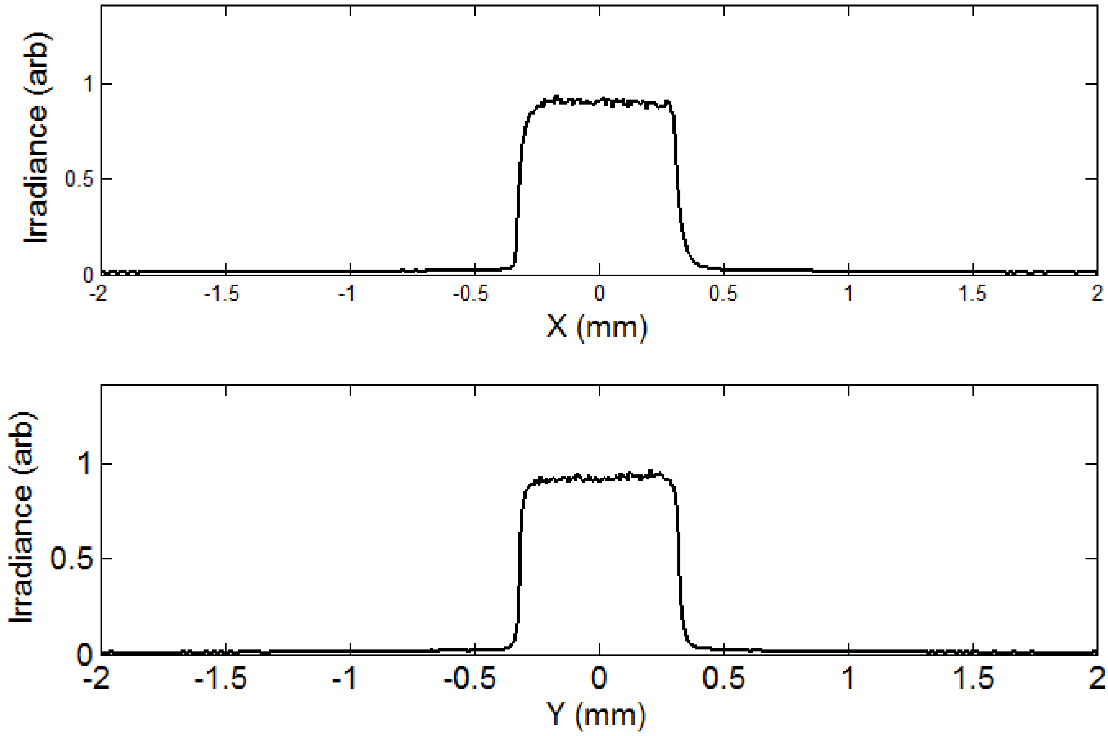

Figure 41 – The homogenised output of a 600 μm fibre shown as line cuts in (a) the X plane and (b) the Y plane.

The homogenisation action of the fibre is at the expense of an increase in the beam parameter product (BPP). Defined in Eqn. (23) below as:

$$BPP = w_0\theta_0 \tag{23}$$

Here *BPP* is beam parameter product, w_0 is the $1/e^2$ beam waist and θ_0 is the beam divergence. When the beam divergence is very small the divergence angle is practically identical to the numerical aperture (NA),in rads, which is defined a NA=sin (θ_0).

Figure 42 shows the output NA emitted from a square core fibre with a diameter of 600 μm and a length of less than 30 m and is plotted as a function of the input NA of the injected laser beam. Is is taken directly from reference [16].

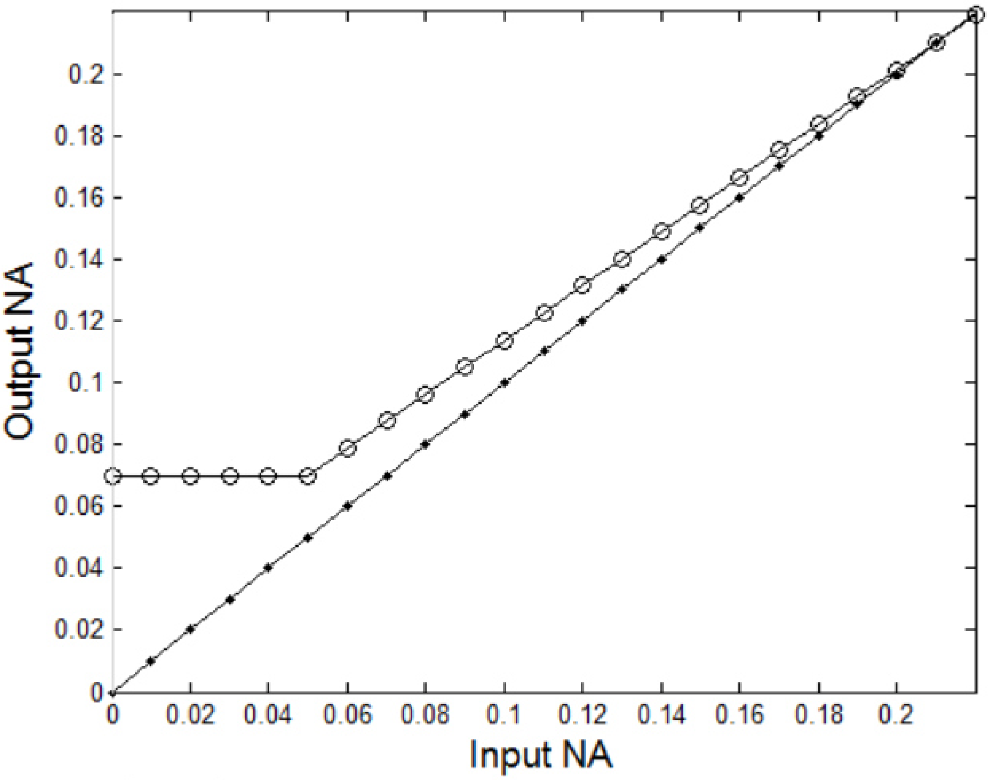

Figure 42 – The resulting output NA for a 600 µm square core fibre for a fixed length of fibre <30 m for a range of input NAs from the focussed laser beam of fixed beam size (550 µm 1/e^{2}diameter).

Eqn. (24) details the relationship parameters that describe the NA of the focussed laser spot that was injected into the fibre. Typical laser beam parameters were, M^2=20, λ=1064 nm, F=100 mm and by placing these values into Eqn. (24), the input NA in the fibre was determined to be 0.024. The output NA measured in the fibre was typically NA=0.07 to 0.08, approximately three times the input NA and in agreement with the graph in Figure 42.

$$NA = \left(\frac{M^2 \lambda}{\pi W_0}\right) \tag{24}$$

Although there was an increase in the NA of the emitted light, an NA of 0.08 is still small enough to facilitate a relatively simple and compact design of the beam shaping and process delivery optics. This small NA < 0.08 is ideal for minimising the number of optics surfaces that form the beam shaping and beam delivery optics.

3.3.1 Other approaches to homogenisation

It is useful to compare the homogenising approach using the fibre to other homogenising approaches that are commonly employed to shape a laser beam in order to compare the effectiveness of the fibre homogenisation approach. A clear area of interest is the possibility where the beam shaping takes place within the processing heads. An option evaluated for this and other applications, potentially without a fibre, was the use of holographic elements to shape the laser beam. These optical components are often referred to as kinoforms [15] or computer generated holograms (CGHs) and consists of transmissive or reflective plates, where the optical phase of the beam is altered across its spatial profile [12]. This spatial variation of optical phase in the near field then alters the far field content as the beam propagates, the far field irradiance pattern can then be reconstructed in the near field by a field lens [62]. By designing the near-field phase profile to generate a desired far-field irradiance profile, complex beam shaping can be performed. A common approach to designing these holograms is the Gerchberg-Saxton [63] phase retrieval algorithm; Figure 43 serves as a demonstration of the technique using fast Fourier transforms [64]. There are many more versions and techniques, which are covered in literature [12, 59, 65-66] and commercially derived versions.

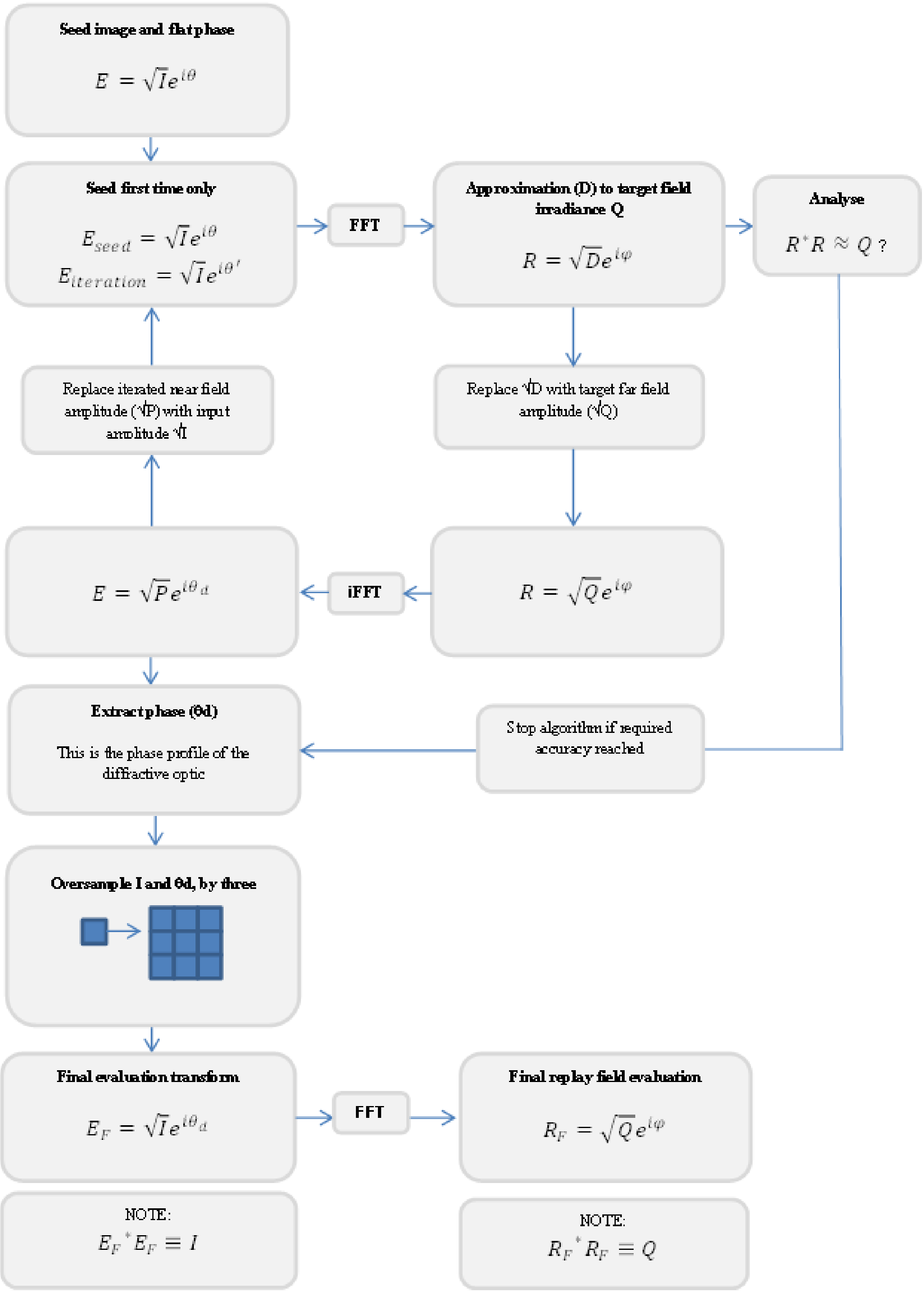

Figure 43 – Gerchberg-Saxton algorithm.

In the application of the Gerchberg-Saxton algorithm shown in Figure 43, an input field profile is given in terms of its measureable irradiance, I and its field phase, θ. Both the field amplitude and phase profile are complete functions in X and Y that describe the profile over a finite domain size chosen by the designer. The first step in the iteration is a fast Fourier transform (FFT) which generates a field amplitude $\sqrt{D}$ and phase ψ that describes the angular profile of the beam in the far field. This is commonly referred to as the replay field in literature [12] and here is given the symbol R. The irradiance profile as a function of angle can be evaluated by multiplying the complete description of the field, R by its complex conjugate. This is then compared to a desired far field irradiance profile Q. If the match fails a prescribed criteria then the iteration repeats and the far field amplitude $\sqrt{D}$ is extracted and replaced with the desired amplitude $\sqrt{Q}$. An inverse FFT is then performed, which generates an altered phase and field amplitude as function of X and Y. The phase, now $\theta_{d,}$ is kept but the field amplitude, $\sqrt{P}$ is discarded and replaced with the original field amplitude $\sqrt{I}$ and the iteration continues until a desired replication quality of far field irradiance profile, Q, is reached. Once the desired quality is reached the algorithm outputs a phase map θ_d in the X and Y dimension, this is oversampled to replicate the physical size of the diffractive optic and to render some features visible in the replay field that would otherwise be hidden, in particular the higher holographic orders. The final oversampled phase profile can then be evaluated or realised into a real physical device made of glass or generated via a suitable spatial light modulator (SLM). These and other techniques are discussed in much more detail in literature [12], but are outside the scope of this thesis.

It's important to note a few features of this algorithm, the first is that it can give a multiple set of solutions for θ_d that are strongly dependent upon the initial seed phase profile, the second point is that the beam shaping desired is of the irradiance profile, not the field amplitude. Potentially of interest to a reader of this thesis is that the algorithm can be altered to create target irradiance profiles at specific positions along the propagation axis Z, either by adding lens functionality to the generated hologram $\theta_{d,}$ or by replacing the Fourier transforms with Fresnel transforms

A modelled example of the Gerchberg-Saxton algorithm is detailed in Figure 43 and Figure 44.

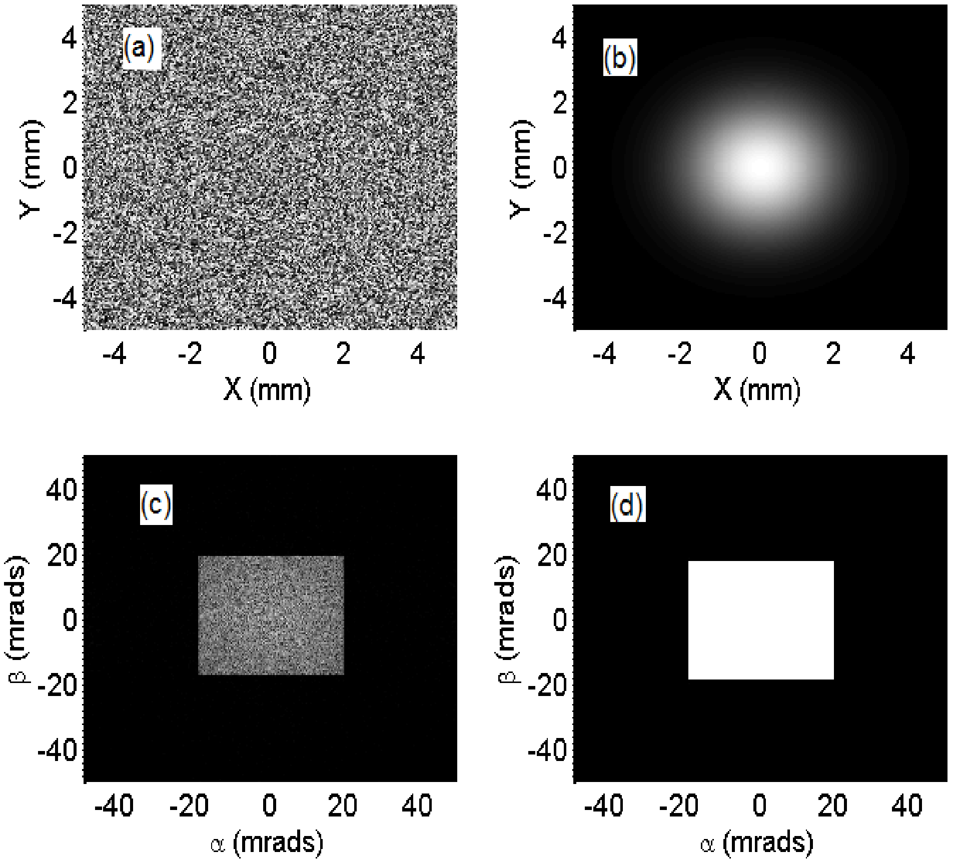

Figure 44 – A modelled example implementation of the Gerchberg – Saxton algorithm as described in Figure 43. (a) is the derived diffractive phase θ_d, (b) is the input irradiance, *I*, profile incident on the diffractive (c) is the modelled oversampled far-field irradiance, *D* and (d) is the target far-field irradiance, *Q*.

Holographic beam shaping is very common in lasers with a single spatial mode [15]. However there is little documentation on how beam quality would be affected by increasing the spatial mode content of the laser. An experimental investigation was devised to investigate the differences between beam shaping quality of lasers with differing spatial mode content. The experimental apparatus was set up as shown in Figure 45 for a single mode infrared laser, the holographic CGH evaluated was a binary phase hologram manufactured by Holoor, part number HM-201-1-Y-A, this had an individual pixel relief size of 120 μm.

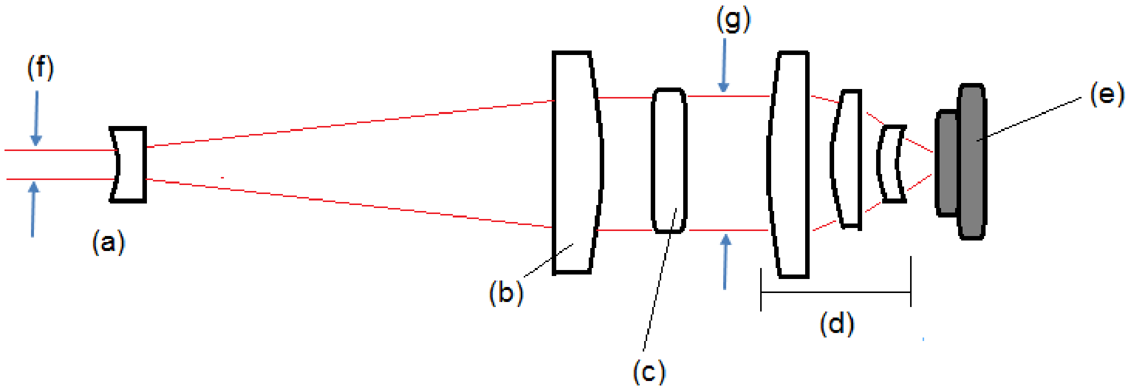

Figure 45 – Experimental set-up, (a) is a -54 mm EFL lens, (b) 500 mm EFL lens, (c) the CGH, (d) 50 mm EFL lens group for the camera, (e) DCC1545M Thorlabs camera, (f) 0.7 mm input beam diameter, (g) 7.7 mm diameter beam at CGH.

$$w_{o'} = \left(\frac{2M^2\lambda}{\pi}\right)F\# \qquad (25)$$

The pixel relief was easily visible in a microscope and is shown, for interest in Figure 46 and the minimum surface feature was determined to be 125 µm, this correlates to a maximum diffracted image size of 85 mrad and a FWHM image in a 50 mm lens of 420 µm.

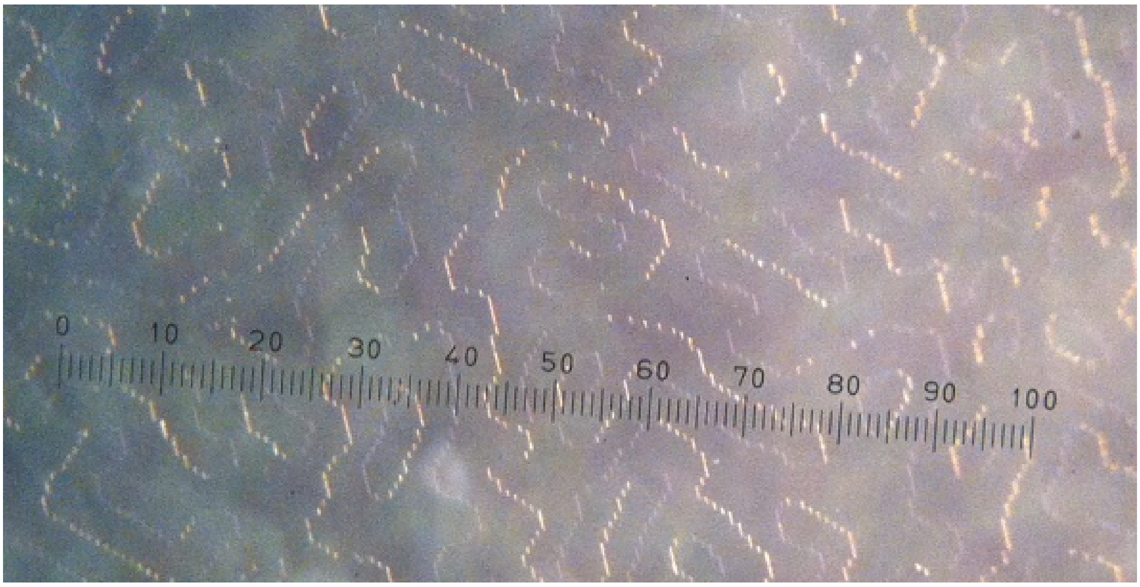

Figure 46- Pixel relief of the GCH from Holoor HM-201-1-Y-A

The image produced at the focus of the 50 mm EFL lens is shown in Figure 47 for a Nd:YAG laser with $M^2 < 1.5$. The presence of laser speckle in the image at the camera was evident and was not desirable for a homogenised beam profile. The Gerchberg-Saxton model, as presented, doesn't model the laser speckle as seen in the replay field.

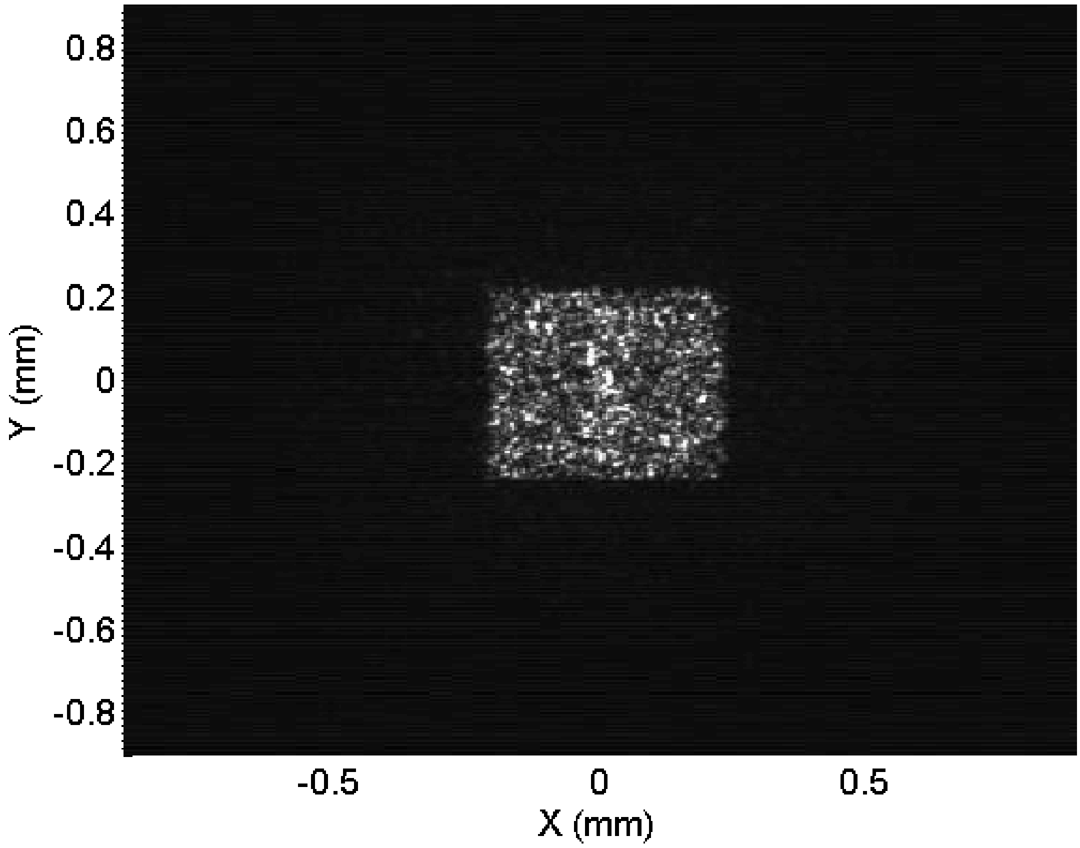

Figure 47 – Holographic profile from a Nd:YAG laser with an $M^2 < 1.5$.

The X-slice through the irradiance profile imaged by the camera is shown in Figure 48, the speckle is evident as sharp discontinuities in the irradiance profile

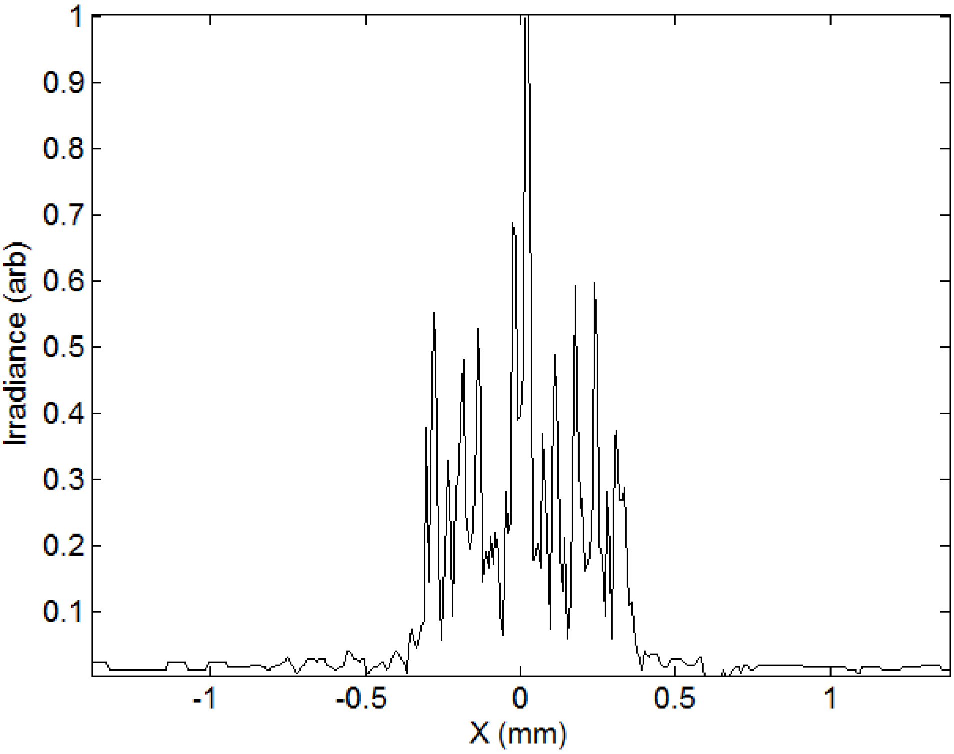

Figure 48 – Holographic profile from a Nd:YAG laser with an $M^2 < 1.5$.

Little is given in literature about the appearance of beam shaped images formed using CGH devices combined with laser beams with large spatial mode content or M^2 significantly larger than 2. Normally the results for lasers with larger M^2 illumination are undesired [15]. The same experimental set-up was used as in Figure 45, but the laser source was replaced with a multimode laser of $M^2=24$, an aperture was placed in front of the CGH to the same illumination size as the M^2 laser and the irradiance profile was imaged, the profile is shown in Figure 51. The image size is maintained but the depth of the speckle was reduced and the image as more homogenous. The larger M^2 had the effect of blurring out the sharp speckle features of the laser.

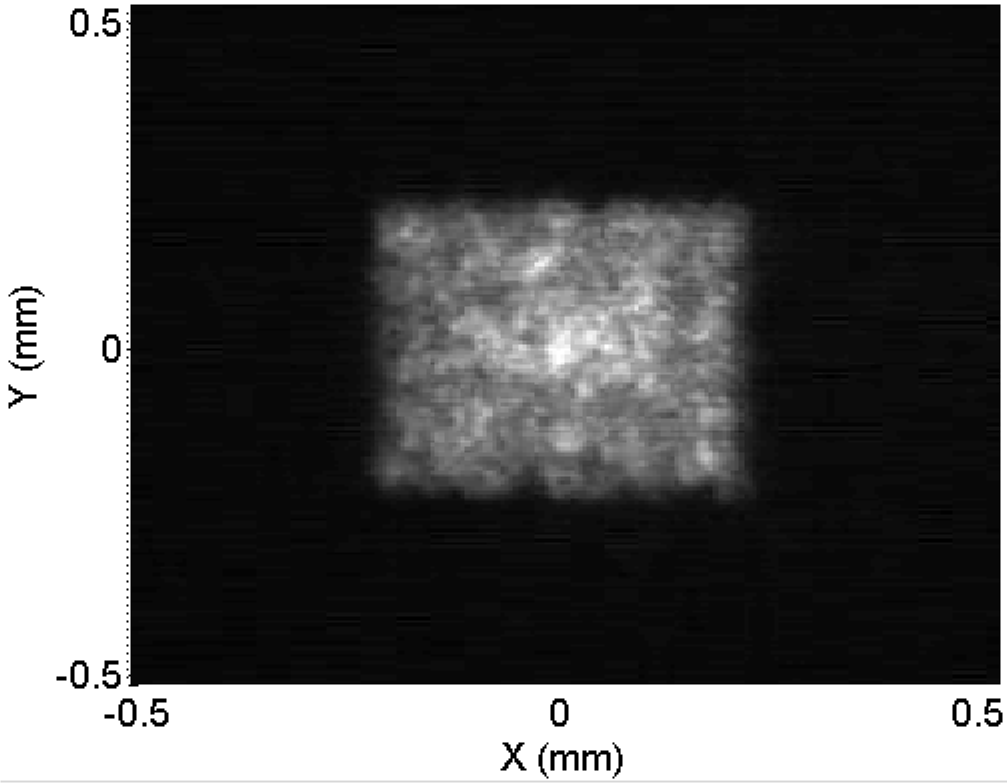

Figure 49 – Holographic profile from a Nd:YAG laser with an M^2 = 24, imaged at F#=6.4.

A slice through the irradiance profile is shown in Figure 50 and the laser speckle pattern was still evident but the depth of the speckle interference patterns was much reduced when compared to the lower M^2 laser but was still much more evident and is poorer homogeneity than the fibre approach.

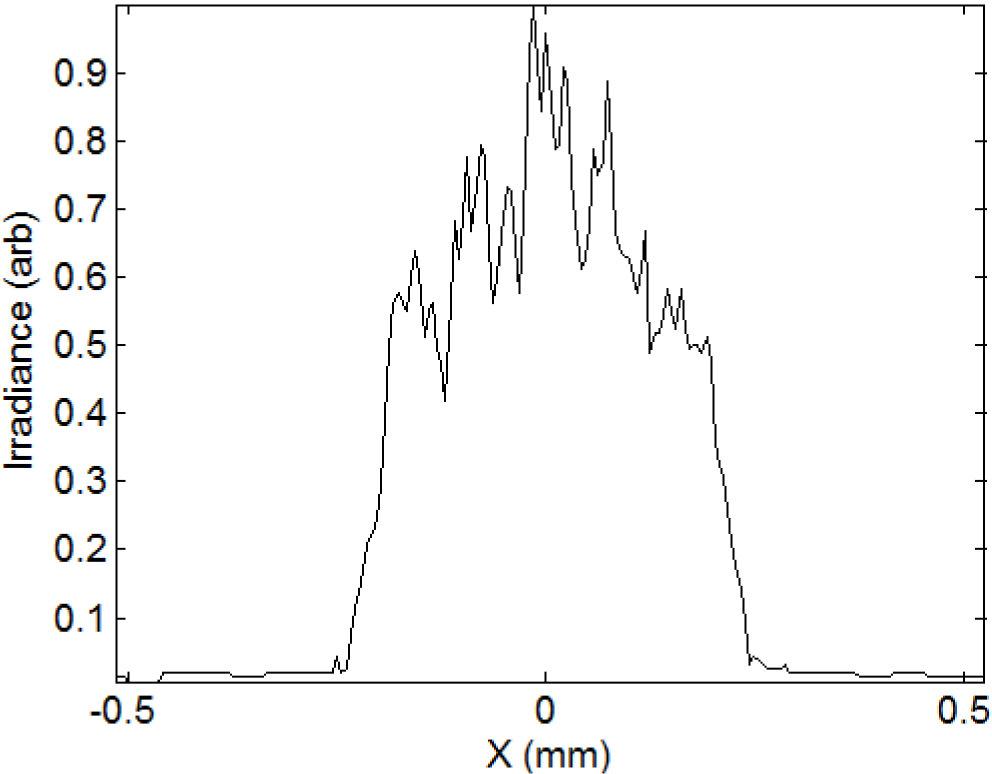

Figure 50 – Holographic profile from a Nd:YAG laser with an M^2 =24 imaged at f#=6.5.

It was discovered that if the illumination size of the CGH was increased with multimode laser then the speckle further reduced. This was characterised by the systems F#, here defined by the illumination diameter of the CGH and the focal length of the imaging lens, which was a constant 50 mm throughout. Figure 51 shows the result where the illumination was 20 mm, resulting in a system F# of 2.5.

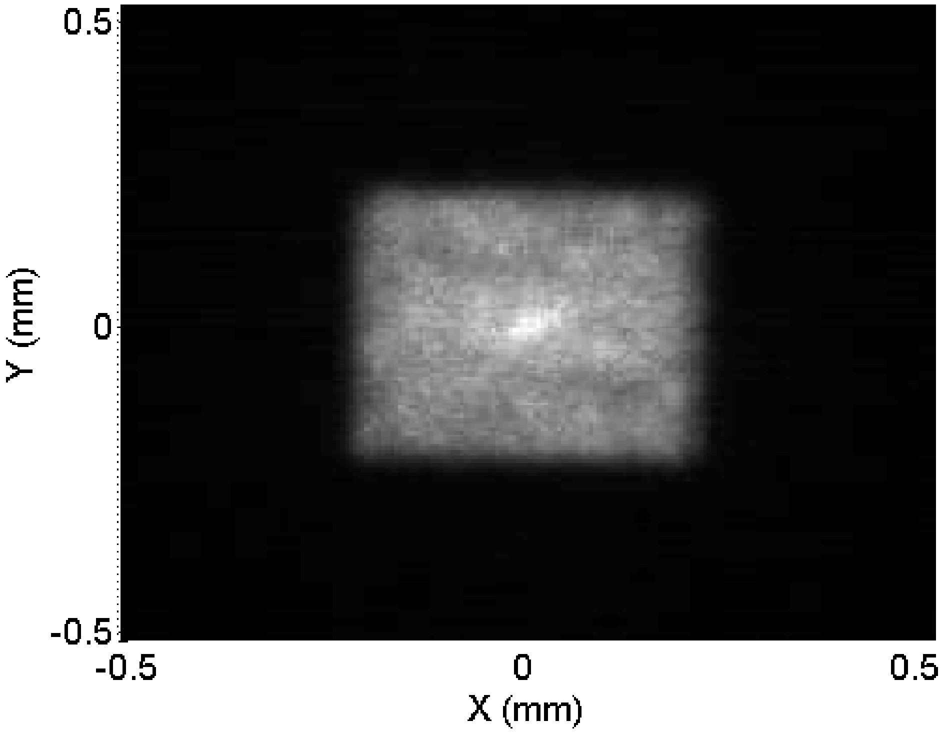

Figure 51 – Same CGH but with larger illumination diameter – 20 mm F# = 2.5.

Figure 52 shows the X- slice through the centre of the irradiance profile and further improvement of the homogeneity was observed.

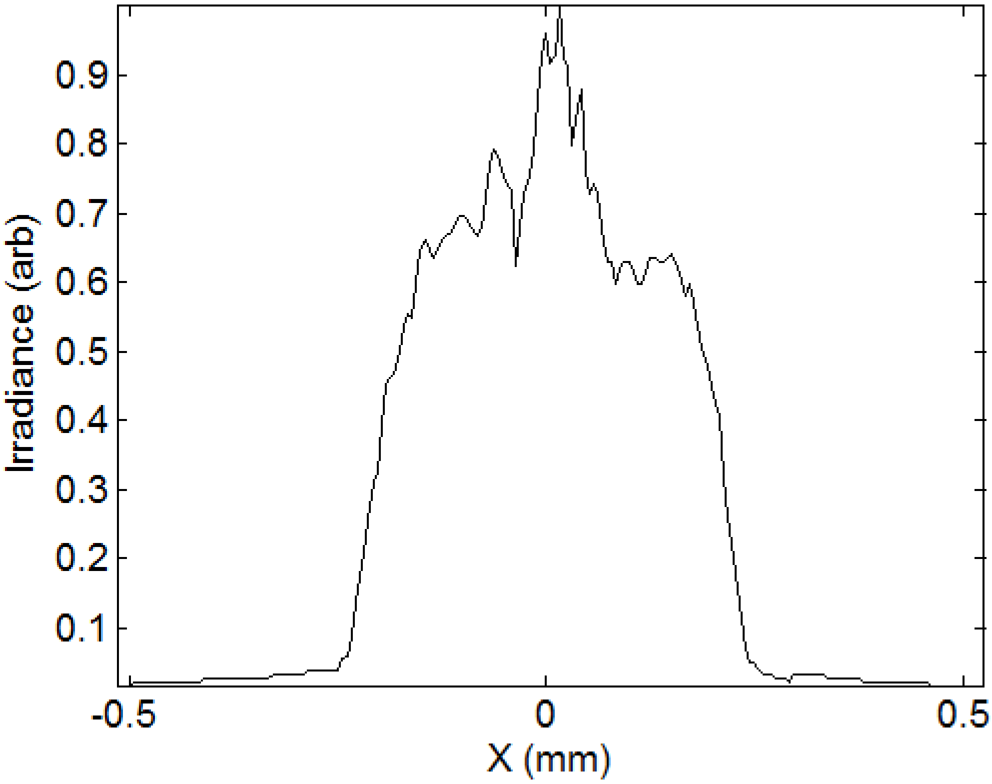

Figure 52 – X slice of irradiance for same condition F# = 2.5.

The variation in the speckle pattern was observed by varying the system F# by means of an aperture in place directly in front of the CGH. The homogeneity of the image was observed to improve for decreasing F#, there was little incremental improvement on in the homogeneity below F# =5.0. The zero order is also present in these images as a bright spot in the centre of the image.

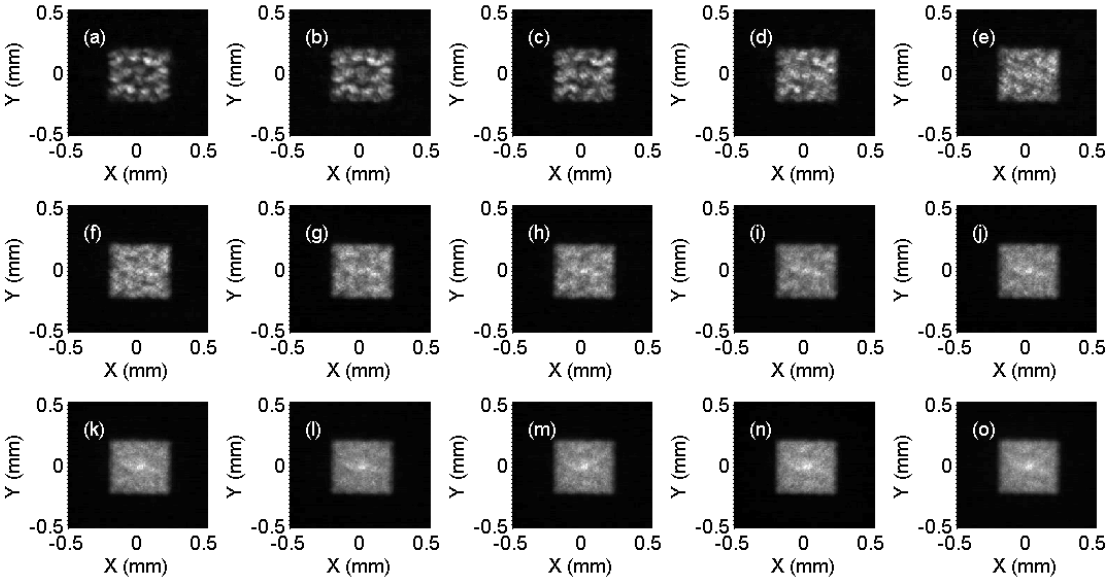

Figure 53 – Replay field of CGH for different F# (a) F# = 25, (b) F# = 20, (c) F# = 17 , (d) F# = 14.3, (e) F# = 12.5 , (f) F# = 10 , (g) F# = 8.3 , (h) F# = 7.14, (i) F# = 6.25 (j) F# = 5.5 (k) F# = 5 (l) F# = 4.6 (m) F# = 4.2 (n) F# = 3.8 (o) F# = 3.5.

X slices through the centre of the irradiance plots are shown in Figure 54.

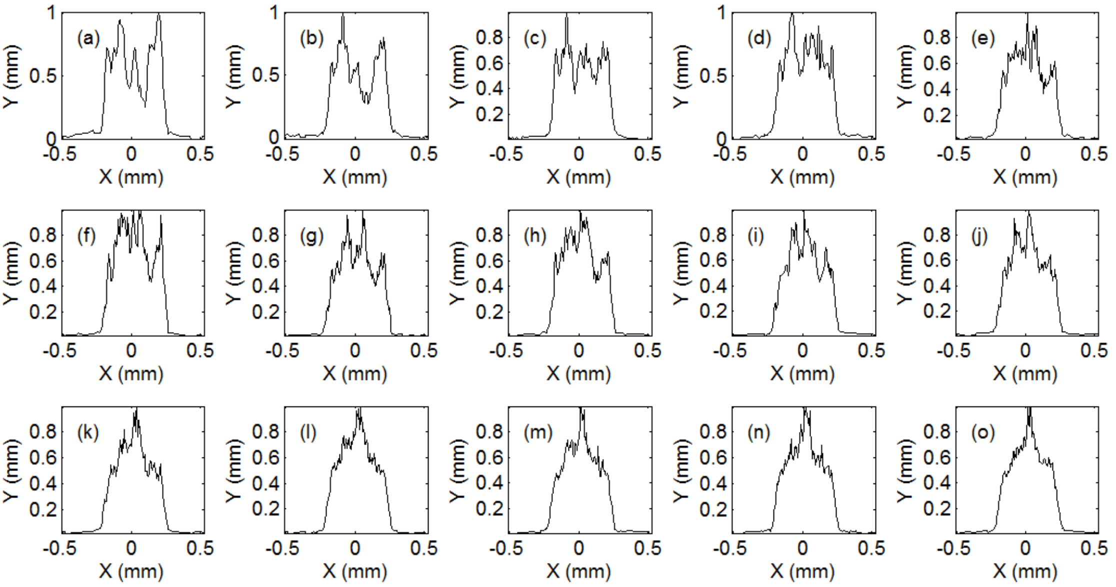

Figure 54 – Slices in X dimension for CGH replay images (a) F# = 25, (b) F# = 20, (c) F# = 17 , (d) F# = 14.3 , (e) F# = 12.5 , (f) F# = 10 , (g) F# = 8.3 , (h) F# = 7.14, (i) F# = 6.25 (j) F# = 5.5 (k) F# = 5 (l) F# = 4.6 (m) F# = 4.2 (n) F# = 3.8 (o) F# = 3.5.

If the best achievable value for the homogeneity for the hologram is taken to be F#=5.0 then this is the equivalent of a system NA of 0.1 and would be marginally larger than the fibre method, but producing a poorer homogenisation figure. The output NA of the fibre was measured to be 0.07. The two methods are compared for the same F# (or NA) side by side in Figure 55.

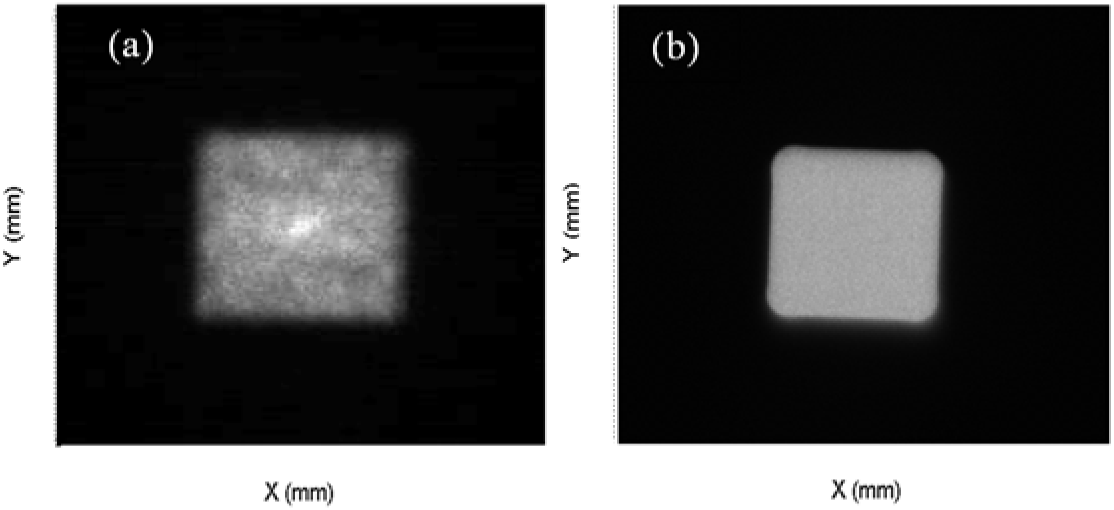

Figure 55 – Comparison of imaged irradiance profiles of (a) CGH and (b) fibre.

The fibre clearly homogenises this laser beam more effectively than the kinoform for a given brightness; this is due to the improved mixing within the fibre, which destroys the coherence and the polarisation of the laser beam effectively giving an incoherent image of the fibre core at the exit of the fibre, in comparison the polarisation of the beam is largely preserved by the transmission hologram and so is homogenised more poorly.

3.3.2 Summary of fibre coupling and homogenisation

An ABCD model of a high average power laser is used to model and design suitable coupling arrangement for a lasers with an average power of 1.6 kW and a pulse repetition rate of 10 kHz to 20 kHz. The optimum spot size of 550 µm 1/e^2 is determined for coupling into a 600 µm ± 15 µm square core fibre, the coupling arrangement was standardised and tested for more than 14 production lasers with no signs of coupling damage over time. Excellent homogenisation of the laser beam is observed to be produced by fibres of length greater than 10 m, the emitted beam provided a geometric square shape with an NA < 0.08 for fibre lengths up to 30m long that can be used for re-imaging through a suitable processing head. The homogenised image was observed to be free from laser speckle even in the case when individual pulses were imaged by a CCD camera (Thorlabs DCC1545M).

3.3.3 Conclusion of fibre coupling and homogenisation

The optimum spot size to minimise the risk to damage from the fibre is determined to be 550 µm $1/e^2$ diameter, which was found to balance the risk of damage to the fibre and maximise the coupling as much as possible. The coupling efficiency was determined to be >95% for all fibres coupled using this method. Homogenisation of the spot by the fibre was determined to be better than the required 15% and the output NA was less than 0.08 up to 30m of square core fibre. These measures of performance were fed forward in to the design of the beam shaping processing heads.

3.4 Development of the processing heads

3.4.1 Determining the optimum shape for the process

The idealised spot shape for the customer's surface removal process is a homogenous rectangular profile; this is due in part to the desired width of the processed track and also due to the processed track being formed by multiple overlaying individual pulses of the laser beam. Figure 56 details the importance of the spot shape by showing the result of overlaying multiple laser pulses for two practical alignments of a laser beam. A homogenous rectangular profile will leave a trench of uniform depth and sharp sidewalls, a diamond shaped profile however had more pulse overlap per unit length in the central section, thus leaving an undesired V shaped trench in the substrate with shallow sidewalls with the deepest removal in the centre of the trail.

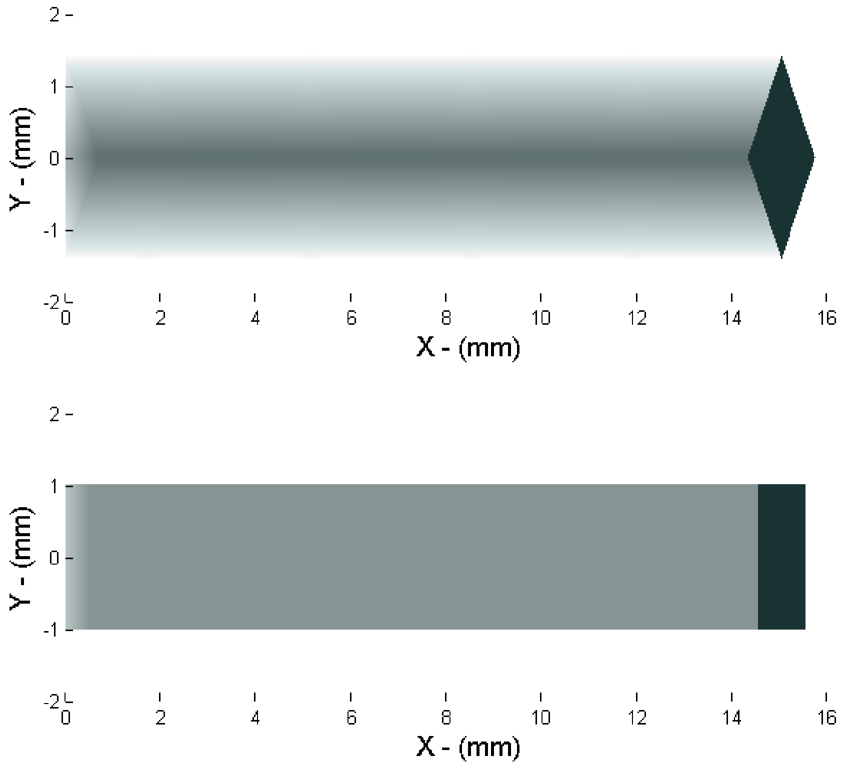

Figure 56 – Different surface removal cross sections formed by the different profiles. (a) shows a diamond shaped profile which leaves a V shaped trench in the substrate (b) shows a rectangular profile and the trail is a trench of even depth.

Integration along the X axis gives the overlapped trench profile and is shown in Figure 57, the optimum trench required by the customer is a rectangular profile, a square profile would leave the same width as the rectangle but the delivered pulse fluence would be less due to the larger spot area, therefore requiring larger pulse energy. Selecting the optimum Y axis profile was the subject of analysis in the processing head design.

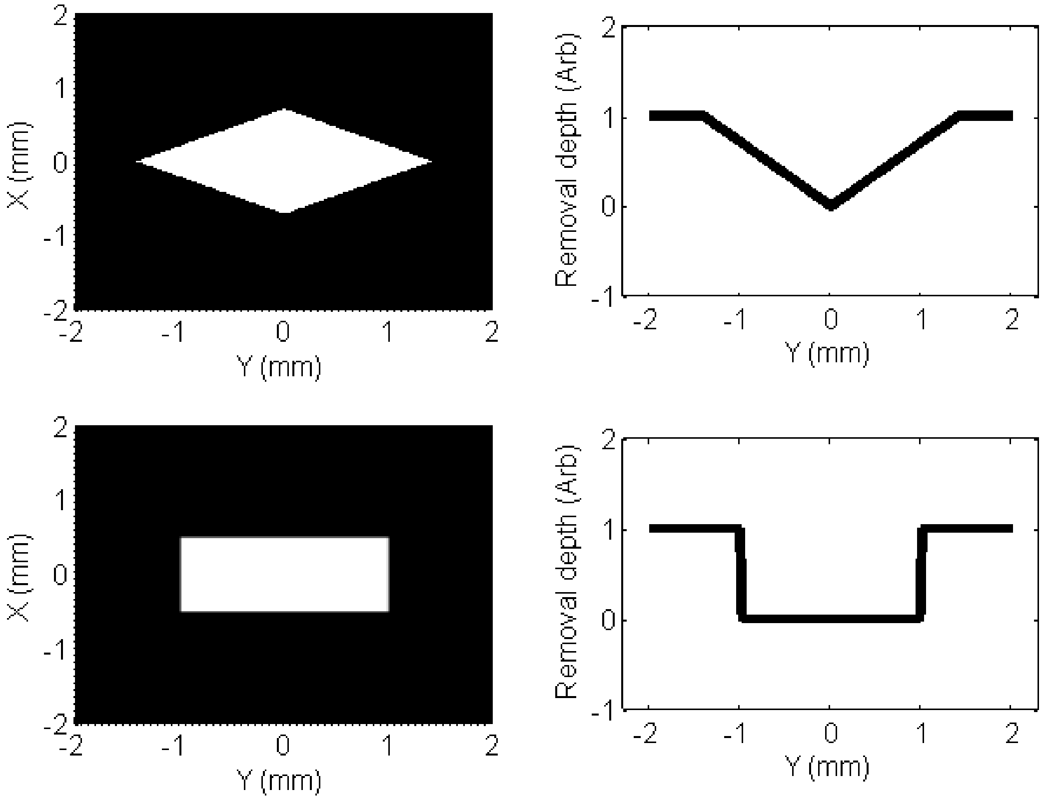

Figure 57 – Surface removal profiles as a function of spot shape (a) diamond shape profile, (b) idealised rectangular profile.

To understand the fluence delivered per unit length to the substrate in the X dimension, the number of overlaps of the rectangular profile needs to be calculated. The number of overlaps of each pulsed rectangular profile is given by Eqn. (26), where N_o is the number of overlaps of the rectangular profiles of spot dimension w_X in the X dimension, R is the pulse repetition rate of the laser and V_X is the substrate speed in the X dimension. A substrate moving at speed 0.1 m/s with a repetition rate of 10 kHz and a spot dimension of 0.4 mm would have 40 overlaps of the rectangular profile.

$$N_o = \frac{w_X}{\Delta X} = \frac{w_X R}{V_X} \tag{26}$$

Given the overlaps of the pulses, the substrate would absorb a total pulse energy of E_{total} as given by Eqn. (27), where A_p is the average power of the laser.

$$E_{total} = \frac{A_p}{R} N_o = \frac{A_p w_X}{V_X} \tag{27}$$

And the final equation of interest is the total fluence, $F_{total,}$ given by Eqn.(28), where w_Y is the rectangular spot dimension in Y.

$$F_{Total} = \frac{A_p}{V_X w_Y} \tag{28}$$

An interesting feature of Eqn.(28) is that the total fluence absorbed by the substrate under motion in the X axis is only dependent upon the spot dimension in Y, hence if thermal losses are ignored, the spot width in X has no influence upon the maximum speed achievable, neither does the repetition rate. In reality heat does dissipate and the individual pulse fluence for a stationary rectangular profile must also be large enough to initiate surface removal, typically in excess of 10 J/cm^2. A reasonable example of this is a substrate in motion at 10cm/s and values for w_X and w_Y, A_p and R of 0.04 cm, 0.2 cm, 1 kW and 10 kHz respectively, the per-pulse fluence, F_{pulse} given by Eqn.(29), would be 12.5 J/cm^2 and the total fluence, F_{total} would be 500 J/cm^2, which is exactly 40 times as per the value given in the example for $N_{0.}$

$$F_{Pulse} = \frac{A_p}{R w_X w_Y} \tag{29}$$

This analysis was used to guide the design, size and aspect ratio of the rectangular spot profile.

3.4.2 Beam shaping optic design

In order to translate the homogenised output profile of the laser to the substrate a method of shaping the square profile of the fibre into a rectangle is required. In addition to the optical transformation of the beam shape the optic also has to fulfil a number of other requirements namely, physically fit the permitted spatial envelope for install and service, and allow a long enough focal length to allow a protective cross-jet to avoid damage from process ejecta. These considerations are used to derive the back focal length of the final optic and the performance metrics used to characterise the processing heads, which are the edge width, homogeneity, spot width in X and the spot width in Y. These performance parameters are described in more detail in the following section.

A measure for homogeneity of the imaged irradiance profile of the system is given by Eqn. (30)

$$H = \frac{1}{\bar{I}} \sqrt{\frac{1}{N} \sum_{i=1}^{N} (I_i(X,Y) - \bar{I})^2} \tag{30}$$

Where H is the measure for homogeneity, I is the irradiance at a given X and Y co-ordinate within the 90% FWHM locus and $\bar{I}$ is the mean average of the irradiance in the 90% FWHM region. The 90% FWHM locus is shown in Figure 58.

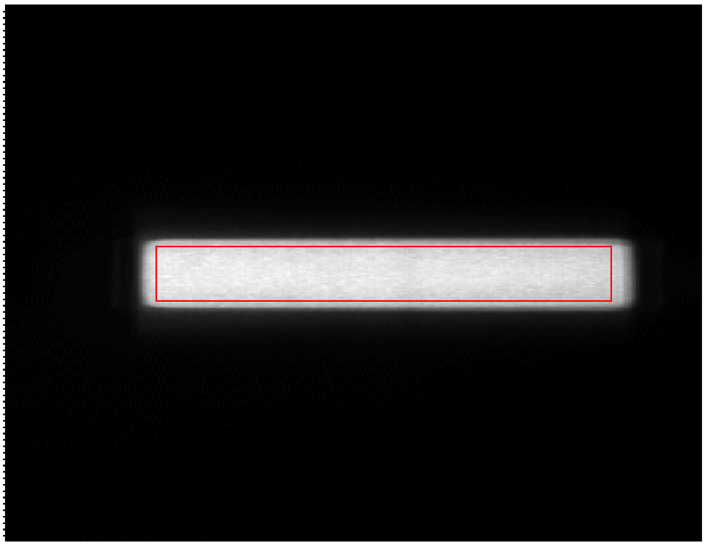

Figure 58- Homogenised and shaped irradiance profile, the red rectangle depicts the 90 % FWHM region.

Edge width is used to define the sharpness of the beam shaped image of the fibre. A temptation for the optical designer is to use the modulation transfer function (MTF) or point spread function (PSF) commonly used as a measure resolution in diffraction limited lenses, however these bear little relation to the required outcome of the processing head. To overcome this difficulty a direct measure of sharpness is used instead and is the edge with, defined as the distance in µm that the irradiance profile varied from 20 % to 80 % this also has a direct relation to the sidewalls generated by the surface removal process. The choice of the 20 % to 80 % is mainly to avoid the high NA cladding features imaged in the optical models, these appear as a knee in the irradiance trace but do not occur in the measured results as the high NA of the cladding modes doesn't transmit through the system. A higher NA cannot be ascribed to the cladding regions in the optical model. Figure 59 shows the 20 % - 80 % edge width diagrammatically; the algorithm used to calculate this on the measured data takes the average of twenty adjacent Y slices though the irradiance profile in order to generate an averaged smoothed curve so the algorithm is unaffected by any speckle or inhomogeneity in the irradiance profile, the edge width is only calculated for the Y axis.

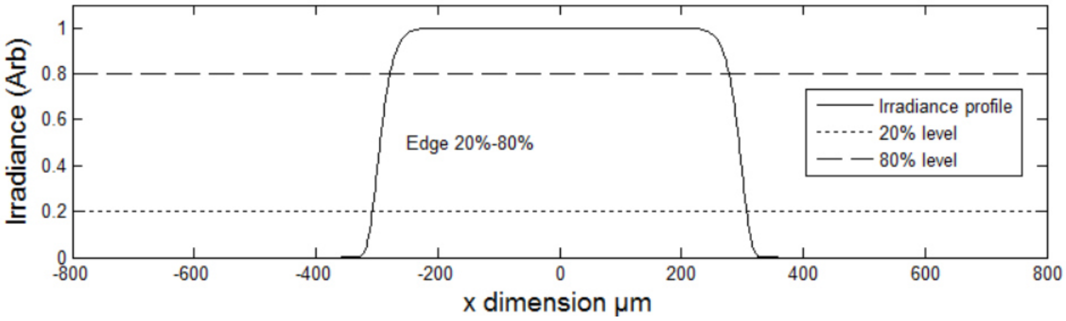

Figure 59 – Definition of edge width 20 %-80 %.

3.5 Optical design approach

The approach for the beam shaping section of the processing head is to use cylindrical lenses to generate a different lateral optical magnification in each axis. This approach is simple and requires the minimum number of optical surfaces to perform the beam shaping and mitigates the possibility for optical damage due to the high peak power of the laser beam. It also reduces the cost and improves the serviceability of the system. The choice of geometric optics to shape the beam also permits physical shaping of the overall envelope of the beam delivery system; this is especially useful for the situation where the space envelope for the installation area is heavily constrained, or the optical train needs to be bent around objects that form obstructions.

There are several possible architectures for the beam shaper optics but the main two types utilised are described and identified as architecture 1 and architecture 2, as shown in Figure 60 and Figure 62. The reason for the two separate architectures is because the first tracking system has a very tight constraint on the placement of the fibre, as it is retrofitted onto an existing system. The additional relay in architecture 1 enables the length of the overall processing head to be increased to make the fibre connection accessible. Architecture 2 is a development upon the optical design implemented after the initial system was successful and more mechanical design flexibility was implemented on bespoke new machines.

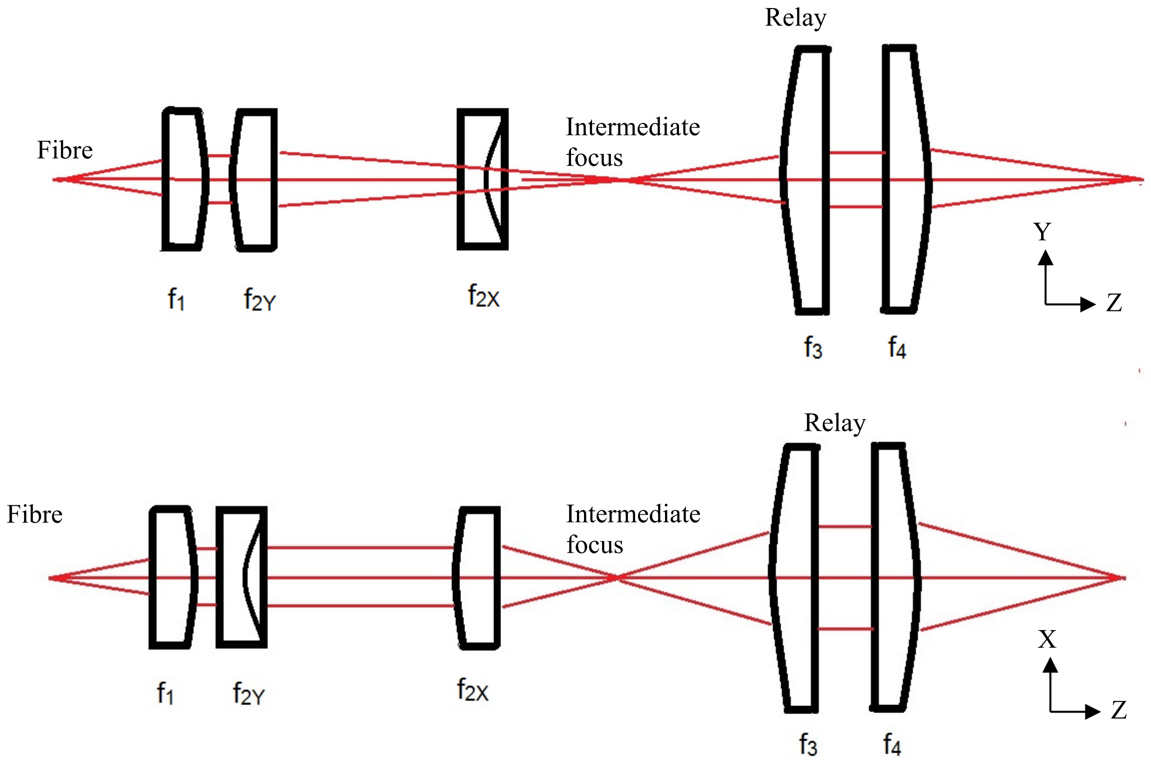

Figure 60 – Processing head architecture 1.

In architecture 1, shown in Figure 60, the homogenised laser beam emitted from the fibre is initially pseudo-collimated via a spherical lens (f_1); this is then focussed in the Y axis (f_{2Y}) by a cylindrical lens then focused in the X axis by a second cylindrical lens (f_{2X}) (or lens pair). The optical path is then further arranged such that the intermediate focal planes for X and Y are located in the same position along the optical axis (Z). The beam is then finally magnified and transmitted via an optical relay consisting of a collimation and focussing optic pair that are both spherical lenses. In this architecture beam shaping was performed between the fibre and the intermediate focus only, the final relay lenses (f_3 and f_4) served only to add more length to the optical train and also to perform a magnification of the spot in both axes at the intermediate focus, mainly to fulfil the requirements for back focal length of the optic and also to increase the length of the optics to permit easy access to the fibre.

In order to predict the spot size at the focus the focal lengths of the lenses are predicted via an optical system model. This system model is given by Eqns. (31) and (32).

$$S_X = \left(\frac{f_{2X}}{f_1}\right)\left(\frac{f_4}{f_3}\right)S_0 \tag{31}$$

$$S_Y = \left(\frac{f_{2Y}}{f_1}\right)\left(\frac{f_4}{f_3}\right)S_0 \tag{32}$$

In Eqns (31)-(32), S_X, S_Y are the final FWHM spot widths, $f_{1}..n$ are the lenses as depicted in Figure 60 and S_0 is the fibre diameter.

The design constraints for this processing head consist of a very tight space envelope so the width of the processing head has to be less than 75mm wide. This in turn placed constraints on the achievable spot sizes with this technique. An estimate of the minimum spot size is calculated by using the beam parameter product of the fibre exit.

$$W_{min} = \left(\frac{f_{focus}}{R}\right)BPP \tag{33}$$

Where w_{min} is the minimum spot size, f_{focus} is the final focussing lens focal length, R is the radius of the final focussing lens and BPP is the beam parameter product of the fibre. Given a typical fibre core diameter of 600 µm, an output fibre NA of 0.08, a maximum final lens radius of 32.5 mm and a focal length of 200 mm this gives a minimum spot diameter of approximately 0.3 mm.

The maximum value for the spot size is a little harder to calculate but is mainly limited in this architecture by the length of the processing head. A practical maximum focal length for f_{2Y} is 250 mm. The maximum spot size is then calculated from Eqn.(32), the fibre diameter of S_0 is 600 µm and f_1=70 mm, f_3=100 mm and f_4=150 mm gives a practical diameter limit of S_Y of 3.0 mm.

A major challenge in the architecture 1 processing heads is the unusual space envelope of the system they are designed for, which resembles a long narrow tube and drives the requirement for a long optical train. This requirement puts physical constraints on the overall form of the optical-mechanical design and also on the parts of the processing head that require access, such as the fibre, water connections and the cover-glass. The tight constraints arise for this processing head as this design is installed as a retrofit on an existing mechanical system.

The general space envelope for the system is referenced in Figure 61 with approximate dimensions, also access points are noted. The figure is of a silhouette of the cross-section of available space within which the processing head and any beam termination needed to be fitted. A heavy shuttle which transports the substrate passes over this cross section in a direction into the page of the figure (X axis). Any part protruding from this cross section would have resulted in a catastrophic crash with the shuttle. Access to the fibre was required in the position as shown and the processing head needed to be long enough to permit the fitting and removal of the fibre.

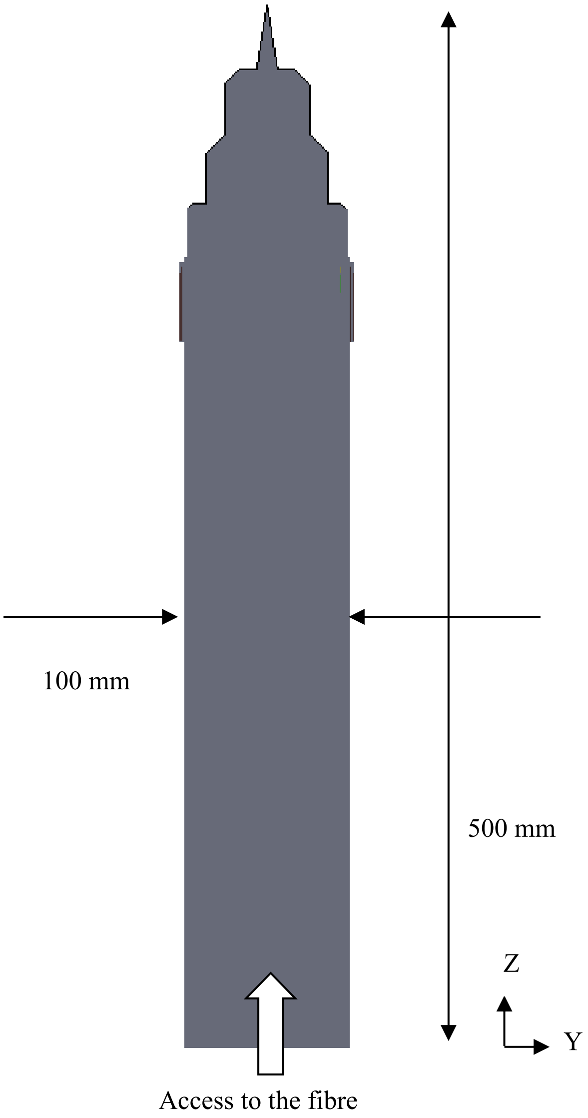

Figure 61 – Space envelope constraints of the first processing heads.

For these initial systems with this space envelope, architecture 1, as shown in Figure 60 is used because the extra length of the processing head permits the fitting and maintenance of the fibre

A second type of processing head architecture is shown in Figure 62.

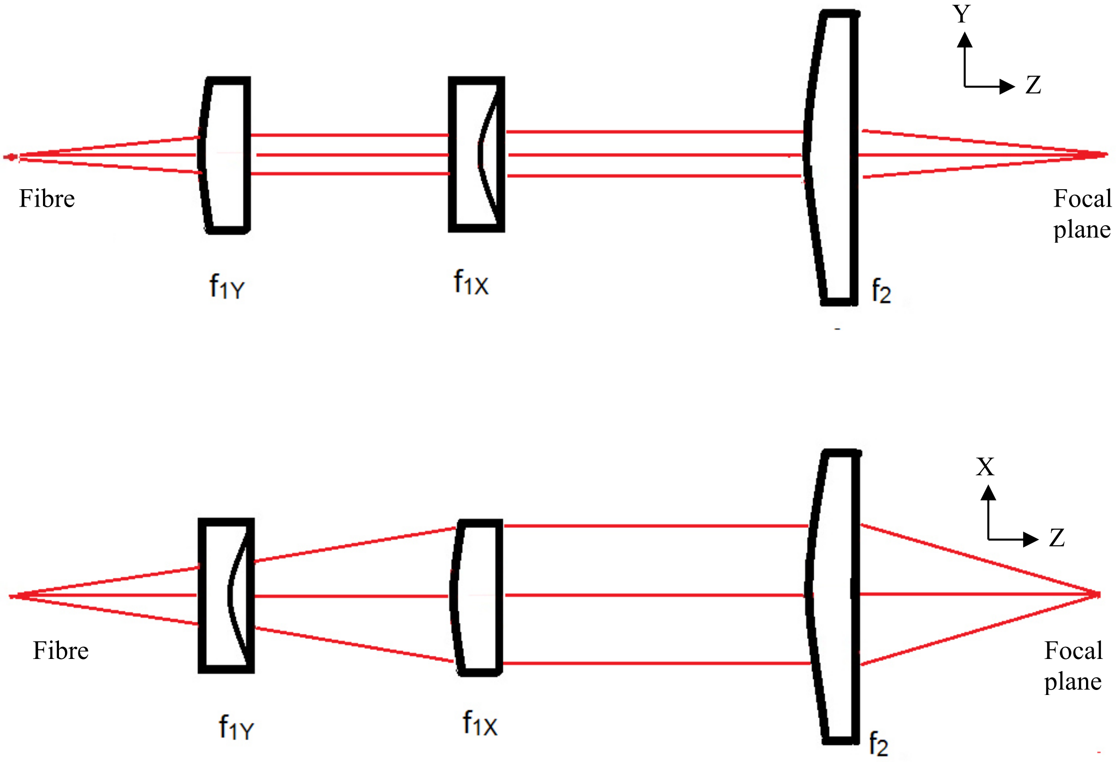

Figure 62 – Processing head architecture 2.

In architecture 2 the homogenised laser beam is collimated in the Y axis by a cylindrical lens, f_{1Y}, the beam is then further collimated in the X axis by a second cylindrical lens f_{1X},. The resulting collimated beam is then focused by a single spherical focussing lens f_2.

This architecture is simpler and results in a shorter optical train, with fewer optical components. The generated spot size is also simpler to calculate being the simple magnification of the optical train, as detailed in Eqns. (34) and (35).

$$S_X = \left(\frac{f_2}{f_{1X}}\right) S_0 \tag{34}$$

$$S_Y = \left(\frac{f_2}{f_{1Y}}\right) S_0 \tag{35}$$

Apart from the optical design requirements for physical size, spot width and homogeneity there is also the requirement to be significantly de-rated from the damage threshold of the glass and coating. The processing head design therefore had to be high transmission and ideally minimise the number of optical surfaces. Coatings also were specified to be at least double the peak irradiance and fluence to damage the optics. Coatings used were rated at a damage threshold of 10 J/cm^2 for a 20ns pulse at 1064 nm, the maximum peak fluence encountered internally in the processing head is 1 J/cm^2.

3.5.1 Zemax modelling, building the source object

The system model is a good tool for the selection of the lenses and initial feasibility study and fit of the optical components into the available mechanical envelope, but is not an adequate tool for predicting the actual spot shape, edge sharpness, blur, homogeneity, actual physical opto-mechanical design and transmission of the optical system.

As the emerging beam from the fibre is a non-diffraction limited beam with effective M^2 value of 60 it is adequate to model the performance of the processing head with ray tracing software. There are many commercial ray trace packages available, notably Code V, OSLO, ASAP, amongst others, but Zemax is chosen for this design. The Zemax package is a market leader in this field and also has a wide array of extensions and functions, which permit non-sequential modelling and also facility to overlay computer aided design with the optical layout

The Zemax model is built by first designing the optical layout in the usual manner, ascribing surfaces, optic orientations, and by modelling positions of target rays through the system. This suffices for the approximation of the spot size but is not adequate for the evaluation of the homogeneity of the beam, or any patterning created as a result of clipping a hard aperture. In order to model these parameters, the geometric analysis tool is used, which propagates a programmable source through the optical train. The editor then outputs the actual representation of the transmitted beam in an editor window, detailing transmission loss and providing an X,Y plot of the irradiance profile.

The programmable source was created using a scaled bitmap image of a recorded irradiance profile of the fibre, as per Figure 63, this was taken using a Thorlabs DCC1545 camera with known pixel pitch of 5.2 µm. This irradiance profile was then converted using a Matlab program into a *.IMA format suitable for the Zemax editor, which consists of grid of ASCII values for irradiance. Using this automated approach, high resolution images of the fibre are scaled and propagated though the optical system at a larger NA than the measured output of the fibre.

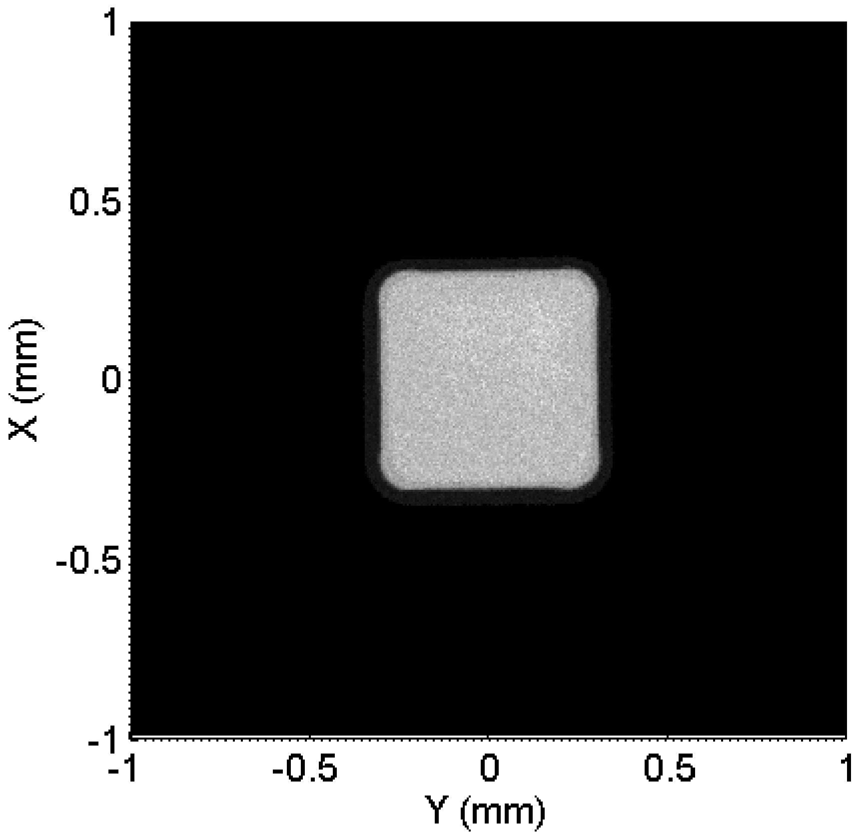

Figure 63 – Irradiance distribution of 600 µm fibre, as programmed into Zemax.

Once the source is created in Zemax, it can be propagated through the model in exactly the same way as the laser beam propagates through the processing heads. Another advantage of this approach is that the modelled results and practical test results are directly equivalent. To ensure similar results from models to measurement the resolution of the Zemax model is also adjusted to be close to the resolution of the Thorlabs DCC1545M used to image the profiles, namely 800 × 800 grid of 4 mm width.

The Zemax optical model is also used to generate an optical design that can be imported into a mechanical Computer Aided Design (CAD) package, in this case Solidworks. This is to ensure that the optics are mechanically mounted in the correct position and also permits the design of optical mounting appropriate to the application, within the tolerances detailed later in this chapter.

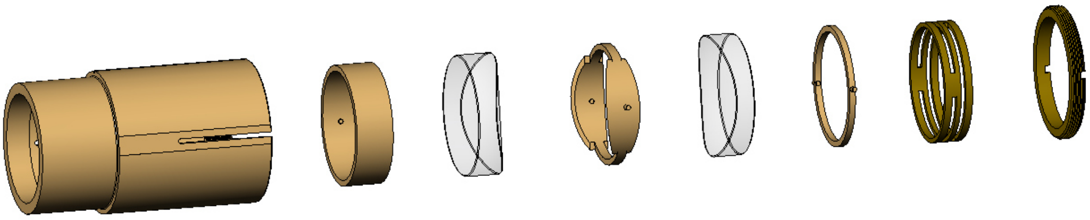

Figure 64 – Exploded view of the clamping mechanism.

The first stage in the analysis is to design and construct the optical layout in Zemax and generate a numerical result for an optimally aligned system. Any limiting spherical aberrations are designed out by use of appropriate doublets and maintaining the correct conventions with respect to the Coddington shape factor [55]. The lenses selected for both the cylindrical and spherical lens elements are almost exclusively plano-convex. The reason for this is their ease of mounting and they are also close to best form for this wavelength in fused-silica, when oriented correctly to the laser beam. The material selection of UV grade fused silica is due to the marginally lower absorption co-efficient at 1064 nm when compared to BK7, both have internal material transmittances of greater than 99.9%.

The Zemax layout of Architecture 1 is shown in Figure 65, some of the lenses are represented as blocks as they were multi-element lenses sourced from a commercial supplier who wished to protect their designs. These designs were diffraction limited multi-element lenses, but were modelled in their entirety within the black box Zemax models of the lenses. The boxed lenses are scaled to mark the physical extent of their housings, so they can be referenced in the CAD software.

Figure 65 shows the Zemax layout of the architecture 1 type processing head in the YZ plane. Figure 66 shows the same architecture in the XZ plane.

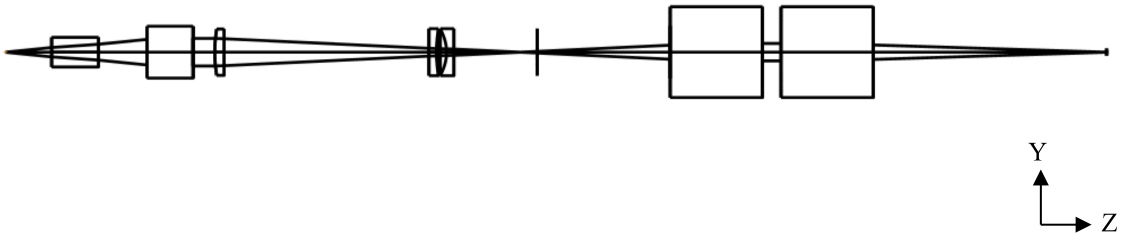

Figure 65 – Original processing head –Architecture 1 – YZ plane.

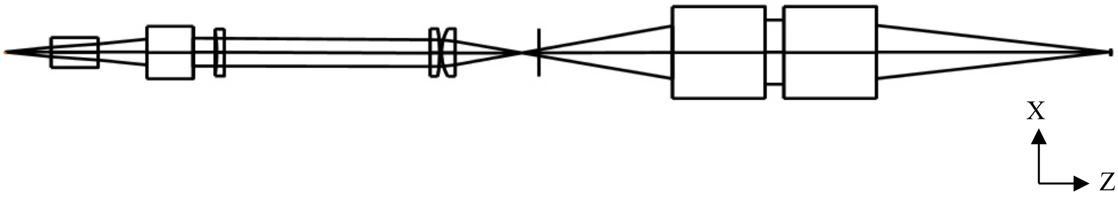

Figure 66 – Original processing head –Architecture 1 – XZ plane.

The positions of the lenses are first determined from the system modes previously described, then a custom merit function is created in Zemax to optimise the final physical positions of the lenses. The result of the geometric propagation of the laser beams through the processing head model is shown in Figure 67 below.

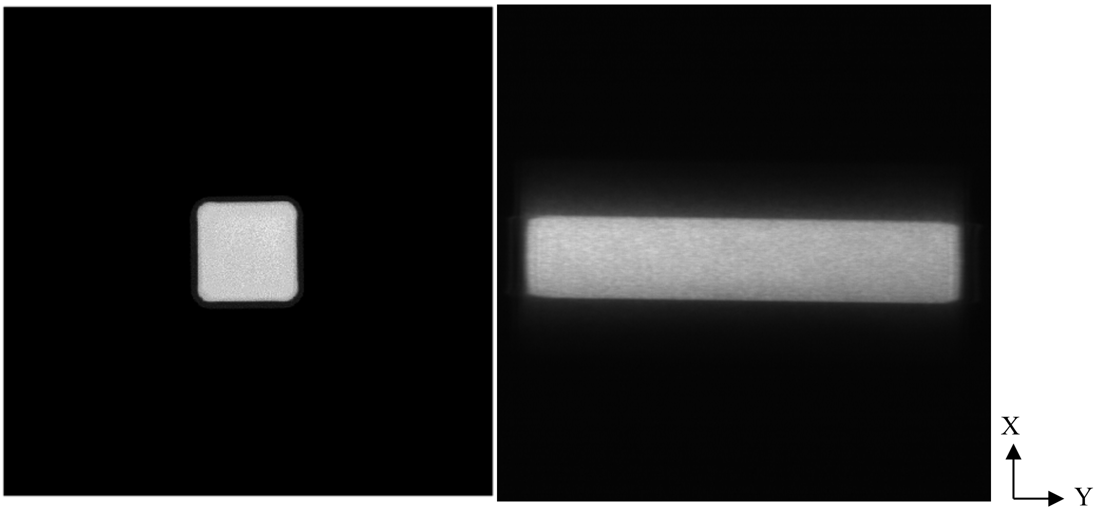

Figure 67 – Modelled source fibre and the resulting rectangular shape created at the focus.

A Matlab script is then applied to this captured irradiance profile to numerically generate the results for the edge width, homogeneity and to find the FWHM spot dimensions. The geometric transmission of the processing head was analysed directly from the Zemax model by carefully specifying apertures within the Zemax model and calculating the losses through the system via the geometric propagation results.

3.5.2 Number of rays required to model the system

A key parameter established when modelling these optical systems is the number of rays required to accurately model it. This is established by modelling and analysing the image produced by the Zemax model for an increasing number of propagated rays. Using this approach the values generated for each of the performance metrics are taken to be accurate when the values for the parameters ceases to change with increasing ray count. This is performed for the spot size, edge-width and homogeneity performance parameters and the results for each parameter are shown in Figure 68, Figure 69, Figure 70 and Figure 71 below.

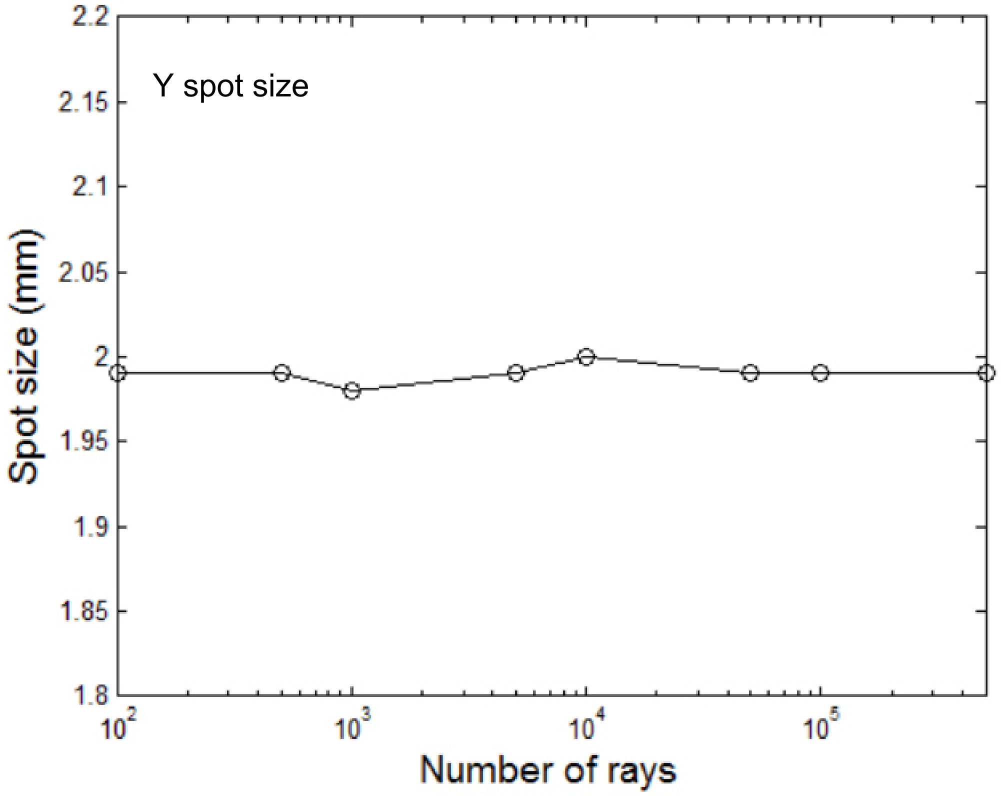

Figure 68 – Change in modelled Y spot size with increasing number of propagated rays.

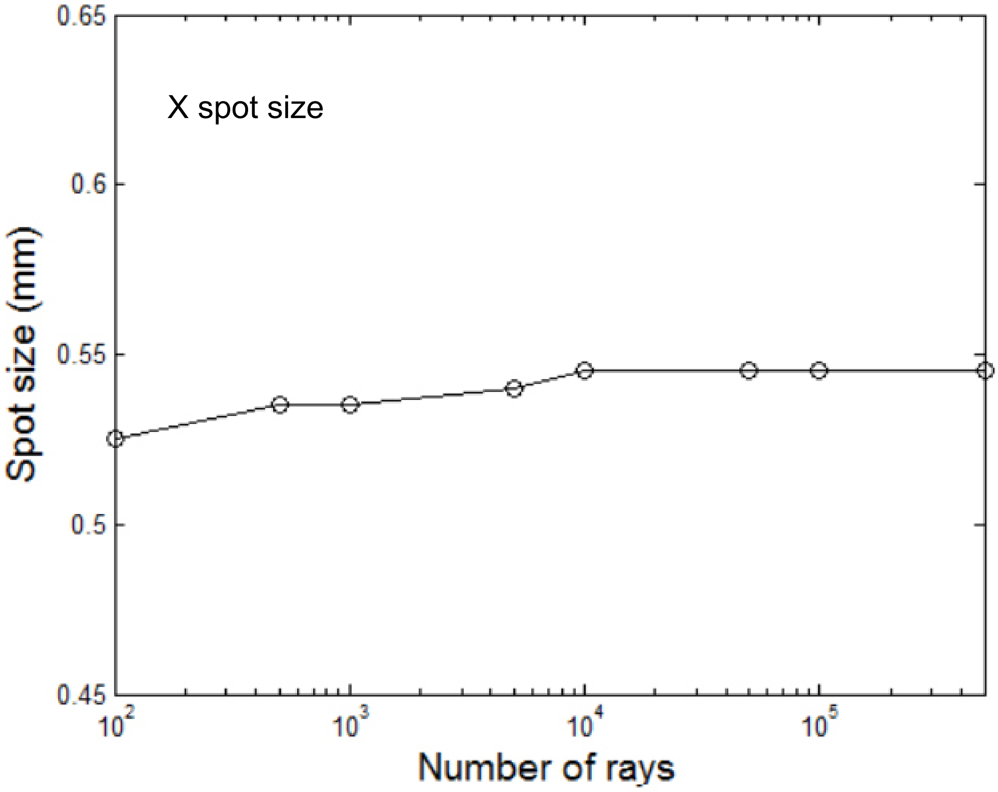

Figure 69 – Change in modelled X spot size with increasing number of propagated rays.

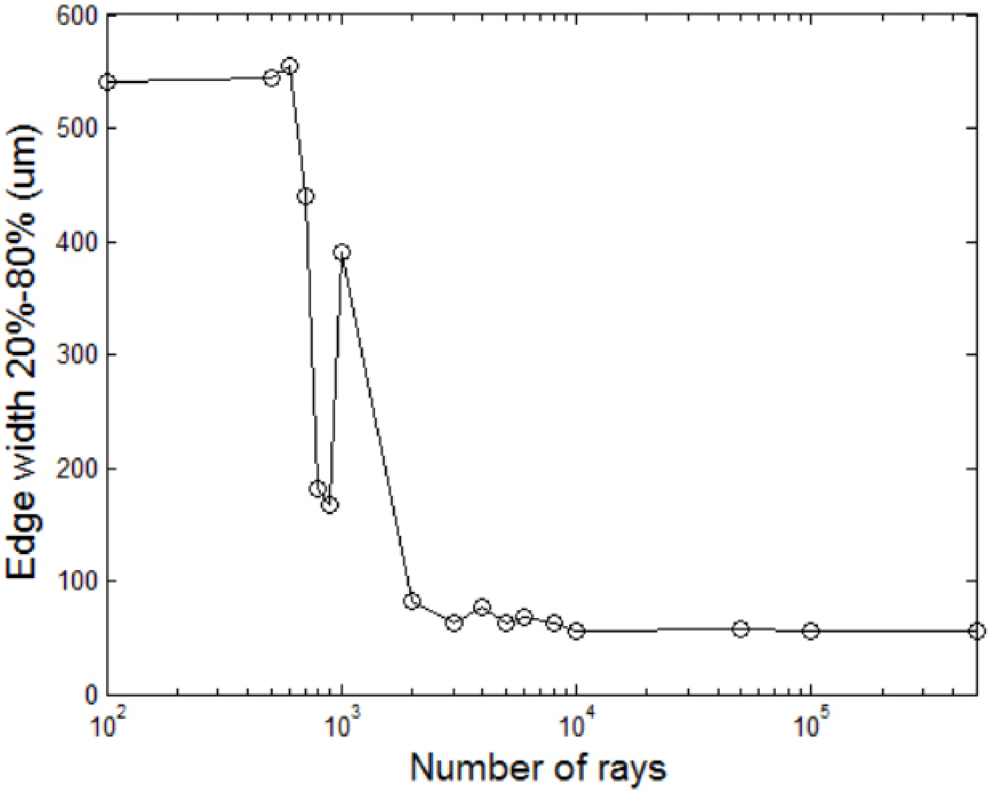

Figure 70 – Change in modelled edge width with increase in rays propagated.

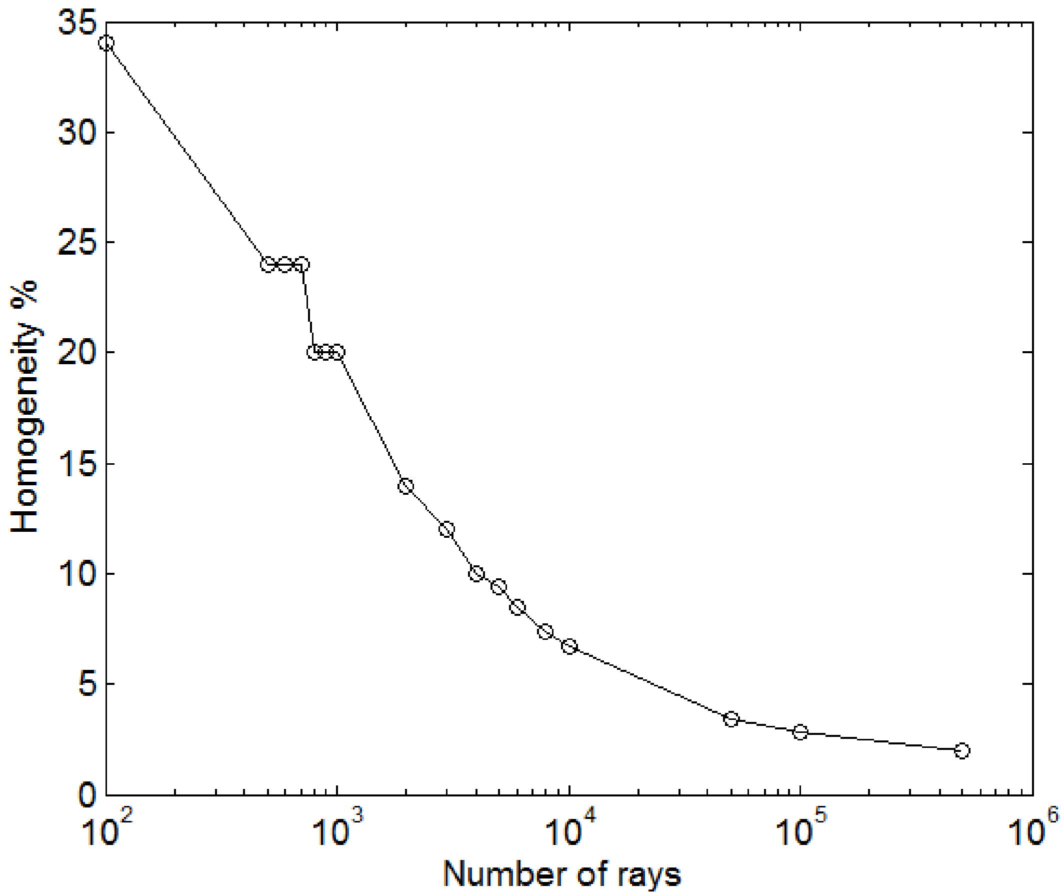

Figure 71 – Change in modelled homogeneity with increase in rays propagated.

The findings of this study are that spot size can be estimated on a relatively small propagation of rays (> 1000), but uniformity and edge sharpness require >10^4 Rays to be propagated before the noise in the modelling is small enough to yield a repeatable result.

The conclusion of this study was that a minimum of 10^4 rays should be used for correlation with measured data where the predictions for edge widths are required. Increasing the number of ray count beyond 10^4 would significantly increase the time taken to model the system but would not improve the resolution of the edge width, 10^4 rays will also resolve homogeneities below 5%, which is well below the specification of 15%, hence if the 5% figure is achieved by 10^4 rays then there is no reason to proceed to a larger ray count. The time taken to model is generally less than 3 minutes for 10^4 rays and greater than 15 minutes for 10^6 rays, which is time consuming for multiple analyses. The spatial resolution of the irradiance profiles are the same for both measured and modelled data and this permits the use of exactly the same algorithms on both modelled and measured results.

3.5.3 Mechanical tolerances

A key output of the optical modelling of the optical train is the mechanical tolerances that the individual lenses need to achieve in order to maintain an acceptable performance. The key tolerances defined for lens each element were; tolerances in the position X and Y and rotation about the Z (optical axis), tilt about X and Y are largely redundant due to the use of plano-convex lenses

The approach to the tolerance analysis is to first construct a perfectly aligned system in Zemax, limited only by the residual aberrations of the system, and then to explore the response of the image to various tolerances applied to each lens element in turn. This forms the first order magnitude of permissible tolerance in the mechanical design. The response of the optical system was analysed by using the previously mentioned metrics, as observed in the Zemax numerical simulation in the image plane. The results were analysed via a Matlab script from the simulation output. The most challenging placement tolerances for the cylindrical lenses in the processing head is the rotational tolerance of the lens elements in Z. A result showing this sensitivity is shown in Figure 72, where the Rotation in Z is plotted against the edge width, which provides a good measure of the sharpness of the focussed image of the spot.

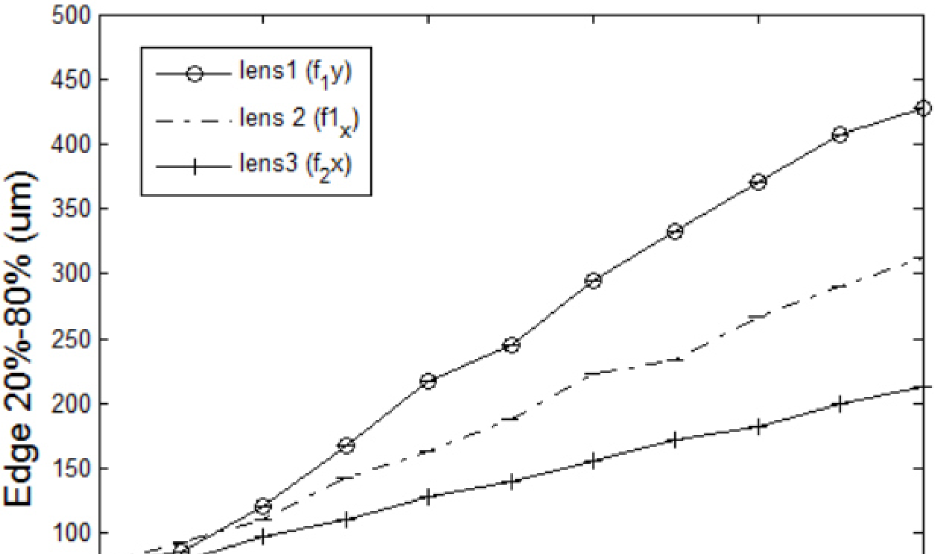

Figure 72 – The effect on sharpness of the image with rotation errors on cylindrical lens elements.

It is observed from Figure 72 that a rotational tolerance of less than 0.25º is desired to avoid cumulative blur of the image.

By contrast the tolerances for X, Y position are always found to be generous and greater than ±1mm. This procedure for establishing the mechanical tolerances of the optical trains was repeated for each design version of the processing heads and the tolerances are also found to be very similar between the two architectures.

A specification of <200 μm for edge width is envisaged. Hence the mechanical design tolerances were ±0.5 mm for X and Y and ±0.2° for rotation about Z and these are readily achievable in the mechanical design.

An additional consideration for the mounting of the optics is the optical power and likely temperature that the lens elements and their housings experience. Given the potential for 1.6 kW source, even a 1 % reflection would lead to significant thermal load and could potentially lead to unwanted movement of the lenses. For this reason the mechanical technique used to house the optics is shown in Figure 64. A shaped clasp arrangement made of brass is used to key the front curved face of the lenses; this ensures the correct rotational orientation of the lens with respect to other lens elements in the group. The brass clasps are then held under compression with a retaining spring. The spring permits the lenses to be held under compression even if the lens group expands under heating. The material selection of brass was twofold; brass is a soft material ideal for surface keying to fused silica avoiding chipping or cracking of the lens under compression and brass also has a thermal expansion close to the rest of the metallic housing made of aluminium; brass being 19 ppm/K, aluminium is 22 ppm/K. The thermal expansion of fused silica is significantly smaller at 0.55 ppm/K. Hence the lens housing was expected to expand and loosen its compression on the lens fixings with temperature, hence the additional reason for the compressive spring in the lens housing unit. The rotational accuracy of the lenses is achieved via pins in the internal mounting structure and slots in the external case of the lens barrel

The modelling results for Architecture 1 processing heads constructed in this way are shown in Figure 73 and Figure 74 against the actual achieved performance of the processing heads.

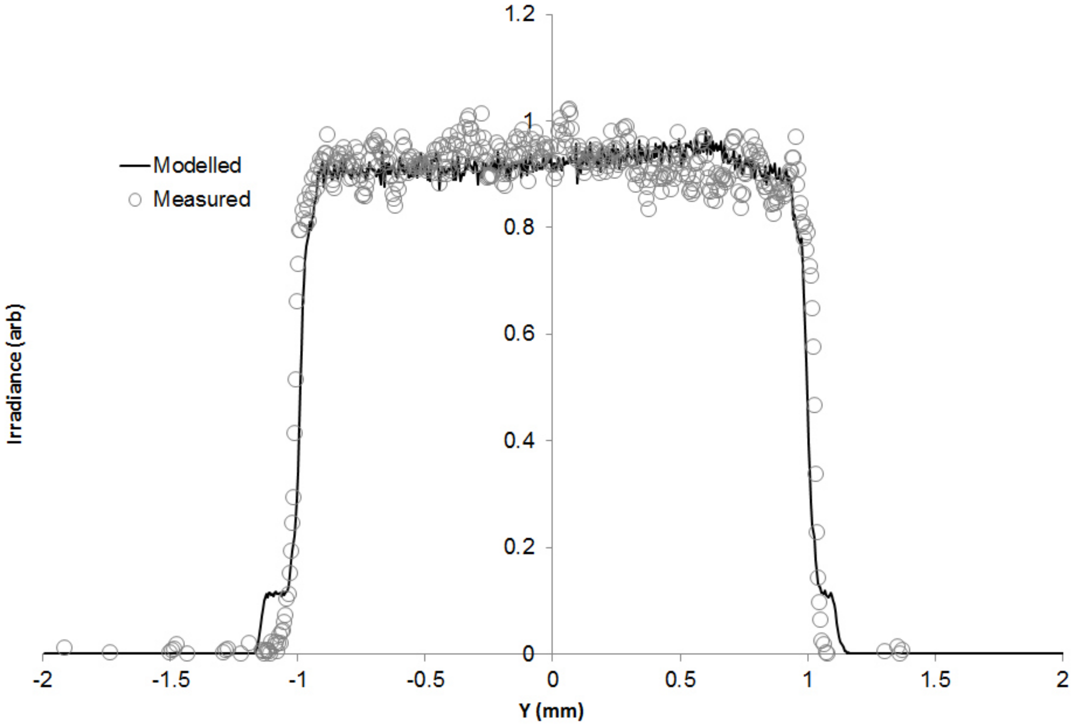

Figure 73 – Slice through the Y irradiance profile comparing modelled and measured results.

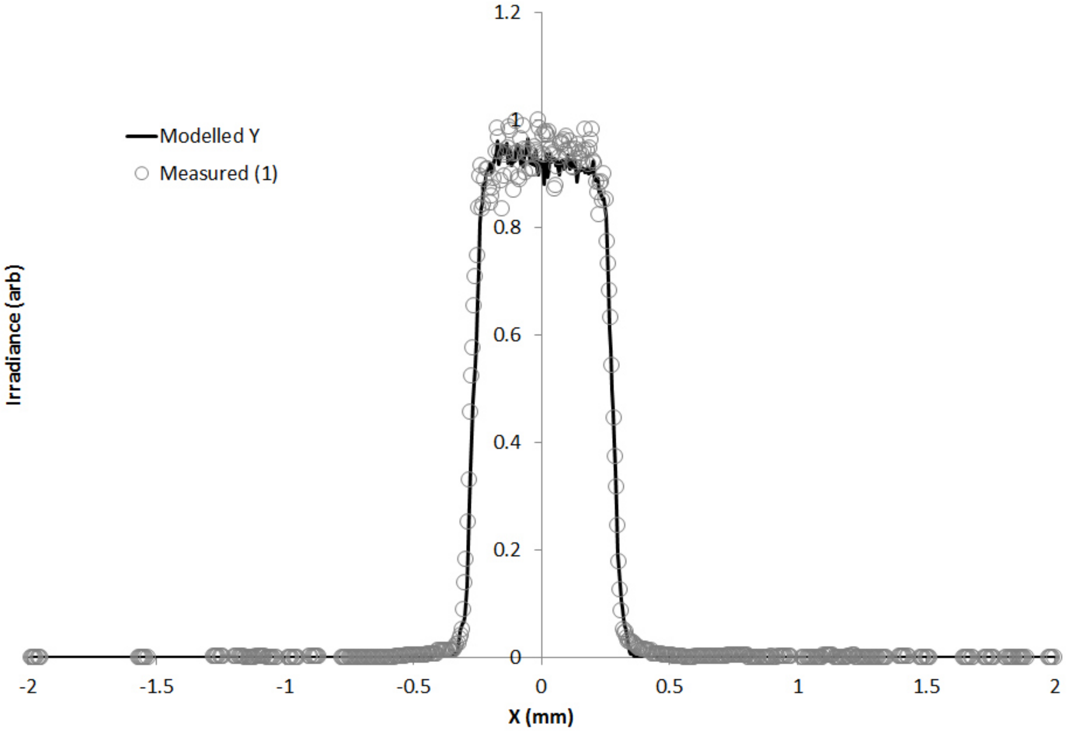

Figure 74 – Slice through the X irradiance profile comparing modelled and measured results.

Zemax layouts for a typical Architecture 2 systems are shown in X any Y planes in Figure 75 and Figure 76.

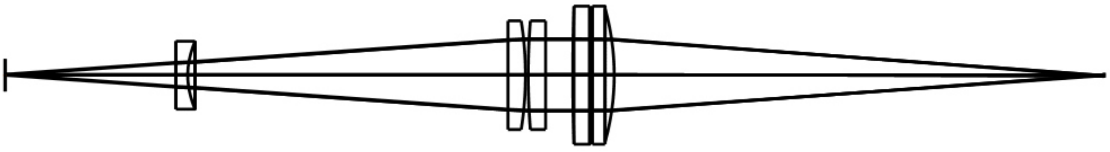

Figure 75 – Zemax layout of Architecture 2 in the YZ plane.

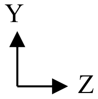

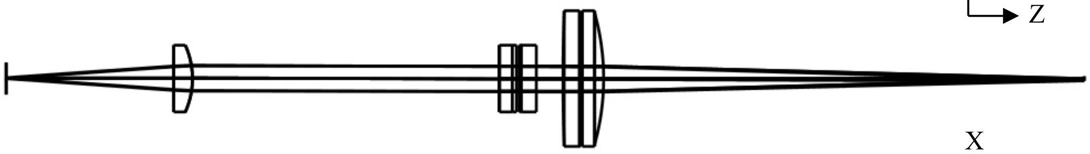

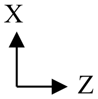

Figure 76 – Zemax layout of Architecture 2 in the XZ plane.

The results of the modelling and measurement comparisons for the X and Y spot dimensions for these architecture 2 processing heads are shown in Figure 77 and Figure 78.

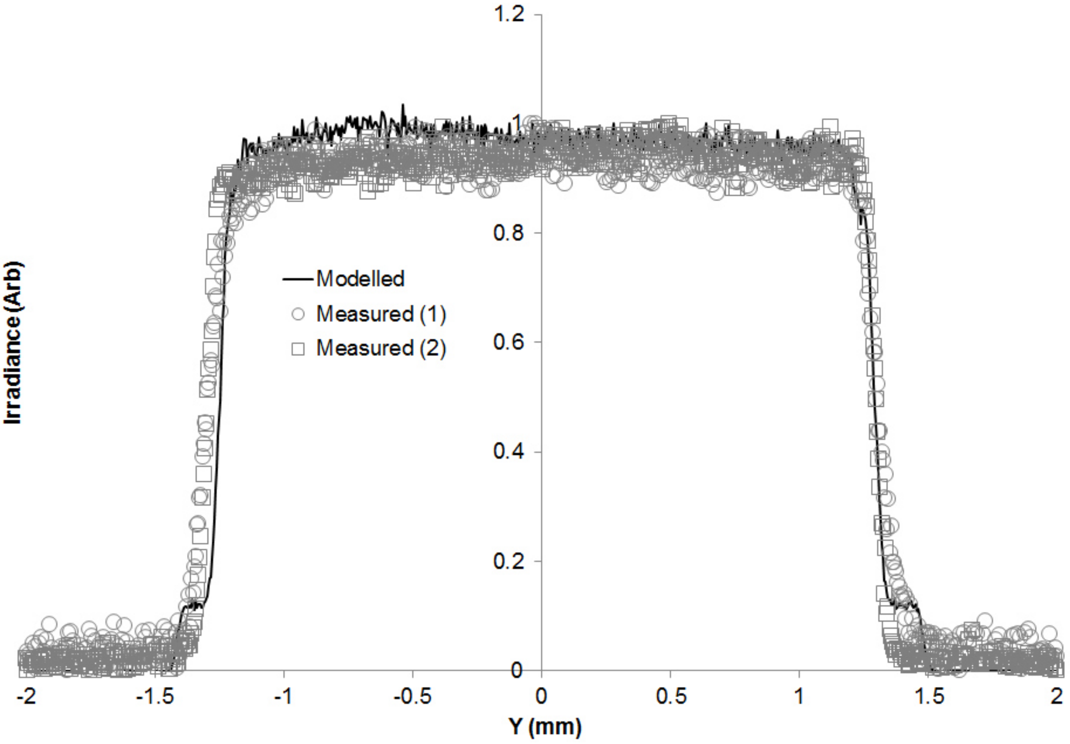

Figure 77 – Modelled irradiance profile for an architecture 2 processing head plotted against two measured processing heads in the Y dimension.

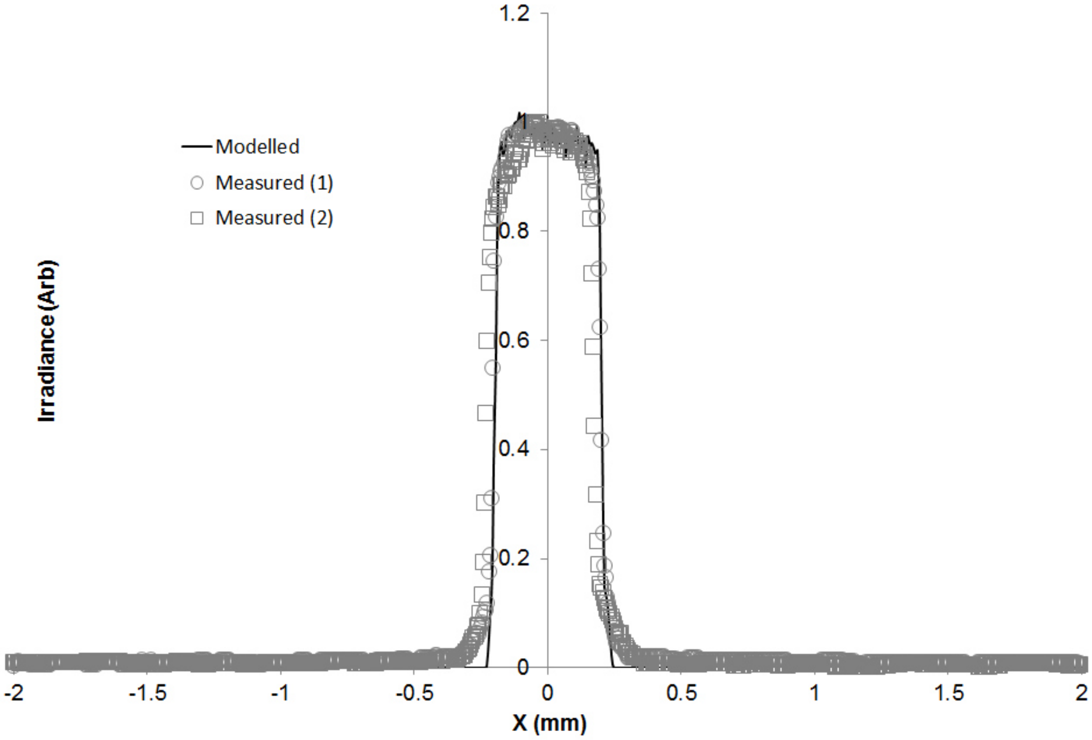

Figure 78 – Modelled irradiance profile plotted against two measured processing heads in the X dimension.

3.5.4 Comparison of measured vs modelled data for all processing heads

Over the course of serial manufacture of these processing heads, the metrics between measured and modelled performance were monitored.

Figure 79 to Figure 82 show plots of the measured vs modelled for both actuated and non-actuated processing heads. For each parameter an overlay of 15 different processing heads is presented, all designed to the techniques detailed in this chapter. The error bars in the spot size plots are derived from a Monte-Carlo simulation of spot size variance with the supply tolerances on the focal lengths of ± 0.5% and ± 5µm on the fibre size.

Figure 79 details the comparison of the predicated modelled spot size to the actual measured for the Y dimension. A ± 6% error is predicted from the modelling based upon the tolerances of the optics and mechanical mounts.

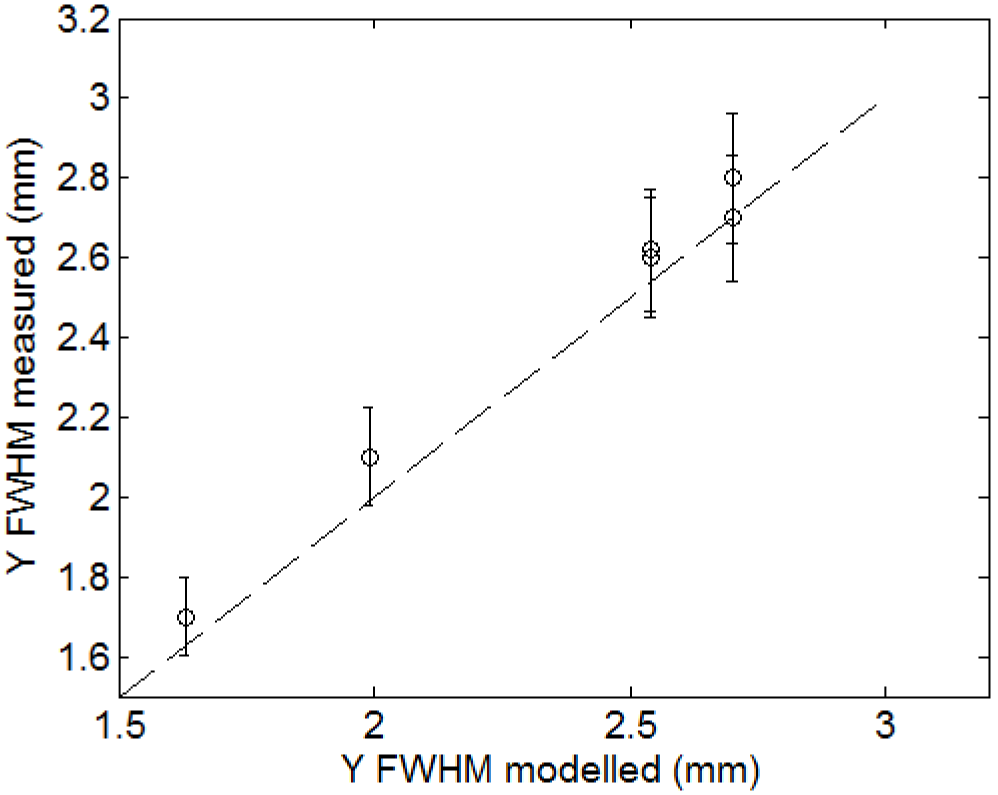

Figure 79 – A comparison of measured Y FWHM to modelled predictions for all processing heads, dashed line shows $Y_{measured} = Y_{modelled}$ for reference.

The same plot for the spot size in the X dimension is shown in Figure 80, the predicted variance for these spot sizes is a larger percentage of ± 10%

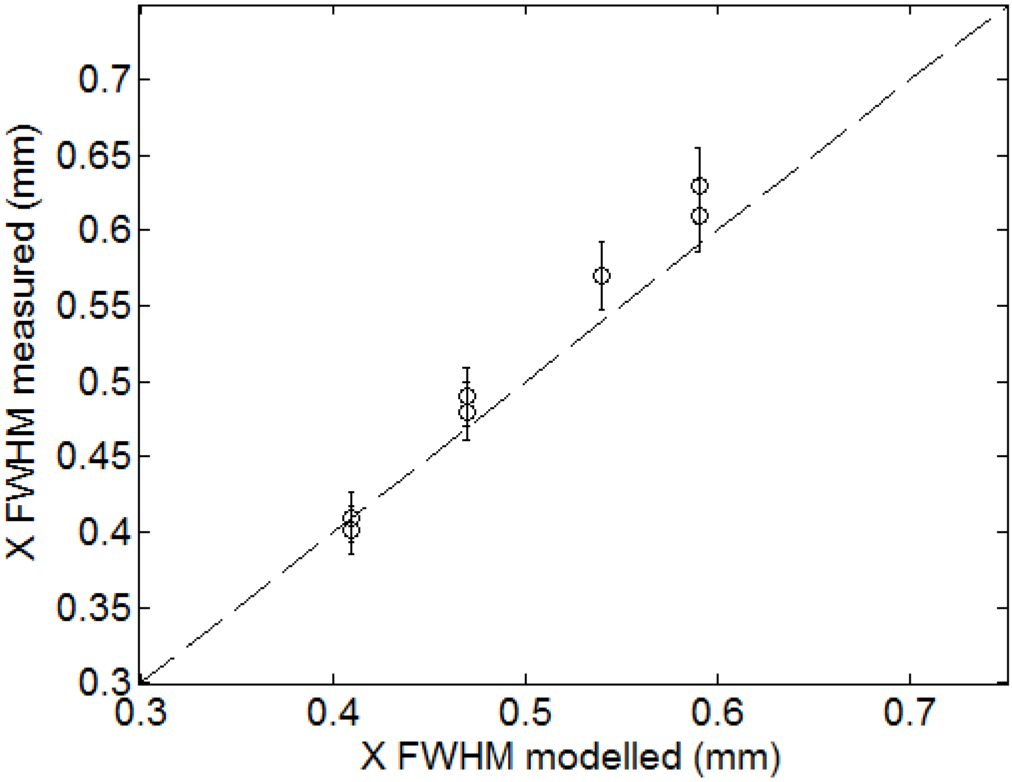

Figure 80 – A comparison of measured X FWHM width to modelled predictions for all processing heads, dashed line shows $X_{measured} = X_{modelled}$ for reference.

A comparison of the measured vs modelled for the homogeneity figure is detailed in Figure 81 this parameter is difficult to model as per the discussion previously in this chapter on the number of rays, but the homogeneity was found to be within the 15% maximum limit imposed by the end customer for all the variants of the processing heads.

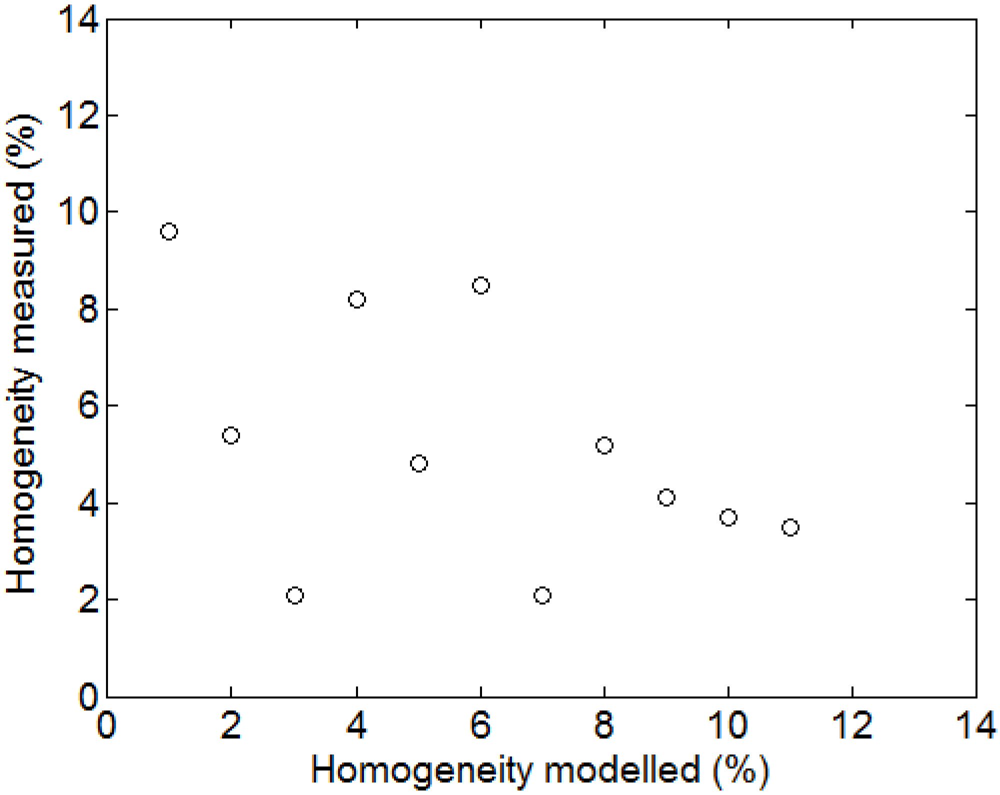

Figure 81 – A comparison of measured homogeneity figure to modelled for all processing heads.

The comparison for the edge widths between measured and modelled are given in Figure 82, the edge widths are always less than 140 µm and typically 100 µm. The measured 20% – 80% edge width can also be represented as a percentage of the overall width of the removed trench of material from the substrate. In the worst case a 140 µm edge width and a minimum spot width in Y of 2.0 mm gives trench side walls that constitute 14% of the overall width of removed region. Even at this worst case the edge width is acceptable for the process.

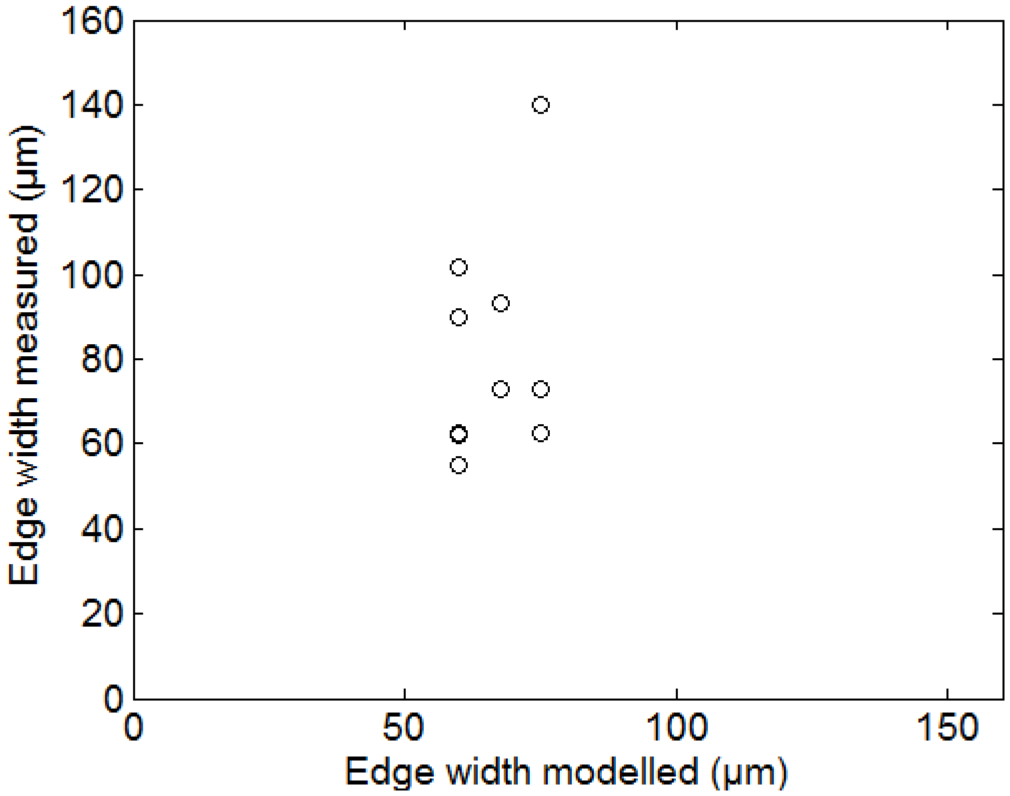

Figure 82 – A comparison of measured edge widths modelled for all processing heads.

The algorithm used to determine these values is given in the appendices as a Matlab script.

3.5.5 *An important note on depth of focus*

Large fluence levels, typically greater than 10 J/cm^2, are desired at the substrate in order to maximise the processing speed of the system and the final aim of the process is to remove a line of material as it traverses underneath the processing heads. As the geometry of the spot in the X dimension does not affect the geometry of the width of the scribed line in the Y dimension it is desirable to increase the fluence for individual pulses at the substrate by reducing the X dimension of the spot in the direction of the substrates travel. Reducing the X dimension is actually undesirable for two reasons. The surface removal is performed by the overlap of the rectangular irradiance profile, each pulse removing a small proportion of surface material at a time. If the spot size was reduced in the X dimension then the number of overlaps per unit length would also reduce and the total fluence that was delivered would actually reduce at the same rate as the overlap increases and although each individual pulse would carry more fluence, the overall speed of the process would remain the same. The second reason to avoid reducing the spot size is that it creates a smaller depth of focus in X dimension for smaller focussed spot dimensions. A numerical study shown in Figure 83 uses the Zemax models described in this chapter to calculate the peak fluence at the focus of the processing head for different positions on the Z axis about the best focus position.

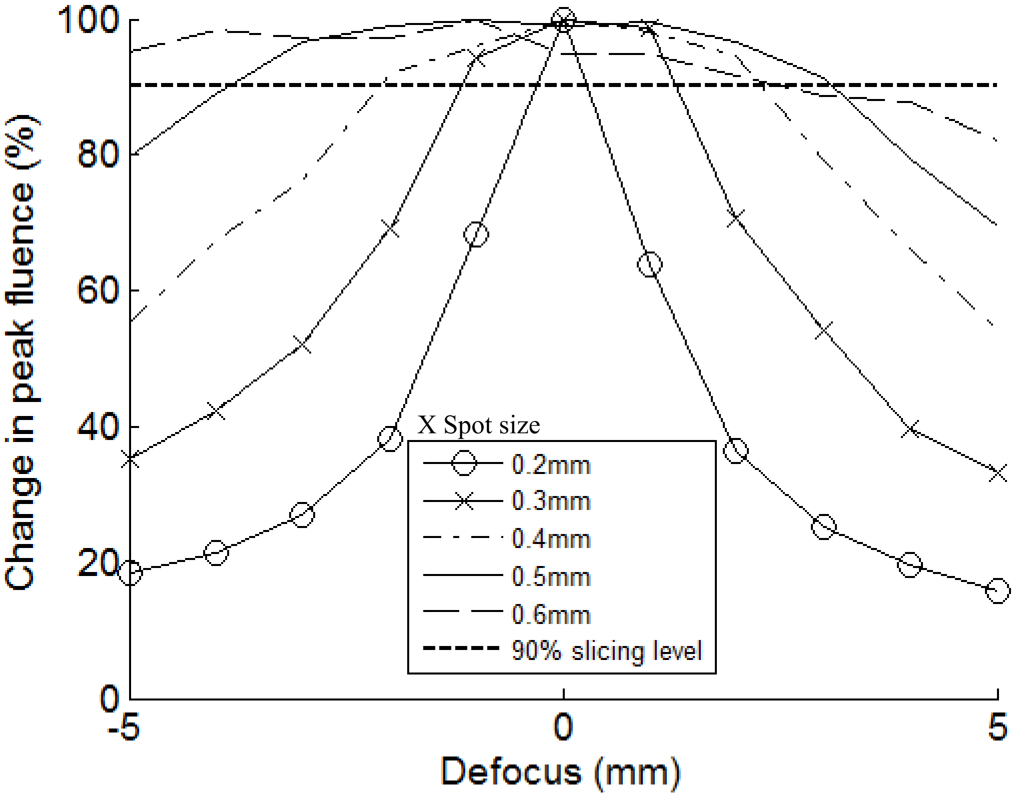

Figure 83 – The change in fluence vs Y spot size delivered to the substrate vs defocus in Z.

For a spot size of 0.2 mm the change in peak fluence is seen to reduce sharply with defocus in Z and consequently this has a small depth of focus. Figure 84 shows the focal range in Z to stay above a 90% of the peak fluence at best focus. The range of differnces in substrate thicknesses between two substrates forming a seam was from 0.5 mm to 4 mm. It can be deduced from the graph that a spot width of 0.45 mm or greater is desired to make sure the peak fluence is within 10% of the best focus and hence provide a stable fluence delivery within this range of substrate heights. One key aspect of the Powerlase Rigel series lasers is that they are market leading in the capability to deliver both high peak powers and high average powers to the substrate. This means the pulse energy delivered to the substrate is sufficient to permit the larger X dimensions for the spot and maintain the fluence to process the material; hence the larger X dimension also yields a larger depth of focus than most of the competitor lasers and neatly leverages an advantage of the solid state laser technology onto the end process.

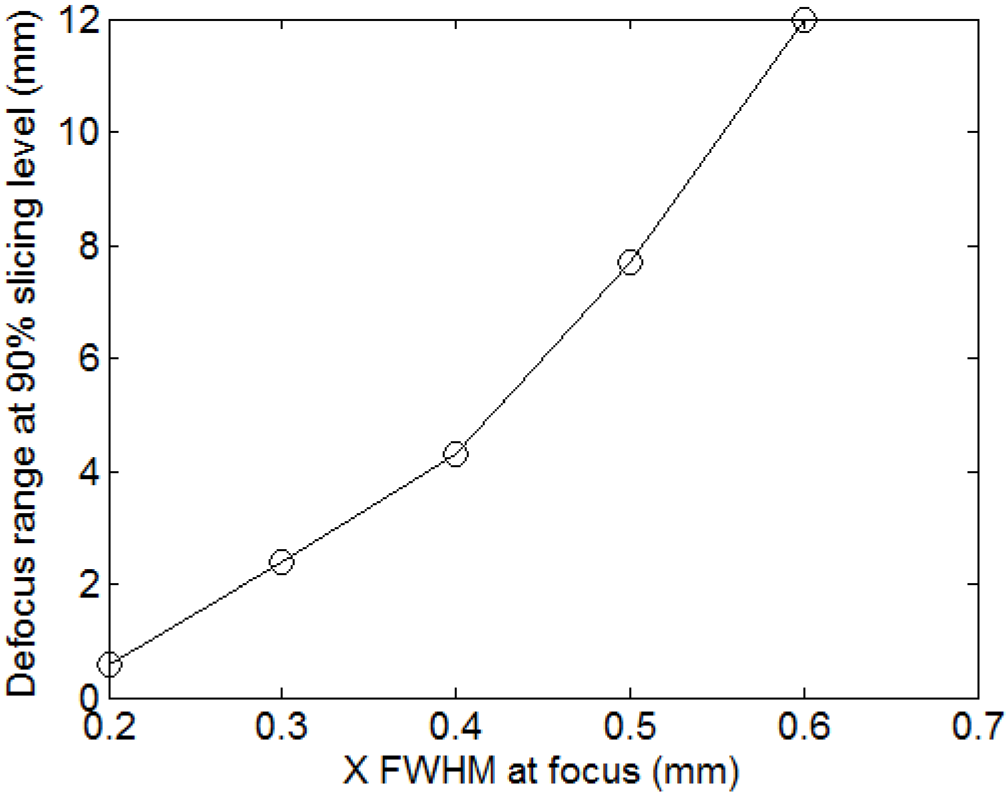

Figure 84 – The focal range in Z for less than 10 % change in fluence at the substrate.

3.5.6 Fluence at each of the internal optical components

An important consideration in the optical design of the processing heads is the susceptibility of the internal optics to damage due to the pulsed laser radiation that is incident upon the lenses of the system. The irradiance profile of the laser beam at each lens is determined by the modelling methods as detailed this chapter. The 1/e^2 of the beam radii is determined from the modelled data and Eqn. (22) is used to determine the peak fluence at each lens surface. Figure 85 shows the architecture 1 processing head and details the optical profile of the beam as incident upon the internal lenses.

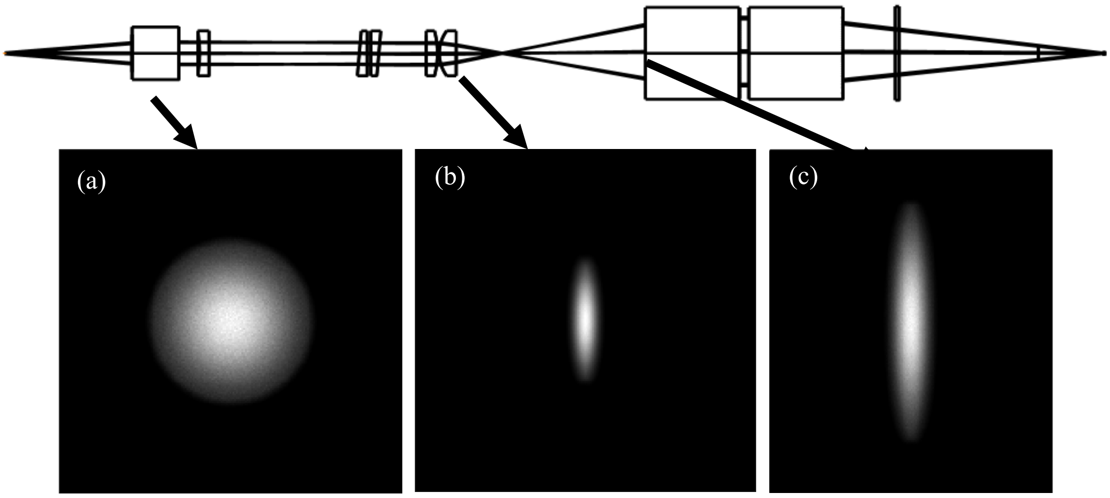

Figure 85 – Architecture 1, irradiance profiles at internal surfaces. (a) at the first collimating lens, (b) at the second cylindrical lens pair and (c) at the input of the relay lens.

In Figure 85, assuming a worst case power of 1.6 kW and a pulse duration of 60 ns. The peak fluences are as per Table 2.

Position	X dimension (mm)	Y dimension (mm)	Peak fluence (J/cm^2)
(a)	5.7	5.7	0.1
(b)	1.1	4.2	0.73
(c)	3.6	17.1	0.05

Table 2 – Peak fluences at each lens for architecture 1

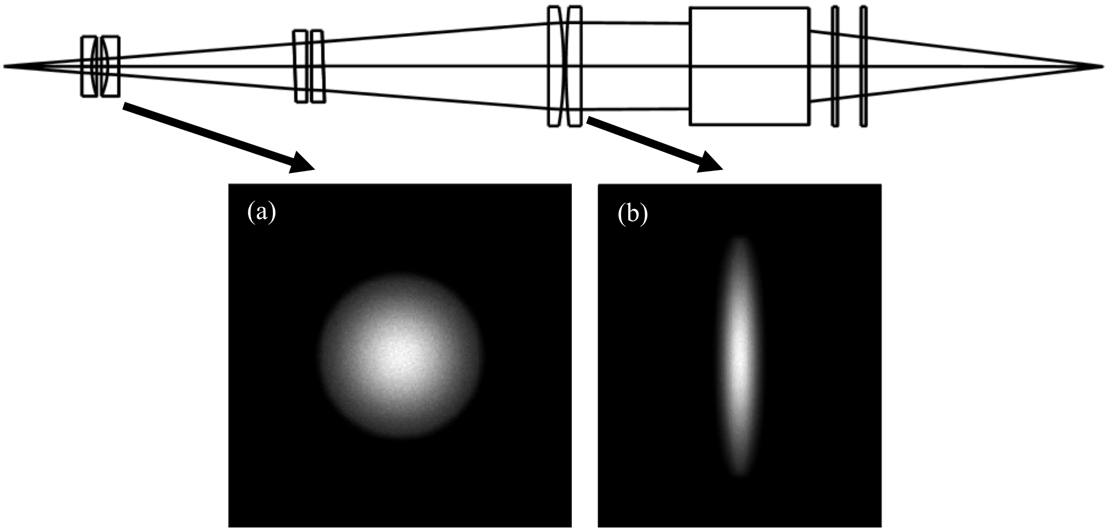

Figure 86 – Architecture 2, irradiance at internal surfaces. (a) at the first cylindrical lens pair, (b) at the second cylindrical lens pair.

Figure 86, assuming a worst case power of 1.6 kW and a pulse duration of 60 ns the peak fluences are given in Table 3.

Position	X dimension (mm)	Y dimension (mm)	Peak fluence (J/cm^2)
(a)	2.6	2.6	0.50
(b)	17.4	3.2	0.06

Table 3 – Peak fluences at each lens for architecture 2

In all cases for the processing heads the fluence at the lens surfaces is well within the specified 10 J/cm^2 at 20 ns at 1064 nm. Architecture 1 is the most prone to damage on the surface of the second cylindrical lens pair, but the fluence at these lenses is still ten times less than the coating damage threshold.

3.6 Summary of processing head design

A method for generating an optimised homogenous rectangular laser beam to a substrate material for surface removal has been presented. The technique utilises a novel exploitation of the multimode mixing of the laser beam within a square core fibre which produces a homogenous beam [16] profile that is devoid of laser speckle. Excellent homogeneity and speckle free profile was observed even when isolating single pulses of the laser. Two refractive architectures for beam shaping the homogenised high power laser beam were presented using cylindrical lenses to provide different magnifications in the X and Y axes, producing the desired homogenous rectangular laser profile.

Modelling techniques and analysis provide the correct predictions of key beam parameters and are effectively used to generate different models of processing heads. The laser system with these processing heads was placed into successful industrial use in 2012 and produced the first trials substrates that led to the further research in chapter 4 and hence is a solid foundation of techniques and system design for the laser design iterations.

3.7 Conclusion of processing head design

Measured spot width parameters show a strong correlation with modelling techniques employed. The correlation with edge width, as shown in in Figure 82 is not strong because the reported model values were for a perfect system and the measured data is subject to the manufacturing tolerances, in particular rotation of cylindrical components about the Z axis. All measured values for the edge width are all less than 160 µm and within expected values for these tolerances. Homogeneity shows little correlation between modelled and measured data because the homogeneity value is so small and all processing heads were well within the target of <15%.

The modelling technique employed on these processing heads was sufficient to design and predict the performance parameters of the processing heads and the processing heads can thus be described with tolerances as; target spot width ± 4%, edge uniformity <200 µm, uniformity < 15%, and transmission >95%.

A final summary comparison of the two architectures is; architecture 1 processing heads are an initial solution to the mechanical retro-fit onto the customer's first machine. While the architecture 1 processing heads are perfectly adequate for the process and still in production use, the simpler design, optical performance, range and design freedom of the architecture 2 processing heads is preferred in future systems where more design freedom is available. Architecture 2 processing heads are also more flexible in the manipulation of the optical axis, especially in the ability to tilt the optical axis prior to the final focus. They also permit a near telecentric output when coupled with an optical actuator as discussed in the following chapter.

Chapter 4 - An actuated laser beam delivery system

4.1 Introduction and motivation for project

In the surface removal process as described in chapter 3, it is found that there is a deviation from the central seam position in the Y axis between the metal substrates as they are loaded into the machine. The metal substrates are loaded in batches and the maximum variation in placement along the Y for these batches is estimated by the customer to be ±3 mm. For reference the seam and substrate configuration is shown in Figure 87.

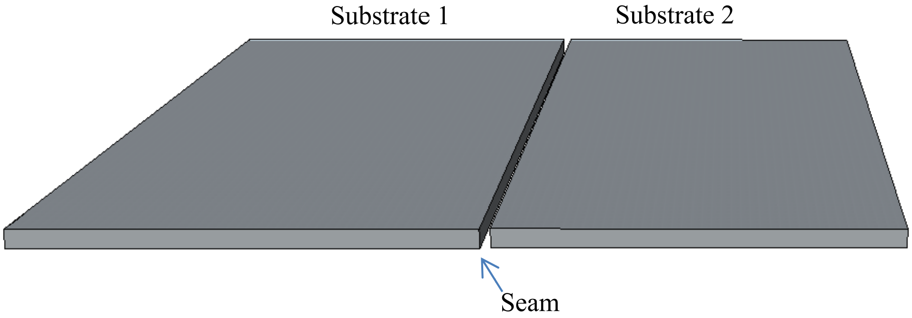

Figure 87 – showing seam between the two substrates.

The approach taken to solve this problem is to implement a seam tracking system consisting of a vision tracking system to follow the seam position and an actuated processing head for the beam delivery to the substrate. A key element of novelty is required as the whole optical system is required to fit within the same tight space constraints as described in chapter 3. The optical trains of the processing heads are also shaped using refractive prisms or mirrors to fit the challenging space envelopes. Commercially available beam deflection systems are either based upon physically moving the beam delivery head, or by using a galvanometer system, there is also no commercial processing head for pulsed lasers performing beam shaping of the irradiance profile. Due to the approach of the commercially available solutions, at the time of writing, they consume too much volume to be viable within the available space envelope. Other technical solutions such as large angle acousto-optic modulators or holographic based solutions would create too much scattered loss as their diffraction efficiencies are typically in the region of 58% to 80%. Actuation of the position of the fibre is prohibited within this space envelope and actuation near the fibre is undesirable because any residual movement (~100 µm) in the Z dimension would cause astigmatism and blur in the focussed image, it is also a region of the processing head that is highly prone to damage due to the large fluence at the exit of the fibre. A floating lens solution would require actuation in a region near to the final focussing lens, which is in close proximity to the heavy moving shuttle that clamps the substrates. It is also unlikely that a floating lens could provide the range of actuation as a single lens and would require a complicated lens construction to compensate for off axis aberration.

A novel solution to this engineering problem is to actuate the laser beam with an in-line optical deflection using a Risley prism that is incorporated into the beam shaping processing head architectures detailed in chapter 3. A schematic of the Risley prism pair is shown in Figure 88. The Risley prism consists of two back to back wedge prisms, in this case arranged so one prism rotates about the optical axis in one rotation sense and the paired prism rotates to an equal degree but in the opposite rotation.

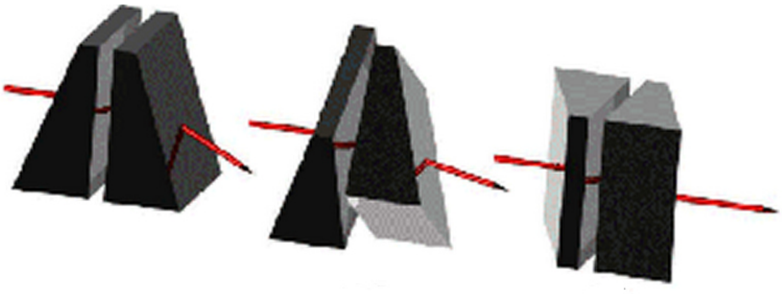

Figure 88 – Risley prism pair

The counter rotation of the Risley prism pair is used to alter the propagation angle of the laser beam within these processing heads imparting a linear phase shift upon the wave-front of the laser beam, this creates a shift in the Y position of the spot at the focus delivered to the substrate. The implementation of this Risley prism approach is subtly different between the two presented architectures and these are presented in detail in this chapter.

Figure 89 shows the implementation of the Risley prism housing and the available space envelope for one of the applications. The outer dimensions of the housing of the Risley actuator is not allowed to exceed 100 mm in width, 125 mm in length and 65 mm in height.

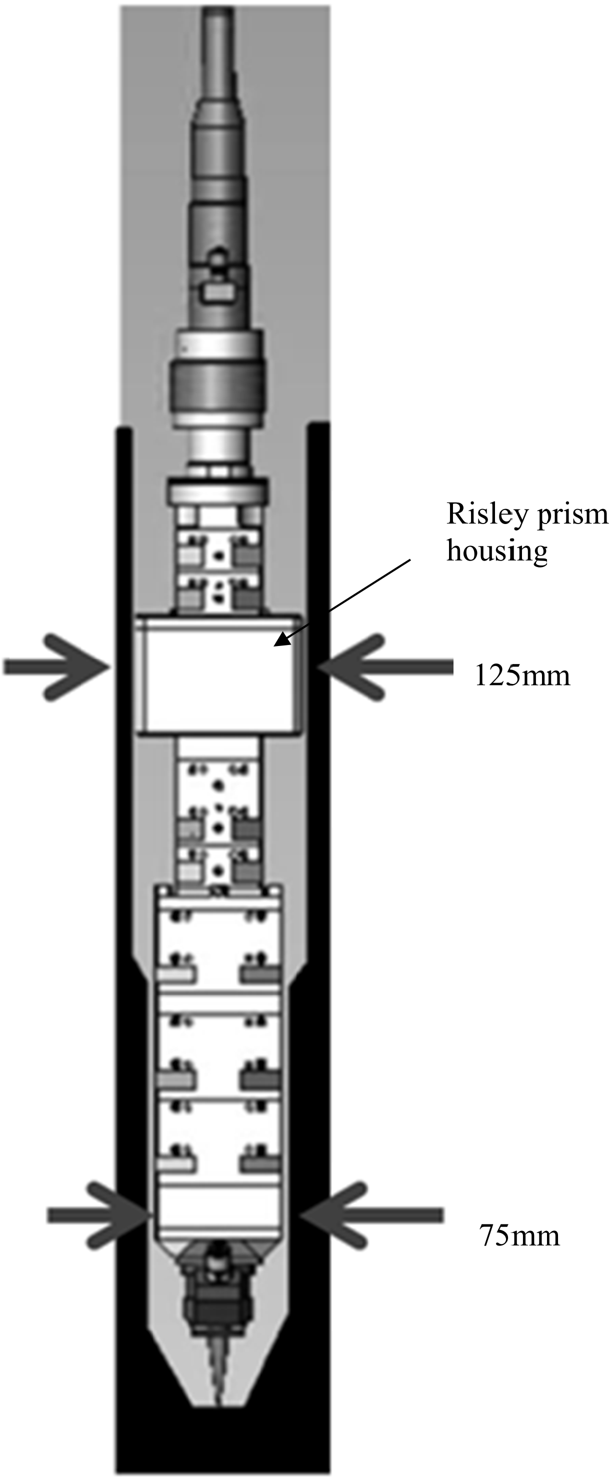

Figure 89 – The Risley prism implementation within the space volume.

4.2 System design and components

The full seam tracking system, minus the laser is shown in system diagram in Figure 90. This diagram shows the components as they were arranged at the final installation at the customer site.

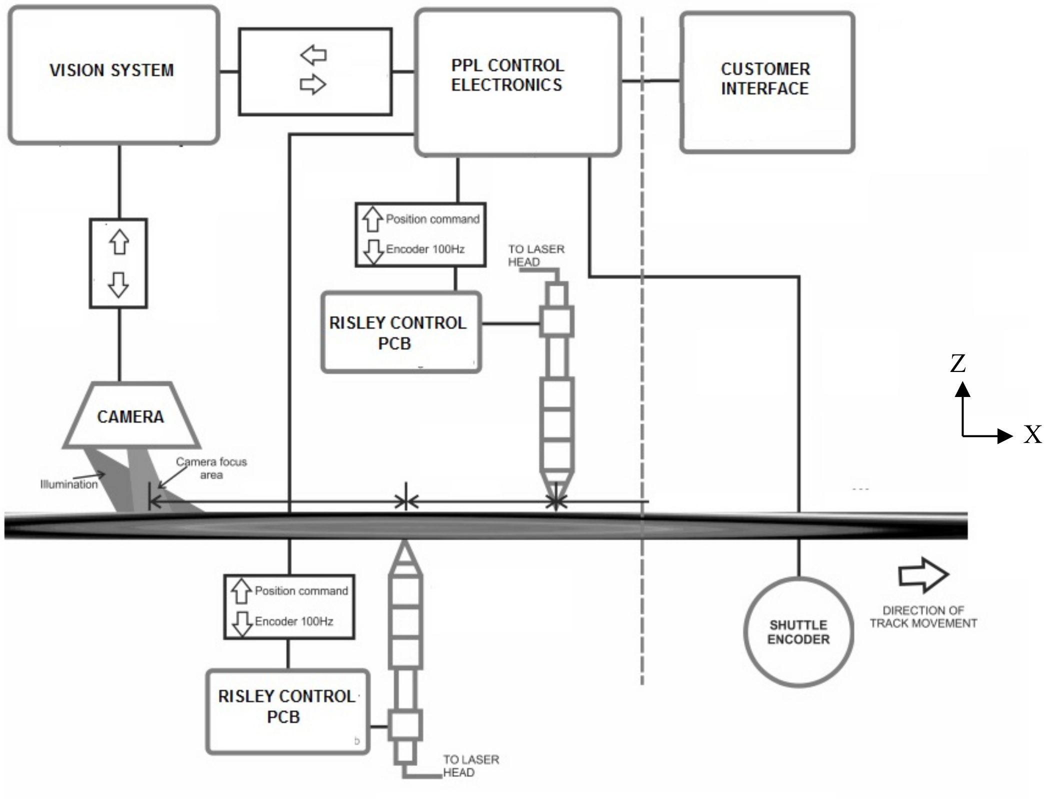

Figure 90 – System diagram of the actuated system.

The first components in the system are a Precitec SD150 camera and a Laser path finder (LPF) vision system; these monitor the position of the seam between the substrates and then produce a control signal that is passed to the control electronics. The control electronics interprets the incoming signals from the Y position control signal from the camera/vision system and the X position from the encoder moving the substrates. Knowing this information and the position of the camera relative to the processing heads, the control electronics synchronises the movement of the Y position of the laser beam to the correct position on the blank by issuing the commands to the processing heads. Control latency algorithms, described in chapter 5, also make sure the processing heads move in advance of any large deviations in seam position. The control electronics also incorporates algorithms to avoid erroneous deviation due to spatter or other false signals from the vision / camera system and thus maintains the correct position of the laser beam on the seam. The laser and the fibre delivery are entirely separate from this system and can be assumed to be permanently emitting, during the process and not linked to the actuator control.

There are three major different types of deviation that the seam tracker needs to be able to eliminate from the manufacture process; these are shown in Figure 91. The first deviation shown is when the substrate is not loaded with the seam parallel to the direction of travel; the second scenario depicts the situation where the central position of the seam varies in the Y dimension from substrate to substrate and the third is the case when each batch is loaded with a different offset in Y. The variation between substrate, as shown in Figure 91 (b) is the biggest challenge as the positional transition in the detected seam signal is potentially a full 6mm shift in position of the substrates and also appears, to the control electronics, as an instantaneous change in the Y position signal as there was no vision signal in the regions between substrates. The spatial distance in X between camera and the processing heads as shown in Figure 90 provides the time to manage the latency as the substrate travels between the camera and the processing head. This enables the control electronics to pre-order the movement of the prisms so the beam is in the correct position when the substrate arrives under the processing head.

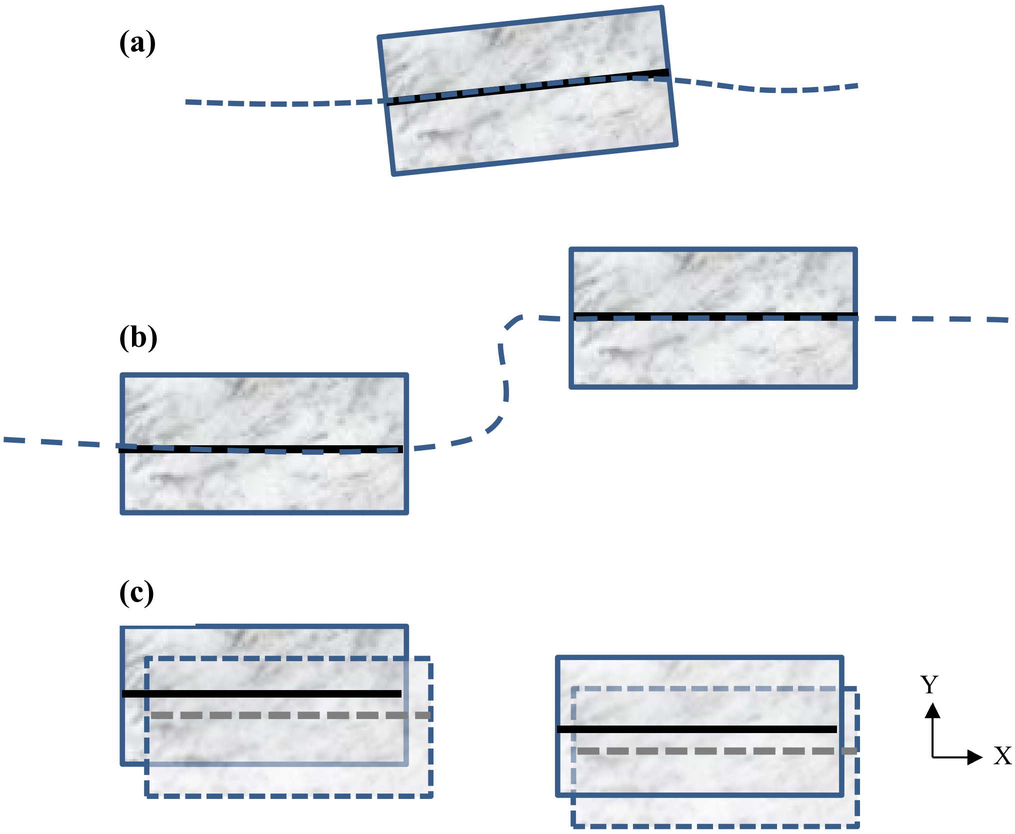

Figure 91 – Types of mechanical misalignment encountered a) tilting of the substrate b) Y offsets between substrates c) batch to batch loading error.

The analysis of the full seam tracker system is described in detail the following sections. This system is sequentially de-risked by specifying the required performance of each sub component and performing de-risking tests on each component to validate their performance and interfaces to the following sub systems. The analysis starts from the camera and vision system and works through to the optical translation performance of the Risley prism actuated processing heads. The systems approach of testing the performance and interface of each component was found to be extremely useful and reduced the debugging time because the interfaces were well defined.

The overall specification for this system was to be able to track the seam between the substrates and deliver a beam shaped laser beam onto these substrates from both sides to an accuracy of ±50 µm in the Y dimension and over a range in Y of ±3 mm and range in Z of ±10 mm. The seams that are tracked were formed by substrates of the same thickness with a gap between them of 50 µm or by substrates of different thicknesses from 50 µm up to 3 mm differential thicknesses, which forms a seam height. The spatial resolution of the system was to be <5 mm in X.

4.3 Camera and vision system

The first components in the communication train are the camera and vision interpretation system; these are required to have a combined resolution that is able to determine the position of the seam between the substrates to within a resolution of 50 µm in Y and the Z axes. The range requirements are ±6 mm in Y and ±10 mm in Z. The positional data for Y is then converted into a single output of ±10 V control signal representing linearly the Y position of the seam so that it can be processed by the control electronics.

The camera, as shown in Figure 92, was a triangulation sensor that is used to detect the position in Y and interpret the depth information of the seam. This camera is sourced from Precitec, part number: P6502-1093-00001, serial number: GD09057, and type SD 150 WD. The general principle of operation of the camera is shown in Figure 92, where the height of the substrate is interpreted as a discontinuity in Y on the CCD image

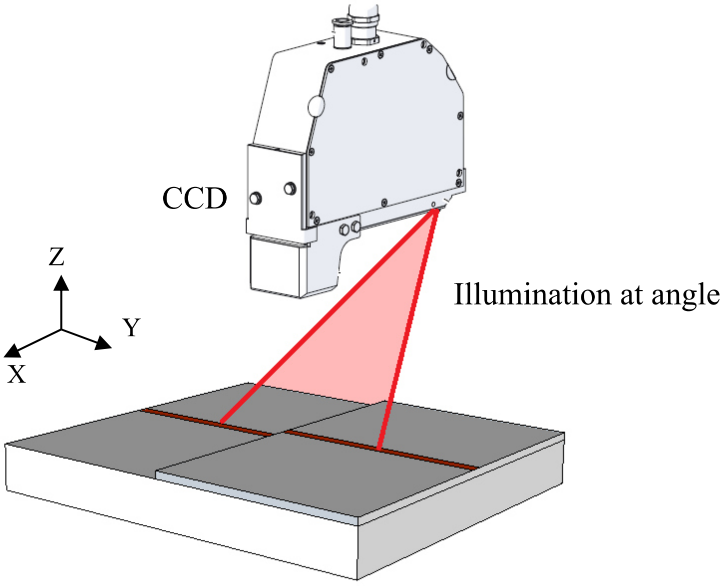

Figure 92 – Diagram of the triangulation camera.

A laser illuminates the substrate at an angle of 37° so that the height of the substrate is perceived by the camera as a positional shift in the X direction. The camera has a two dimensional Charged Coupled Device (CCD) array so any height differences between the substrates along the Y dimension perceived by the image formed in the camera as a break in a solid illuminated line. The image from the CCD array is therefore a representation of the seam in the YZ plane, the seam position in Y was determined from the discontinuity in Z from this signal. The datasheet values for the optical performance of the system are, Y resolution 14µm, Z resolution 20 µm, 184 frames/s, Y measurement range of 10.7 mm Z measurement range of 13.4 mm and an optical standoff distance of 149 mm. These datasheet values are sufficient for this application, but the tests in following section confirm the actual performance.

The pure optical resolution of the camera is not the only determining factor in the system resolution, the settings for the Laser Path Finder (LPF) vision system also determine the performance of the seam tracking signal. The vision system is a Precitec Laser Path finder (LPF) P5500-0000-QEN50 optical seam tracking system, running software WinLPF version 1.8.6.0. The purpose of this system and software is to interpret the captured YZ visual data from the camera and process into the single DC voltage of ±10 V, which is linearly proportional to the Y position of the seam. The vision system consists of bespoke electronics and software to perform this task and is configurable for many different applications via a programming and settings interface in the software. The configurations are called from an internal memory either from the graphical user interface (GUI) or by digital hardwire lines available via a terminal block rail inside the machine. Two notable modes of usage are required to detect the seam, using the terminology in the LPF manual these are the multi-straights and discontinuity modes and are used to locate the seam in the CCD images produced by the camera for two different detection scenarios. Multi-straights is used to find a seam position in the case when the two mated substrates are of unequal height, typically <0.3 mm difference. Discontinuity mode is used in the case where the two substrates are of nearly the same height. The terminology of multi-straights and discontinuity mode and their respective settings are set in the user manual and in the software settings of the LPF and the terminology is repeated in this thesis.

Figure 93 shows the physical appearance of the LPF system and Figure 94 shows a typical seam as visualised in the Graphical User Interface (GUI) as provided by the supplier.

Figure 93 – (LPF) P5500-0000-QEN50 optical seam tracking system.

Interpretation of the camera image

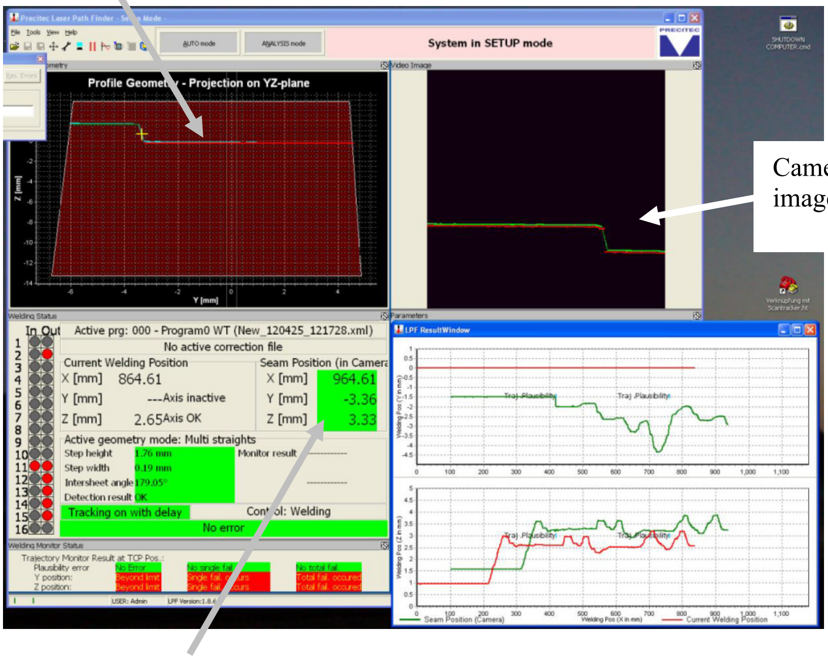

In Out

Active prg: 000 - Program0 WT (New_120425_121728.xml)

No active correction file

Current Welding Position
X [mm] 864.61
Y [mm] ---Axis inactive
Z [mm] 2.65Axis OK

Seam Position (in Camera
X [mm] 964.61
Y [mm] -3.36
Z [mm] 3.33

Active geometry mode: Multi straights
Step height 1.76 mm
Step width 0.19 mm
Intersheet angle 179.05°
Detection result OK
Monitor result -----------

Tracking on with delay
Control: Welding
No error

Trajectory Monitor Result at TCP Pos.:
Plausibility error No Error No single fail No total fail.
Y position: Beyond limit Single fail. occurs Total fail. occured
Z position: Beyond limit Single fail. occurs Total fail. occured

USER: Admin
LPF Version:1.8.6

Camera CCD raw image

Seam positions
Colour indicates if the
seam is detected

Figure 94 – Typical visual layout of Win LPF software.

Once the vision system imports the raw image from the triangulation camera, one of the two vision interpretation algorithms is be used to determine the Y position of the seam. In the case where the seam was created between two substrates of the same height, the discontinuity mode is selected. In this mode the seam data is obtained via determining a minimum in the CCD sampled data that corresponds to a gap or burr between the substrates. A schematic of the general principle of the technique is shown in Figure 95 and an actual screenshot of the LPF software using this algorithm is shown in Figure 96

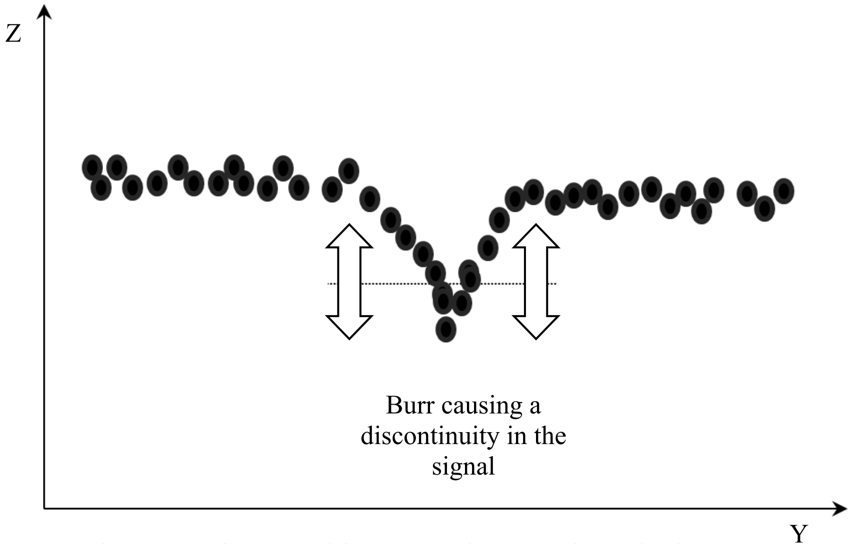

Figure 95 – Seam position determined by discontinuity mode.

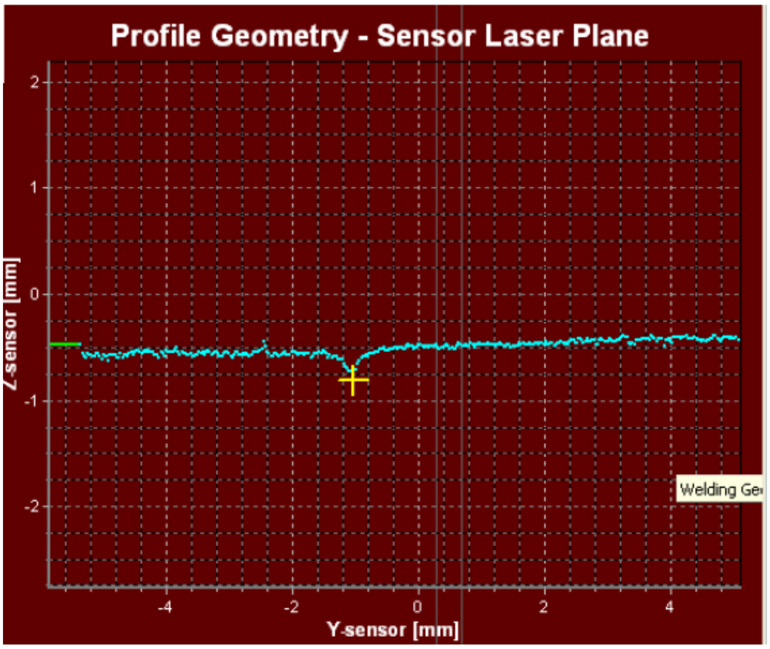

Figure 96 – LPF visualisation of the discontinuity, seam position marked by yellow cross.

In the case where the two substrates are of sufficiently dissimilar height in Z, multi-straights mode is used to determine the Y position of the seam. In this mode the Y position of the seam was found by fitting two lines to the data, one fit is started from the left hand side of the dataset and the other line fitted from the right hand side of the data set. The Y position of the seam is found where a mismatch is found between the two lines. A schematic of the technique and the LPF representation of the seam are shown in Figure 97 and Figure 98.

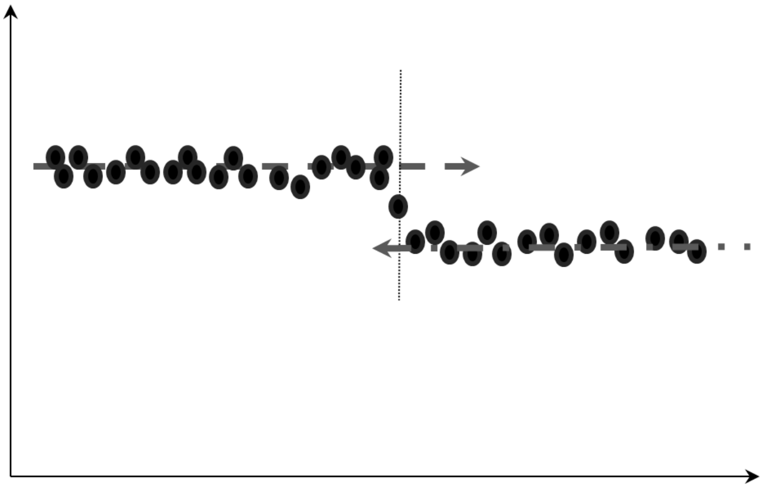

Figure 97 – Seam position determined via multi-straights mode.

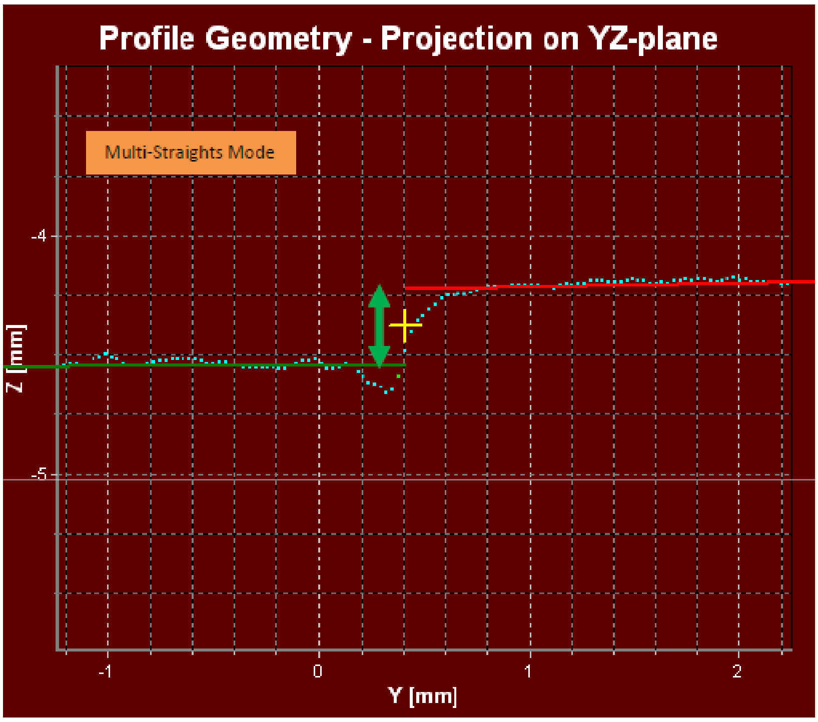

Figure 98 – LPF visualisation of the multi-straights mode.

In the multi-straights case there is no need for a burr to be present on the substrates and the seam position can be determined even if the substrates had sharp edges

The discontinuity and multi-straights algorithms are controlled via a set of control parameters which can be adjusted to increase or decrease the sensitivity of the seam detection. These included options for averaging the data, which effectively reduces the resolution of the system and also restrictions on the region of interest (ROI) to avoid any process spatter interfering with the imaging. A full list of the parameters is given in the results of the following experiments to establish the capability of the camera and LPF system.

4.3.1 Camera and laser path finder tests

The first experiment presented is to establish if the camera and vision system is actually capable of detecting seams where a 50 μm a gap is between two identical height substrates using the discontinuity mode setting in the LP. In order to test this, a gap is formed between two substrates by using a set of using calibrated engineering shims (manufacturer h+s, Prasizisionfolien sortiment 25). These have a precision tolerance of 0.3 % thickness variation and were manufactured to ISO 9445-2:2009. The gap is created by clamping two of these precision shims together with a feeler shim of known thickness separating them, the feeler shim is then removed leaving a gap of known width in Y. The idealised engineering shims are used as the substrate to ensure sharp and straight edges as a worst case scenario, as seen later in this report; the actual substrate material has a burr, which is easier to detect. The experimental set-up of the shims is shown in Figure 99.

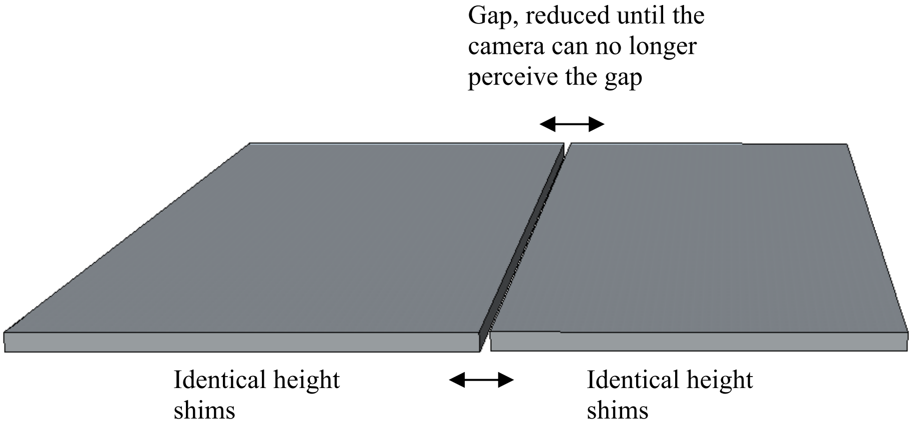

Figure 99– Gap between substrates.

The ability to measure the seam is tested by forming ever smaller gaps with the feeler shims until the seam can no longer be detected within the LPF system. The LPF settings are adjusted on the first few passes in order to optimise the sensitivity of the system.

Once adjusted to their most stable settings the experiment is then performed with the same settings for all gap widths generated by differing thicknesses of engineering shim and the results are shown in Figure 100.

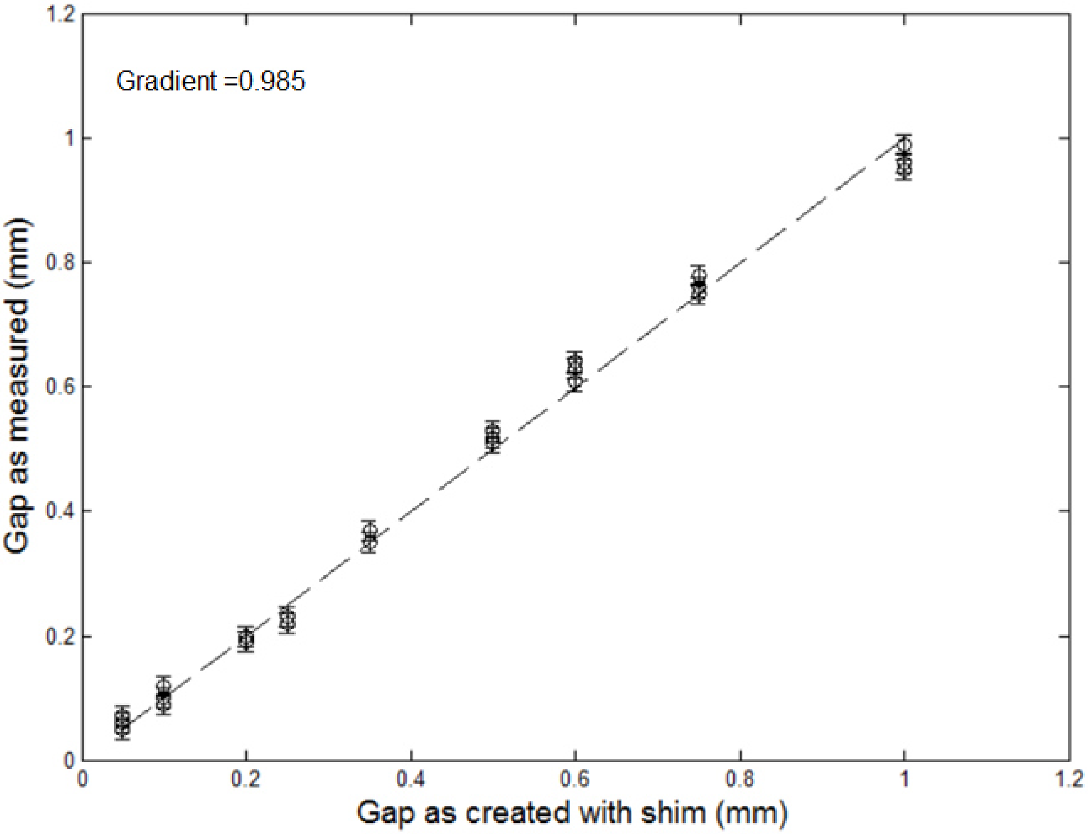

Figure 100 – Graph of gap vs measured width in LPF software, dotted line indicates y=x for reference.

It is found that the minimum resolvable gap is 40 μm. If the gap is smaller than this, the vision system faults and reports no seam in the LPF report window. This figure is poorer than the 14 μm value claimed in the datasheet but still just within the project aim of 50 μm resolution. The LPF settings are captured for this trial and are shown in Table 4. This test is likely to indicate that the specified resolution performance of the camera on the datasheet is referring to individual pixel resolution not the resolution of the smallest seam, which would require a minimum of two pixels to be resolvable by the software.

Parameter	Setting
Laser power	133
HP distance	10
Detection threshold	19
Weight of second moment	1373
Width of Barycentre	24
Min Group length	2
Max deviation of group	7
ROI	0
ROI	512
ROI	0
ROI	512
X averaging	1
Max hole length	21
Video source	Camera 2
Light source power	
Profile is vertical	Off
Profile pt default position	0
Min valid profile	20

Parameter	Setting
Segmentation tolerance	7
Min segment length	116
Gap measurement	yes
Sensitivity	44.78
Min gap width	0
Max gap width	5
min gap height	-3
Max gap height	3
Y shift	0
Z shift	0

Table 4- LPF settings used for discontinuity mode.

The following tests are also carried out to establish the ability of the camera and LPF system to resolve seams that are formed by two substrates of different thicknesses. In this case the multi-straights algorithm is used. Again the LPF settings for multi-straights are adjusted to optimise the sensitivity and stability of the algorithm to the substrates an the precision engineering shims were used, this time to form idealised sharp seams at different heights.

These tests are performed by firmly clamping the engineering shims onto a thicker, >1mm engineering shim as shown in Figure 101, note there is no actual gap between the substrates as the determination of the discontinuity is from the substrate thicknesses alone is being evaluated.

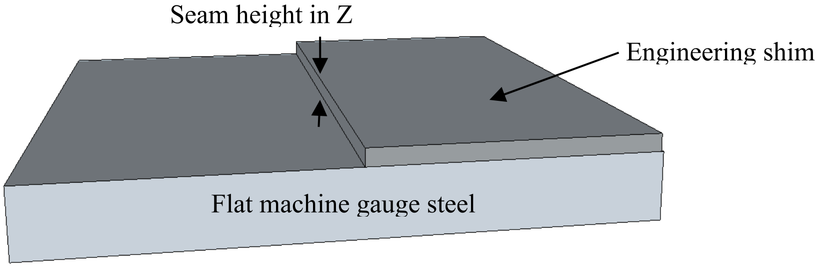

Figure 101 – Seam heights created with engineering shim.

The seam detection is evaluated for seam heights of 1000 µm, 500 µm, 250 µm, 100 µm and 50 µm. A Y position for the seam is found to be correctly detected for each of the shim heights and the correlation to the measured height vs the actual height of the shims is shown in Figure 102.

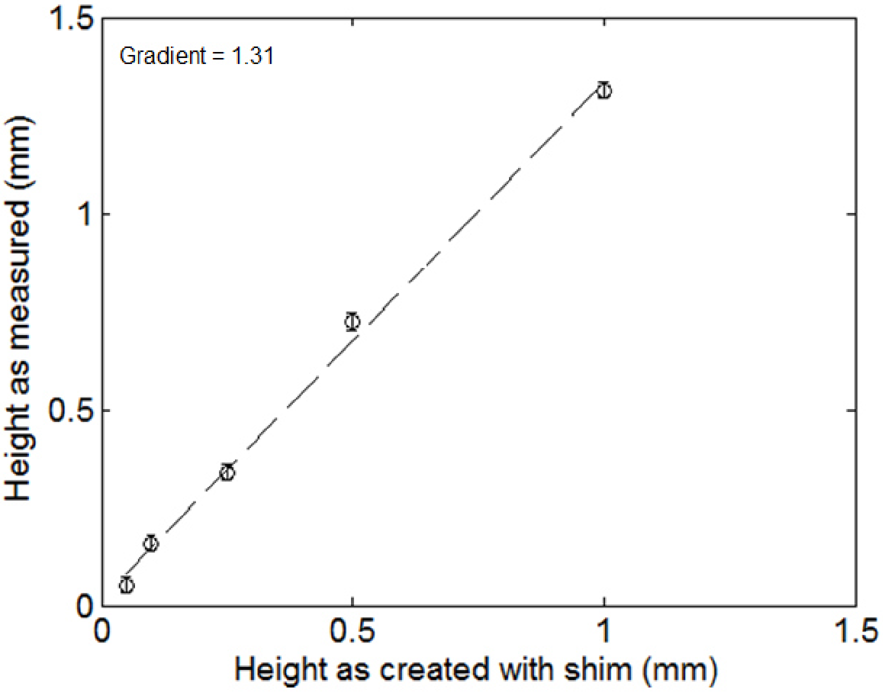

Figure 102 – Graph of seam height vs measured height in LPF software, the dashed line indicates a linear fit to the data, gradient = 1.3, intercept = 0.02, R^2 = 0.99.

The correlation between the measured seam height from the LPF and the shims is linear but uncalibrated. As this value for the actual seam height is not a required measurement it is left untouched but can be changed by calibration in the software. The minimum detectable seam height with no loss of seam in the Y dimension is 50 µm and the optimum settings established for the LPF system in multi-straights mode for are captured in Table 5

Parameter	**Setting**
Segmentation tolerance	19
Min segment length	16
min step height	0.75
Max step height	-1.64
Angles sheets	180
Angle tolerance	30
Min step width	0.3
Max step width	1
z shift	50
Z shift enable	off

Parameter	**Setting**
Laser power	166
HP distance	19
Detection threshold	20
Weight of second moment	2943
Width of Barycentre	30
Min Group length	4
Max deviation of group	7
ROI	0
ROI	512
ROI	0
ROI	512
X averaging	3
Max hole length	20
Z shift enable	

Table 5- LPF settings captured for multi-straights.

To establish the ability of the system to track the seams across the range of travel in Y, an experiment is devised to estimate the ability of the system to track the seam over the entirety of the Y axis. Seams are created, as previously described, using the engineering shims of 50 µm, 100 µm, 250 µm and 500 µm and 1000 µm to generate seams of each height. The seams are then translated under the triangulation camera in the Y axis using a precision micro-meter stage translated in 5 µm steps. The position set on the micro-meter is then plotted against the measured reading in the LPF display. By using this method the accuracy and linearity of the Y position reported by the LPF is determined by linear regression and analysis of the residuals.

The calibration graphs for the 250 µm, 100 µm and 50 µm seams is shown in Figure 103 to Figure 105, each show a good correlation of measured LPF position to set position using the micro-meter indicating a good accuracy of the LPF measurement.

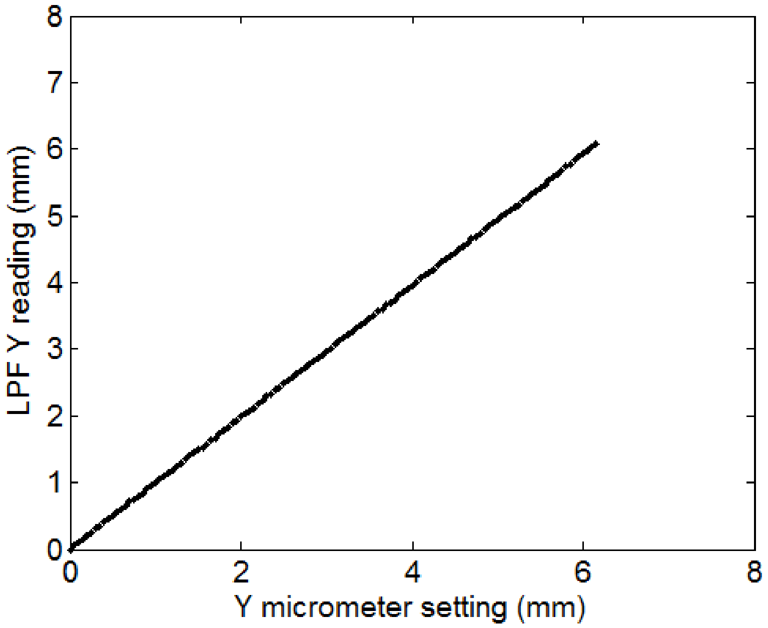

Figure 103 – Micro-meter measurement of Y position seam while detecting a 250 µm seam height.

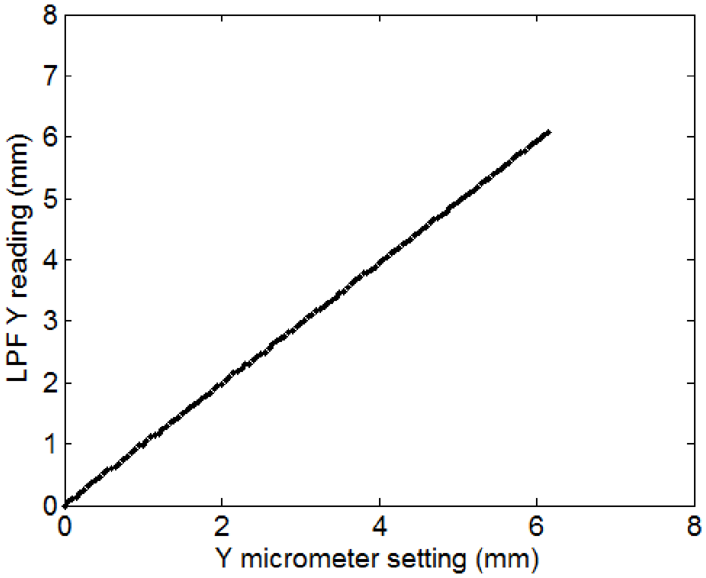

Figure 104 – Micro-meter measurement of Y position seam while detecting a 100 µm seam height.

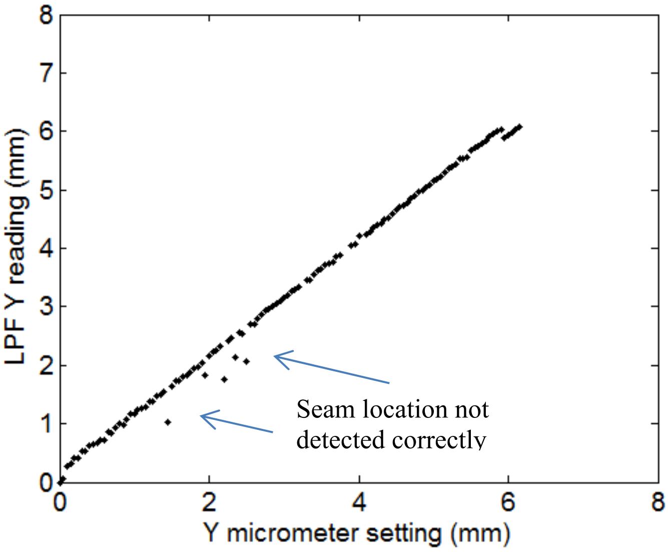

Figure 105 – Micro-meter measurement of Y position seam while detecting a 50 µm seam height, the dashed line indicates y=x for reference.

It is observed that there is a close correlation between the micro-meter setting and the reading in the LPF system for the Y dimension but the integrity of the seam tracking signal starts to break down as the seam height approaches the absolute resolution limit of the camera, this was determined in the previous study to be approximately 40 µm. It is also observed in Figure 105 that there are a few areas of the seam that are not detected properly and the LPF did not report a correct value for the position of the seam. Managing this behaviour of the signal is very important to the overall stability of the system and an important consideration in the design of the control electronics.

A figure of merit is generated for the seam tracking accuracy by subtracting the set position of the micro-meter from the measured LPF data and then plotting a histogram of the residuals and this is plotted as a histogram for each of the seam heights in Figure 106, Figure 107 and Figure 108.

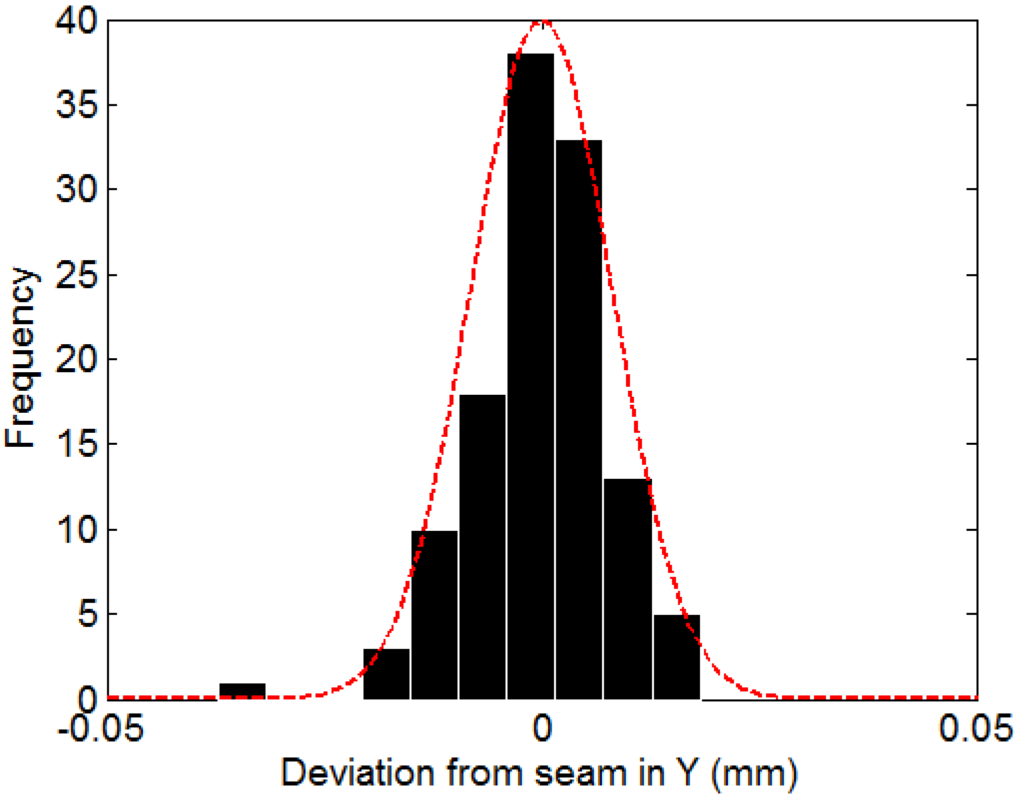

Figure 106 – Histogram of Y seam tracking error for a 250 µm shim, σ=8 µm.

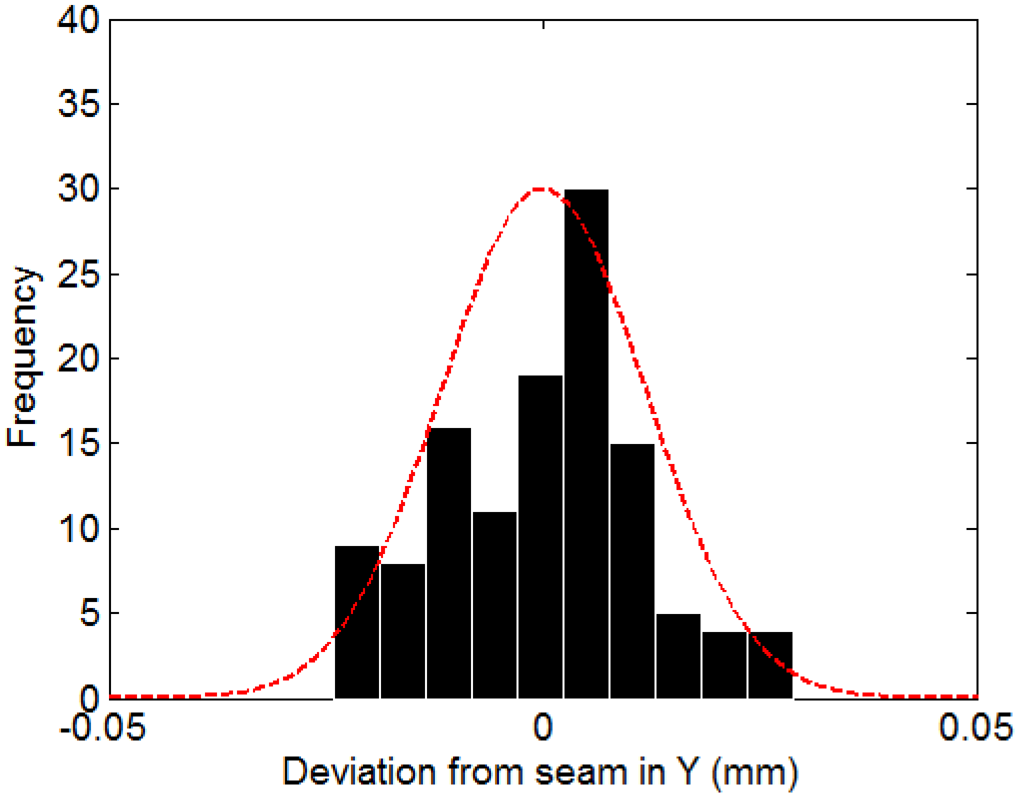

Figure 107 – Histogram of Y seam tracking error for a 100 µm shim, σ=12 µm.

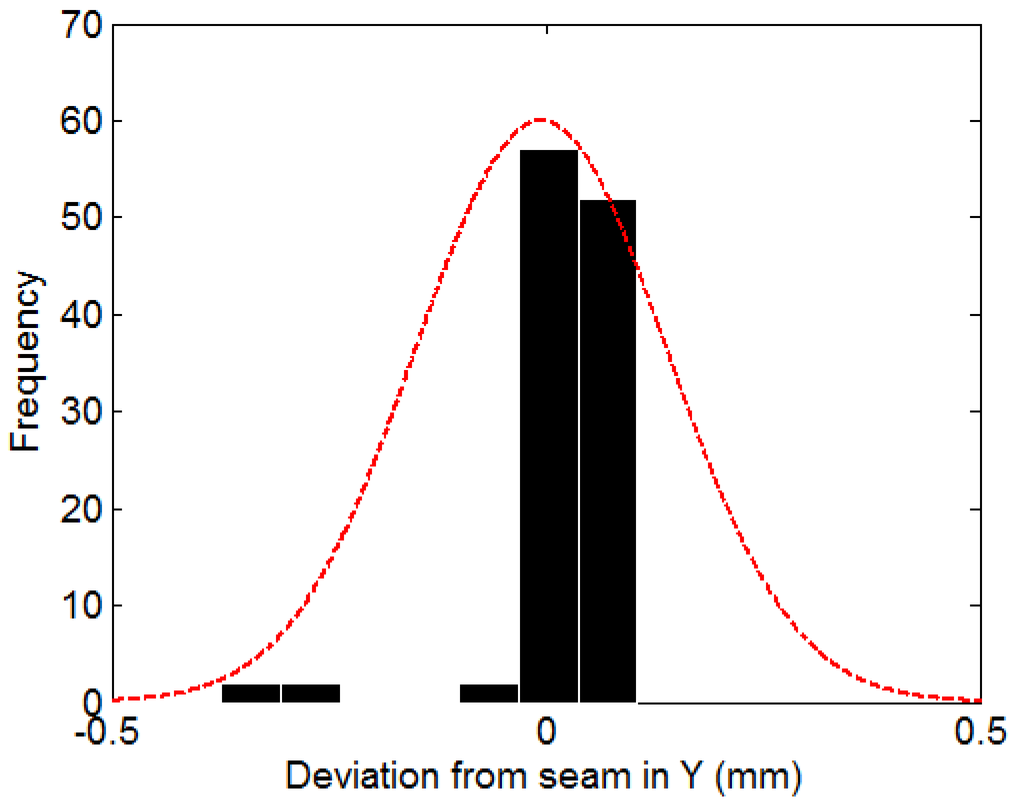

Figure 108 – Histogram of Y seam tracking error for a 50 µm shim on raw data, σ=107 µm.

It is seen that the standard deviation from the set values for 250 µm and 100 µm seam heights have tracking accuracies of 8 µm to 12 µm but as the seam height approaches the resolution limit of the camera and LPF system, the accuracy drops to 107 µm. A decision is therefore made so the multi-straights algorithm was restricted to seam heights greater than 100 µm; hence the static tracking error was determined to the 2σ, 95 % confidence limits to be ± 24 µm. In the case where the seam was less than 100 µm then the discontinuity mode would be used. In the case where the discontinuity mode is used for substrates of the same height, the tracking error is determined by the same method to be ±24 µm, but relies upon a feature with a dimension of greater than 50 µm such as a burr or a gap in order to maintain a stable tracking signal.

A natural question of this study is what would happen to the actual analogue voltage signal produced by the LPF as the seam height approaches the resolution limits of the camera and determining the integrity of the analogue signal. To address this, the seam is physically moved under the camera with a programmable linear stage providing a smooth linear motion of the substrates in the X axis. The aim of this experimental investigation is to confirm that the detection of a 50 µm gap is possible and reliable on a substrate in motion. To investigate this shims are mounted as depicted in Figure 109 and the seam is mounted at an angle to the motion of travel.

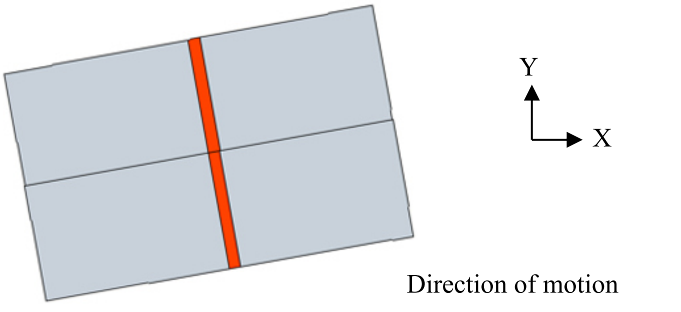

Figure 109 – Orientation of seams.

The angle of the shim from parallel to the direction of motion is deliberately aligned, so that the position of the seam in Y varies as the substrate moves by a known amount in the X direction underneath the camera. This then gives signal for Y in the analogue output of the LPF which can be recorded using a digital oscilloscope (Tektronix TDS3054B). As the shims used are also known to be precision machined straight parts, the linear regression of the recorded signal under constant velocity, can be used to generate measurement statistics on the Y axis and to evaluate noise on the signal that may be of an issue to the following control electronics. The calibration between the seam Y position and the analogue voltage is performed prior to the tests by manually running the substrates under the camera and noting the Y values in the LPF GUI and measuring the voltage using the oscilloscope, in this way the LPF is calibrated to output 0.75 mm/V. A signal generated by this experiment is shown in Figure 110.

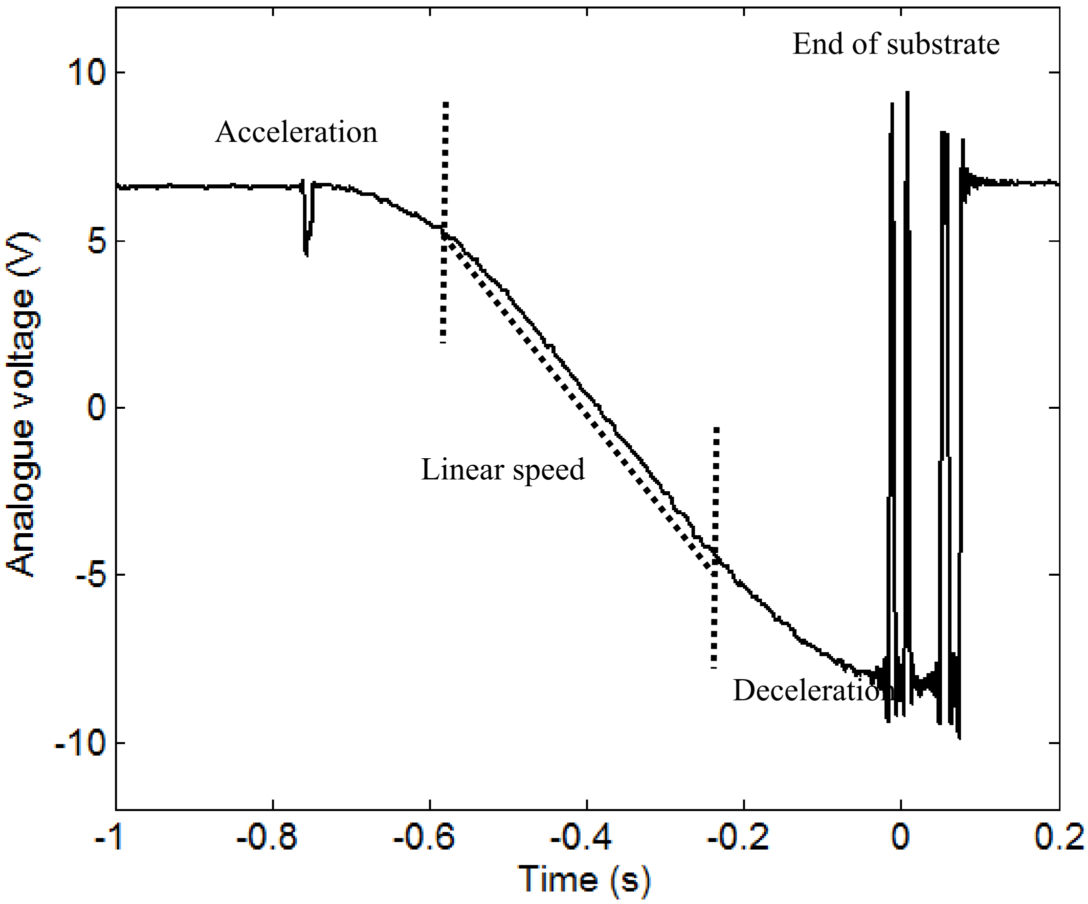

Figure 110 – Analogue tracking signal of the LPF system with a 50 µm seam height.

The statistics performed on the linear region of the graph under constant velocity provide the tracking error of the system. The seam tracker is set up to track a 50 µm seam heights for four substrates and then the seam tracked by the LPF with the optimum settings whilst monitoring the analogue output signal. A sample of the recorded data in the linear regions is shown in Figure 111.

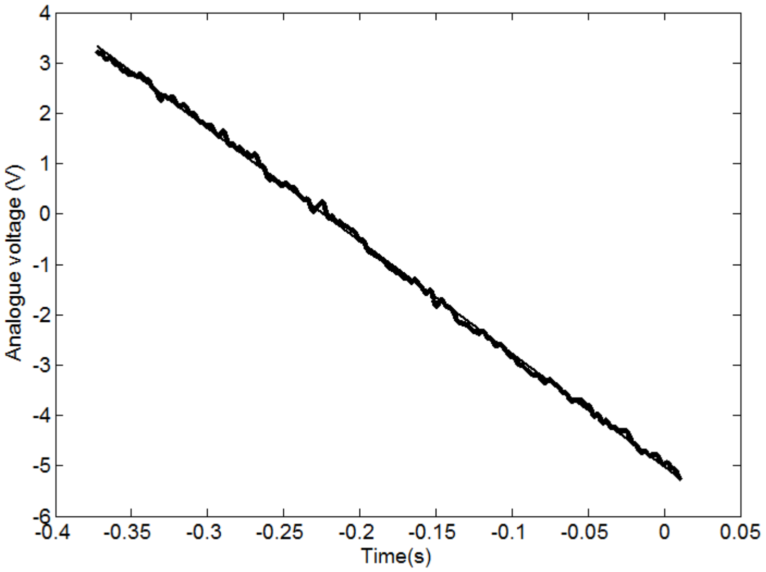

Figure 111 – Analogue voltage as measured from the LPF A2D card for a 50 µm seam.

Figure 112 shows the derived statistics from analysing the residuals in the linear regions straight line fit for four seams made of 50 µm shims.

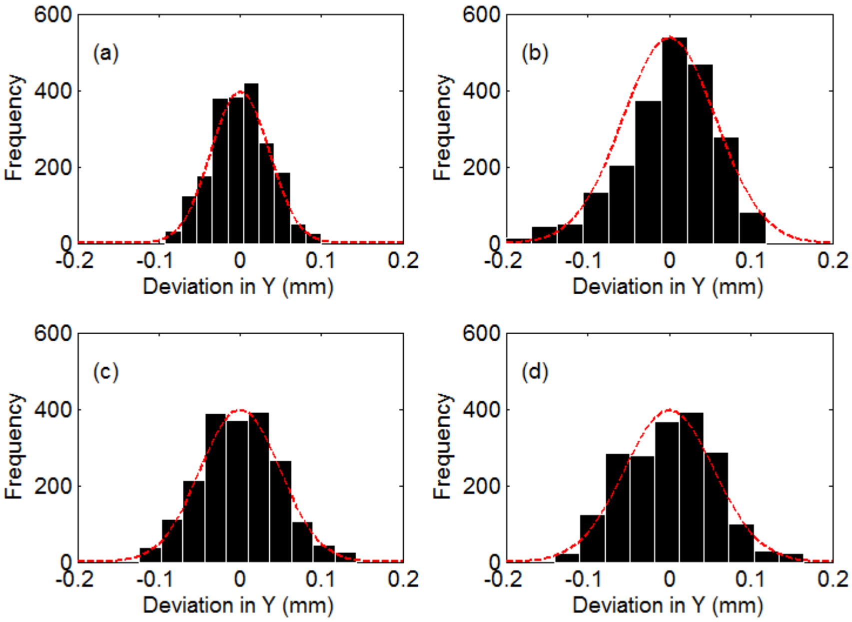

Figure 112 – Histograms of the residuals from the straight line fits, for 4 consecutive runs of a 50 µm seam height at 200 mm/s. The ±2σ values for each substrate were (a) ±53 µm,(b) ±85 µm,(c) ±73 µm,(d) ±82 µm.

The maximum tracking error encountered on this test is ±85 μm tracking error, These tests were repeated 15 times for different seam heights and the maximum tracking error encountered on this test was ±85 μm to ±2σ.

4.3.2 Summary of vision system tests

In order to establish the performance and interface behaviour of the camera and vision system several experiments were performed to establish the smallest possible seam trackable by the camera. Experiments were also carried out to determine the performance and behaviour of the analogue voltage output from the LPF system of the detected seam, also observing the reset behaviour of the analogue signal in the case where the seam was lost by the LPF system.

4.3.3 Conclusion of vision system tests

The seam tracker system based upon this camera and with careful appropriate setting of the parameters in the vision system could detect and track seams or substrates of differing heights down to 50 μm before the signal was lost. The normal tracking accuracy for seams heights that were 50 μm or greater to 95% confidence limits was ±85 μm. A linear setting of 0.75 mm/V was standardised on the digital to analogue card giving ±7.5 mm of vision range in Y.

To complete the investigation of the camera and LPF system two additional and independent studies were carried out in the same manner on the actual physical metal substrates instead of idealised shims. The findings were much the same as reported for the engineering shims but the substrates were found to always have a significant burr that was larger than the 50 μm dimension in Y. It was found that it was easier to track the substrate, when compared to the shims and they could always be tracked with this vision system and triangulation camera.

4.4 Risley prism control

The accurate evaluation of the performance of the Risley prism is crucial to the success of the project. The Risley prism incorporates all technical elements of the disciplines of this project; electronically the command latency needs to be known to accurately position the beam under the substrate, characterisation of the electro-mechanical response of the prism is needed and the mechanical designs are required to make the prism assembly suitable for the high power pulsed laser beam and the optical performance of the prisms needed to be optimised for the process.

The basic operation of the Risley prism is typically the angular deviation of a collimated beam by means of two prisms as shown in Figure 113. The prisms can be rotated fully in 360º and combinations of positions give rise to different angular deviation of the beam. Typically there are many different orientations of the individual prisms for a given output angle and this can cause issues with the control of targeting algorithms. The basic use of this prism assembly in this project is to translate the angular shift imparted on the beam by the Risley prisms into a positional shift at the focal plane where the substrate is located. Conceptually this is best envisaged as a collimated beam, deflected in angle by a Risley prism pair in one plane and then subsequently focussed by a lens. The lens acts as a Fourier transform element, transforming the angular displacement collimated beam into a positional movement in the focal (or Fourier) plane of the lens as shown in Figure 114.

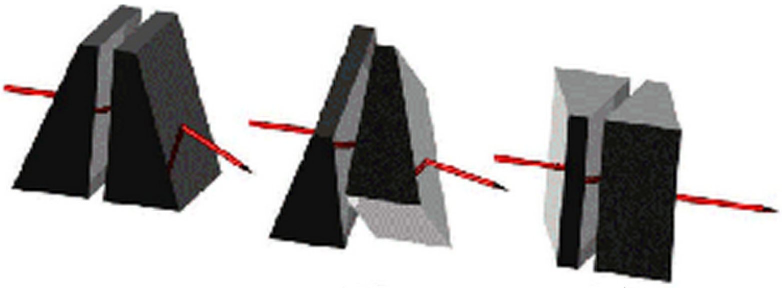

Figure 113 – Showing the principle behind the Risley prisms.

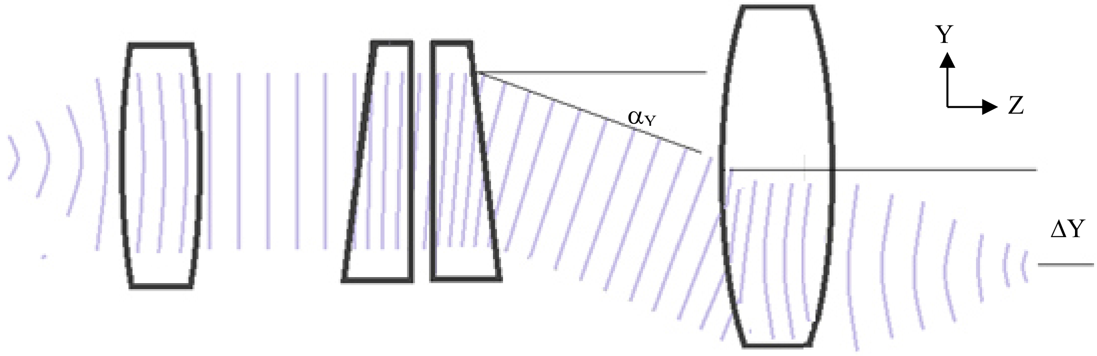

Figure 114 – Simple implementation of beam steering using Risley prism and a focussing lens.

A mathematical description of this, using Fourier optics is expressed by the following transform.

$$A(\theta_X, \theta_Y) = \iint_{-\infty}^{\infty} a(X,Y)e^{ik((\alpha_X+\theta_X)X+(\alpha_Y+\theta_Y)Y)}dXdY \qquad (36)$$

Where *a(X,Y)* is the irradiance profile of the laser beam, α_X and α_Y are the phase-front angles of this beam relative to the lens due to the influence of the Risley prism and the following terms are the Fourier transforms of the beam in terms of its spatial variables *X*, *Y* and the laser beam far field angles θ_X and θ_Y, *k* is the wave-vector. To convert the angular far field image A(θ_X θ_Y) into the image formed in the focus of the lens, the axis transform of , $X=F\theta_X$ and $Y = F\theta_Y$ is performed where *F* is the focal length of the lens.

The function *a(X,Y)* is the irradiance profile of the beam incident upon the prism and its width dictates the focussed spot size in the Fourier plane of the lens, the greater the physical extent of *a(X,Y)* then the smaller the focussed spot in Fourier plane of the lens. Eqn. (36) can be simplified into a single dimension as an example and making the assumptions that the spatial profile is a uniform top hat, i.e. *a*=1 when $1 > Y > -1$, then Eqn. (37) is derived.

$$A(\theta_Y) = \int_{-1}^{1} e^{ik(\alpha_Y+\theta_Y)Y}\, dY \qquad (37)$$

In the absence of the Risley prism, the image of top hat collimated beam formed in the focus of the lens at X = Y = 0 has a sinc^2 irradiance profile where the position in Y of the first nulls are given by Eqn. (38).

$$Y = F\theta_Y = \frac{\lambda}{D} \tag{38}$$

Where *F* is the focal length of the lens, θ_Y is the diffraction far field angle, λ is the laser beam wavelength and *D* is the diameter of the laser beam incident on the lens. The full sinc^2 irradiance profile is described by Eqn. (39), where the additional term, denoted $\alpha_{Y,}$ describing the linear phase shift imparted on the laser beam is included. Any additional linear phase shift, $\alpha_{Y,}$ applied to the beam by the Risley prism is seen to lead to a positional shift of the sinc^2 irradiance profile in the focal plane of the lens.

$$Irradiance = A(\theta_Y)A^*(\theta_Y) \propto \frac{sin^2(k(\alpha_Y + \theta_Y))}{(k(\alpha_Y + \theta_Y))^2} \tag{39}$$

An illustration of Eqn. (39) showing the way in which the Risley angle affects the position of the focussed beam is shown in Figure 115. A laser beam of wavelength 1064 nm with diameter 4 mm is focussed by a 200 mm focal length lens. A relatively small shift of 0.29° in Y position is demonstrated so that the sinc^2 irradiance profile of the focussed beam and the position shift are visible on the same scale. In practice the movement of the beam can be much larger.

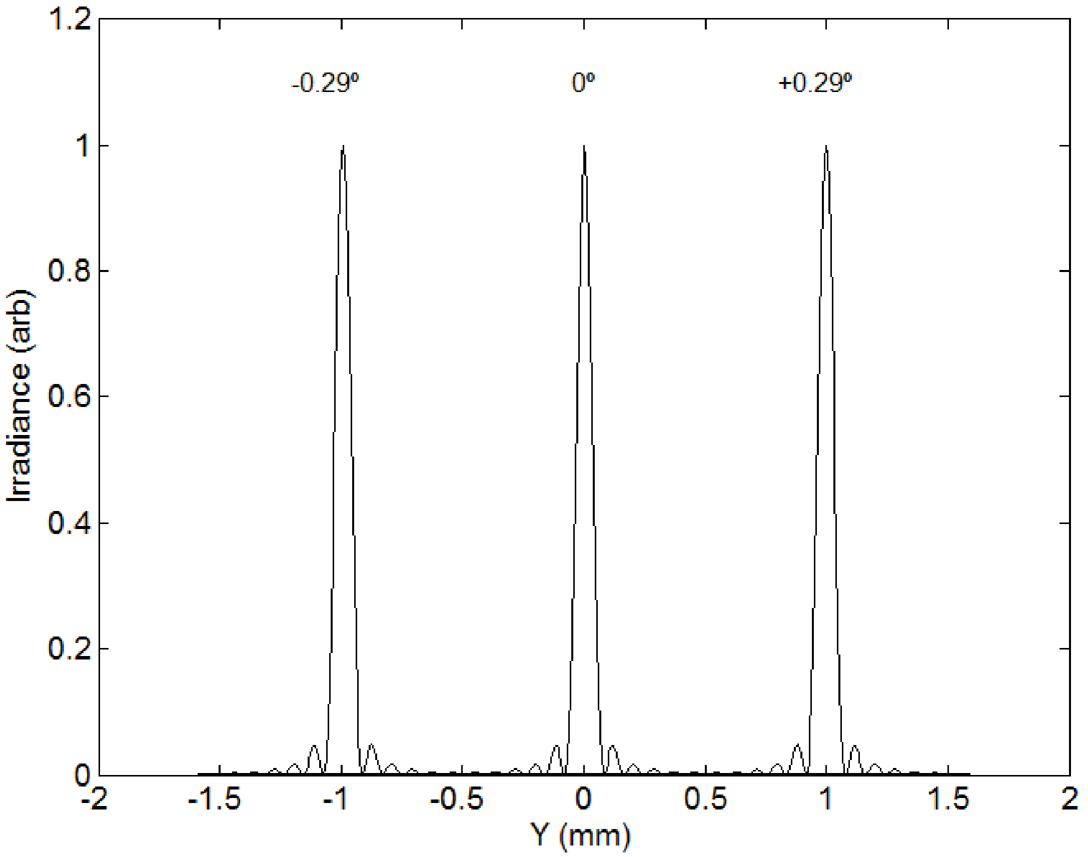

Figure 115 – Results of Eqn. (39) for Risley rotations, for a 1064 nm laser beam focal length of 200 mm, beam waist of 4 mm.

This description of the way in which the laser beam was translated in the Y axis is only strictly true for processing heads constructed to architecture 2. In processing heads based upon architecture 1 the translation of the beam is performed on the beam as it was focussed to a spot in the Y axis; however the principle of a linear phase front shift yielding a position shift in the focus is still valid. The translation of the beam from angular deflection to positional deflection was dependent upon the choice of wedge angle on the Risley prisms and also the positional placement of the Risley prisms along the Z axis. Wedge angles were between 1° and 7° and the material was the UV fused silica with AR coatings with damage threshold of 10 J/cm^2 at 20 ns 1064 nm, the same as all the optical components in the processing heads.

An important change to the mechanical design to make the Risley technology suitable for use in high power laser systems is the removal of any organic material from the presence of the beam, as this can carbonise on the optics and damage the internal optics.

The original fixing method for the Risley prisms was epoxy applied to the outer rim of the prisms as shown in Figure 116.

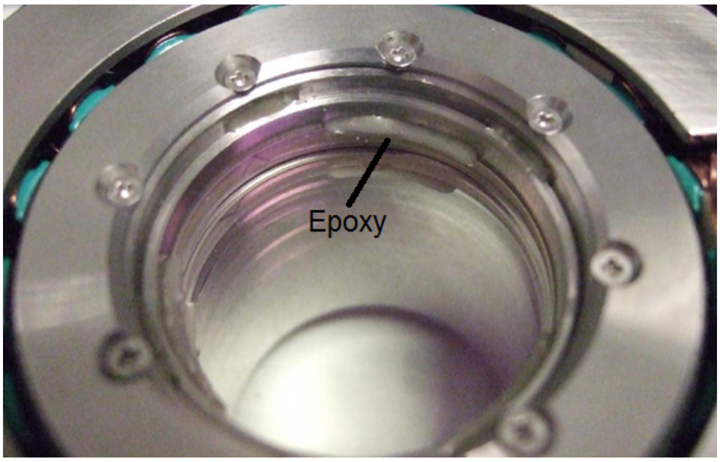

Figure 116 – Risley prisms showing original epoxy based fixing method.

This is an inappropriate fixing method for the prism for this application as any scatter from the laser will soften the epoxy and risk failure of this fixing method. It is replaced with a compressive sprung steel clasp, as shown in Figure 117, for all the processing head designs. The design method and implementation of this is similar to that detailed earlier in Figure 64 and is a successful mounting technique for optics in these applications where there is transmission of high average power.

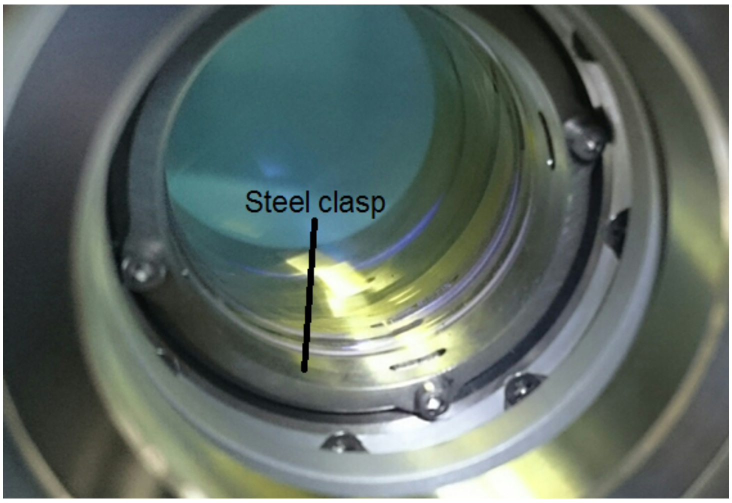

Figure 117 – Risley prism architecture for production versions.

4.4.1 Encoder control

The Risley prism motor assembly includes rotational encoders that report the rotational position of the prism by means of a quadrature signal. The resolution of these encoders is critical to the spatial resolution that the prisms achieve to steer the beam across the substrate. Figure 118 details the layout of an experiment to directly measure the number of counts on the encoder signal for revolutions of the prism housing.

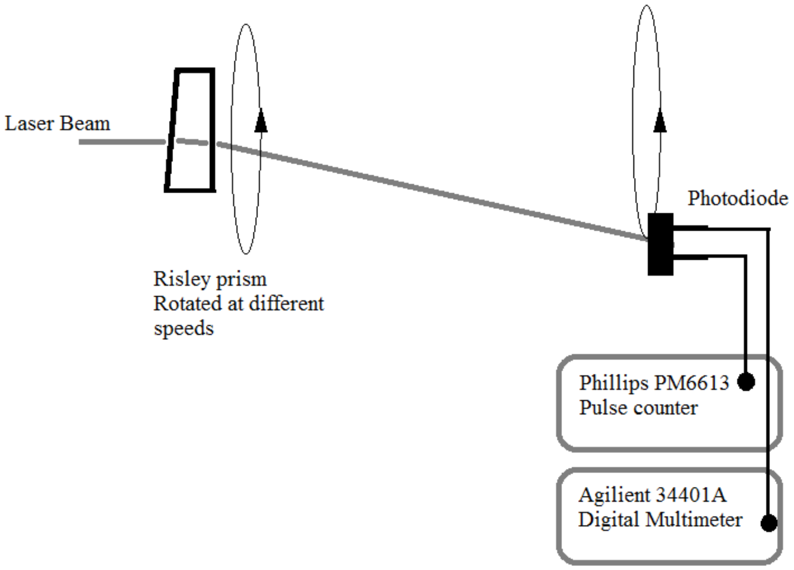

Figure 118 – Schematic of the Risley encoder experiment.

A single prism is rotated to translate a laser beam from a helium neon (He:Ne) laser in an circular path. Each time a revolution is completed the laser beam traverses across a small area photodiode, which provides a signal from which a pulse counter and digital multi-meter can be triggered. By setting the rotation speed of the Risley to different speeds, the frequency of the trigger signal and the pulse counts can be compared and the number of encoder counts per revolution be established. The results are shown in Table 6

Encoder frequency (Hz)	Revolution Frequency (Hz)	Count
68435	6.683	10240.16
102654	10.024	10240.82
136872	13.366	10240.31
171090	16.707	10240.61
205307	20.049	10240.26
239524	23.391	10240.00

Table 6 – Encoder measurements.

In all cases the number of counts recorded was 10240 counts per revolution on a single encoder output. As the encoder is a quadrature encoder the encoder positional accuracy was 40960 counts per revolution. Hence the rotational accuracy of the Risley prism motor was 0.009º and this was in exact agreement with the reported accuracy on the RP25S datasheet.

4.4.2 Latency tests

The latency of a system is described in this report as the time delay between the command sent to a system to change state and the actual completion of the system to change to that state. The latency of each component of the control system has an impact upon the temporal resolution and also has the potential to create issues with the synchronisation of the system as a whole.

In the case of the Risley prism the definition of the latency is the time between the start of the electrical command to move the prism and the final physical completion of this move. An experiment to determine the command latency is devised where the first bit of the command signal to move the prism can be observed on a Tektronix TDS3054B oscilloscope and the physical movement is detected by monitoring the rotational encoder signal from the Risley prism. In addition to the set command, the Risley prism electronics also has a proprietary damping circuit to prevent overshoot and ringing. The Risley prism used is an RP25S unit supplied by Optra Inc.

Figure 119 shows a plot of the encoder position of the Risley prism when the prism is commanded to rotate through 90º, which is half the largest feasible physical movement required of the prism under normal operating conditions. The time axis is commenced from the time the first bit of the digital move command is sent and the time taken by the prism to get from its rest position to 90% completion of the move was approximately 100 ms.

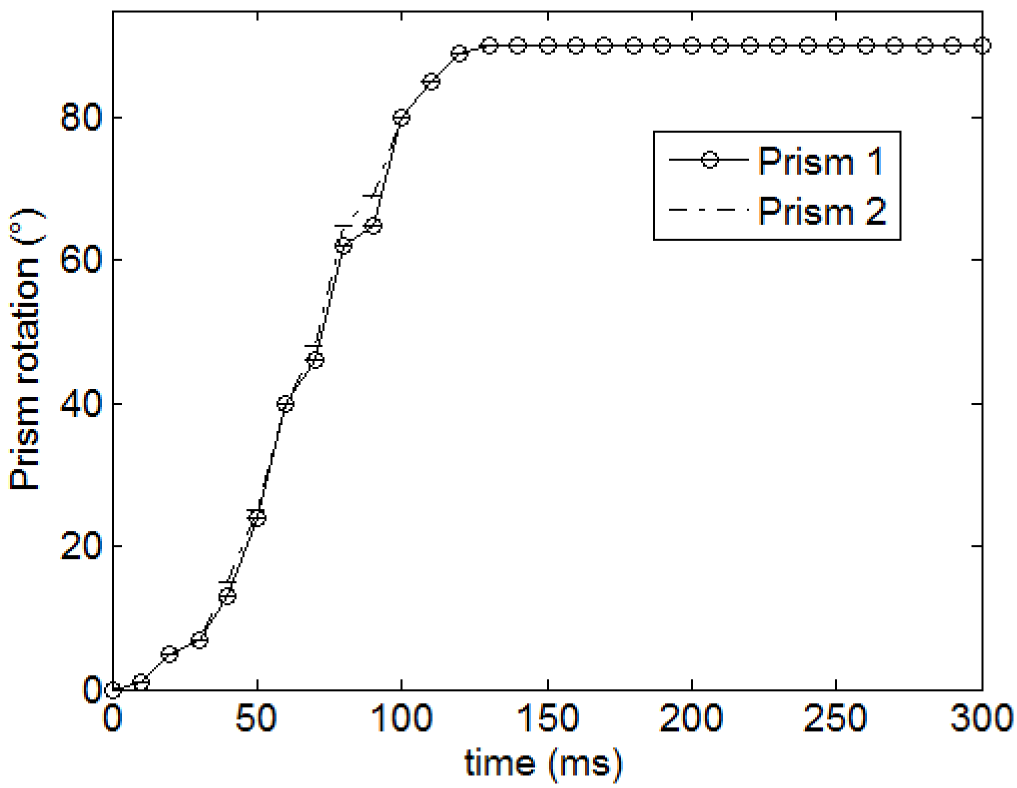

Figure 119 – Risley prism actuator latency for full 90° rotation.

Figure 120 shows a similar latency plot where the prism is commanded digitally to move 1º from its present position, in this case it took approximately 20 ms to reach its rest value.

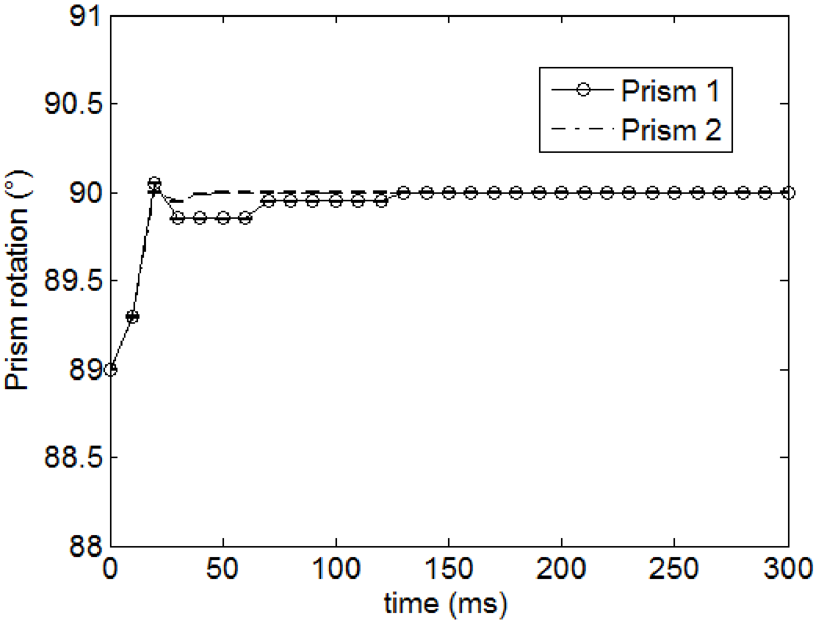

Figure 120 – Risley prism actuator latency for 1° rotation.

Finally Figure 121 shows the latency plot for the case where a 0.5º shift command was placed upon the Risley prisms. In this case it took the Risley prism 10 ms to reach 90 % of its rest value.

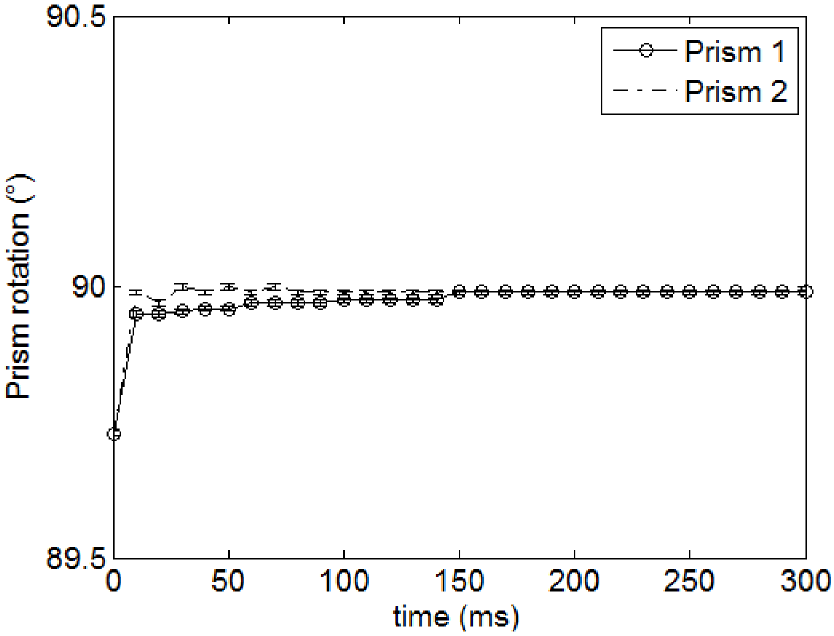

Figure 121 – Risley prism actuator latency for 0.25° rotation.

The conclusion of this section was that the rotary motor takes between 10 ms to 100 ms to settle to within 90 % of its rest value depending upon the amplitude of angular motion requested. At a substrate speed of 0.1 m/s, a reasonable estimate of latency value for all reasonable movements of the prism would be under 50 ms, this would give an X resolution of 5 mm at 0.1 m/s. It is possible to reduce the latency of the system by using steeper wedge prism angles, however this could lead to the possibility that the beam can be actuated to a degree that the beam is clipped inside the processing head and lead to internal damage, this is discussed in the optical design considerations later in this chapter.

4.4.3 Summary of Risley prism tests

Tests completed on the Risley prisms establish their transmission, rotational encoder resolution and their latency response to positional commands. The results of the tests show that the Risley prism has a rotational resolution of 0.009° and that the latency is variable depending on the amplitude of the movement. A 0° to 90° movement gives rise to a latency of 100 ms but the prism is more likely to experience an absolute maximum shift of -40° to 40° between blanks where this resolution is not required. Under normal operating conditions where the seam is being tracked continuously the prism movement will be small, <1°, this gives a figure for latency < 20 ms. In between substrates, where the largest deviations occur, the prism movement is likely to be a maximum of ±14° giving latency of 50 ms for a ±5 mm. Provided the distance between the camera and the first processing head is large enough a latency algorithm can be created that will move the head in advance of the seam before it reaches the processing area.

4.5 Optical design of the actuated processing heads

The optical layout architectures of the processing heads are presented in chapter 3 of this thesis and the addition of the Risley prism into their layouts is a direct iteration of those designs. In both cases the Risley prism is located in between the cylindrical beam shaping optics. In this section the application of the Risley prism actuator to alter the focused beam positon in Y is described, as applied to both the optical design architectures detailed in chapter 3.

4.5.1 Architecture 1 actuated processing heads

The Zemax modelling, test techniques and performance metrics of chapter 3 are applied in exactly the same manner with the addition of repeating the measurement for each across the field of motion of the beam. Additional parameters measured were the translation of the beam relative to the angular setting on the Risley prism encoder and the transmission of the processing head over the full range of motion. Care is taken that the heads were designed to have high transmission from input to the substrate through all foreseeable ranges of motion, even under control failure of prisms. This is not only to ensure that there is no damage to the processing head but also to make sure the laser beam is contained within the housing for reasons of operational safety.

The collimator and relay sections also contain lens housings that have user adjustable Z positions. This also permits changes to the focal positions in the XZ and YZ axes, hence the ability to correct the astigmatism of the system, which arises as a result of using cylindrical lenses to split the X and Y axes. Figure 122 and Figure 123 show the implementation of the Risley prism within architecture 1. In this architecture the Risley prism is steering the beam in the YZ axis as the beam is brought to a focus. This approach works but is a departure from the usual beam steering performed on a collimated beam as described in Figure 114. The main penalty for using the approach is that the beam tends to blur, or suffer from coma as the beam reached larger deviation in the Y axis, but the processing head was designed to be within a range of motion that the irradiance profile didn't change appreciably.

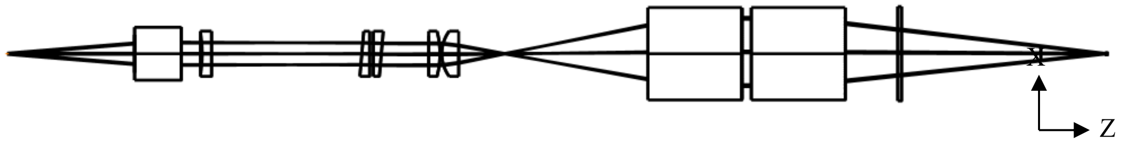

Figure 122 – Architecture 1 XZ plane detailing position of Risley prisms.

Figure 123 – Architecture 1 YZ plane detailing position of Risley prisms.

An important aspect of the optical design of the actuated processing heads is that the beam is confined under all conditions of operations including complete failure of the Risley prism control. Figure 124 and Figure 125 show the full range of actuation in the

YZ and XZ planes showing the full extent of the deviation of the beam paths though the processing heads and that the beam is fully transmitted to the focal plane through all range of motion.

Figure 124 – Architecture 1 YZ plane showing full range of actuation.

Figure 125 – Architecture 1 YZ plane showing full range of actuation.

Figure 126 shows the actuation range design based upon architecture 1 under the normal range of motion of ± 3 mm.

Figure 126 – Architecture 1 XZ plane showing normal range of actuation.

Figure 127 shows the modelled performance of the processing heads as the beam is translated via the rotation of the Risley prisms, the strong presence of off axis aberration, such as coma is evident in the shaped image of the fibre if the prisms are rotated beyond 20º, but this equates to a Y field position of ± 4 mm. The prism selection and placement of the Risley prism in the optical train is chosen so that the ±3 mm required range was achieved within ±14º of rotation.

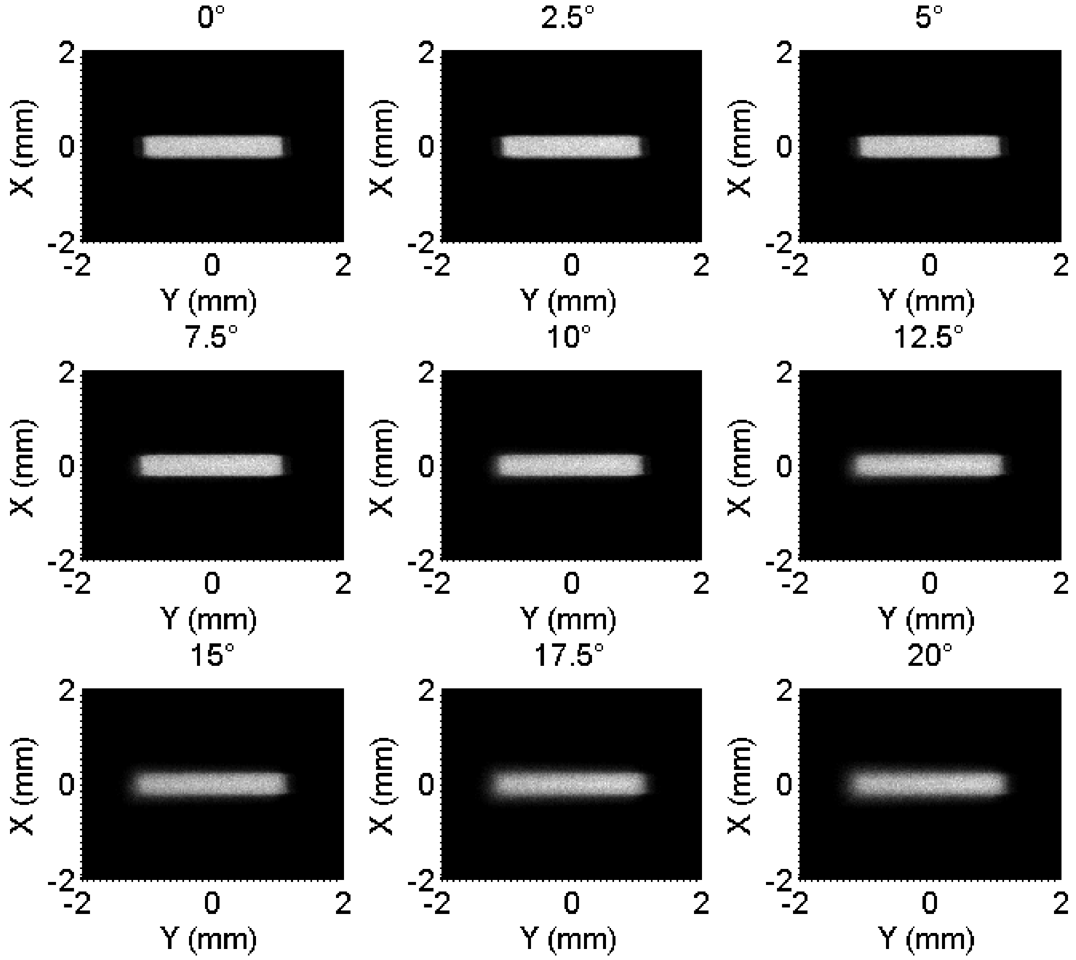

Figure 127 – Modelled irradiance profiles in the focus of the processing head vs angular rotation of the Risley prism for architecture 1.

The measured results for the architecture 1 processing heads are shown in Figure 128. As per the modelling predictions the irradiance profile is seen to degrade as the prism rotation exceeded 20º. The source of the defocus in Figure 127 is due to the curved focal plane with respect to the actuation and, at larger angles the presence of the off axis aberration coma.

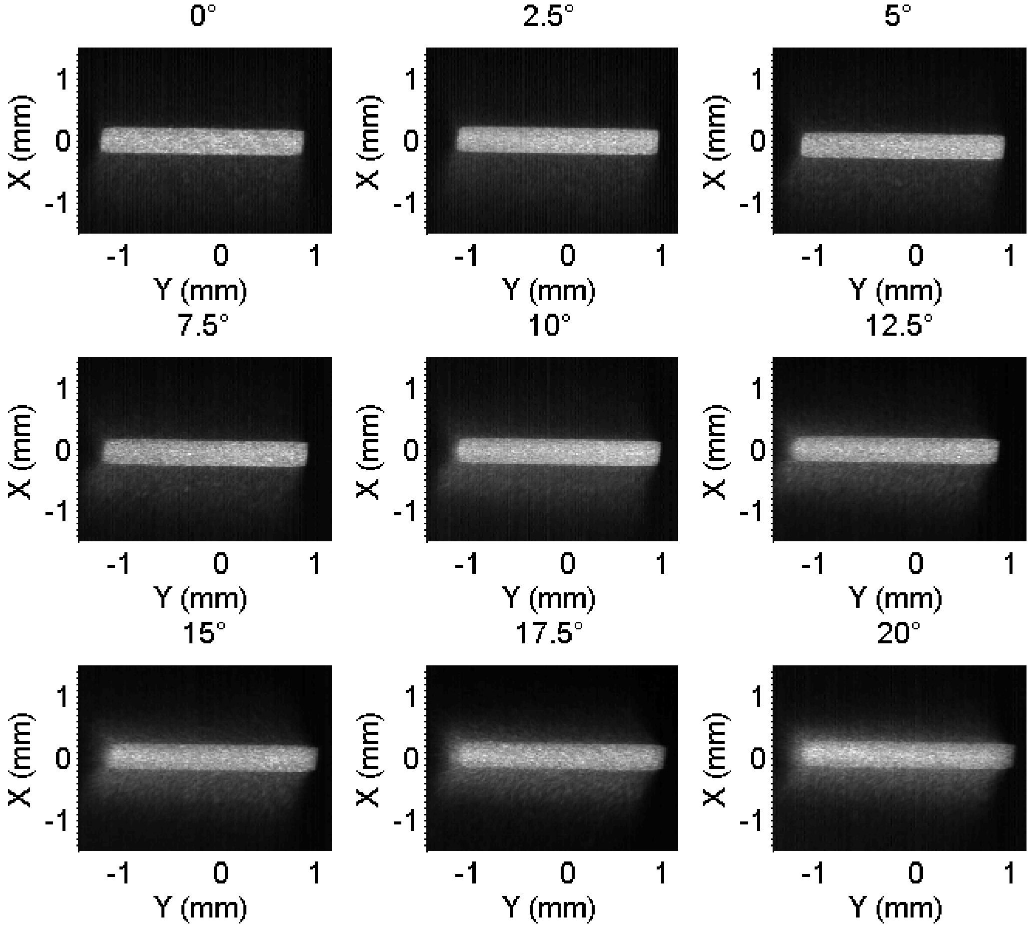

Figure 128 – Measured irradiance profiles in the focus of the processing head vs angular rotation of the Risley prism for architecture 1.

The transfer function of the translation of the irradiance profile in millimetres against rotation in degrees is shown in Figure 129. If the prisms keep rotating beyond the ± 90º range the position of the irradiance pattern would start to return to the central Y position reaching zero at 180º as the Y position is a sin function with angle. The region of the curve marked as the working region is the approximately linear section where the processing head was used and the gradient of this region gives the linear transfer characteristic in mm/º and this is used to control the position of the prisms during operation. The architecture 1 processing heads have transfer functions of 0.2 mm/º ±0.05 mm/º, yielding a spatial resolution of 1.8 µm/º.

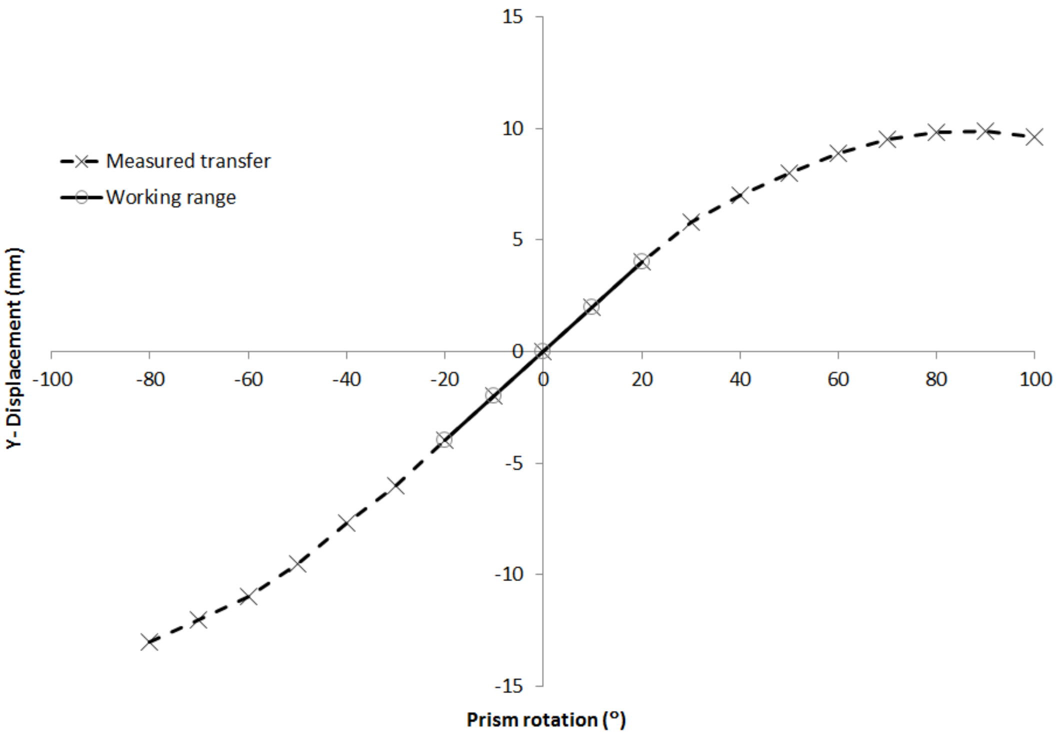

Figure 129 – Transfer characteristic of the Risley rotation angle vs the positional displacement of the spot in the Y position ~0.2mm/º showing the linear range where is was used (±15º).

The transmission of the processing heads for all angles is shown in Figure 130. The processing heads typically have a transmission of 95% which does not vary with prism angle indicating that there was no clipping of apertures within the processing head.

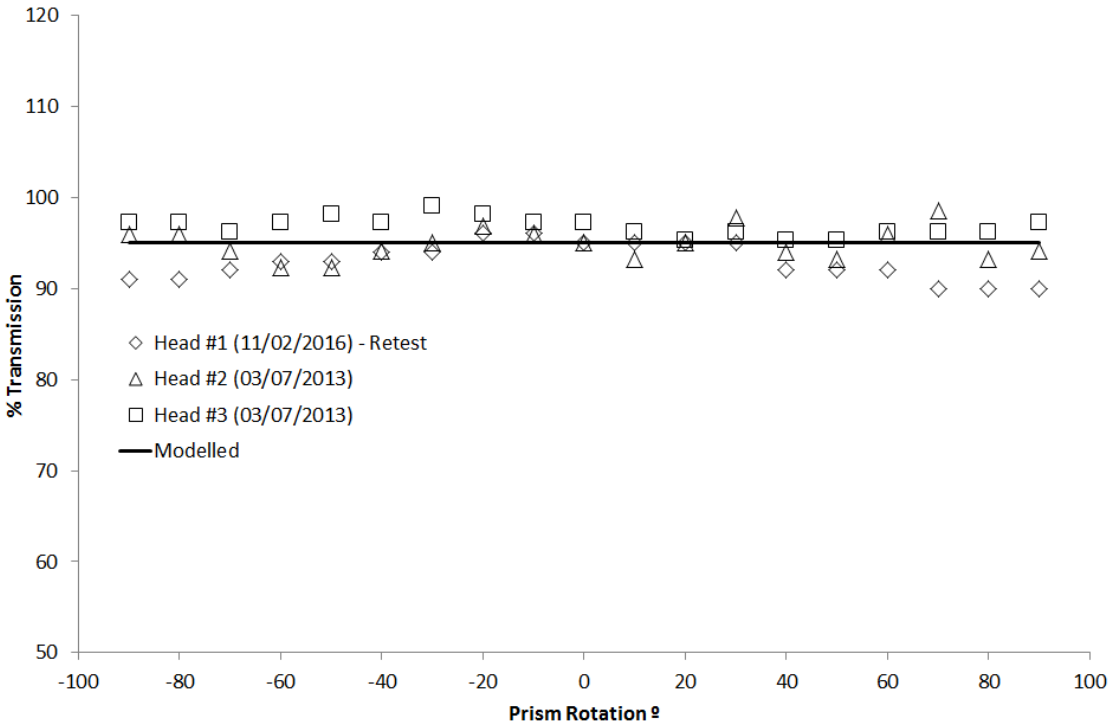

Figure 130 – Transmission against Risley prism angle over the full ranges of rotation for architecture 1. The heads were designed so they always transmitted power even under Risley failure condition.

The change in the FWHM of the irradiance profile in the Y dimension is detailed in Figure 131. The profile is seen to vary less than ± 2.5% over the working actuation range of ± 15º

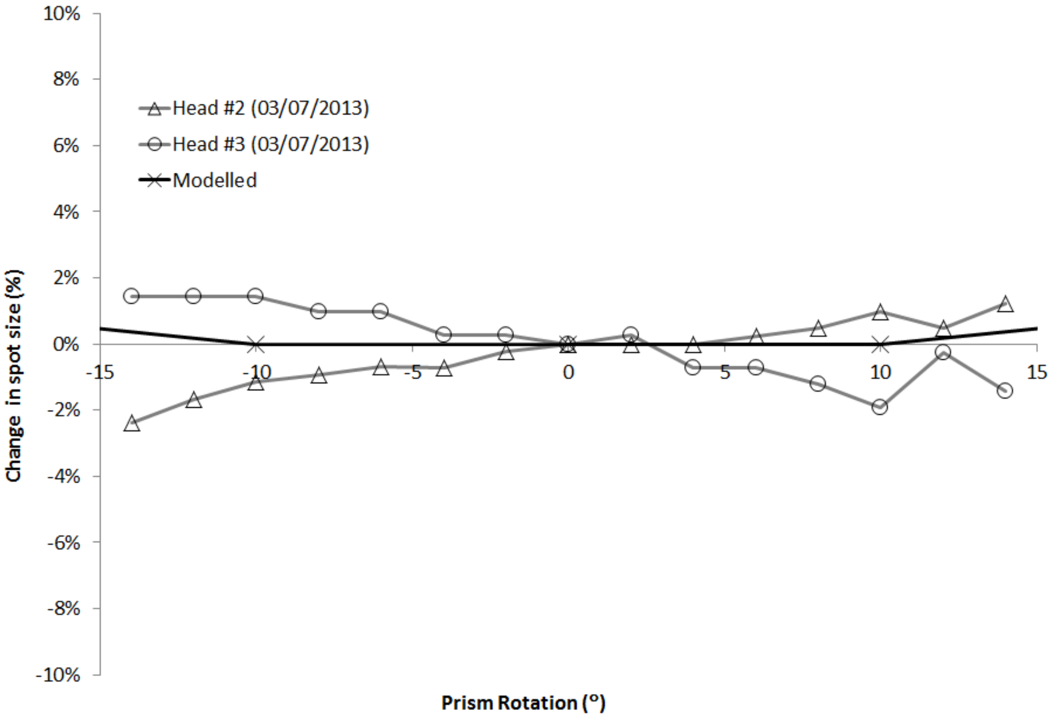

Figure 131 – Percentage change in FWHM of the Y spot size for architecture 1 processing heads.

The change in the FWHM of the irradiance profile in the X dimension is detailed in Figure 131. The profile is seen to vary less than ± 4% over the working actuation range of ± 15º. There is an indication of a difference between the two tested processing heads for both axes, which is believed to be due to slight mechanical alignment differences between the cylindrical lenses.

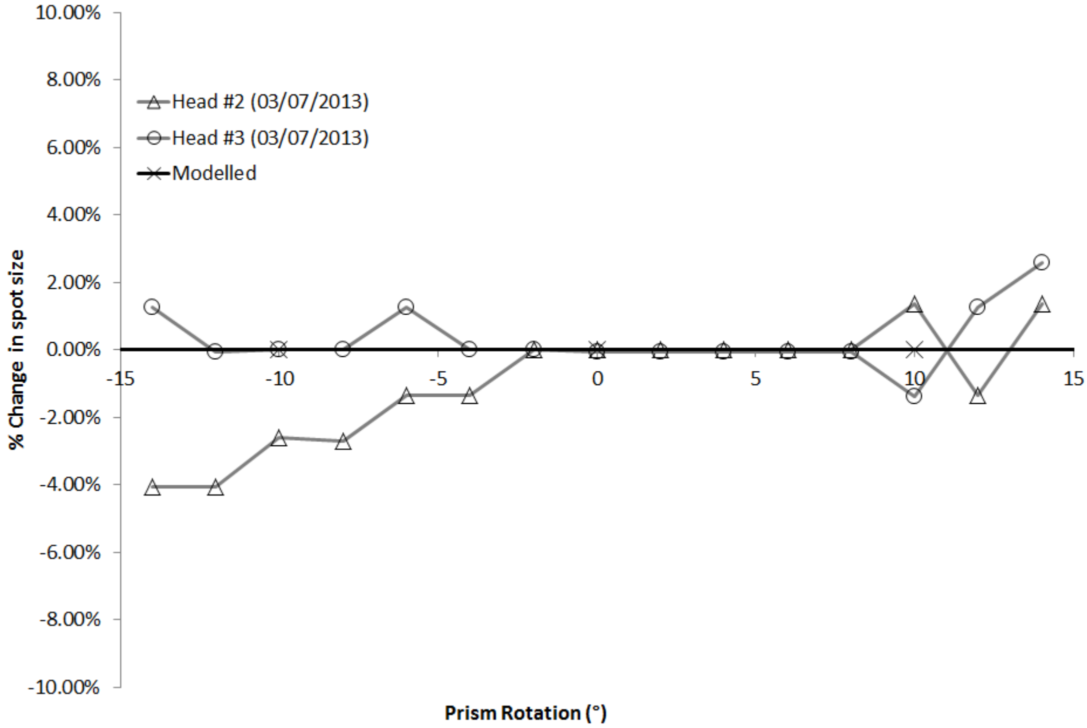

Figure 132 – Percentage change in FWHM of the X spot size for architecture 1 processing heads.

The measured homogeneity figures are shown in Figure 133 for two tested processing heads, the homogeneity is well within the accepted target value for homogeneity .

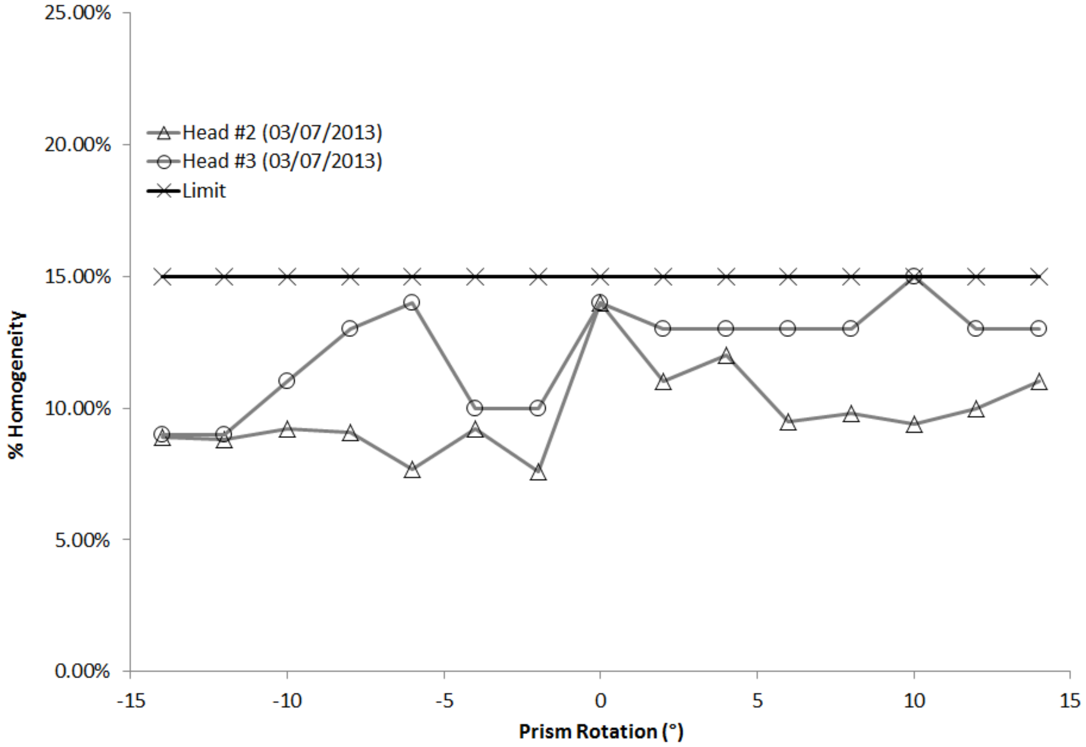

Figure 133 – Change in homogeneity over the actuation range of the architecture 1 processing head.

The edge width is observed to increase, as predicted, as the angle increased due to off axis aberrations. There is also a shift in the focal positions in Z of the beam as the beam is translated across the field of view as the lenses were not arranged in a telecentric configuration. The edge width however was less than 100 μm over the practical range of the device only increasing to unacceptable levels when the beam was out of the working range.

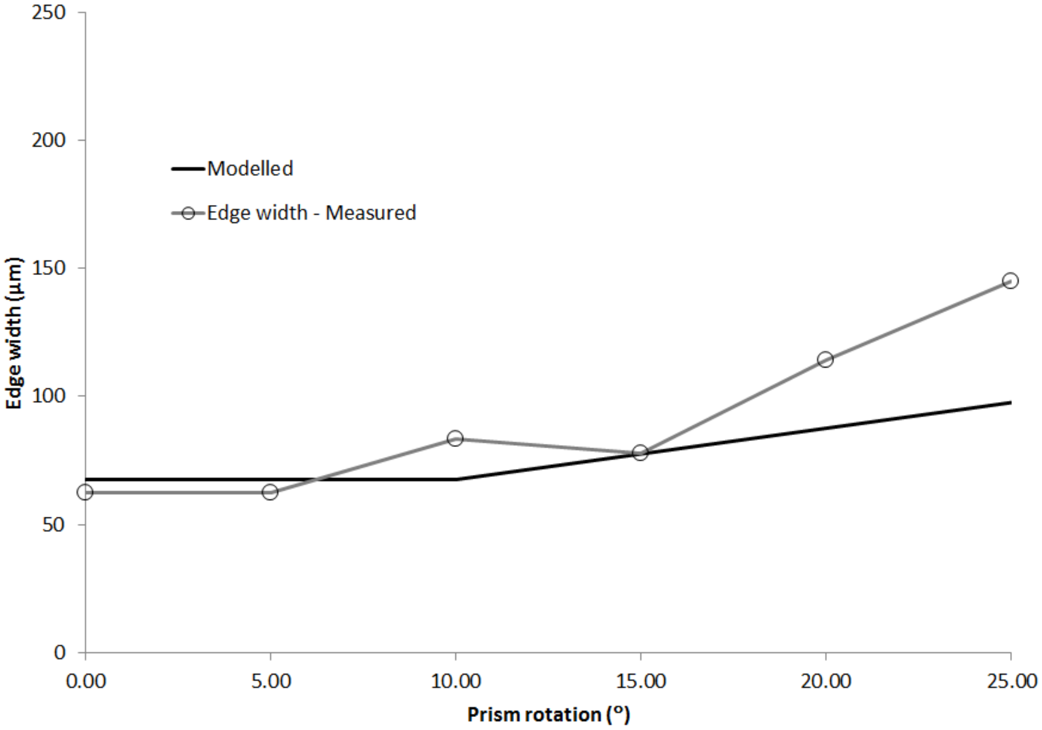

Figure 134 – A comparison of modelled and measured edge width.

The processing head based upon architecture 1 has irradiance profiles that varied less than 2.5 % in the Y dimension and 4 % in the X dimension. The transfer characteristic was 0.2 mm/° and transmission does not vary for all values of the prism rotation.

4.5.2 Architecture 2 actuated processing heads

The implementation of the architecture 2 processing heads is subtly different from the architecture 1. Because the Y axis is collimated after the fibre by a cylindrical lens instead of a spherical lens, as in architecture 1, the beam in the Y axis is collimated as it passes through the Risley prism and the beam is divergent in the X axis as it passes through the prism. As the actuation of the beam is exclusively in the Y axis, this means the actuation of the beam, in Y, is as depicted in Figure 114. This means the integrity of the irradiance pattern is more robust against the rotation of the prisms and less likely to encounter off axis aberration or curvature of the focal plane as it is collimated in the Y axis when actuated.

Figure 135 and Figure 136 show the position of the Risley prism within the optical train of the architecture 2 processing heads.

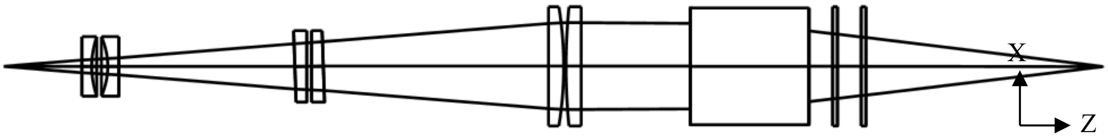

Figure 135 – Architecture 2 XZ plane showing position of Risley Prisms

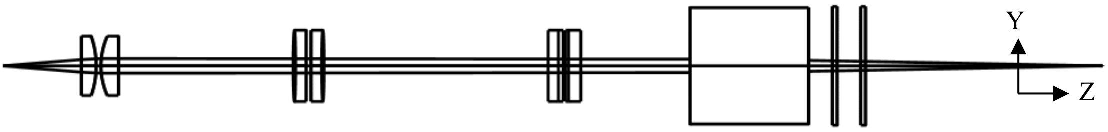

Figure 136 – Architecture 2 YZ plane showing central position.

The full range of actuation in the Y axis is shown in Figure 137 and Figure 138 for a Risley prism pair with a wedge angle of 2º. In contrast to the beam layout for the full range of architecture 1, as per Figure 124, the beam trajectory is observed to be almost telecentric, this permits a much wider ±14 mm usable range of actuation.

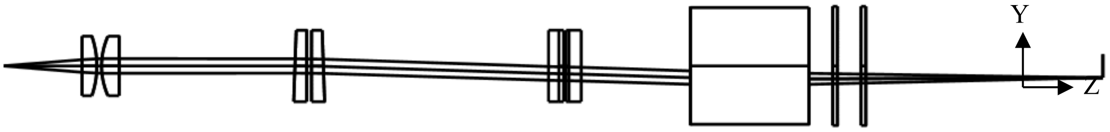

Figure 137 – Architecture 2 YZ plane showing full range of actuation

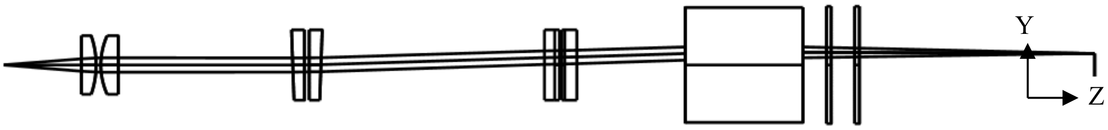

Figure 138 – Architecture 2 YZ plane showing full range of actuation.

Another advantage of this design is that the beam is fully collimated after the final set of cylindrical lenses. This permits deflections in the optical train, either with mirrors or with a deflecting prism as shown in Figure 139 that did not distort the beam at the focus. The advantage of this design freedom is that the processing head can be designed to fit in volumes with even tighter space constraints, without the need to lose the functionality of the actuator. An implementation of this is shown in Figure 139 and Figure 140, where the beam path has been deviated by a turning prism.

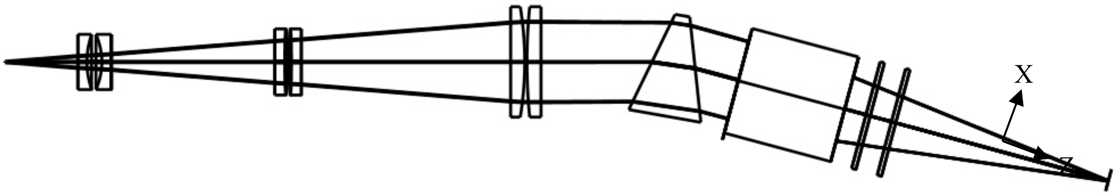

Figure 139 – Architecture 2 XZ plane with Risley and beam steering prism to fit an awkward shape.

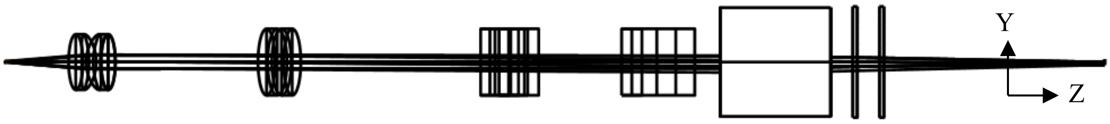

Figure 140 – Architecture 2 YZ plane with Risley and beam steering prism to fit an awkward shape.

Figure 141 shows the modelled irradiance profiles for the architecture 2 processing heads over the full actuation range of the Risley prisms. For this architecture the irradiance profile is observed to alter very little in appearance as the prism rotation is altered.

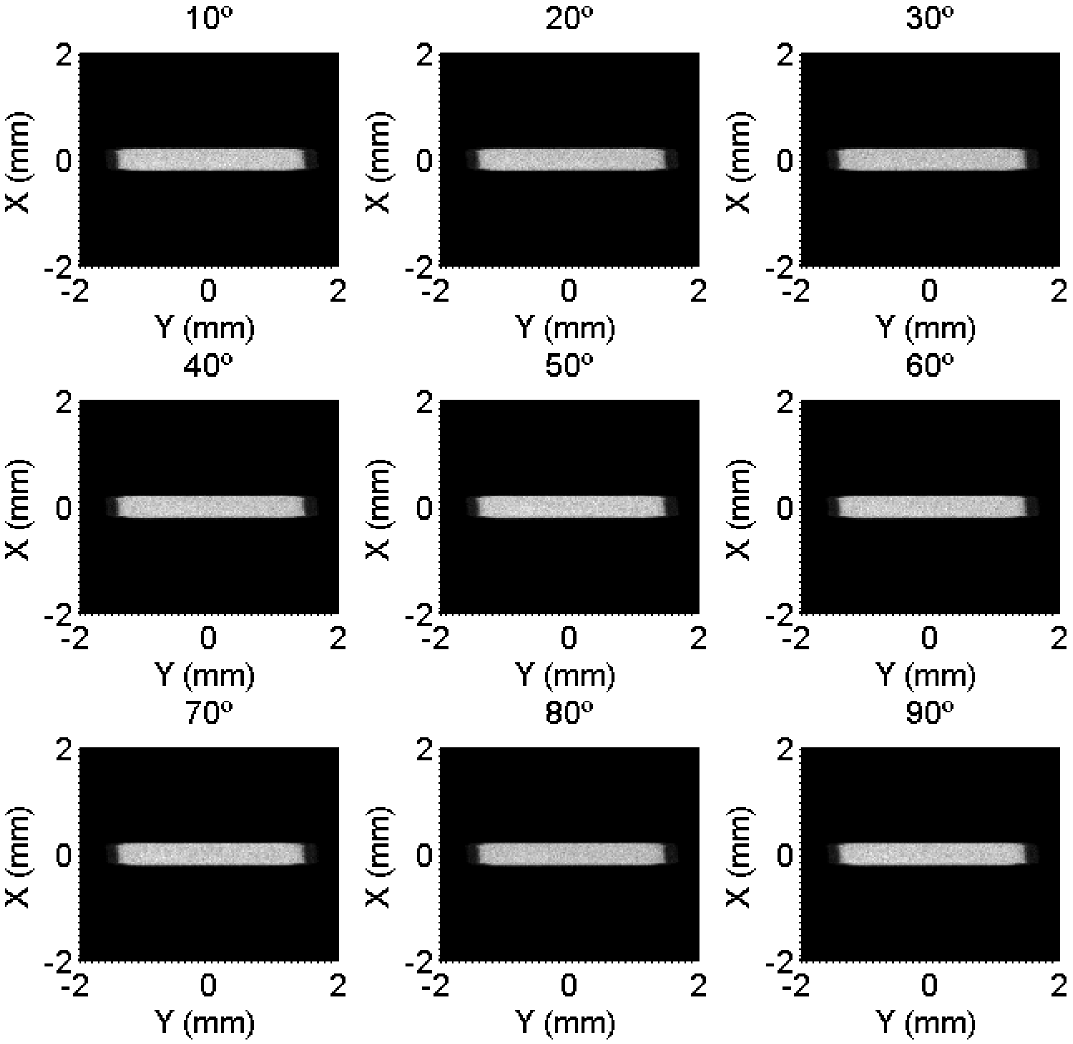

Figure 141 – Modelled spot shape vs angular rotation of the Risley prism for architecture 2.

Figure 142 shows the measured irradiance profiles for comparison, again little change is evident in the profile as the prism is rotated confirming the modelled predictions.

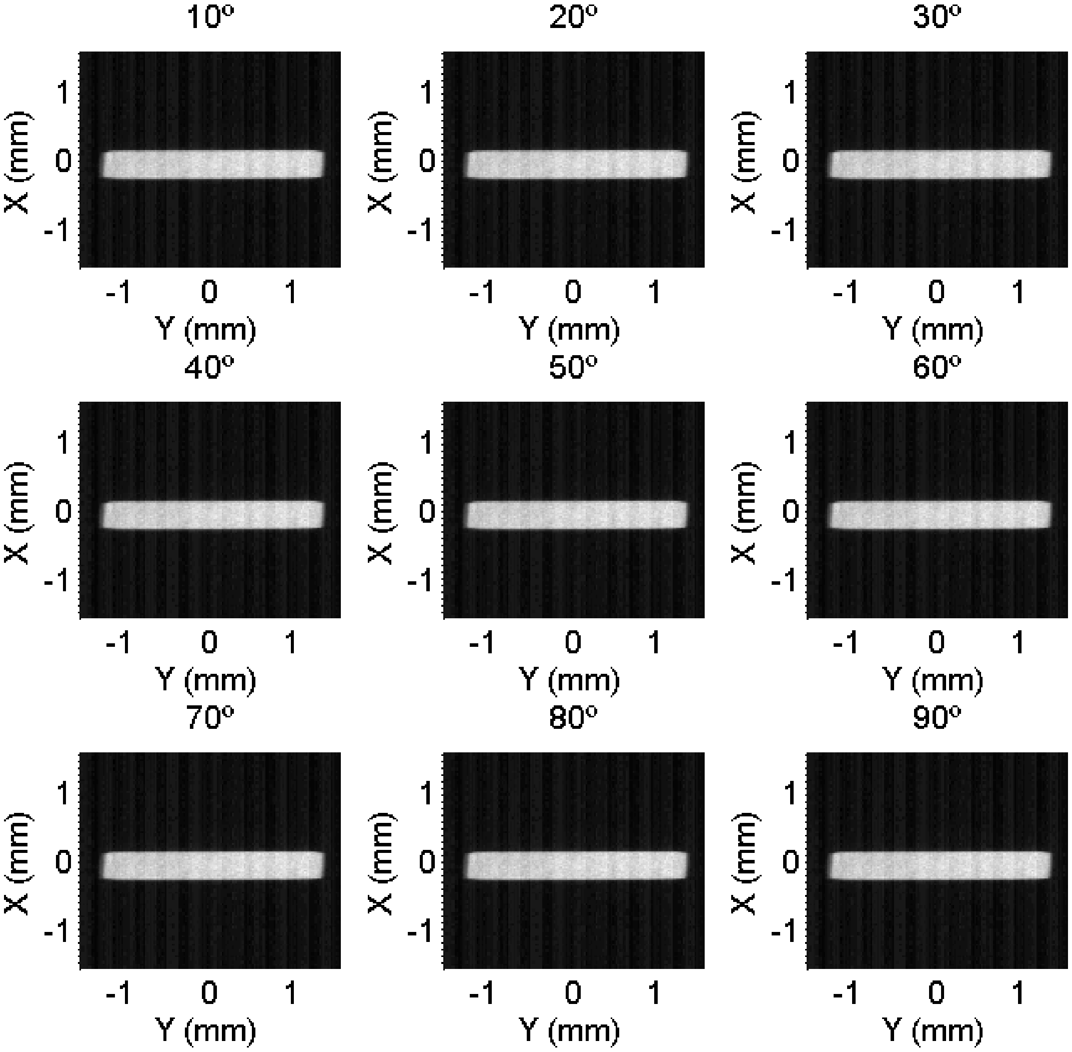

Figure 142 – Measured spot shape vs angular rotation of the Risley prism for architecture 2.

The transfer function for the architecture 2 processing heads between the angle of the prisms and the Y displacement in mm is shown in Figure 143. In the working range of the prism the linear transfer coefficient was 0.083 mm/° at a resolution of 0.7μm/°, considerably smaller than the architecture 1 designs.

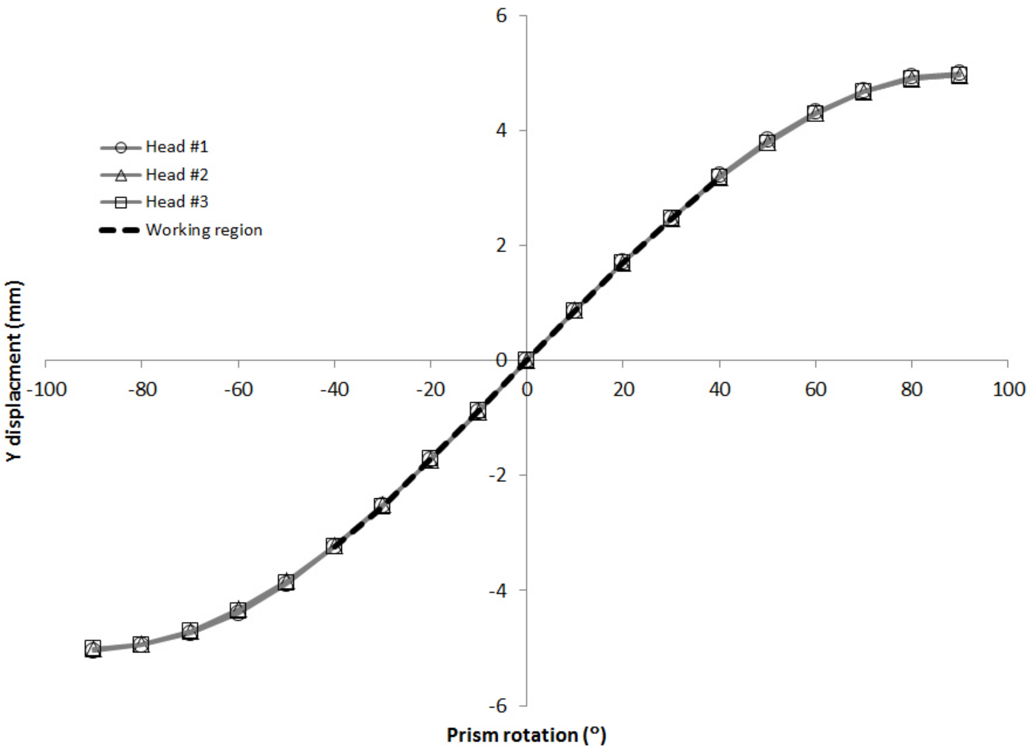

Figure 143 – Transfer characteristic of the Risley rotation angle vs the positional displacement of the spot in the Y position ~0.083 mm/º and showing the linear range where is was used (±40º).

The transmission of the processing heads is also greater than 95 % over the full actuation range of the prisms as shown in Figure 144, the majority of the loss being reflections from the coatings on the lenses.

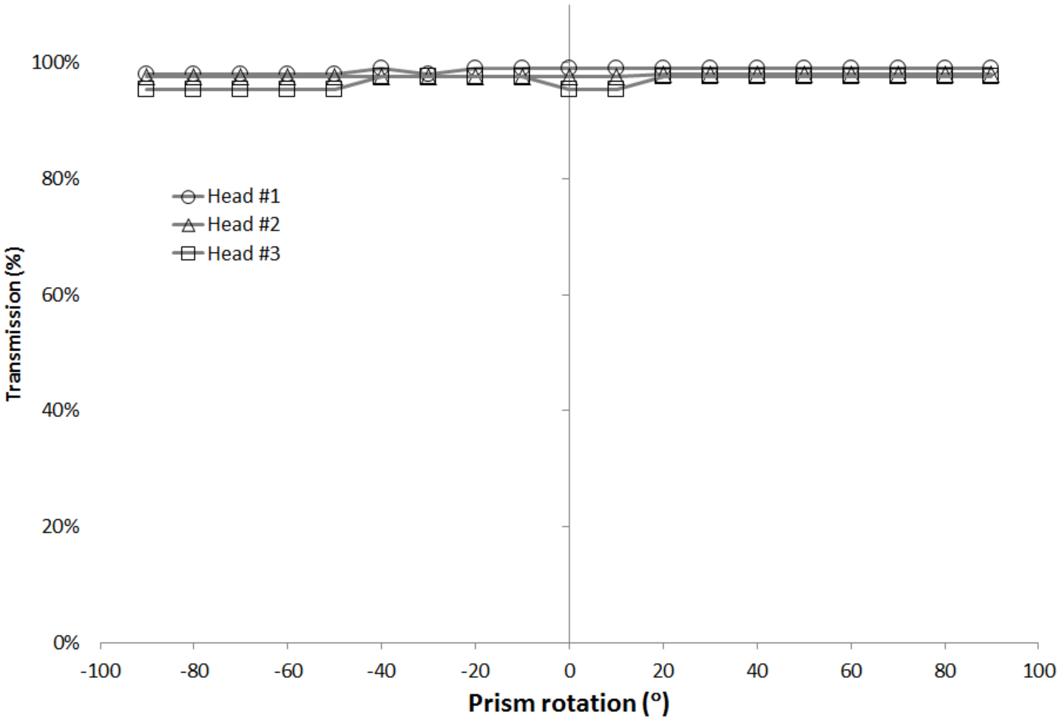

Figure 144 – Transmission against Risley prism angle over the full ranges of rotation for architecture 1. The heads were designed so they always transmitted power even if the Risley failed at an extreme position.

A comparison of the change in the spot size in the Y axis is shown in Figure 145, there is less than 2 % change in the irradiance width in the Y dimension also so confirming the improved actuated performance over the architecture 1 processing heads.

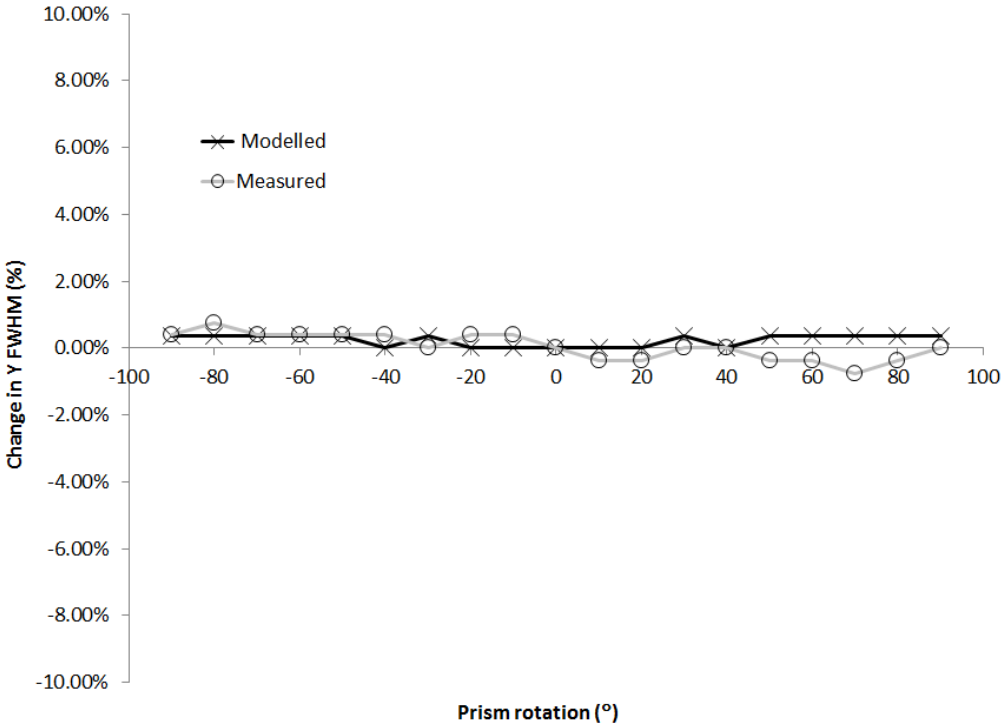

Figure 145 – A comparison of modelled and measured percentage change in Y spot size over full range of actuation.

A comparison of the change in the spot size in the X axis is shown in Figure 146, there is less than 2 % change in the irradiance width in the X dimension.

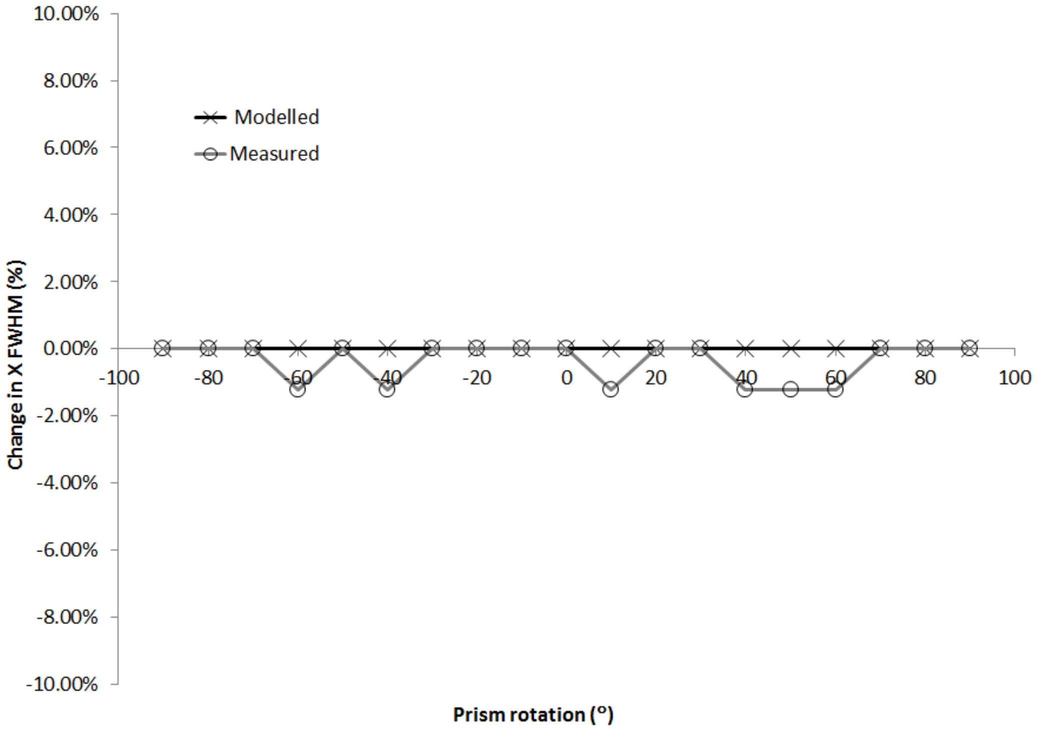

Figure 146 – A comparison of modelled and measured percentage change in X spot size over full range of actuation.

The change in homogeneity is shown in Figure 147, this is well below the limit of 15 % required by the customer and remains relatively unchanged over the actuation range.

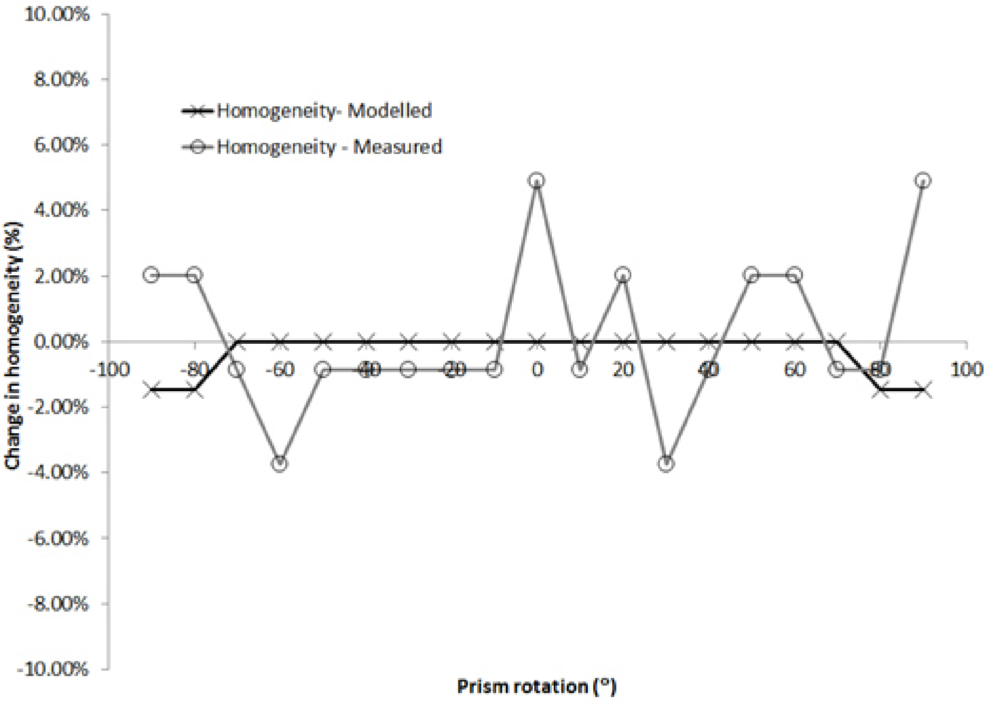

Figure 147 – A comparison of modelled and measured change in homogeneity spot size over full range of actuation.

The edge width measure is also well below the limit of 160 µm over the entire actuation range as shown in Figure 148.

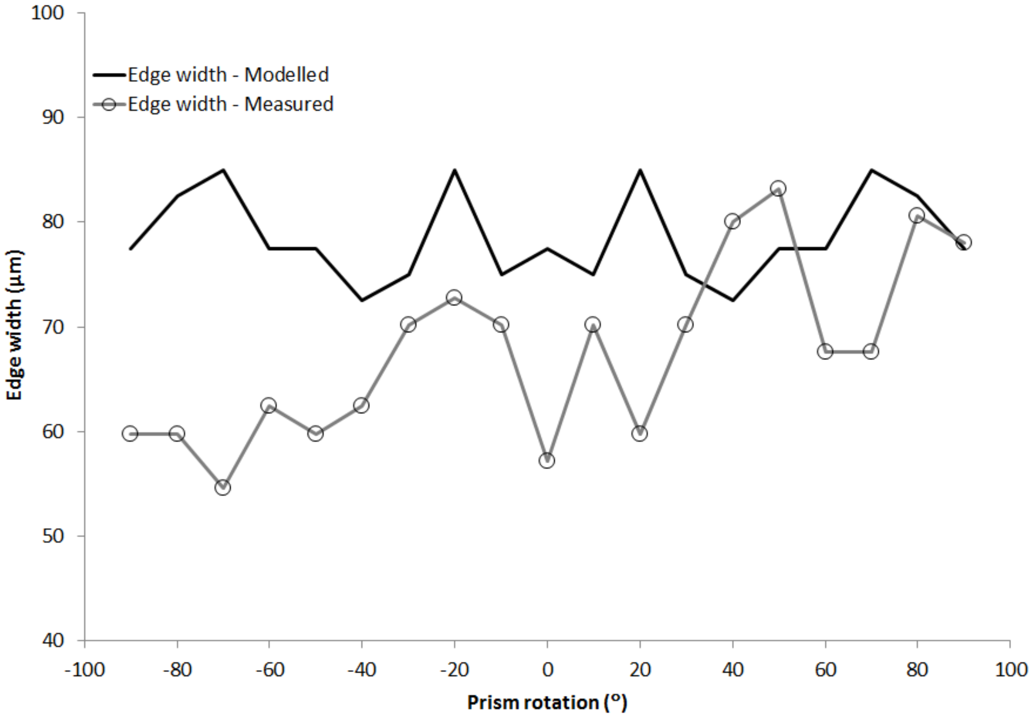

Figure 148 – Comparison of modelled and measured edge width over full range of actuation.

4.5.3 *Summary of the actuated processing heads*

Two separate implementations of a compact inline Risley actuator are presented for use in steering a beam for tracking a seam between two substrates for surface removal. The technique enables the actuated use of the homogenised beam shaping techniques, as described in chapter 3 in very small space envelope. The beam characteristics are maintained over the useful actuation range and this technique opens up the possibility to actuate the Y position of the irradiance profile for a wide variety of design architectures.

4.5.4 *Conclusion of the actuated processing heads*

Processing heads with a Risley prism architecture 1 are capable of a ±3 mm actuation range with less than a 2.5 % change in Y irradiance profile width and 4% change in X irradiance profile width. Homogeneity and edge width are within specification limits of 15 % and 160 µm respectively. The transfer of prism rotation to translation of the irradiance profile in the Y dimension is 0.2 mm/° ± 0.05 mm/°. By comparing this with the 0.153 mrad resolution of the Risley prism encoder gives a theoretical accuracy in Y at the substrate of 1.75 µm, far beyond what is required. Actuated processing heads based upon architecture 2 are capable of a ±14 mm actuation range with less than a 2 % change in Y and X irradiance profile width. Homogeneity and edge width are well within specification limits of 15 % and 160 µm respectively over almost the entire range of motion. The transfer characteristic of prism rotation to translation of the irradiance profile in the Y dimension for the architecture 2 processing heads is 0.083 mm/º. By comparing this with the 0.153 mrad resolution of the Risley prism gives a theoretical accuracy in Y at the substrate of 0.8 µm again far beyond the resolution required for this application.

4.6 Powerlase bespoke electronics

The next component in the system train is the control electronics, which are bespoke electronics designed to interpret all of the incoming telemetry data and then move the beam to the correct position on the substrate. The control electronics are linked to telemetry inputs namely, X encoder position from the shuttle that moves the substrates and the analogue voltage signal taken from the LPF. The control electronics calculate the correct position of the heads correcting for the positional displacement of the camera and the latency of the actuator. The control box also provides additional signal filtering to avoid any large deviations from the seam centre.

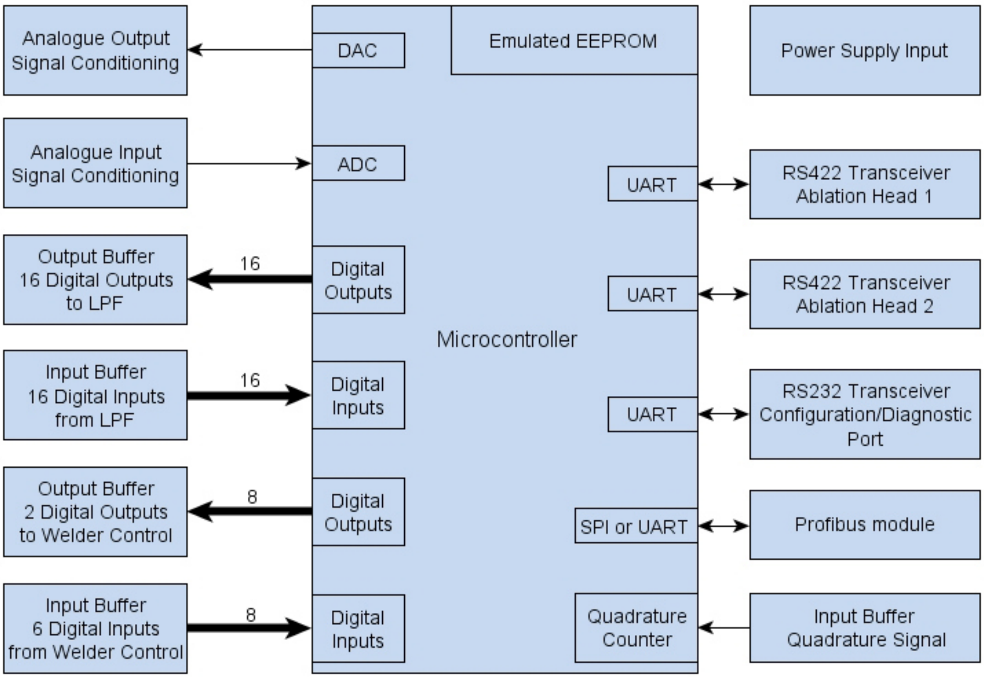

Figure 149 – System diagram of the PPL control electronics.

Figure 149 details the schematic functions of the control PCB, starting from the top left and working anti-clockwise each input and output is described; The analogue output was a 0 to 10 V feedback of the processed Y position which included the alterations to the signal from the averaging and sorting algorithms embedded within the firmware, the output was a 12bit digital to analogue (DAC) signal. The analogue input is a 12 bit analogue to digital convertor (ADC) which took in the unprocessed 0 V to 10 V voltage signal representing the Y position of the seam, from the LPF system. The input and output buffers are a series of 0 V-24 V digital signals that select and control the mode (discontinuity or multi-straights) of the LPF system and digitally select the various programs stored in the LPF system. These programs contain the specific settings for different products and consisted of 0-255 programs called by these digital signals. The incoming digital hardware lines were feedback signals to confirm the settings were received correctly by the LPF and fed back to the PPL control electronics. There are four universal asynchronous receiver / transmitter (UARTs). The first UART is reserved for a customer interface using a Profinet interface. The second UART is used for setting the data manager settings, error codes and alarm values, which are detailed later, via an RS232 protocol. The final two UARTs that use the RS422 communication protocols are the control lines, which send and receive commands to the Risley prisms control electronics. One UART is the upper head control and the other the lower head. The reason for this RS422 protocol is due to the extended length of the cable where RS232 is no longer feasible; a final reconversion back to RS232 is performed close to the processing head control PCBs as this was the standard control interface to the Risley control boards. The profibus UART can also be used to digitally output the seam telemetry in RS232 protocol, this RS232 output of telemetry was continuously monitored during the early commissioning phase of the project via a laptop running a Matlab script to monitor the seam tracker performance; this data is also time-stamped for correlation with events occurring on the production line. The telemetry data output consists of the X encoder position, the Y command signal of the PPL electronics, the Y position of the feedback from the Risley encoder and the timestamp. Finally a digital input line was to the encoder on the shuttle system which could interpret the X position of the seam and synchronise it with the Y position signal from the camera.

The microprocessor at the heart of the system is an advanced reduced instruction set (ARM) micro-processor; this is programmed via a JTAG with C software.

Figure 150 details the layout schematic of the PPL control electronics printed circuit (PCB) boards, the connectors are all numbered.

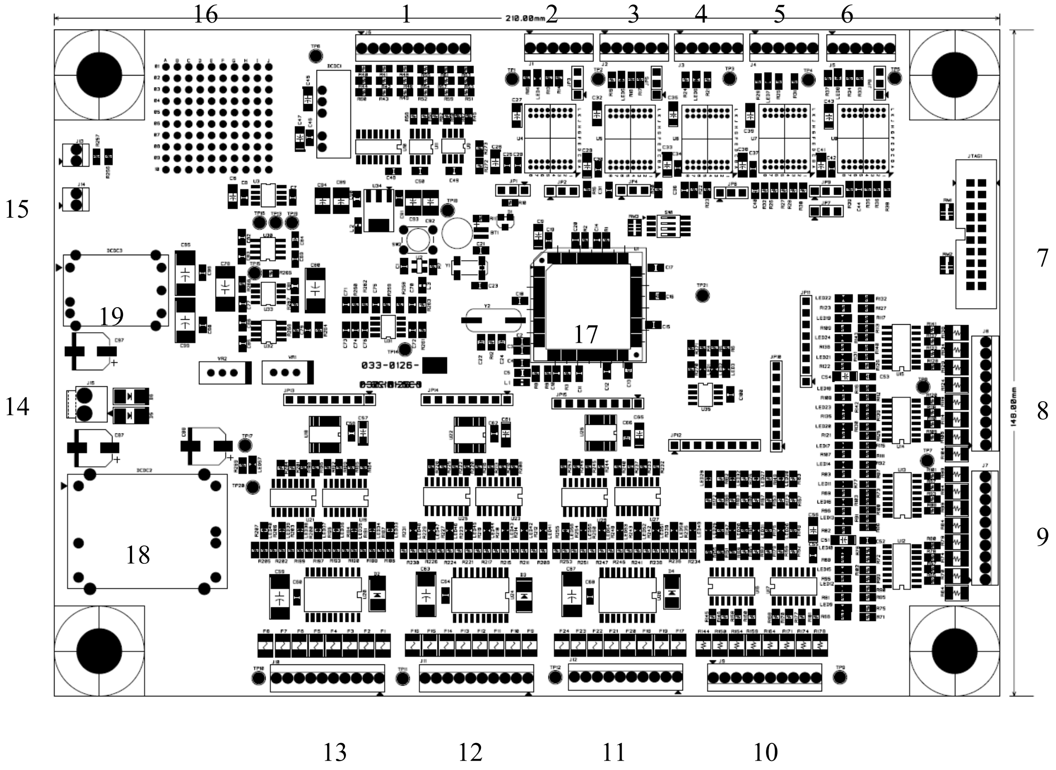

Figure 150 – Physical layout of the PCB board.

The positions of the interfaces, referencing Figure 149 are; 1 - X Encoder in, 2 –UART (RS422), 3- UART (RS422), 4 - UART (RS232), 5 – UART (RS232), 6 - UART (RS422), 7 - JTAG, 8 - Digital input, 9 -Digital input, 10- Digital input, 11 – Digital output, 12- Digital output, 13 – Digital output, 14 - VDDC Input power (24V), 15 - DAC output, 16 – ADC input, 16- Expansion board, 17 – ARM microprocessor,18 – 24V-5V convertor, 19 – 24V to 15V convertor.

All of the digital signals 8 – 13 in Figure 150 are protected with 30 V, 15 mA fuses, due to the sensitivity of the 24 V digital control and feedback lines they are also further protected by opto-couplers at both the PPL electronics box and the LPF system.

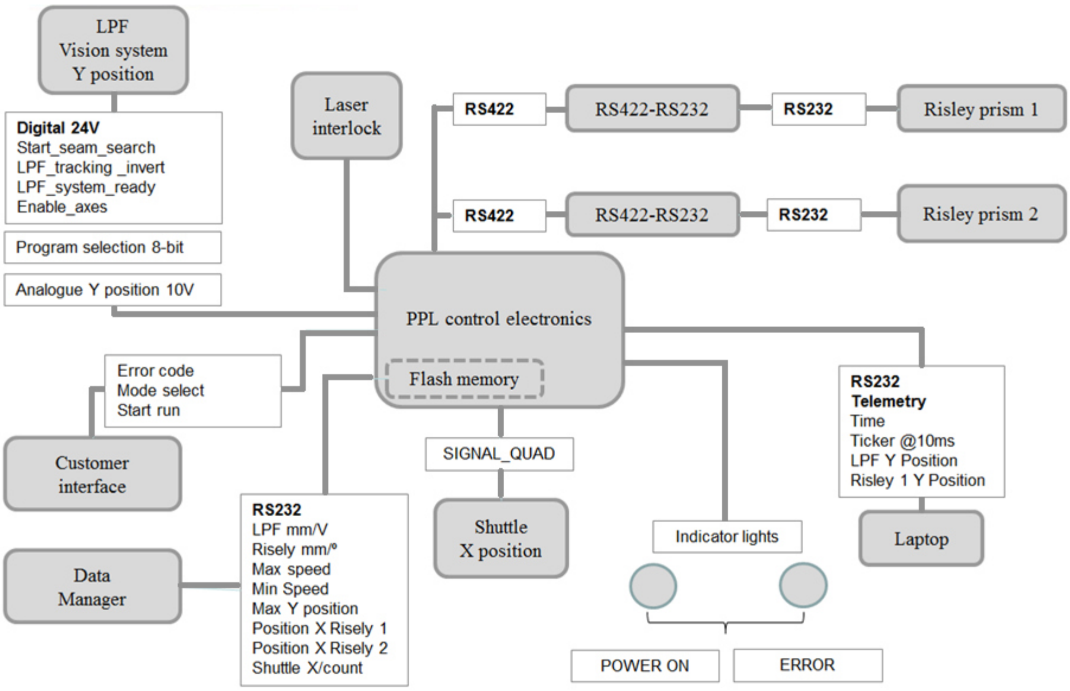

Figure 151 – Schematic of electrical connections.

The actual electrical significance of the connections from the board to the sub systems are given in more detail in Figure 151 again starting at the digital connections and working anti-clockwise these are; The digital 24 V signals for the LPF shown are signals given to the LPF system to indicate start of tracking and to set the orientation of the axes. The program selection is an 8 bit connection to select from 255 user created pre-sets on the LPF main system. The interlock is to rest the system and prevent unsafe operation of the laser on the camera, this is also of key importance as this re-sets the whole system during each run, once closed the system only has 60 seconds to start and locate a seam before a timeout occurs. The customer interface selection selects between one of three modes via a 2 bit digital commands. Mode 00 operates the seam tracker in isolation from the customer interface, mode 01 operates the seam tracker with feed-forward information via the RS232 profibus interface and mode 11 operates the camera positional feedback at full speed without moving the Risley prisms. The Risley prisms and their positional feedback is delivered via the RS422/RS232 connections, the X position of the substrate is delivered to the electronics via a quadrature encoded signal, two visual indicators are also added to the front of the control box panel to indicate power and error status. In the initial phases of the installation of the seam tracker product a laptop was connected to the control electronics in order to monitor the performance of the system.

An important part of the system is the data manager, it allows performance and calibration parameters to be set in-situ, this makes it possible to tune or calibrate specific parameters without physically disturbing the apparatus when the system is installed at the customer site. The data manager is addressed via an RS232 port. It was programmed and accessed using a command line text interface such as telnet or real-term. The settings for this connection are: baud rate = 38400, 8 data bits, Parity =none, stop bits =1 and flow control = none.

The protocol for delivering the command to memory is given in Figure 152 and some example commands are given in Table 7.

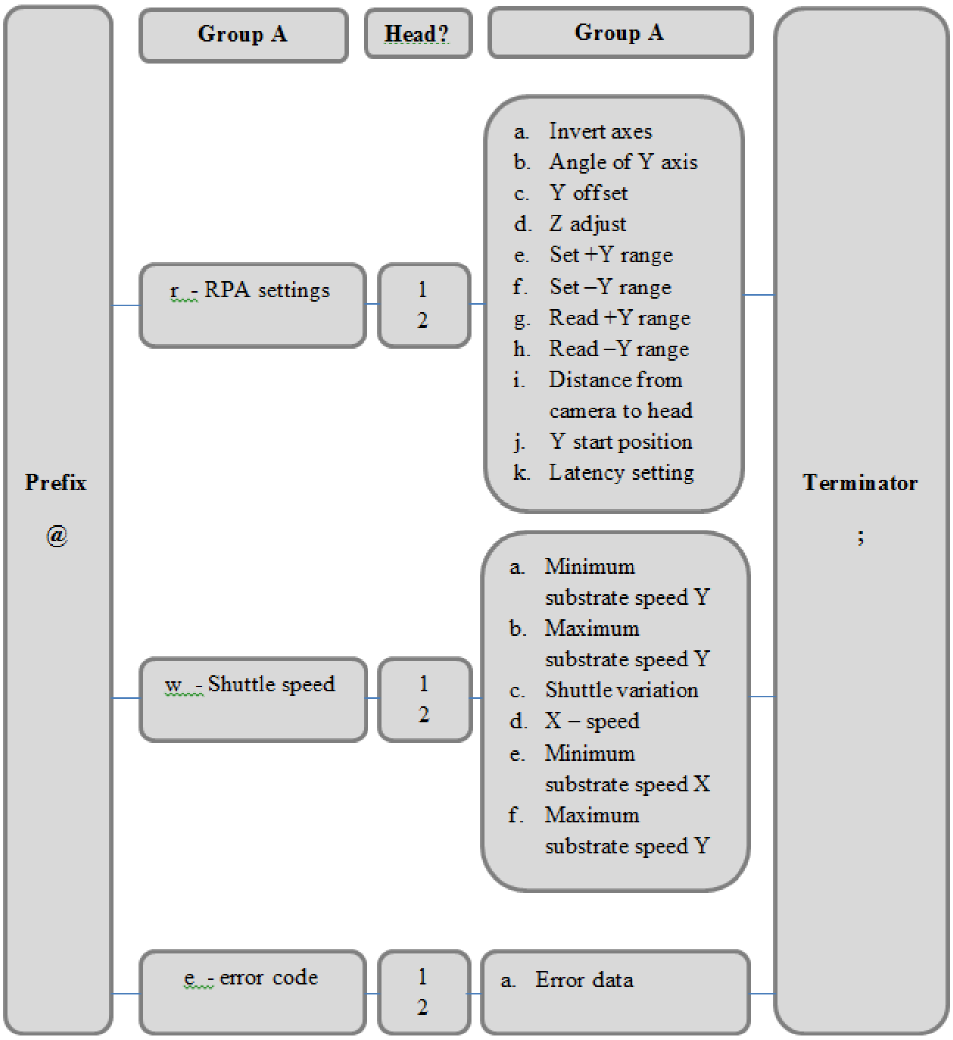

Figure 152 – Data manager protocol.

Command	Meaning
@e1a?;	What is the error?
@r2c:-090;	Set Y offset of processing head 2 to 90µm
@r1l:2200;	Set the µm/° of processing head 1 to 2200µm/°
@r2l?	Query what is the lower head µm/° set to?

Table 7 – Data manager example commands.

The conditions are saved to the memory permanently with a command of @SAVE;

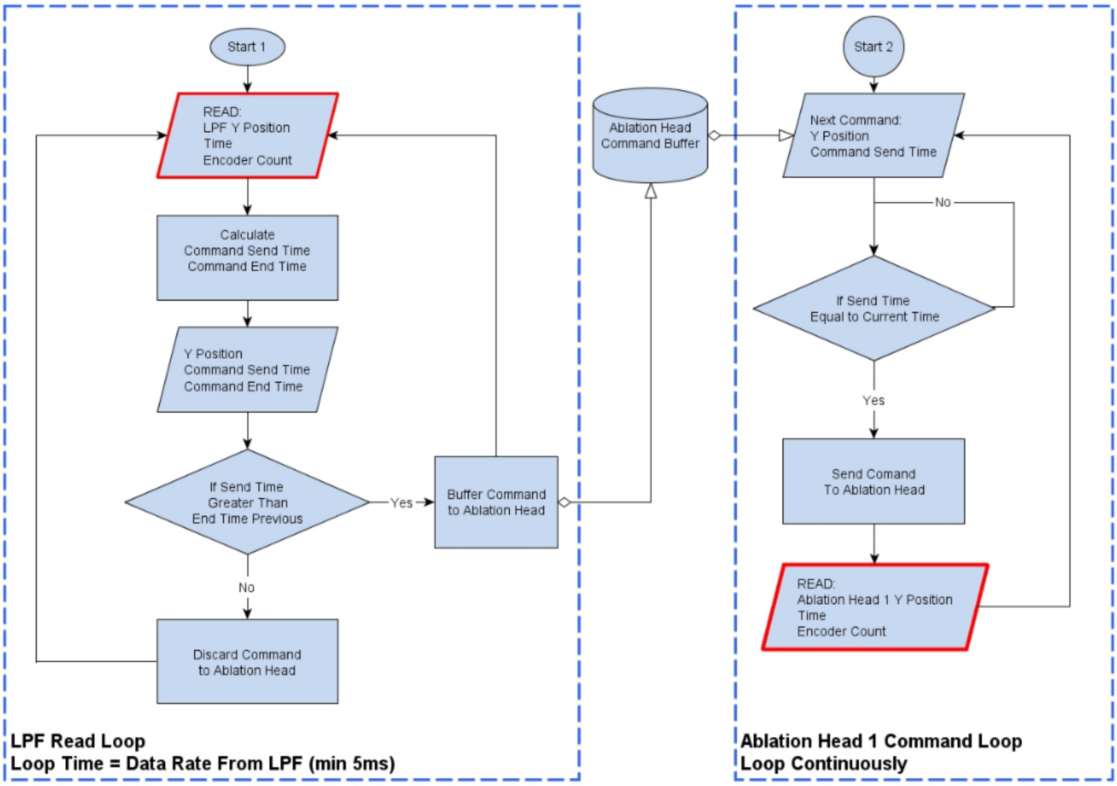

Figure 153 – Data flow diagram for the telemetry and control of the Risley prisms.

Figure 153 details the data flow from the electronics to the Risley prisms. Firstly the system reads the Y and X positions from the encoder at a given timestamp. This information is then processed for two events, the first event to be calculated is when the Risley prism should be moved calculated from the information received from the X encoder position and the distance to the processing heads as stored in the data manager, the second is the latency correction needed to be applied to the Y position, this establishes if the prism needs to be moved in advance of the substrates arrival under the processing head. Once the processing is completed, the correct command is sent to a timing buffer, at the correct X encoder interval these commands are delivered to the processing heads and the rotational encoder telemetry of the prism is returned to the electronics, checked against the send data and exported through the RS232 interface.

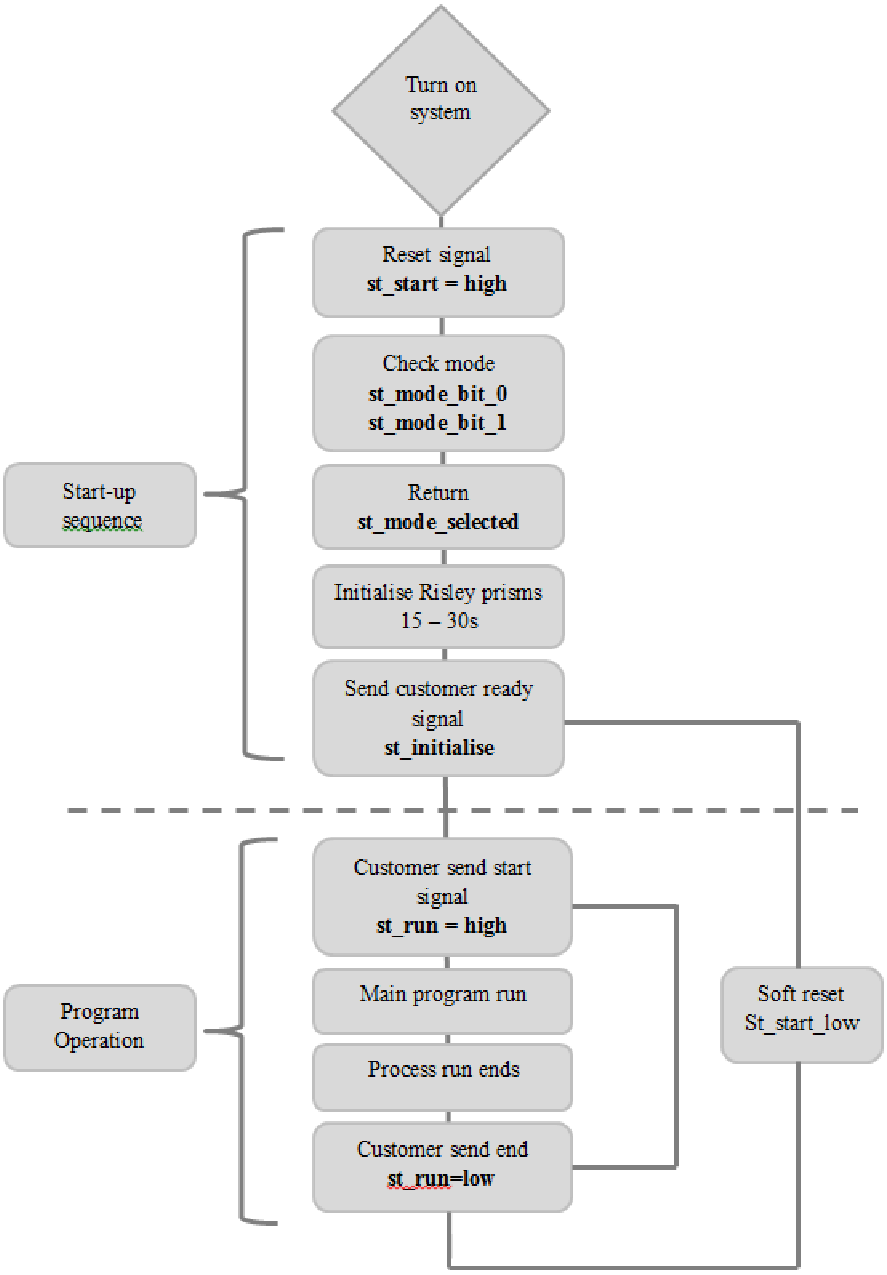

Figure 154 – Start up and run sequence for the seam tracker.

Figure 154 details the start-up sequence for the seam tracker. The first signal relates to the start / run sequence in Figure 151. Prompted by this signal the electronics then checks its mode status then sends the initialisation command to the Risley prism, during this initialisation period the Risley prism is rotated and the encoders read back for initial calibration and report any errors. If the initialisation concludes without errors the electronics then centre the Risley prisms onto their start positions as recorded in the data manager. After this is completed the control electronics sends a signal to the customers system that it is ready (st_initialise). The customer then starts the process by sending the st_run signal to the control electronics; this starts the tracking of both the LPF vision system and the control electronics. Additional production runs of substrates can then be processed by toggling the st_run signal between high (24 V) and low (0 V) without requiring a system reset. If a reset of the system is required this can be performed by toggling the st_start signal, this is without requiring a hard reset or powering off the system.

4.7 Software and firmware algorithms

The combining and synchronisation of the incoming telemetry, data settings and control signal is all performed by proprietary software loaded into the ARMcore processor. The software contains the algorithms that calculate the latency and also calculate a filtering system which eliminates any deviations from the incoming data that are caused by a loss of seam or erroneous readings as observed from the LPF vision system study.

The filter used is a binary filter applied to the data as it is read from the LPF analogue signal representing the Y position of the seam. The algorithm scans forward of the existing data point and takes the difference between the present reading and the five preceding readings. If the readings are all within a prescribed limit or behave in a monotonic manner the data would be accepted, if not then the data can be examined and eliminated and averaged to smooth the data in a manner similar to a Kalman algorithm [20].

An explanation of how the binary filter was implemented is shown in Figure 155, Figure 156 and Figure 157. These figures show different scenarios depicting how the binary filter detects discontinuities in the data and how it eliminates them. Figure 155 shows the scenario where the data is stable but with one error in the data received from the camera. The incoming data stream values are all similar except for one value, 5.0, this large deviation is detected by one of the binary tests resulting in a 1.

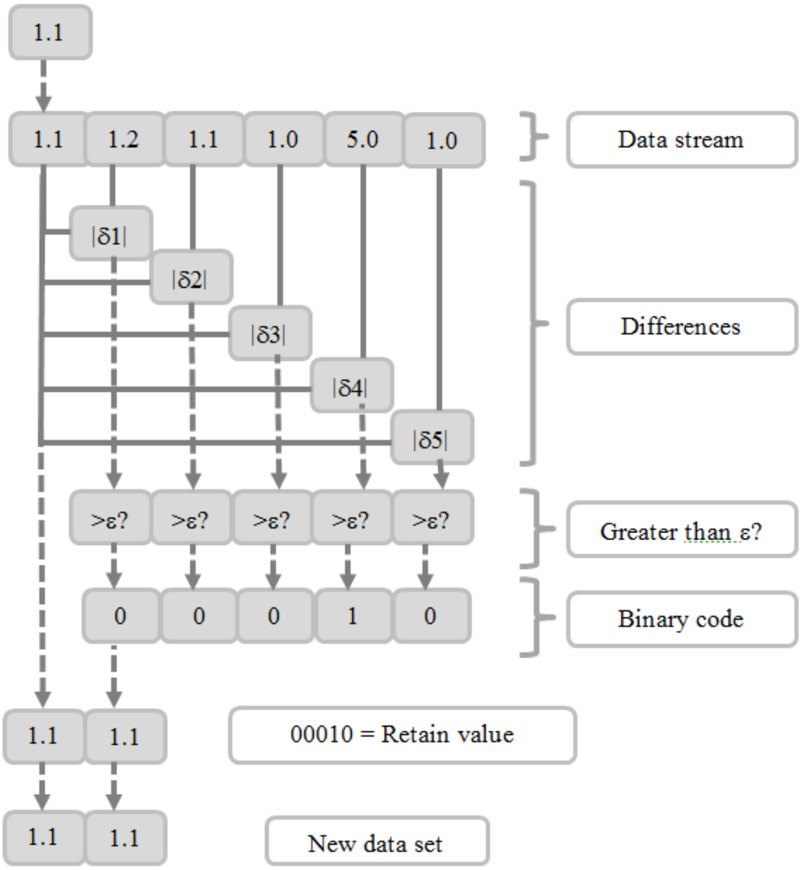

Figure 155 – Stable data with one erroneous signal.

As the data stream progresses through the buffer the binary coded signal changes until it becomes 1000, this is indicating that this signal is erroneous as no previous or following signal levels are comparable to this value. This value is ejected from the data set and replaced with the average of the previous two values as shown in Figure 156.

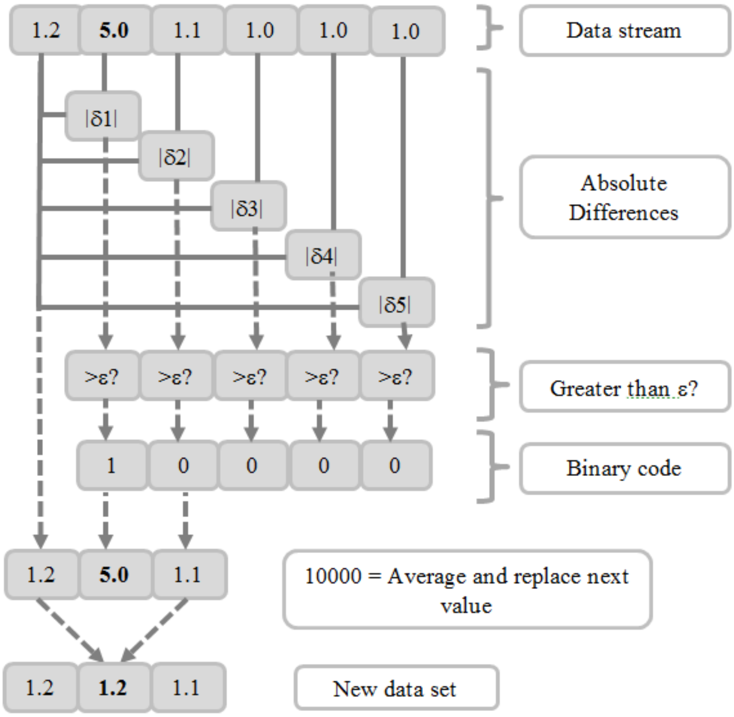

Figure 156 – Erroneous signal removed by filter.

The scenario shown in Figure 157 depicts when the data is genuinely increasing in a monotonic fashion, in this case every reading is larger than the next reading and the binary code generated by the filter is 11111, it is clear that this binary code should maintain the original signal values and so this case leaves the data unaltered.

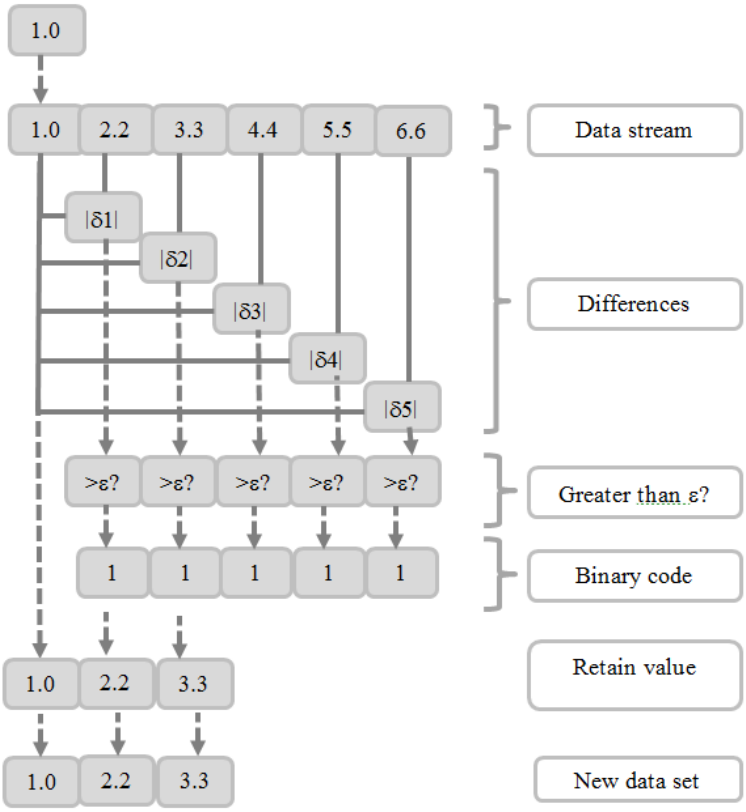

Figure 157 – monotonically increasing data.

The binary filter can be scanned through the data in real time, as shown in Figure 158 and different binary codes cases can be used to filter the data in different ways or to optimise the process.

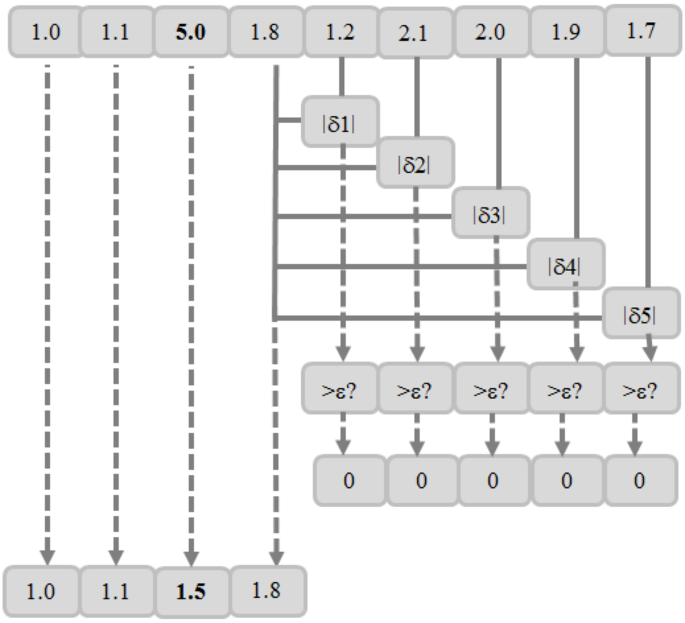

Figure 158 – Filter being scanned through data set and generating new filtered data.

This filtering technique is important as a large step in the data would inform the electronics that a step separation between two substrates had been detected, as per Figure 91 and the latency to move the prisms would be adjusted in X to move before the substrate was beneath the camera, in the case of a very noisy signal it could skip away from its position close to the centre of the seam. An example of the binary filter as applied to a noisy signal is shown in Figure 159 where a signal is corrupted by a series of noisy events simulating a loss of Y position signal.

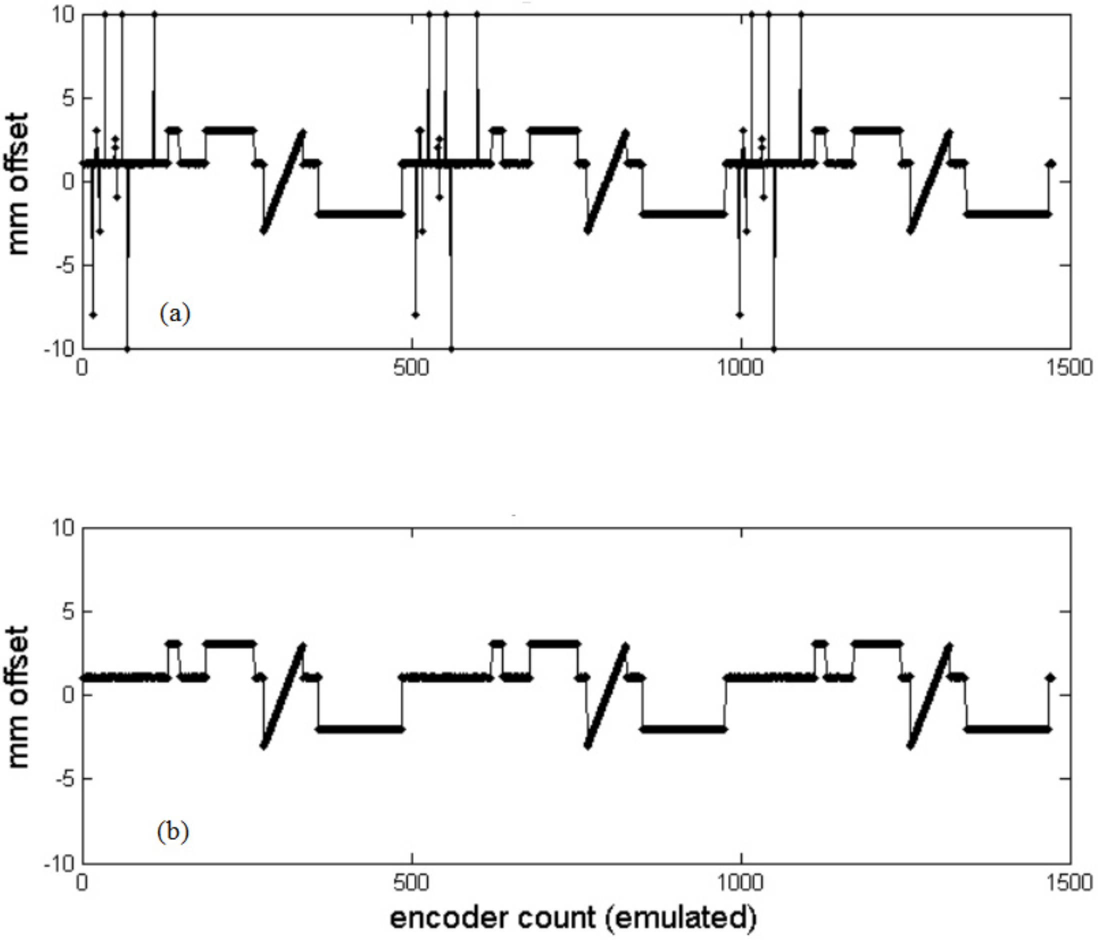

Figure 159 – Simulated application of binary filter to noisy signal (a) is the raw data, (b) is with the binary filter applied and ε = 0.9.

A noise free signal is recovered in Figure 159(b) maintaining the correct signal features by using the settings given as an example in the following cases.

$$Case(1\ 0\ 0\ 0\ 0) \quad : \quad data(i+1) = \frac{[data(i) + data(i+2)]}{2}$$

$$Case(1\ 1\ 0\ 0\ 0) \quad : \quad data(i+1) = \frac{[data(i) + data(i+3)]}{2}$$

$$Case(1\ 0\ 1\ 0\ 0) \quad : \quad data(i+1) = data(i)$$

$$Case(1\ 0\ 0\ 1\ 0) \quad : \quad data(i+1) = data(i)$$

$$Case(1\ 1\ 1\ 0\ 0) \quad : \quad data(i+1) = data(i)$$

If a large step in the data was generated by noise, then the latency algorithm would try to move the prism from the measured seam position in advance and move away from the seam causing a seam deviation in the removal trail. Hence the filter algorithm is applied before the latency algorithm as described in the next chapter.

4.7.1 Latency algorithm

The latency algorithm is required to resolve the scenario when the blanks were separated as per Figure 91(b). Given the latency findings of the Risley prism chapter, the latency of reaction to this motion could be a large as 100 ms, by which, given an example substrate speed of 0.1 m/s would mean the beam would only start moving 1 mm into the substrate. This is not an acceptable scenario and will spoil the substrate being marked. In order to eliminate this error a latency algorithm is constructed that reads ahead in the data and pre-orders a movement when a large step change is detected. This does not affect the scenario when the signal approaches the end of the substrate as the signal would stay on the particular last recorded value as the seam was lost and this known behaviour is known from the previous system study of the LPF.

An example of how the latency algorithm is implemented is shown in Figure 160, the streaming data of the X and filtered Y positions are subjected to a rolling algorithm that detects any sustained deviations in Y that are large enough to need correction for latency, the X encoder position of the deviation is then stored and the required shift in the X encoder position that is been calculated is applied to the Y data array. The algorithm is a rolling algorithm across the data and this approach is compatible with real time processing and avoids potential stitching errors in the data.

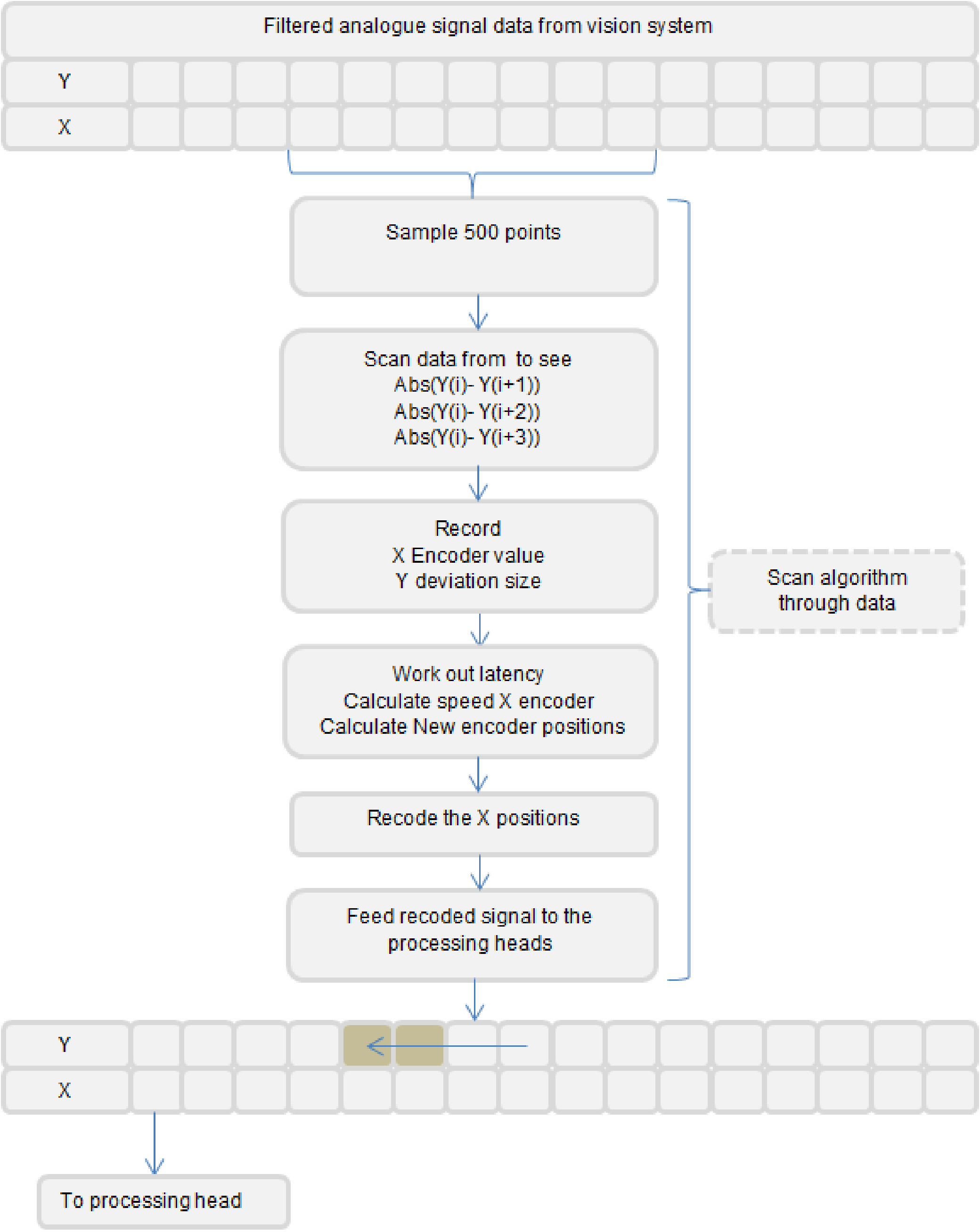

Figure 160 – An example of the latency algorithm.

Figure 161 shows a typical signal problem that the latency algorithm is required to solve, the dotted line is an uncorrected signal identical to the vision system, and the original vision system signal is artificially offset in Y by 0.2 mm to make it visible in the overlay.

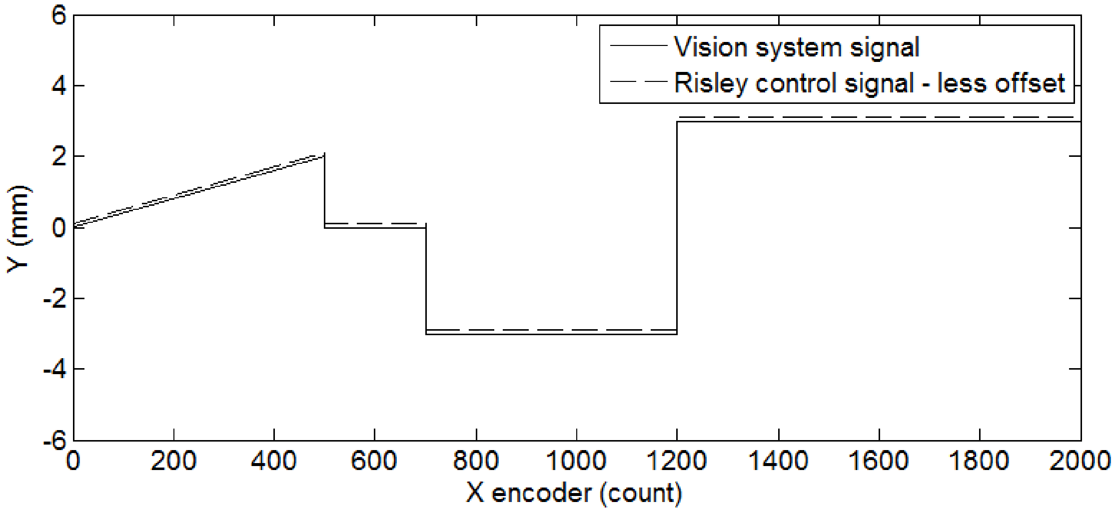

Figure 161 – Seam tracking signal before latency algorithm applied

Figure 162 shows the same input signal but with the latency algorithm described in Figure 160 applied to the Risley control signal. In this case the latency correction is a linear function of the deviation in Y and hence the latency correction in X is larger for increasing Y deviations. This can be observed as the comparatively large correction in X at the encoder value of 1200.

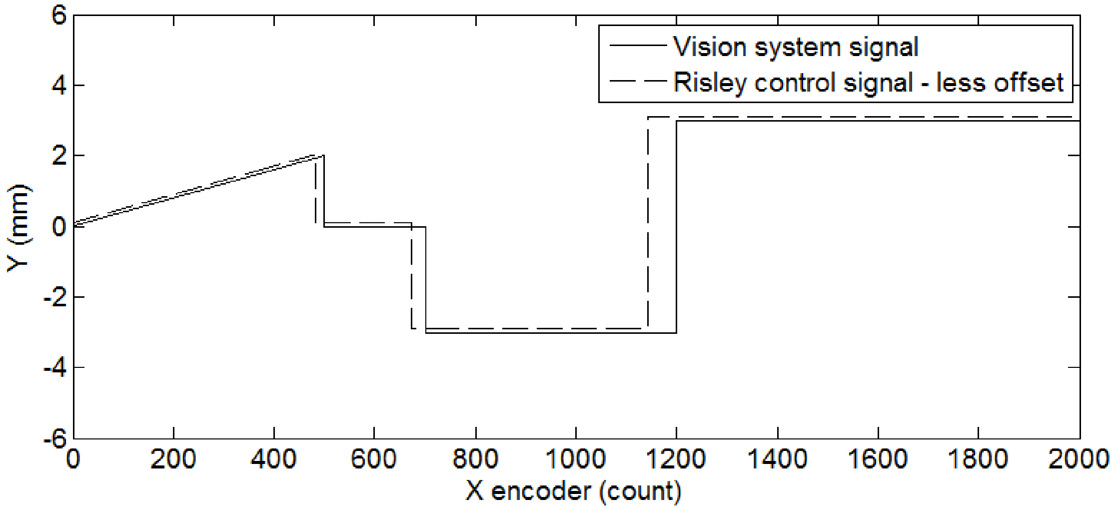

Figure 162 – After the latency algorithm has been applied.

4.7.2 Testing the latency algorithm

In order to practically test the latency algorithm a guide seam is created so the system would follow it. At the end of the guide seam another seam is created but with a 6 mm displacement from the guide seam, providing a direct test of the algorithm's ability to correct the latency and move in advance between two separate substrates. The practical results of this algorithm is shown in Figure 163.

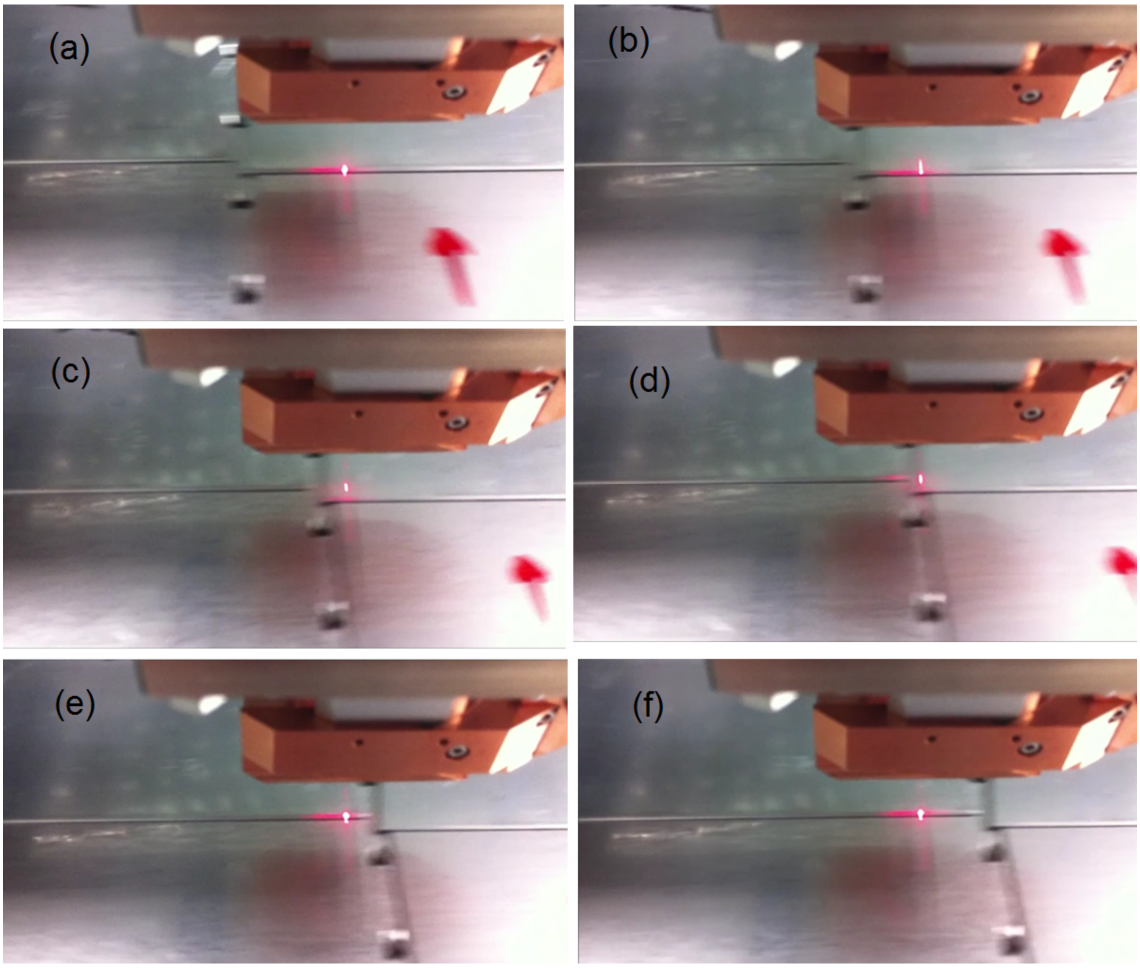

Figure 163 – Experiment to ensure latency correction, with red target laser beam visible on the substrates. (a) Beam following guide seam, (b) motion initiated approaching the new seam, (c) motion completed ready to follow new seam, (d) approaching new seam, (e) new seam picked up and (f) now following new seam.

The algorithm is linked to the X encoder so that the technique is independent of the shuttle speed. In order to confirm this, the test video method as shown in Figure 163 was repeated for various speeds, confirming the algorithm covered all manufacturing scenarios.

The PCB and control electronics are packaged in an industrial 19 inch, 3U rack and the internal physical layout is shown in Figure 164. The main board appears in the right hand side of the picture with Molex connections made to the external interfaces. Sub-D type connectors are visible in the lower part of the figure. On the left hand side of the figure is an Anybus adaptor to convert the RS232 feedback channels to be compatible with the industrial Profinet format for communication to the customer systems. At the very top of the photo is the 28 V power supply, feeding power to the Risley prism controllers.

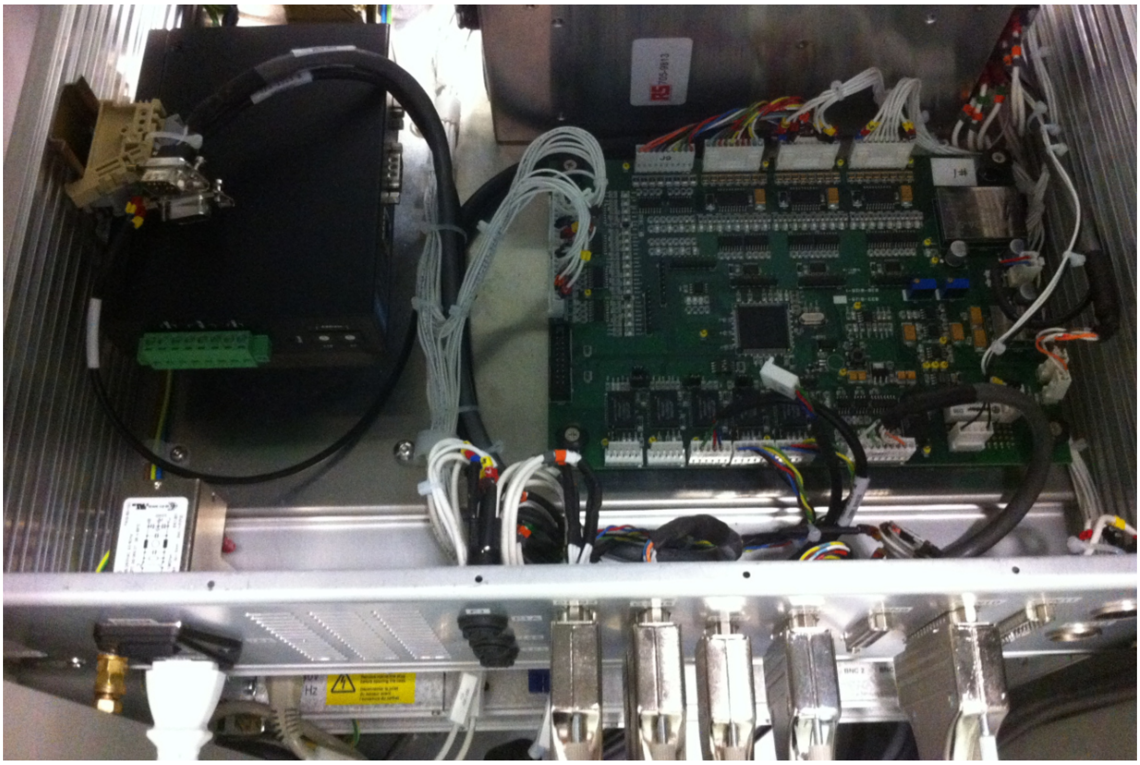

Figure 164- The electronics PCB as implemented in the main seam tracker cabinet.

The control PCB is installed in the main LPF rack as shown in Figure 165. There are two LEDs indicators on the front panel, one for indication of power to the unit and one flashing LED to indicate an error or absence of interlock. The blue button is programmed such that if held for one second, the system will clear and reset the electronics and re-calibrate the encoders on the Risley prism actuators. If a persistent error occurs, error diagnosis is performed via the @e1a? command via the RS232 data connection and the error code can be examined.

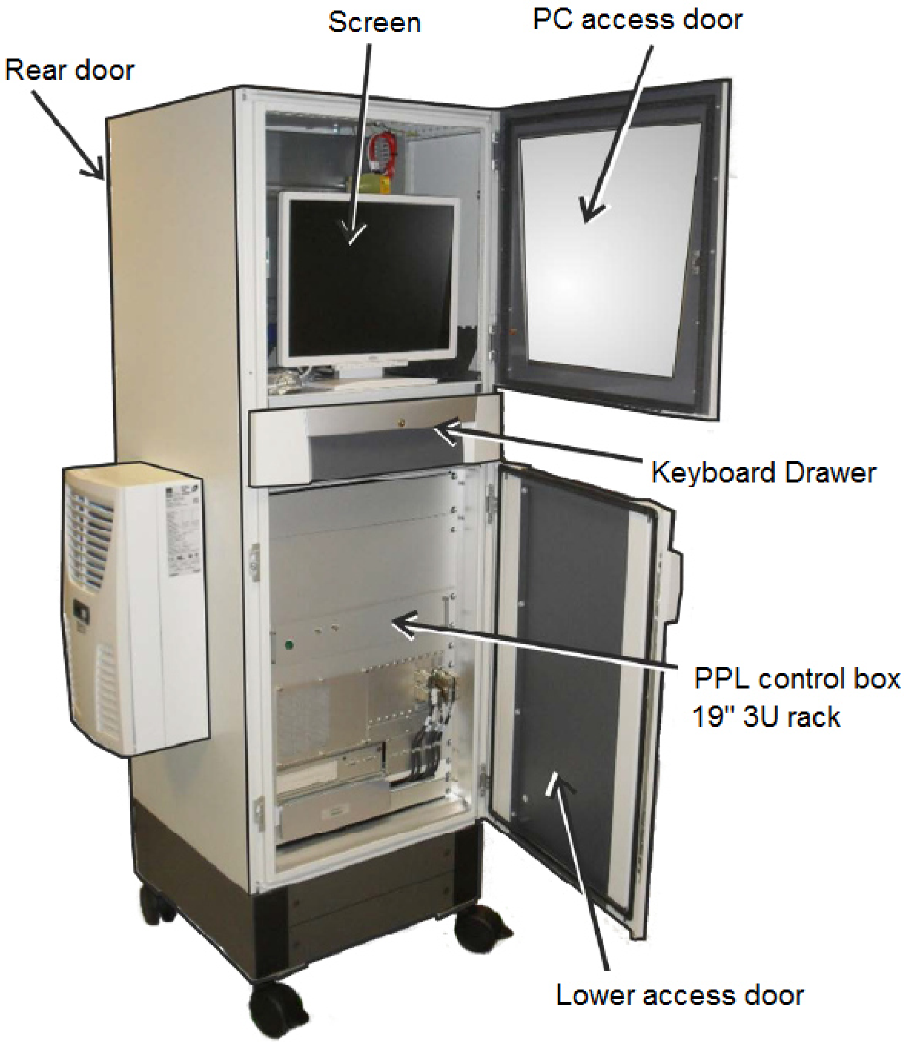

Figure 165 – Position of the PCB control box in the LPF system.

4.7.3 Summary of control electronics and software

The electronics architecture for the seam tracker system has been presented in this chapter, detailing the interconnections made to each of the attached subsystems. The proprietary algorithms which resolve issues of signal dropout and latency have also been presented, and the design of these was driven by the preceding sub-systems studies of the camera, LPF and Risley responses. In order to minimise any control interferences, all control feedback and power cabling is shielded from each other to ensure there is no instability either from crosstalk or from machine EMF interference.

A control electronics system was designed to cope with the expected latency of up to 100 ms, as found in the Risley prism studies and a binary filter was implemented within the software to eliminate analogue signal drop out voltages, as found in the camera and vision system studies.

Prior to shipment of the unit into the industrial environment the system successfully cleared independent inspection for CE certification for both the electronics and the processing heads.

4.8 System integration

The system integration and commissioning was approached in two stages. The first stage was to integrate the system at the Powerlase Photonics premises and the second stage was to install and monitor the system at the end customer's site.

Tests conducted at the Powerlase site consisted of testing the reliability and functionality of the system as a whole. Tests were carried out to determine the timing of the latency algorithm by transmitting a red beam through the system and videoing the response of the system to substrates of a maximum -3 mm to 3 mm displacement. The binary algorithm was tested by running the blanks under the system as different speeds and monitoring the integrity of the return signal from the Risley prisms. Throughout the duration of the experiment an Aerotech A3200 XYZ scanning table was used both to translate the substrates at a known speed under the processing heads and also to provide the crucial X position feedback via the stage encoder. Figure 166 shows a processing head based upon architecture 1 mounted for testing above the XYZ stage.

Figure 166 – Architecture 1 processing head mounted above Aerotech A3200 XYZ stage.

Figure 167 shows an example of tracking telemetry and the elimination of an analogue signal drop out from the positional data of the Risley prism. If this filter was turned off, the latency algorithm reacts and takes the spot rapidly to this location, leaving an undesired skip in Y location of the surface removal trail. The vision signal (solid line) shows a spike in the Y deviation signal, the prism telemetry feedback (dashed line) is offset in Y so that the return telemetry can be seen to be free of the spike.

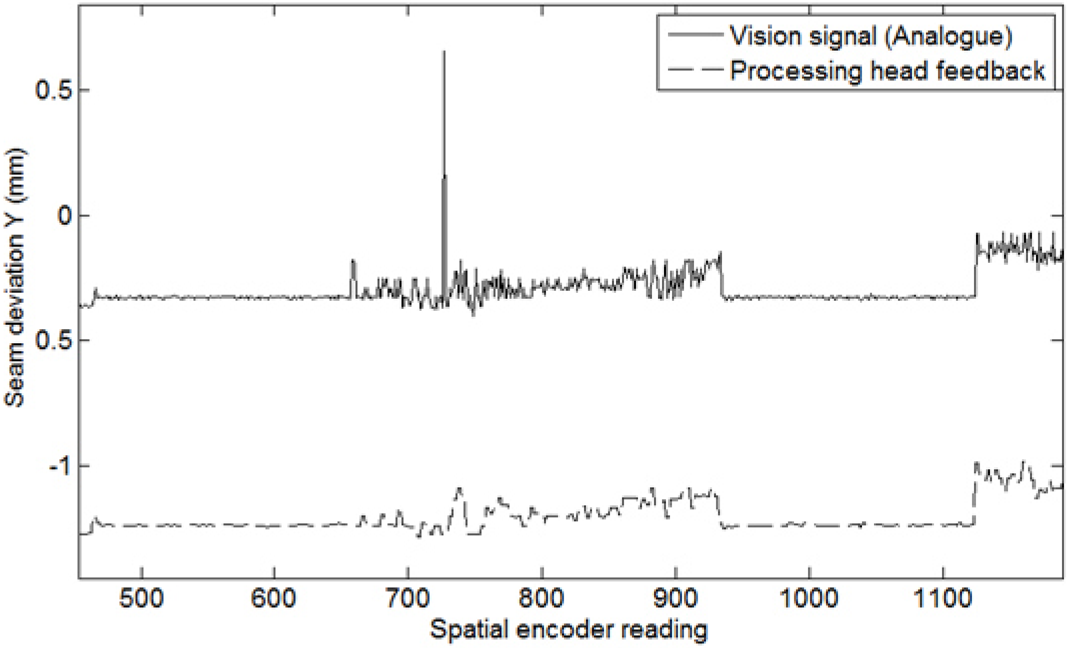

Figure 167 – Vision signal (solid line), feedback (dashed line).

In normal use the seam tracker eliminates processing and positioning errors on substrates which are all straight seams. To prove the seam tracker functionality, and calibrate the movement of the system upon installation at the customer's site, a seam with saw-tooth profile is constructed with a known and varying deviation in the Y position along the length of the substrate. This approach provides undisputable evidence to the customer that the seam tracker is functioning and is also essential for the calibration of the system to the substrates.

Figure 168 and Figure 169 show the position and feedback telemetry for two substrates with a deliberate and known variation in the seam profile in Y along their length.

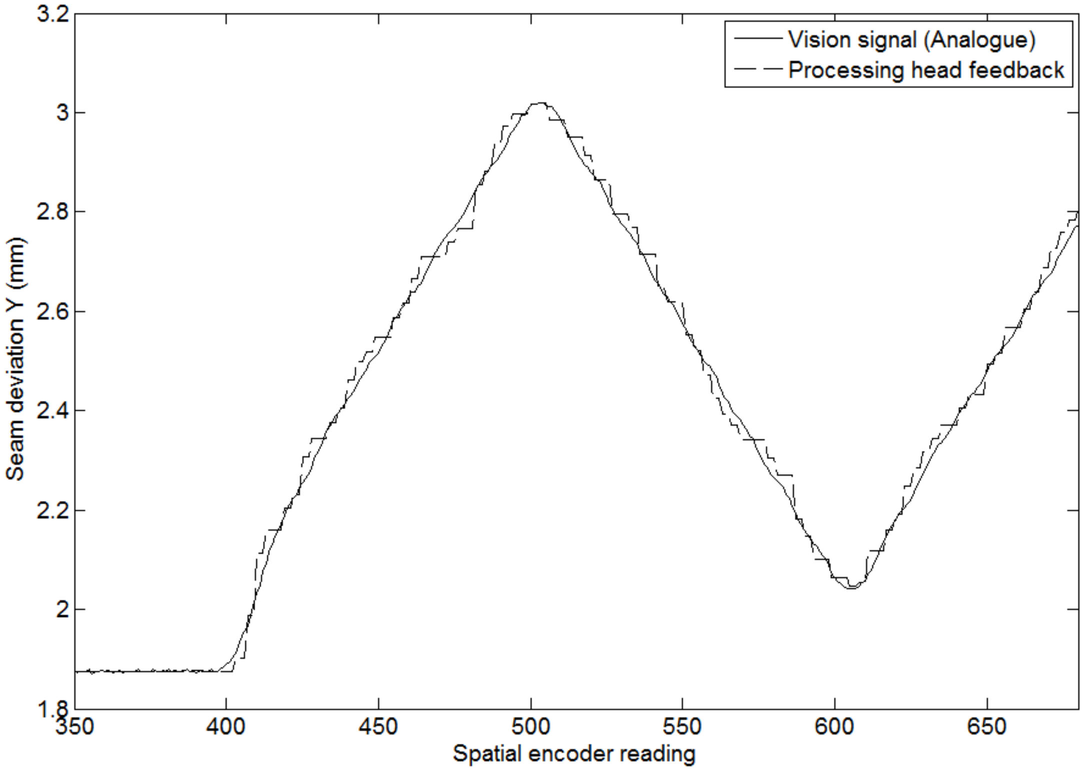

Figure 168 – Risley feedback telemetry signal vs vision signal feedback from the LPF – Substrate 1.

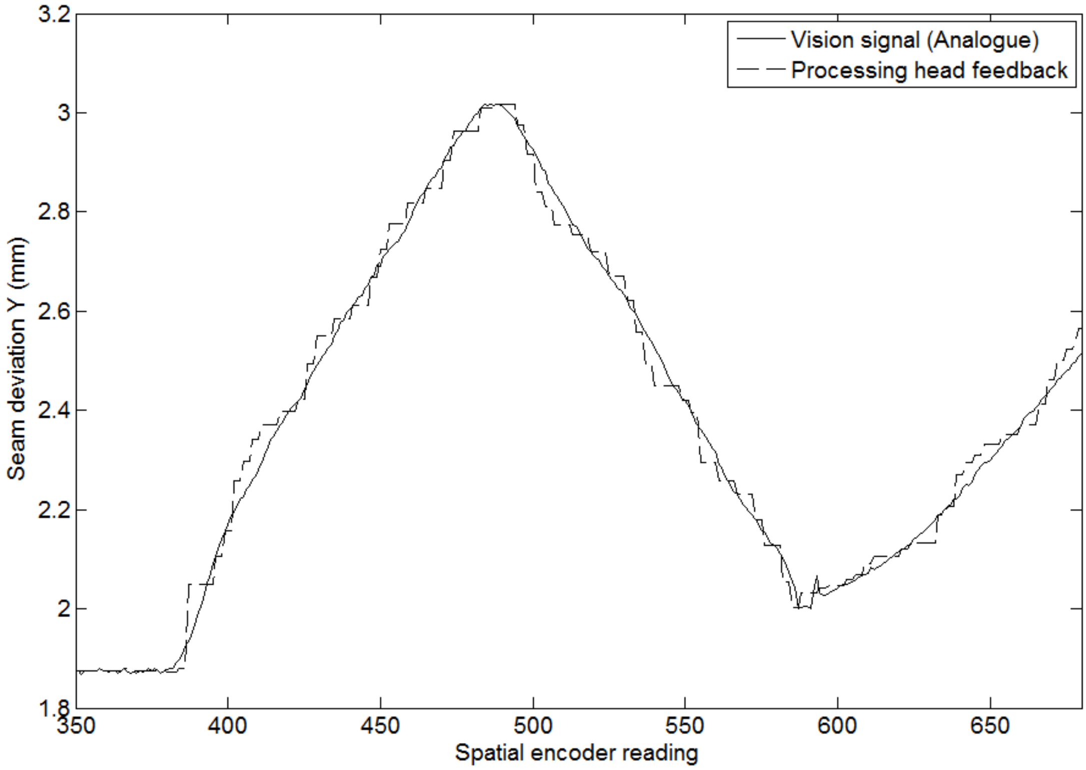

Figure 169 – Risley feedback telemetry signal vs vision signal feedback from the LPF – Substrate 2.

The physical trails left by the surface removal are shown in Figure 170 and in close up in Figure 171. The trail is observed to faithfully follow the seam on both the upper and lower side of the substrates accounting for the different X separation of the upper and lower processing heads from the camera. This approach is also employed on the customer site in order to re-calibrate the positional feedback due to changes in the position in Y and X of the processing heads and changes in the X encoder resolution.

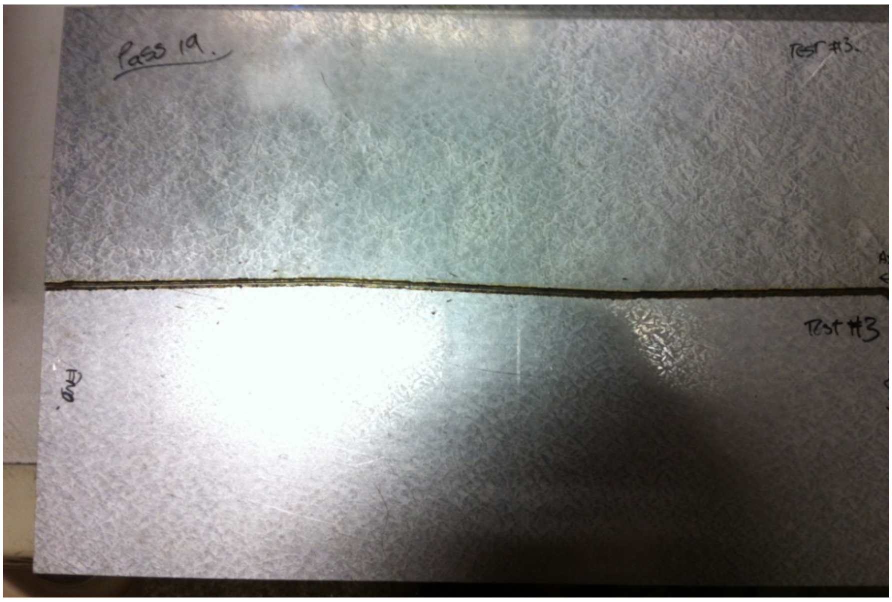

Figure 170 – Physical surface removal trail for the seam tracker.

Figure 171 – Close up of physical surface removal trail for the seam tracker.

4.8.1 Commissioning tests

Installation of the system took place at the customer site over a period of two weeks and was monitored for a period of three months afterwards. During this time the system was tuned and monitored to gain data. The seam tracker and the ability to record telemetry data in the seams was not only of interest to the optimisation of the system, but also permitted a study of the process as a whole.

The production cycles are broken up into six substrates per batch and an example of the telemetry data recovered from the seam tracker system is detailed in Figure 172. Each of the signals produced by the substrates is noted on the figure and the separation periods between the substrates, where the signal is relatively stable is also noted.

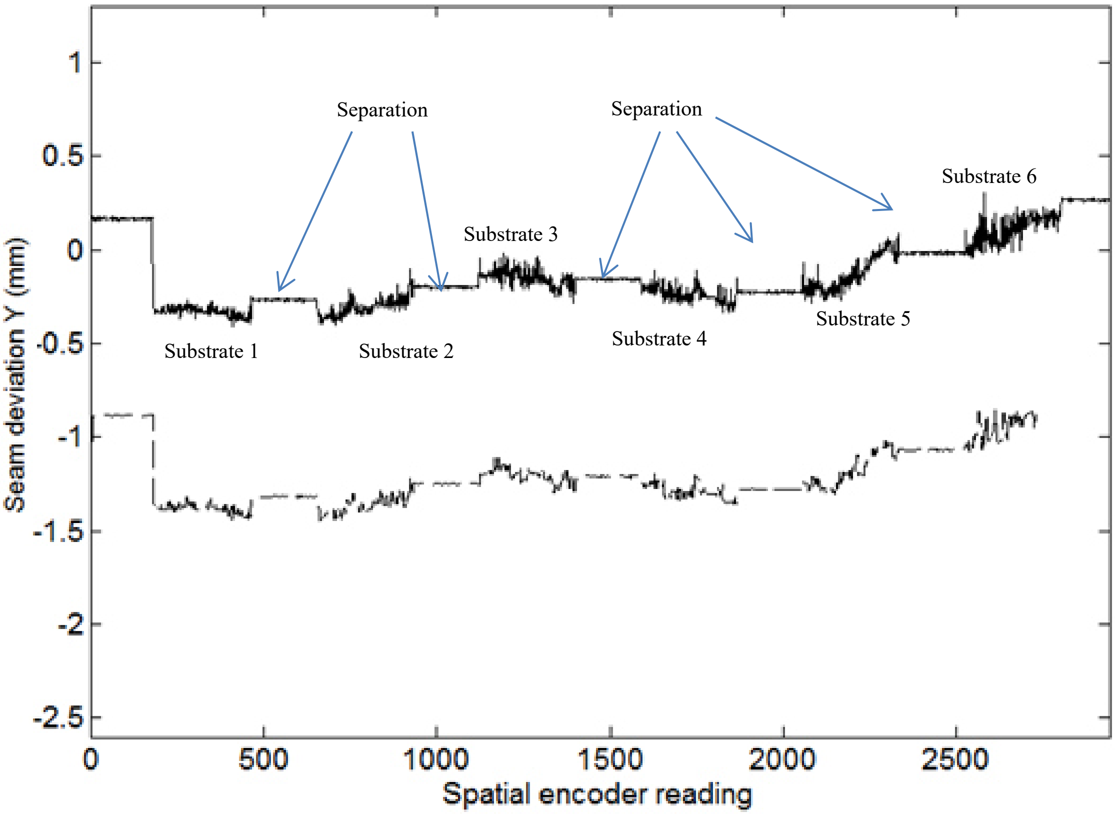

Figure 172 – Telemetry signals for a typical batch of substrates.

The telemetry is monitored for every blank via a laptop running a recording program from the RS232 output of the control electronics system. From this data, statistics on large volumes of blanks can be analysed. Figure 173 shows the mean average positions of the substrates as a function of the X encoder position. The first substrate is seen to have a linear change in seam position, along with substrate four and five. Substrates two, three and six all appear relatively close to stable values of Y across their length. An odd deviation is seen along the length of the substrate in substrates two and five, which seem to be consistent with a mechanical clamping issue. The substrate to substrate placement variance on average is deduced to be approximately 0.4 mm from beginning to end of cycle.

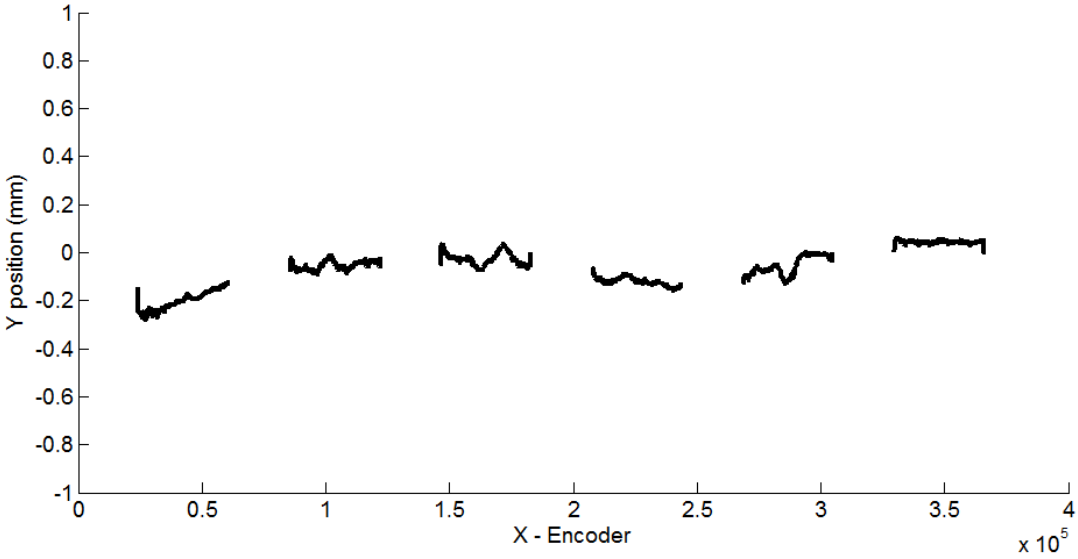

Figure 173 – Averaged positions of substrates over 100 production cycles.

Statistical analysis of the placement of the substrates is also performed for 100 production cycles; in this analysis the placement positional accuracy of the substrates per cycle can be deduced. The results shown in Figure 174 show a histogram, for each substrate, of a single position in X roughly central to the substrate over 100 production cycles.

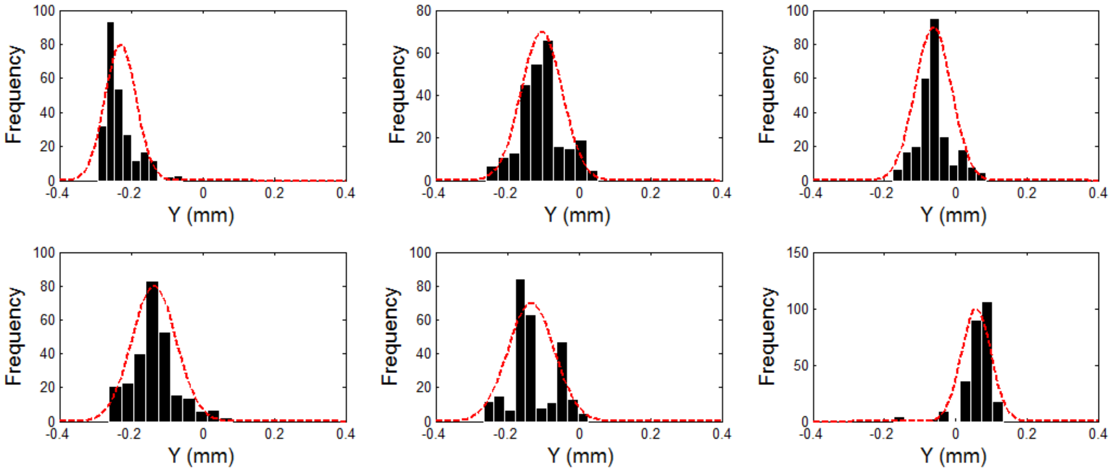

Figure 174 – Histogram of placement accuracies of substrates for 100 cycles.

This data is also repeated in Figure 175, which shows the positional feedback of the Risley prisms, the position in X has been corrected for the offset between the head and the camera so the same sample point on the substrate was used. The positional offset reported in Y is due to the offset in Y between the camera and the physical position of the processing head. It was deduced that the processing head is approximately 0.6 mm offset from the camera in Y, which is used for the calibration of the Y position of the beam as set from the Risley actuator.

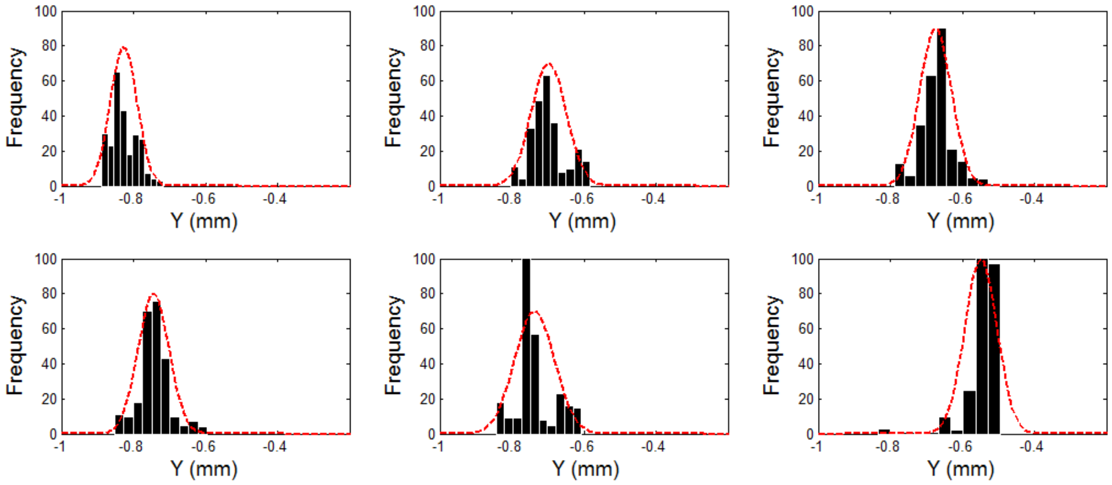

Figure 175 – Positional feedback signal from the seam tracker same 100 cycles.

Table 8 details the statistical summary of the collected data for both the mean position of the seam in Y and the value for the 95 % confidence limits (2σ). It is observed that the placement tolerances for the process are ±122 μm and the maximum difference in mean substrate position in Y is 282 μm.

Substrate	Mean position measured	Standard deviation measured 2σ	Mean position feedback	Standard deviation feedback 2σ
1	-229	86	-826	72
2	-98	122	-693	106
3	-58	112	-671	94
4	-131	136	-743	92
5	-128	140	-734	114
6	52	106	-655	112

Table 8 – Comparison of camera measured position and control feedback from the Risley prism for 300 production cycles.

By taking the worst case scenario of placement tolerances the overall range of movement experienced by the seam tracker in the Y dimension during production is 523 μm to the 2σ confidence limits. A deviation from centre of ±100 μm would potentially cause a process failure; hence the seam tracker is effectively maintaining and improving the process yields, if it were it not present then the process yield would be significantly worse.

An important lesson learnt from the implementation of the seam tracker, both by the supplier and customer was that management of swarf produced by this process and is crucial to the long term performance of the system.

Eqn. (40) estimates the mass of the swarf generation for this surface removal system, where R is the repetition rate, ρ is the density of the material being removed, T is the total length of time the process is applied and w_X, w_Y, w_Z are the spot width in *X*, *Y* and *Z* respectively.

$$S_f = R\rho w_X w_Y w_Z T \tag{40}$$

Assuming a material of steel with a density of 8050 kg/m^3 and w_X =2 mm, w_Y =0.5 mm, w_Z=1 µm and a 24 hour process time, this equates to 7 kg of swarf generated every day of production. If left unmanaged this swarf accumulates around the processing heads and causes optical damage. Even though protective cover slides and high speed cross-jets are used, these will eventually be overwhelmed and damage will occur on the optics. The lower optic is particularly prone to this issue as gravity assists the deposit of debris into the optics. This is resolved by the addition of industrial extraction that removes the swarf away from the process.

To complete this section of this chapter a picture of the original actuated processing head is shown in Figure 176 on a service visit after greater than two years continuous service.

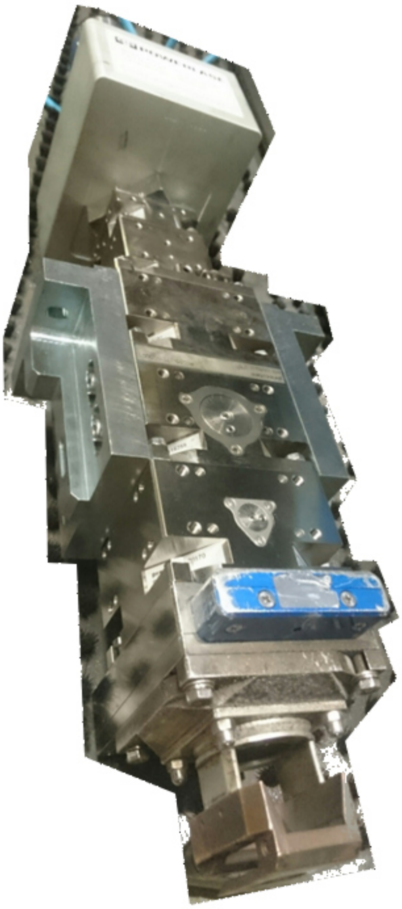

Figure 176 – An architecture 1 processing head after two years of service.

Chapter 5 – Conclusions

5.1 Summary

The development of a novel approach to a compact actuated beam delivery system has been presented that has extended the capabilities of the host company and enabled the exploitation of the high power laser technology in new applications. The development of the technology has been presented from the cavity and free space modelling of the lasers beams produced by the Rigel i-series lasers. This produced fibre coupling schemes which transmitted over 95 % of the average power and were shown to successfully couple average powers up to 1.6 kW at pulse energies of 0.16 mJ into a square core fibre of diameter 600 μm. The beam homogenisation exploited by the multimode mixing in the fibre produced a homogenised square form with no visible speckle, an output NA < 0.08 and 20% - 80% edge width < 60 μm. This square form was transformed by means of two possible architectures of processing head, which shaped the beam into the optimum homogenised rectangular shape for the process. A novel compact beam actuation system based upon Risley prisms was designed to be compatible with either beam shaping architecture, capable of translating the beam greater than ±6 mm in the Y axis with less than 4% distortion in the beam size. And with a theoretical accuracy of ±2 μm in the Y dimension. Both architectures of the processing heads confined the beam and maintained a transmission of >95% over all failure conditions of the Risley prism. Architecture 1 was deployed first and was the subject of the majority of this thesis, later systems based upon architecture 2 also proved equally, if not slightly more successful.

This optical arrangement was coupled with a vision system and proprietary control electronics that tracked seam positions to ±50 μm in Y and were capable of eliminating positional latency and erroneous tracking data. Each element of the system was evaluated prior to integration ensuring that the interfaces between each component were understood and the performance was evaluated. The camera and vision system was found to detect seams of dimensions >50 μm in both Y and Z axes. The analogue output of the seam tracker was evaluated and found to track to within ±85 μm to 95% confidence limits. The control electronics were designed to be able to manage the 100 ms latency of the prisms and also a binary filtering technique for removing erroneous data from the positional data was presented.

System integration at Powerlase showed that the system was able to cope with the full range of actuation required by tracking blanks with deliberate shapes in the y dimension, the behaviour of system when separate blanks were offset by the maximum 6mm was also tested and showed that the latency algorithm would detect and correct the position of the beam 100 ms in advance of the blank appearing under the processing head.

Installation and analysis of the system at the customer site showed that in practice the system was tracking substrates over a mean range of 282 μm and correcting placement tolerances of ±122 μm (2σ) giving a total range of correction in the Y dimension of 523 μm to 95% confidence limits. Y positional deviations of ±100 μm would cause issue with production yield hence the seam tracker system was contributing to the maintenance of the production yield on this system.

5.2 Conclusions

The system successfully tracked seams with dimensions >50 μm over a range of ±6 mm correcting for latency and seam positional signal integrity. The compact approach of this system enabled a process for the customer that was not possible with commercially available systems based upon the cheaper galvanometers technology. Neither would the supplier offer the beam shaping requirements at the time of development. The beam actuation system developed as a result of this thesis offers stable seam tracking that is comparable or better than commercially available systems, the two main features where this technique advances the state of the art is the increased resolution of the optical positioning of the laser beam and the compact size of the inline Risley actuator. The Risley actuation technique is much smaller than any commercially available system. This compact size coupled with the in-line actuation of the beam, which requires no space consuming beam deflection, enables the optical design of processing heads that can fit within space constraints that are currently unachievable with commercial processing heads.

Seven systems were deployed based upon the beam shaping technology as a result of this study, which exploited the technology development in chapter 3 of this thesis. Three systems based upon the seam tracker technology were deployed into service as a result of the studies in chapter 4. All these systems are in heavy industrial environments and are typical producing for the full 24 hour period. The systems have, so far, proven to be robust and have produced a cumulative total of > 6 million substrates at the time of writing.

The systems have proven to be a commercial success and the novel approach to the beam delivery has opened up a new manufacturing technique for the customer and added to the system capability of Powerlase photonics.

5.3 Further work

There are many areas of further research that can be completed on this topic. The first major item to broach would be the cost. The Risley prism actuation system is approximately three times more expensive than an equivalent, larger, system based upon a Galvanometer. Until this cost is significantly reduced the market for this device will remain niche and based upon optical delivery where tight form factors are required. There are some areas of trade that are potentially likely to yield cost reduction, the angular resolution is far more accurate than required and simpler encoders could be used. The action of the beam is restricted in two dimensions in normal use; this leads to the possibility of removing optical components and potentially motors and electronics by either altering the optical design or mechanically gearing the motion of the two prisms together, or only moving one prism. There are also several beneficial changes that can be made to simplify the mechanical construction of the processing heads. Although the modular approach to their design permits a wide range of configurations with little design effort, it also imparts a cost that could be avoided by creating sections of the processing heads with fewer connections between mechanical parts.

A final subtle area of improvement to this project would be the extension of the scope to include a better understanding of how the laser radiation interacts with the substrate material. Research in this area may yield a better understanding of the process and impact both the laser and the processing head design.

REFERENCES

1 – EPIC Worldwide Lasers Market and Technology Report (2014).

2 – J. W. Dawson, M. J. Messerly, R. J. Beach, M. Y. Shverdin, E. A. Stappaerts, A. K. Sridharan, P. H. Pax, J. E. Heebner, C. W. Siders and C. P. J. Barty , "Analysis of the scalability of diffraction-limited fiber lasers and amplifiers to high average power," Optics express. **96**, 13240 (2008).

3 – H. Hugel, "New solid-state lasers and their application potentials," Optics and Lasers in Engineering. **34**, 213 (2000).

4 – J. Canning, "Fibre lasers and related technologies," Optics and Lasers in Engineering. **44,** 647 (2006).

5 – E. Armandillo and C. Norrie, "Diode-pumped high-efficiency high-brightness Q-switched Nd:YAG slab laser," Optics Letters. **22**, 1168 (1997).

6 – Y. F. Chen, "Optimization in Scaling Fiber-Coupled Laser-Diode End-Pumped Lasers to Higher Power: Influence of Thermal Effect," IEEE Quantum electronics. **33**, 1424 (1997).

7 – C. M. Jefferson, J. A. Hoffnagle, "An achromatic refractive laser beam reshaper," Proc. society of photo-optical Instrumentation engineers SPIE. 5175, 1 (2003).

8 – Z. X. Feng, B. D. Froese, C. Y Huang, D. L Ma, R. G. Liang, "Creating unconventional geometric beams with large depth of field using double freeform-surface optics," Applied optics. **54**, 6277 (2015).

9 – A. Laskin, V. Laskin, A. Ostrun, "Square shaped flat-top beam in refractive beam shapers", Proc. Of SPIE, 9581, 95810K (2015).

10 – A. Laskin, V. Laskin, A. Ostrun, "Freeform beam shaping in optical systems of high-power lasers". Proc of SPIE, 9345, 93450J (2015).

11 – J. A. Hoffnagle, C. M. Jefferson, “Design and performance of a refractive optical system that converts a Gaussian to a flattop beam,” Applied Optics. **39**, 5488 (2000).

12 – B. Kress, P. Meyruies, *Digital diffractive optics*, ISBN 0-471-98447-7 (2000).

13 – S. Li , Y. Wang , Z. Lu , L. Ding , C. Cui , Y. Chen , D. Pengyuan, D. Ba, Z. Zheng, H. Yuan, Lei Shia, Z. Bai, Z. Liu, C. Zhu, Y. Dong, L. Zhou. “Spatial beam shaping for high-power frequency tripling lasers based on a liquid crystal spatial light modulator,” Optical Communications. **367**, 181 (2016).

14 – T. Haist, W. Osten, “Holography using pixelated spatial light modulators-Part 2: applications,” Journal of Micro-nanolithography MEMs and MOEMS. **14**, 041311 (2015).

15 – M. Ghisoni, J. Bengtsson, J. A.Vukusic, H. Martinsson, A. Larsson, “Single and multimode VCSELs operating with continuous relief kinoform for focussed spot- array generation,” IEEE Photonics Technology letters. **9**, 1466 (1997).

16– O. Blomster, M. Blomqvist, S. Campbell, M. Palsson, “Superior power handling in optical fiber cables for multi-kW lasers,” Proc SPIE, **8963**, 89630B, (2014).

17 –X. D. Gao, S. J. Na, “Detection of Weld Position and Seam Tracking Based on Kalman Filtering of Weld Pool Images,” Journal of Manufacturing Systems. **24**, 1 (2005).

18 – Z. Ye, G. Fang, S. Chen M. Dinham. “A robust algorithm for weld seam extraction based on prior knowledge of weld seam,” Sensor Review. **33**, 125 (2013).

19 – L. N. Gaxiola, V. H. Diaz-Ramirez, J. J. Tapia, P. García-Martínez, “Target tracking with dynamically adaptive correlation,” Optics Communications. **365**, 140 (2016).

20 – R. E. Kalman, "A New Approach to Linear Filtering and Prediction Problems," Journal of Basic Engineering, 82:35 (1960).

21 – D. Xu, M. Tan, X. Zhao, Z. Tu. “Seam Tracking and Visual Control for Robotic Arc Welding Based on Structured Light Stereovision,” International Journal of Automation and Computing. **1**, 63 (2004).

22 – Y. Q. Chen, X. D. Gao, J. Y. Huang, Q. Wen, “Detection of Weld Seam Position based on Infrared Image during High Power Fiber Laser Welding,” Chemical engineering and material properties II. **549,** 1007 (2012).

23 – X. D. Gao, “Seam tracking based on Kalman filtering of micro-gap weld using magneto-optical image,” International journal of advanced manufacturing technology. **83**, 21 (2016).

24 – Highyag “Laser Processing Head PDT-B,” http://www.highyag.com/Laser-Processing-Heads/laser-processing-PDT-B.html

25 – Precitec “ScanTracker,” http://www.precitec.de/en/products/joining-technology/processing-heads/scantracker/

26 – J. E. Kesner K. M. Hinrichs, L. E. Narkewich, T. Stevens, “Compact optical gimbal as conformal beam director for large field of regard lasercom applications,” Proc. of SPIE, 9354 (2015).

27 – J. I. Montagu, H. DeWeerd, P. Honkanen, “XY scan engine with micro-radian accuracy,” Proc. SPIE. 2383, 449 (1995).

28 – D. A. Henderson, M. R. Wrona, “Compact wide angle optical beam steering device for use in galvanometer scanners,” Patent US2015219892-A1.

29 – H. D. Tholl, “Novel Laser Beam Steering Techniques,” Proc. of SPIE. 6397**,** 39708 (2006).

30 – J. Montagu and H. DeWeerd, "Optomechanical scanning applications, techniques and devices," SPIE Infrared & Electro-Optical Systems Handbook. **3**, (1996).

31 – J. Y. Wang, Q. Hao, Y. Song, Y. Hu, “Novel MOEMS-based beam steering method,” International Conference on optical instruments and technology optical systems and modern optoelectronics instruments. Proc. SPIE, 8197, 81971D, (2011).

32 – M. T. Johnson, G. S. Seetharaman, “Thermo-optic variable blazed grating for beam steering - art. no. 671505,” Proc of SPIE, 6715, 71505, (2007).

33 – V. Hinkov, “Beam steering without moving parts,” Proc. SPIE. 2783, 126-134 (1996).

34 – Y. Shen, X. G Luo, “Efficient bending and focusing of light beam with all-dielectric subwavelength structures,” Optics Communications. **366**, 174 (2016).

35 – J. Mur, B. Kavcic, I. Poberaj, “Fast and precise Laguerre-Gaussian beam steering with acousto-optic deflectors,” Applied Optics, **52**, 6506 (2013).

36 – Gooch and Housego, “4200 Crystal Quartz AOM,”
https://www.goochandhousego.com/wp-content/pdfs/4200_UV_97_002890_02_Rev_A.pdf.

37 – J. Y. Li, Q. Peng, K Chen, C.Y Fu. “High precision pointing system based on Risley prism: analysis and simulation,” Proc. SPIE. 9255 (2015).

38 – S. T Hartford, H. Gutierreez, M. Newman, R. Pierce, T. Quakenbush. “Infrared Risley Beam Pointer,” Proc. SPIE. 8971 (2014).

39 – V. F. Duma, “Risely prism scanners with different configurations: a multi-parametric analysis,” Proc. SPIE. 89250P, (2014).

40 – C. Schwarze. “A new look at Risley prisms,” Photonics spectra. June (2006).

41 – Y. Zhou, Y. F. Lu. “Motion control of the wedge prism in Risley-prism based beam steering system for precise targeting,” Applied Optics. **52** (2013)

42 – V. Lavigne, B. Ricard. “Fast Risley prism camera steering system calibration and image distortion correction through the use of a three-dimensional refraction model,” Optical Engineering. **46**, 043201 (2007).

43 – A. Li, X. Gao, W. Sun, W. Bian, H. Liu, L. Liu. “Inverse solutions for a Risley prism scanner with iterative refinement by a forward solution,” Applied Optics. **54**, 9981 (2015).

44 – Y. Yang, “Analytic solution of free space optical beam steering using Risley prisms,” Journal of lightwave technology. **26,** 3576 (2008).

45 – E. Hecht, *Optics* - 4th Edition, ISBN 0-8053-8566-5 (2001).

46 – C. L. Xu, W. P. Huang, J. Chrostowski, and S. K. Chaudhuri, “A full-vector beam propagation method for anisotropic waveguide,” J. Lightwave Technol. **12**, 1926 (1994).

47 – H. Kogelnik, T. Li, “Laser Beams and Resonators,” Proceedings of the IEEE. **54**, 1312 (1966)

48 – W. P. Huang and C. L. Xu, “Simulation of three-dimensional optical waveguides by a full-vector beam propagation method,” IEEE J. Quantum Electron. **29**, 2639 (1993).

49 – P. A. Bélanger, "Beam propagation and the ABCD ray matrices," Opt. Lett. **16**, 196 (1991).

50 – A. E. Siegman*, Lasers*, University Science Books, ISBN 0-935702-11-3 (1990)

51 – A. E. Siegman, “How to (Maybe) Measure Laser Beam Quality,” Optical Society of America Annual Meeting Long Beach California. (1997).

52 – A. Yariv, *Optical Electronics,* Saunders College Publishing - 4th Edition (1971).

53 – W. Koechner, M. Bass, *Solid-state lasers,* ISBN 0-387-95590-9 (2003).

54 – W. Koechner, *Solid State Laser Engineering*: ISBN 038729094X (Springer 5th Edition 1999).

55 – Frank L Peldrotti, *Introduction to optics.* ISBN 1292022566,Pearson 3rd Edition (2013).

56 – B. Chen, J. Dong, M. Patel, Y. Chen, A, Kar, M. Bass, “Modelling of high power solid-state slab lasers,” Proc. SPIE. **4968**, 1 (2013).

57 – H. Shu, Y. Chen, M. Bass, “Modelling a diode pumped Nd:YAG rod laser,” Proc. SPIE. **6100**, (2006).

58 – H. Shu, M. Bass, “Three-dimensional computer model simulating realistic solid-state lasers,” Applied Optics. **4**, (2007).

59 – J. Carroll, J. Whiteaway, D. Plumb, *Distributed feedback semiconductor lasers*, ISBN 0-8194-2660-1 (2006).

60 – A. Smith, B. Do, R. Shuster, D. Collier, “Rate equation model of bulk optical damage of silica, and the influence of polishing on surface optical damage of silica,” Proc. SPIE. 6873, U118 (2008).

61 – J. Y Natoli, L. Gallais, H. Akhouayri, C Amra, “Laser-induced damage of materials in bulk, thin-film, and liquid forms,” Applied Optics. **41**, 3156 (2002).

62 – P. A. Cheremkin, N. N. Evitikiev, V. V. Krasnov, L. A. Porshneva, V. G. Rodin, S. N. Starikov, “Comparison of kinoform synthesis methods for image reconstruction in Fourier plane,” Proc. SPIE. **9131**, 913124 (2014).

63 – R. W. Gerchberg and W. O. Saxton, “A practical algorithm for the determination of the phase from image and diffraction plane pictures,” Optik. **35**, 237 (1972).

64 – J. W. Cooley, J. W. Tukey. “An algorithm for the machine calculation of complex Fourier series,” Math. Comput. **19**, 297 (1965).

65 – A. P. Bondareva, P. A. Cheremkin, N. N. Evtikhiev, V. V. Krasnov, V. G Rodin, S. N. Starikov, “Increasing quality of computer generated kinoforms using direct search with random trajectory method,” Proc. SPIE, **9216**, 92161J (2014).

66 – J. Xia, L. Yang, W. Lei, Z. Yang, J. Chen “Speckle-suppressed phase-only holographic three-dimensional display based on double-constraint Gerchberg–Saxton algorithm,” Applied optics. **54**, 6994 (2015).

67 – Y. M Chen, Y. Q Wei, D. Y. Liu, D. Boutat, X. K Chen, “Variable-order fractional numerical differentiation for noisy signals by wavelet denoising,” Journal of Computational Physics. **311**, 338 (2016).

APPENDIX A

This chapter contains additional information for reference

5.4 Matlab code used to analysis the focussed beam

```
% Version 12 - (30/11/2015)
%Program to take in beam profile data and calculate FWHM, homogeneity
and Edge width

clear all;
clc;

A=imread('number_23_105_-105.bmp');  % Read in the Irradiance bitmap
%B=imread('Dark.jpg');               % Read in the dark levels
A=double(A);                         % Convert image to a double float
%B=double(B); B=0;                   % Convert dark to a double float
B=0;
% Note : even though camera is monochrome, it stores as RGB array
B=B(:,:,1);B=B';      % Select one of the RGB channels and flip axes
A=A(:,:,1);A=A';      % Select one of the RGB channels and flip axes
A=A-B;                % Subtract the dark field form the image

[yoffset,xoffset]=find_centre_fn2(A);
% Custom function to find the Irradiance profile centre

%%%%%%%%%% Homogenisation algorithm %%%%%%%%

Xwidth=0.4; % Select the  FWHM in X (mm)
Ywidth=2.0; % Select the  FWHM in Y (mm)
Rangex=round(((Xwidth./5.2)*0.9*1000)./2)
% Work out the 90% X FWHM range
Rangey=round(((Ywidth./5.2)*0.9*1000)./2)
% Work out the 90% Y FWHM range

XL=(xoffset-Rangex);XR=(xoffset+Rangex);
% X Subset where the homogeneity is measured
YL=(yoffset-Rangey);YR=(yoffset+Rangey);
% Y Subset where the homogeneity is measured
Unisub=A(YL:YR,XL:XR);
% Subset of A

figure(1);
% Draw the overlay as a visual reference
line([XL XR XR XL XL],[YL YL YR YR YL],[1000 1000 1000 1000 1000]);

av=mean(mean(Unisub));            % Mean value for the subset XYplane
uniformity=(Unisub-av)./av;       % Homogeneity of each
uniformity=mean(std(uniformity)) % Final summed figure for Homogeneity

% Image the Irradiance profile for review
figure(1);
surf(A,'edgecolor','none');view(0,90);
colormap jet

% Set up a camera calibration
Ycalib=5.2;        %um per pixel  - Thorlabs DCC1545M
Xcalib=5.2;        %um per pixel  - Thorlabs DCC1545M
S=size(A);         % establish the size of the domain being measured
```

```
Y=[1:S(1)]; Y=Y-yoffset;Y=Y.*Ycalib;  % set up and scale the Y axis
X=[1:S(2)]; X=X-xoffset;X=X.*Xcalib;  % set up and scale the X axis

% Averaged line slice made of twenty individual lines for X and Y
for i=1:21
    xdata_av(i,:)=A(yoffset-(11-i),:);
% Sample 21 lines about the irradiance centre
end;

for i=1:21
    ydata_av(i,:)=A(:,xoffset-(11-i));
% Sample 21 lines about the irradiance centre
end;
xdata=mean(xdata_av); % Average 21 lines about the irradiance centre
ydata=mean(ydata_av); % Average 21 lines about the irradiance centre


% Use the sampled slices to establish the 20-80 Edge width
ticker=1;                               %%%%%%%%%%%%%%%%%%%%%%%%
while xdata(ticker)<0.2*max(xdata);     % Find the left 20% edge
    ticker=ticker+1;                    %%%%%%%%%%%%%%%%%%%%%%%%
end;
left20=X(ticker);

ticker=1;                               %%%%%%%%%%%%%%%%%%%%%%%%
while xdata(ticker)<0.8*max(xdata);     % Find the left 80% edge
    ticker=ticker+1;                    %%%%%%%%%%%%%%%%%%%%%%%%
end;
right20=X(ticker);

x20_1=right20-left20;                   %left side 20%-80% value
% and other side
ticker=xoffset;                         %%%%%%%%%%%%%%%%%%%%%%%%%
while xdata(ticker)>0.8*max(xdata);     % Find the right 80% edge
    ticker=ticker+1;                    %%%%%%%%%%%%%%%%%%%%%%%%%
end;
left20=X(ticker);

ticker=xoffset;                         %%%%%%%%%%%%%%%%%%%%%%%%%
while xdata(ticker)>0.2*max(xdata);     % Find the right 20% edge
    ticker=ticker+1;                    %%%%%%%%%%%%%%%%%%%%%%%%%
end;
right20=X(ticker);
x20_2=right20-left20;        %left side 20%-80% value

x20=(x20_1+x20_2)./2         % Average the two 20%-80% values

%%%%%%% Find FWHM %%%%%%%%%%%%%%%%%%%%%%%%%%%%%%

ticker=1;
while xdata(ticker)<0.5*max(xdata);   % Same algorithm as 20%-80%
    ticker=ticker+1;
end;
FWHMleft=X(ticker);
                    % Finds X values at either side of the
                    % irradiance profile at 50% slicing level
ticker=xoffset;
while xdata(ticker)>0.5*max(xdata);
    ticker=ticker+1;
end;
FWHMright=X(ticker);
```

```
FWHMx=FWHMright-FWHMleft;
%%%%%%%%%%%%%%%%%%%%%%%%%%%%%%%%%%%%%%%%%%%%%%%%%%%%%%%%%%%%%%%%%%%%%%%

%%%%%%%%%%%%%%%%%%%%%%%%%%%%%%% FWHM in Y axis %%%%%%%%%%%%%
ticker=1;
while ydata(ticker)<0.5*max(ydata);
    ticker=ticker+1;
end;
FWHMleft=Y(ticker);

ticker=yoffset;
while ydata(ticker)>0.5*max(ydata);
    ticker=ticker+1;
end;
FWHMright=Y(ticker);

FWHMy=FWHMright-FWHMleft;
%%%%%%%%%%%%%%%%%%%%%%%%%%%%%%%% End of FWHMy %%%%%%%%%%%%%

%%%%%%%%%%%%%%%%%%%%%%%%%%%%%%%%% Plot results %%%%%%%%%%%%
figure(2)
subplot(2,1,1);h=plot(X./1000,xdata,'LineWidth',3);
title({['FWHM= ' num2str(FWHMx./1000,3) 'mm'],['Homogeneity = '
num2str(uniformity*100,2) '%']});
axis([-2.0 2.0  0 1.5*max(xdata)]);
set(h,'color','black');
xlabel('mm');set(gca,'XMinorGrid','on')
subplot(2,1,2);h2=plot(Y./1000,ydata,'LineWidth',3);
title({['FWHM= ' num2str(FWHMy./1000,3) 'mm'],['Edge 20-80 = '
num2str(x20,4) 'um']});
set(h2,'color','black');
axis([-2.0 2.0 0 1.5*max(xdata)]);
xlabel('mm');
set(gcf,'color','white')
set(gca,'XMinorGrid','on')
%%%%%%%%%%%%%%%%%%%%%%%%%%%%%%%%%%%%%%%%%%%%
```